Dynamic synchrotron imaging of brittle failure in crustal rocks

Neelima Kandula

THÈSE

Pour obtenir le grade de

DOCTEUR DE L'UNIVERSITÉ GRENOBLE ALPES

Spécialité : Sciences de la Terre et de l'Univers et de l'Environnement

Arrêté ministériel : 25 mai 2016

Présentée par

Neelima KANDULA

Thèse dirigée par **Jérôme WEISS**,Directeur de Recherche, Université Grenoble Alpes
et codirigée par **François RENARD**,Professeur, UJF

préparée au sein du **Laboratoire Institut des Sciences de la Terre**
dans **l'École Doctorale Sciences de la Terre de lEnvironnement et des Planètes**

Utilisation du rayonnement synchrotron pour l'imagerie dynamique de la rupture fragile dans les roches crustales

Dynamic synchrotron imaging of brittle failure in crustal rocks

Thèse soutenue publiquement le **28 juin 2021**,
devant le jury composé de :

Monsieur Jérôme WEISS
DIRECTEUR DE RECHERCHE, CNRS délégation Alpes, Directeur de thèse
Monsieur Daniel BONAMY
INGENIEUR HDR, CEA Paris-Saclay, Rapporteur
Madame Marie VIOLAY
PROFESSEUR ASSISTANT, Ecole Polytechnique Fédérale de Lausanne, Rapporteure
Monsieur Knut Jørgen MÅLØY
PROFESSEUR, Universitetet I Oslo, Président

Dynamic synchrotron imaging of brittle failure in crustal rocks

Neelima Kandula

THESIS

for the degree of

Philosophiae Doctor

Faculty of Mathematics and Natural Sciences

University of Oslo

Doctoral School Earth, Environmental and Planetary Sciences (STEP)

University of Grenoble

Acknowledgements

Four and half years have been a lot of new experiences in many ways. For the very first time I traveled outside India. I was a physicist aspiring to take up geosciences, when applying for my PhD. Therefore, it was a shift in that sense. Through my PhD, I was able to address scientific questions in geosciences from the perspective of Physics and (I feel) I have learned some geology. The journey was exciting. Also, I have got some maturity in my research.

First, I would like to express my gratitude to Prof. François Renard, my advisor for providing me an opportunity to take up geosciences in PhD. I thank him for trusting me that I could take up a geoscience project, coming from a physics background. Throughout my PhD he played many roles, PhD advisor, mentor, friend, guardian. I have learnt a lot from him. He encouraged me to think independently. I am thankful to him for introducing me to scientists from diversified backgrounds and stimulating discussions. I am also grateful to Dr. Jérôme Weiss and Prof. Dag Dysthe, my other advisors for being as a constant support and providing insightful feedbacks. I thank François, Jérôme and Dag for being as a constant source of inspiration and sharing their knowledge. I also thank the Njord family (then PGP), being here is a big experience of diversity in science and culture. Research at PGP is more of inter disciplinary and young researchers like me feel adaptable. It is definitely an advantage for my future prospects.

I would like to thank Benoît, François, Xiaojiao, Jessica, Adriane, my experimental team at ESRF, for exciting experiments during night shifts. Though the experiments looked quasi-static, when the rocks were approaching failure stage, we were all curious to get a first glimpse of the rock microstructure. This curiosity kept me excited and awake during the nights. I was happy that I was part of those experiments. I would also thank Benoît, Jessica and Maya, Post Docs in our group for their help during my PhD. I would also thank my office mates, Claire, Xiaojiao, Kristina, the girls gang. It has been pleasure being with you. I will be missing you and our evening chats. Your association made me feel comfortable at work.

Herculus School, 2017 organized by ESRF gave me an exposure to different experimental techniques that are functional at ESRF. This is a big advantage and I thank François for suggesting me the course. As part of ESS & MAX IV project I got an opportunity to travel to Niels Bohr Institute, University of Copenhagen. I would like to thank Prof. Joachim Mathiesen of Niels Bohr Institute for introducing me to Finite Element Modeling. Another important part of my PhD is meetings in Blesle. Discussing science in the backdrop of French countryside. These discussions were more relaxed but insightful and formed basis for structuring my research articles. Thank you François for those meetings. This PhD is a cotutelle with University of Oslo and University of Grenoble. I would like to thank all the laboratory heads and administrative coordinators of both the universities. I would also thank all my course instructors, PhD committee and coordinators.

I would like to thank my parents for supporting me to achieve by goals. I thank my father for inspiring me to pursue science from a young age. I would also thank my previous institute JNCASR for nurturing me with research aptitude. At last, I thank Ruchika, Sophia, Paul, Anne, Vilde, Elisa, Amrit, Anmol, Amit, Vishali and Gaurav for all our adventures and providing warmth of a home in Oslo.

Contents

1 Introduction

The Earth's crust deform under the accumulation of loading instigated by tectonic, fluid overpressure, and gravitational forces, which result in slow and fast events like earthquakes, volcanic eruptions, and landslides. Regions of accumulated strain may be concentrated along localized zones, such as faults, or extend pervasively over hundreds of kilometers inside continents. Material deformation characteristics and failure modes of crustal rocks determine the deformation profile of the crust at all scales. Rocks in the upper crust deform in a brittle and localized manner, and with increasing depth, deformation regime evolves from brittle-frictional to ductile-viscous in the lower crust (e.g., Scholz, 2019). Mechanical deformations of the crust, which sometimes manifests by nucleation of earthquakes, are influenced by several parameters including rock compositions, loading conditions, interactions with fluids and associated microstructural characteristics. A large number of parameters makes the understanding of crustal deformation a complex phenomenon.

Deformation at crustal scale is linked to localized inelastic deformation, which is evident from the global seismicity that localizes mainly at plate boundaries. For example, interactions of seismicity in complex fault networks result in nucleation of earthquakes that may propagate over tens to hundreds of kilometers (e.g., Southern California and Japan), as discussed in a recent review (Kato and Ben-Zion, 2021). Though the accurate prediction of magnitude, location and occurrence time of earthquakes remain elusive (Bakun et al., 2005), statistical power-law distributions of seismic events provide convergence for predictability (Sornette and Sammis, 1995). Robust power-law were observed for the magnitude of seismic events (Gutenberg and Richter, 1944), their spatial distribution (Hirata et al., 1987) and the temporal evolution of aftershocks following a major earthquake (Omori, 1894). These statistical distributions show scale invariance in the brittle regime at scales ranging from laboratory rock specimen to Earth’s crust (Amitrano, 2012; Main 1996; Jaumé and Sykes, 1999). Active fault systems show statistical self-similarity (fractal structure) for a range of scales from 20 km down to 1 cm (Hirata, 1989; Scholz, 2019), which extends down to micro fracturing in laboratory specimen (Scholz, 1968). Thus, the macroscopic brittle deformation in crust is intimately related to the micro scale mechanisms of deformation in rocks. According to theories of brittle deformation, validated by numerous experiments in the past 50 years (e.g.

Paterson and Wong, 2005), damage originates at grain boundaries and pore spaces, which are the microscale heterogeneities in rocks (Tapponnier and Brace, 1976). Deformation mechanisms like nucleation and propagation of fractures at microscale give rise to complex macroscopic properties, because of long-range elastic interactions. Therefore, understanding microscopic mechanisms that control mechanical failure in crustal rocks is necessary to better characterize natural and anthropogenic dynamics in the Earth's crust such as natural earthquakes, landslides, and seismicity induced by fluid injections or exploitations and mining activities in the subsurface.

This thesis addresses the microstructural changes in centimeter scale rock samples during brittle compressive failure. I focus on the microscale mechanisms guiding system-size brittle deformation of crustal rocks, which are yet to be fully described. Brittle deformation is a complex phenomenon influenced by several mechanical (Guarino et al., 1998), structural (Castillo-Villa et al., 2013) and statistical (Alava et al., 2008) factors and sometimes preceded by precursory phenomena. The present study aims at correlating, using laboratory experiments, material deformation properties of rocks to earthquake, faulting, slip, sliding and tectonic deformation of the crust. I use a novel experimental technique, dynamic X-ray microtomography, to image the microstructural changes in rock specimen subjected to triaxial compression under quasi-static loading. This technique facilitates mapping of strain events at the microscale during brittle deformation toward system-size failure. The dynamics of these events characterize the microscale mechanisms of growth and propagation of microfractures, and micro pore collapse, which guide the failure in non-porous and porous brittle rocks.

Microscale heterogeneities that guide nucleation and localization of damage corresponds to grains and grain boundaries in non-porous rocks, while they include complex pore space in porous rocks. Large variations in microstructure of rocks with varying porosity indicate dissimilar microstructural mechanisms for each rock type. Dynamics of microscale events guiding brittle failure was first proposed for heterogeneous material and have been studied using theoretical (e.g., Alava et al., 2008; Sammis and Ashby, 1986; Bhatt et al., 1975; Gurson, 1977; Curran and Carroll, 1979) and computational (e.g., Amitrano, 2012; Amitrano et al., 1999; Girard et al., 2010; Girard et al., 2012) models. Further, laboratory experiments on crustal rocks (e.g., Lockner et al., 1991; Baud et al., 2000; Vajdova 2004; Wong and Baud, 2012; Renard et al., 2019a) have explored fault nucleation in brittle regime and argued for a systematic microstructural characterization to provide a consistent description of the possible multiscale mechanisms. Therefore, a comprehensive

analysis of precursors to faulting and microscale mechanisms guiding strain localization in crustal rocks of varying porosities is still lacking. Here, I attempt to integrate failure mechanisms originally proposed for heterogeneous material using theoretical and computational models with rock deformation at conditions relevant for fault nucleation. Statistical models for brittle failure (Amitrano, 2012; Amitrano et al., 1999; Girard et al., 2010; Girard et al., 2012) have captured the dynamics of precursors in non-porous rock where damage is essentially dilatant microfracturing events. In computational models and Acoustic Emission (AE) experiments, damage is recorded by fracture avalanches which are essentially seismic. Conversely, the experimental technique I used allows for real time imaging of microstructure in 3D and damage is accumulated through both dynamic crack propagation (seismic) and slow crack propagation (aseismic).

Localization of strain in porous rocks is strongly determined by the complex microstructure and pore geometry. Using the computational algorithm of Digital Volume Correlation (DVC) applied to my experimental data, strain can be dissociated into components of dilatation, contraction and shear. Therefore, microstructural changes can be directly linked to the accumulation of strain during triaxial compression on sandstones and limestones.

My PhD research in experimental rock physics has given me an opportunity to utilize my previous knowledge in material science to address the following questions using a novel experimental technique of 4D X-ray microtomography coupled with triaxial deformation apparatus.

- Can statistical models of brittle failure explain the dynamics of precursors in non-porous and porous rocks subjected to triaxial compression?
- What are the microscale mechanisms guiding localization of a shear fault?
- Which insights are obtained from our experiments to understand faults and earthquakes?
- How are porosity evolutions linked to the strain evolutions?
- What are the dominant strain localization mechanisms for respective rock types that determine macroscopic failure?
- What are the factors that influence porosity variations and in turn damage localization?
- What are the differences in the failure modes and strain localization mechanisms between two classes of reservoir rocks (sandstones and limestones)?

This thesis provides an elaborate discussion on answering these questions. In the following, I present the results of experimental deformation of two end-member rock types either with low porosities <1% (Carrara marble - Kandula et al., 2019; McBeck, Kandula et al., 2019), Westerly granite (McBeck, Kandula et al., 2019) and monzonite (Renard, McBeck, Kandula, et al., 2019b; McBeck, Kandula et al., 2019); or with high porosities in the range 20-23%, Adamswiller and Bentheim sandstones, and Anstrude limestone (Kandula et al., 2021). This thesis focuses on, (1) computing the growth of microfractures and strain increments between stress loading steps applied to the samples, which are analogous to populations of earthquake magnitudes recorded from seismic sensors; (2) testing existing models of compressive brittle failure in heterogeneous materials by obtaining scaling laws between the statistical and geometrical parameters of microfracture increments; (3) elucidating the microstructural mechanisms of strain localization in brittle porous rocks.

The thesis is submitted to get a joint PhD degree between the University of Oslo and the University Grenoble-Alpes, through a cotutelle agreement between these two universities. The thesis contains six chapters including this introduction (Chapter 1). Chapter 2 summarizes the scientific background and motivation for the thesis. It aims at presenting the current understanding of strain localization in the crust, earthquake nucleation, brittle faulting, and statistical power-laws obtained for foreshocks and aftershocks. This chapter also describes several theoretical models developed to explain microstructural changes associated with brittle failure. A summary of previous attempts to understand brittle processes at geological scales from laboratory experiments and their limitations are also detailed. Chapter 3 presents a unique experimental approach, where I used dynamic synchrotron X-ray microtomography to measure how cores of rock approach brittle failure in a series of laboratory experiments. The data were acquired on the beamline ID19 at the European Synchrotron Radiation Facility. This technique is complementary to other experimental approaches such as acoustic emission monitoring, and I used it to unravel the microstructural mechanisms in brittle rocks (Kandula et al., 2019; 2021). I have developed a fracture tracking algorithm explained in Chapter 4. This algorithm computes incremental changes in the microfracture events between successive stress loading steps during the triaxial deformation experiment. This technique was used in two articles where I am a co-author (McBeck, Kandula et al., 2019; Renard, McBeck, Kandula et al., 2019b). Chapter 5 summarizes the main findings of two studies where I am the leading author (Kandula et al., 2019; Kandula et al., 2021) and several

other studies where I have brought important contributions by participating to the experiments and processing the data. The innovative experimental approaches of individual manuscripts are listed in Chapter 6. My contribution for each manuscript is also detailed. Chapter 6 contains four manuscripts that contribute for this thesis and that are not part of any other thesis. I am the main author of two of these articles and co-author in two other contributions (Kandula et al., JGR 2019 Kandula et al., submitted to Pure and Applied Geophysics, McBeck et al., 2019; Renard et al., 2019b). Other co-author publications during my PhD but not included in the thesis are listed at the end (Renard et al., 2020; Mukherji et al., 2019; Renard et al., 2019a; Renard et al., 2018; Renard et al., 2017). Finally, Chapter 7 provides concluding remarks on the findings of thesis and an outlook on future prospects.

2 Scientific background

2.1 Faults, shear zones and localization in the crust

In Earth's crust, strain localizes into zones that are weaker than the surrounding intact rock, which appear as natural fault systems. In these zones, slip may occur as slow aseismic creep or unstable sliding causing rapid earthquake. Localization of strain also produces features that extend at depth below crustal faults and known as shear zones (Ramsay and Graham, 1970; Sibson, 1977), which separate less strained regions of the lithosphere subjected to compressive, extensional and strike-slip settings (Sibson, 1977; Coward and Kim, 1981; Scholz, 1968; Fossen, 2010). Shear zones are characterized by the localized accumulation of large amounts of strain in the plastic or viscous parts of lithosphere (Sibson, 1977; Vauchez et al., 2012). Accumulation of strain is facilitated through the development of features like distributed microscale flaws, mesoscale fractures and dikes which are mechanically weaker than the surrounding wall rock. As shear zones accumulate large strain, they grow from small outcrop size individual zones to mature composite structures forming shear zone networks by segment linkage (Fossen and Cavalcante, 2017).

In the crust, because of overburden, compressive stresses increase with depth, and the deformation style shows a transition from brittle frictional to ductile regime (Figure 2.1). Majority of large earthquakes nucleate in the upper crust (Das and Scholz, 1983; Ellsworth and Beroza, 1995; Lapusta and Rice, 2003; Bouchon et al., 2011) which is essentially brittle. However, signatures of earthquake nucleation is also observed in the ductile region of lower crust (Tape et al., 2018; Campbell et al., 2020) and lithospheric mantle (Prieto et al., 2017). Therefore, strength profile in the crust controls the nucleation of earthquakes. On the other hand, in some cases, shear zones or shear zone systems can transect the entire crust and lithosphere (Vauchez et al., 2012; Blenkinsop et al., 2013), indicating complexity in microstructural and rheological regimes, and deformation faces that may vary with depth as shown in Figure 2.1 (Fossen 2016; Figure 3 in Fossen and Cavalcante, 2017).

In this thesis, I explore the process of brittle compressive failure in crustal rocks and respective microscale mechanisms responsible for strain localization as faults and shear zones, which can further provide insights into understand nucleation of earthquakes in the brittle crust.

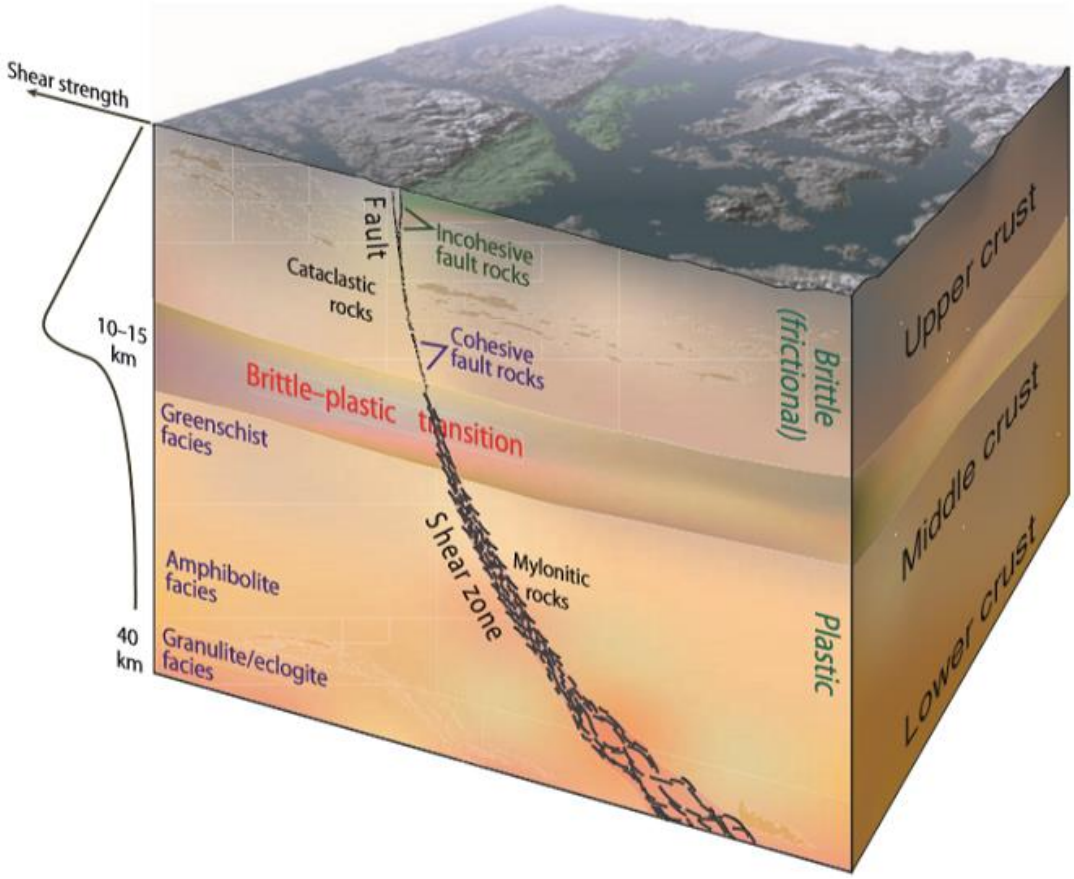

Figure 2.1: Strength profile and localization profile with increasing depth in the Earth's crust. Variations of rheology with depth manifest as faults in the upper crust, transition zone of brittle-plasticity in the middle crust and ductile-plastic shear zone in the lower crust. Figure from Fossen (2016).

2.1.1 Earthquakes

Unstable sliding within faults cause rapid earthquakes. Elastic energy is stored in the surrounding wall rock during the tectonic loading of the crust. When strength of the fault drops following the onset of slip, stored elastic energy in the surrounding rock transforms as frictional heat or surface energy (Lockner and Beeler, 2002). This causes an instability and elastic energy is radiated as seismic waves (Byerlee, 1970; Dieterich, 1979).

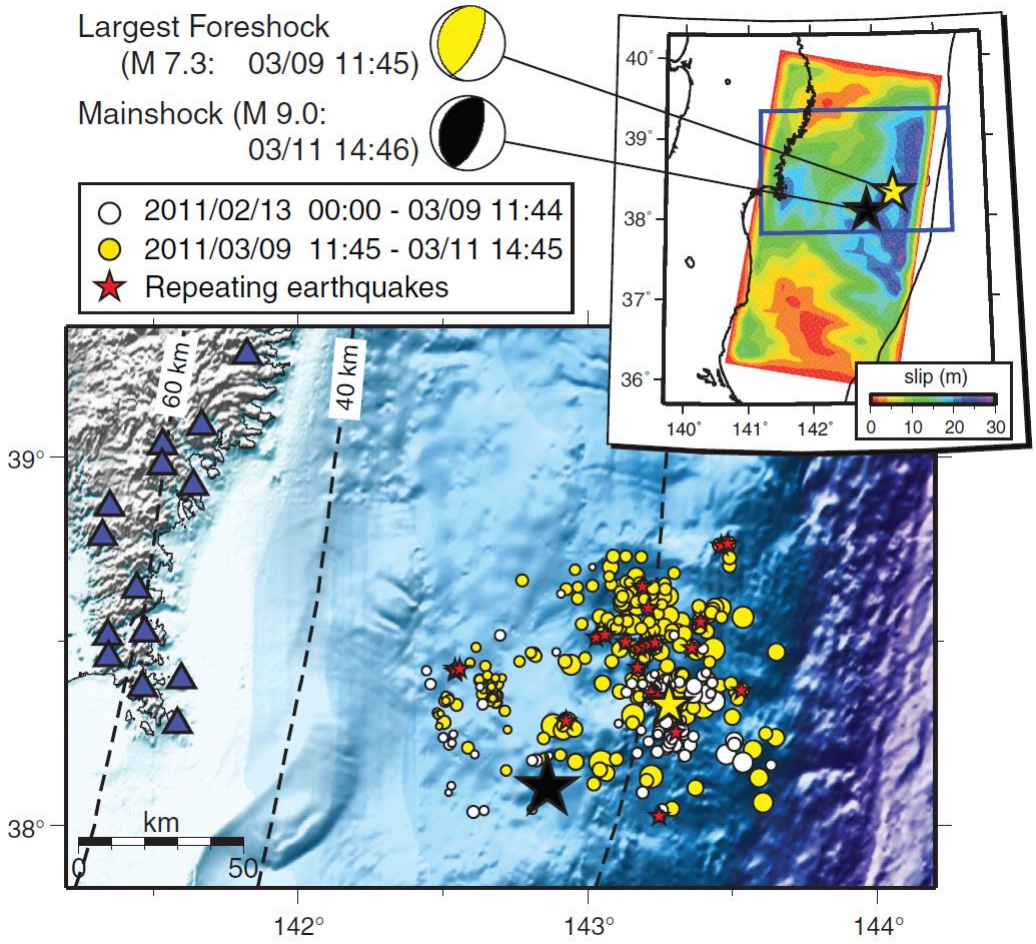

Figure 2.2: Map of foreshocks and main shock for Tohoku-Oki earthquake (2011) from Kato et al. (2012). Epicenters of 9 March, M 7.3 largest foreshock (yellow star), 11 March, M 9.0 mainshock (black star). White and yellow circles: event catalogue between 13 February 2011 and11 March 2011 (scaled to magnitude), red stars : epicenters of small repeating earthquakes, blue triangles : seismic stations. Inset: Distribution of the total mainshock slip. Yellow/white and black/white spheres denote focal mechanisms of the largest foreshock and the mainshock, respectively.

The largest earthquakes are recorded at the plate boundaries and in some cases show seismic activity preceding the largest event or mainshock (Bouchon et al., 2011; Kato et al., 2012). Preceding events are called foreshocks and correspond to a stable nucleation process in the vicinity of mainshock hypocentre. This results in the development of unstable, high-speed rupture within the fault, which is recorded as the mainshock. However, the relation of foreshocks to nucleation of mainshock remain unresolved. Also detection of foreshock activity may vary from minutes to days and in some cases longer before mainshock. For example, 72% of earthquakes in Southern California are preceded by precursory quakes between 3 to 35 days before the mainshock

(Trugman et al., 2019; Pollitz et al., 2012). Foreshock activity for M 9.0, Tohoku-Oki earthquake is shown in Figure 2.2 (Kato et al., 2012). It shows increased foreshock activity prior to the mainshock and the largest foreshock of magnitude 7.3 was detected two days prior to the mainshock (M 9.0).

Theoretical studies have argued that earthquake activity drives the Earth's crust to a critical state (Sornette et al., 1989). Characterizing the critically stressed character of the Earth's crust is an active research problem. Multiscale fracturing of an earthquake event can be theoretically related to fractal clustering of fracture in both space and time (Kagan and Knopoff, 1980). These events are observed to remain at criticality in a marginally stable state (Main, 1996). This is because, we see that either Earth's crust does never fails apart completely. This might be explained by compensating healing mechanisms to deformation. Hence, laboratory experiments can bridge observed deformations in the crust to theoretical explanations. This can be done by using scaling relationships, such as the Gutenberg-Richter (GR) law (Gutenberg and Richter, 1944). It describes the power-law relationship between the number of earthquakes and their magnitude:

$$\log_{10} N(m) = a - bm \qquad (2.1)$$

where $N(m)$ is the number of earthquakes of magnitude $\geq m$, b is a scaling parameter and slope in the log-normal distributions of N versus m, a is a constant of proportionality, also called earthquake productivity. The GR law is an expression of self-similarity in the statistics of earthquakes.

In general, the b parameter has a value close to 1 in seismically active regions and the variations of the b-value was proposed to predict the occurrence probability of an earthquake. GR law, when applied to catalogues of earthquakes, shows a fluctuation in b-value that is dependent on the magnitude range of a catalogue (Frohlich and Davis, 1993). Factors influencing the spatial and temporal variability of the b-value range from strength heterogeneity of the material (Ogata and Katsura, 1993), degree of fracturing (Scholz 1968), focal mechanisms (King, 1983), dependence of depth on frequency-magnitude variations (Mori and Abercrombie, 1997), variations in statistical estimations of b-value (Amitrano, 2003; Schorlemmer et al., 2005) and proximity to failure (Meng et al., 2019). Theories of statistical physics attribute possible variations in the b-value to both the exponent and the tail-shape in the power-law distributions of failure events (Amitrano, 2012) and can contribute for forecasting large events from smaller ones. Decrease in

b-value prior to the occurrence of a main shock (western Nagano earthquake, Sep. 1984, M 6.8, Imoto, 1991) as well as macroscopic failure in laboratory (Lockner and Byerlee, 1995) have led to a confirmation of precursory signal (Smith, 1981) to major failure either in the crust or in the laboratory rock specimen. However, such variation of the b-value before a main event is not ubiquitous and cannot be used reliably to predict all earthquakes.

In addition to the GR law, temporal correlation is observed in the aftershock sequence as given by the Omori law (3), which represents aftershock decay as a function of time,

$$N(T) \sim T^{-\alpha} \qquad (2.2)$$

where $\alpha \approx 1$. Therefore, earthquakes display a complex spatiotemporal behavior in addition to the self-similarity in the power-law statistics of their magnitudes. Such power laws are interpreted as related to the strong heterogeneity of the Earth's crust, at all scales, that control local stress concentrations and long-range elastic interactions. Several of these heterogeneities have a microstructural origin as grains and microfractures in rocks. Fault systems have complex geometry with irregular, interlocked regions, off set segments, and involve fracturing of asperities, which are typically fractal in nature (Lockner and Beeler, 2002). Grain crushing and breaking of asperities may control the position and timing of earthquake nucleation. All these heterogeneities may participate to earthquake preparation process.

2.1.2 Shear zones

Large variations in strain geometry, orientation, length, thickness and coaxiality act as boundary conditions that control deformation mechanisms in shear zones. At microscale, mineralogy, crystal plasticity, grain size, presence of fluids, strain rate, temperature and pressure (depth), influence the nature and type of shear zone localization. According to the dominant microscale mechanisms, shear zones are classified mainly as; (i) plastic shear zones characterized by crystal plastic mechanisms of dislocation creep, twinning and diffusion and (ii) frictional or brittle shear zones characterized by brittle deformation mechanisms of fracture nucleation, slip or friction sliding, grain breakage, and rotation (Fossen and Cavalcante, 2017). Brittle shear zones manifest as faults, fault zones or fault cores dominated by episodic seismic activity rather than aseismic creep observed in plastic shear zones (Rutter et al., 2001). However, shear zones are observed to have components of both seismic and aseismic deformation components (Figure 2.1). In case of dominant brittle component, shear zones are further classified as brittle-plastic (Rutter,

1986), brittle-viscous (Fusseis and Handy, 2008) or frictional-viscous shear zones (Stipp et al., 2002). This thesis is focused to explore microstructural signatures of strain localization in the brittle regime of the crust and near the brittle-ductile transition.

Presence of randomly scattered mechanical heterogeneities (e.g., weak mineral phases, and fractures at microscale) are necessary and sufficient to initiate a shear zone. This is evident from field observations (Ingles et al., 1999) and numerical and rock experimental studies (Mancktelow, 2002; Mandal et al., 2004; Misra and Mandal, 2007). All rocks comprise of microscale heterogeneities and fractures at microscale that may serve as nucleation points for initiation and growth of a shear zone. Shear zones develop either using preexisting brittle fractures (Mancktelow and Pennacchioni 2005) or decimeter to meter scale brittle fractures formed during early stages of shear zone development (Segall and Simpson 1986; Austrheim 1987). Field observations (Segall and Simpson, 1986; Austrheim, 1987; Guermani and Pennacchioni, 1998; Mancktelow and Pennacchioni, 2005; Pennacchioni and Mancktelow, 2007; Pennacchioni and Zucchi, 2013; Goncalves et al., 2016) have showed an evidence for shear zone initiation on brittle fractures (Figure 2.3) that further transitioned to strain controlled brittle-plastic deformation (Fusseis and Handy, 2008). Therefore, shear zone initiation may be seismic (Austrheim and Boundy, 1994), but further growth and evolution of thickness is essentially aseismic. Fractures acting as shear zone precursors are the main pathway for fluids in the crust (Figure 2.3 a) and interaction of these fluids with mineral phases in the host rock result in wall softening that facilitate plastic shearing (Austrheim 1987). Along with fractures, porosity generation induced by grain boundary sliding, creep activation, dissolution and precipitation play an important role in the transport of fluids (Fusseis et al., 2009) and shear zone growth and re-activation.

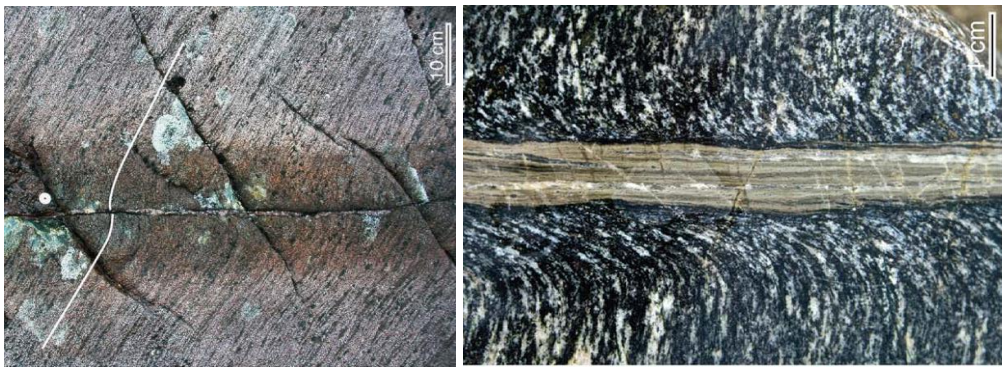

Figure 2.3: a) Initiation of shear zone on brittle fracture that form pathways for fluids in the lower crust and b) its development on large vein, which is converted to shear zone core, Caledonian Jotun Nappe, Norway. Figures are taken from Fossen and Cavalcante (2017).

Growth characteristics of shear zones are qualitatively similar to that of faults. They grow by accumulation of displacement but their precise length is difficult to estimate as they tend to connect with other shear zones, forming composite networks (Vauchez et al., 2007; Fossen and Cavalcante, 2017). Like in brittle faults (Cartwright et al., 1995; Soliva and Benedicto, 2004; Soliva et al., 2006; Fossen and Cavalcante, 2017), shear zones show growth by linkage (Pennacchioni and Mancktelow, 2007) that develop further as dense shear zone swarms, rather than in-plane growth by tip propagation. Maximum displacement is often observed near the central part with displacement decreasing toward the tip of the shear zone and maximum displacement scales with length (Pennacchioni and Mancktelow, 2007). Based on theoretical models that link accumulation of strain and displacement with evolution of thickness (Means, 1995; Hull, 1988; Vitale and Mazzoli, 2008; Phillips et al., 2016), shear zones are categorized as four types. Type 1: zone widens leaving the central part inactive, Type 2: strain localizes at the centre of the zone, Type 3: zone remains active by maintaining its thickness, Type 4: zone widens and increase its thickness.

Field observations and numerical models of strain localization (Ramsay and Woods, 1973; Ramsay, 1980) suggest that localization of strain within the shear zone manifests as plane strain zones and non-planar strain zones, i.e. zones involving two- and three-dimensional strain, respectively. Plain strain zones consider a plane containing maximum and minimum principle strain axes that correspond to diagonal elements of strain (Fossen and Cavalcante, 2017). On the other hand, non-planar strain zones involve 3D deformations that involve the off-diagonal elements of the strain tensor. Volume changes resulting from compaction across the shear zone is also observed (Fossen and Cavalcante, 2017).

In porous sedimentary rocks, although the shear zones initiation may occur through seismic fractures, their growth and development is mediated through the formation of aseismic structures called shear/deformation bands (Fossen et al., 2018). Based on the deformation mechanisms, shear bands are kinematically classified between end-members of compaction, simple shear and dilation as detailed in Figure 2.4. These shear zones are

produced through complex strain localization mechanisms, which is evident in the respective strain tensor.

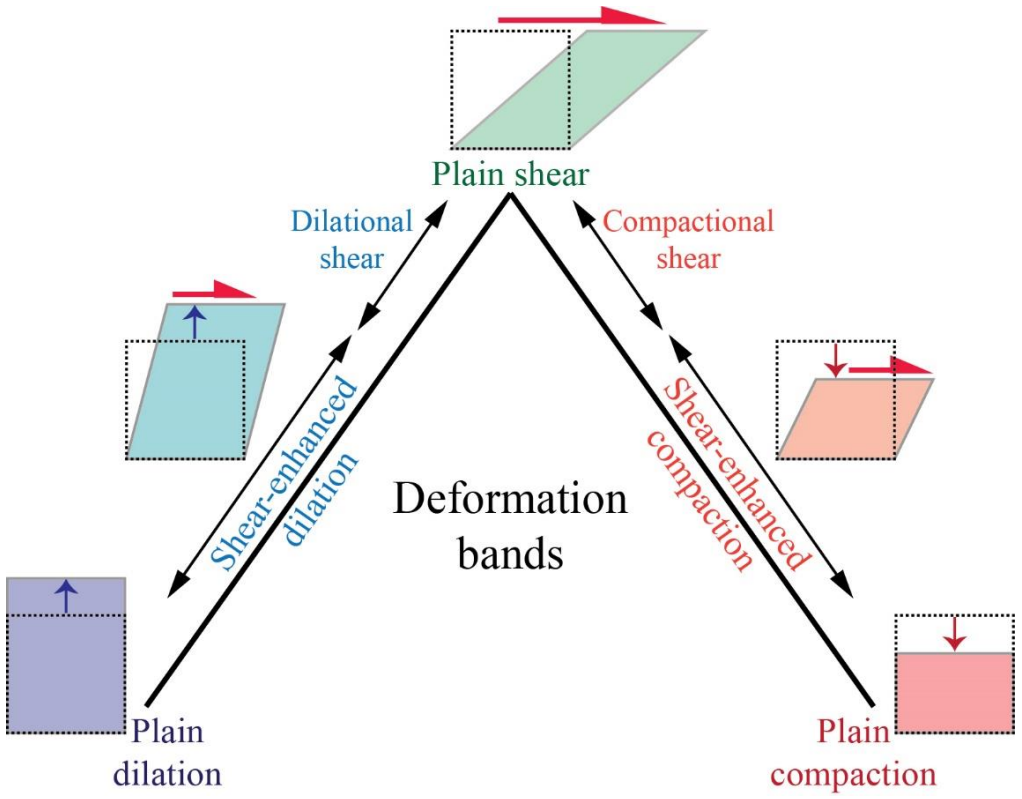

Figure 2.4: Kinematic spectrum of deformation bands between the end members of dilation, simple shear and compaction. This figure is constructed from Fossen et al. (2018).

A review of shear zones in the crust by Fossen and Cavalcante (2017) have mentioned the limitations of field observations and argued for better characterization of shear zone microscopically. Mechanisms of shear zone development and their properties in terms of complex strain localization, from microscale to the scale of lithosphere are yet to be understood. Field based observations can quantify deformation history marked as finite strain, only indirectly. Obtaining steady-state deformation measurements that provide deformation history of shear zone is both necessary and challenging. Some of these challenges are explored in this thesis. Mechanisms of strain localization at microscale are identified in rock specimen during steady-state triaxial loading conditions. Some porous rock samples studied in this PhD failed through the formation of shear zones, and the strain tensor was computed during steady-state loading, which showed localization.

Dominant strain localization mechanism was identified by computing the invariants of the strain tensor.

2.2 Micromechanical models of brittle failure

A micromechanical model that can capture the physics of the deformation mechanism should be able to explain the macroscopic failure, which could be connected to earthquake, dynamic slip and development of shear zone in the crust (Wong et al., 2006).

2.2.1 Failure in intact rock

Natural faults produce slip through either slow aseismic creep or rapid earthquake. Earth's crust is usually pervaded by pre-existing fractures and joints that act as rupture nucleation sites. Most theoretical and numerical studies consider that earthquakes occur on pre-existing faults. The percentage of earthquakes that occur either on pre-existing faults or as new fault resulting from rupture nucleation, is not known. Nevertheless, deformation on faults and intact rock deformation show numerous similarities. Microscale mechanisms for both nucleation of a fracture and sliding on faults include grain breakage, grain rotation, crack propagation (Lockner and Beeler, 2002). Also, both fault zone and intact rock material properties are altered during interaction with fluids.

Well before earthquakes were related to faults, empirical relations for strength of faulted and intact rock properties were developed (Paterson and Wong, 2005). For example, the Mohr-Coulomb failure criterion was initially proposed to describe brittle fracture in intact rocks and granular material (Ottosen and Ristinmaa, 2005). Later, it was used to describe nucleation of rupture and strength of pre-existing faults (e.g., Escartin et al., 1997). The Mohr-Coulomb criterion states the conditions for an isotropic material to fail, as described by the equation,

$$|\tau| = c + \mu_i \sigma_n \qquad (2.3)$$

where τ and σ_n are the shear and normal stresses resolved on the fracture/fault plane, c is cohesion and μ_i is the coefficient of internal friction. When shear and normal stresses are plotted against each other (Figure 2.5), $\mu_i = \partial\tau/\partial\sigma_n$ (Jaeger et al., 2009) represents the slope (ϕ in Figure 2.5) of the failure surface or envelope, which is the solution for the failure criterion, with the normal stress. In this thesis, I follow the convention that σ_n is positive for compression.

In laboratory experiments subjected to varied stress conditions, the failure envelope refers to the locus of points that define failure in the shear stress versus normal stress plots. Testing conditions

relevant to rupture nucleation and earthquake require higher normal stress and more than one independent principal stress. Thus, experimental geometries that have access to such variations are direct shear and triaxial compression. A direct shear apparatus can tune variations in shear and normal stresses on a sliding interface, while a triaxial setup can impose a confining stress as high as 1 GPa (Lockner and Beeler, 2002). Thus, triaxial compression is the ideal choice for exploring brittle deformation mechanisms at microscale in intact rocks, which could possibly address the microscale mechanisms of brittle faulting in the crust. A Mohr-Coulomb failure envelope for a triaxial setup is as shown in Figure 2.5.

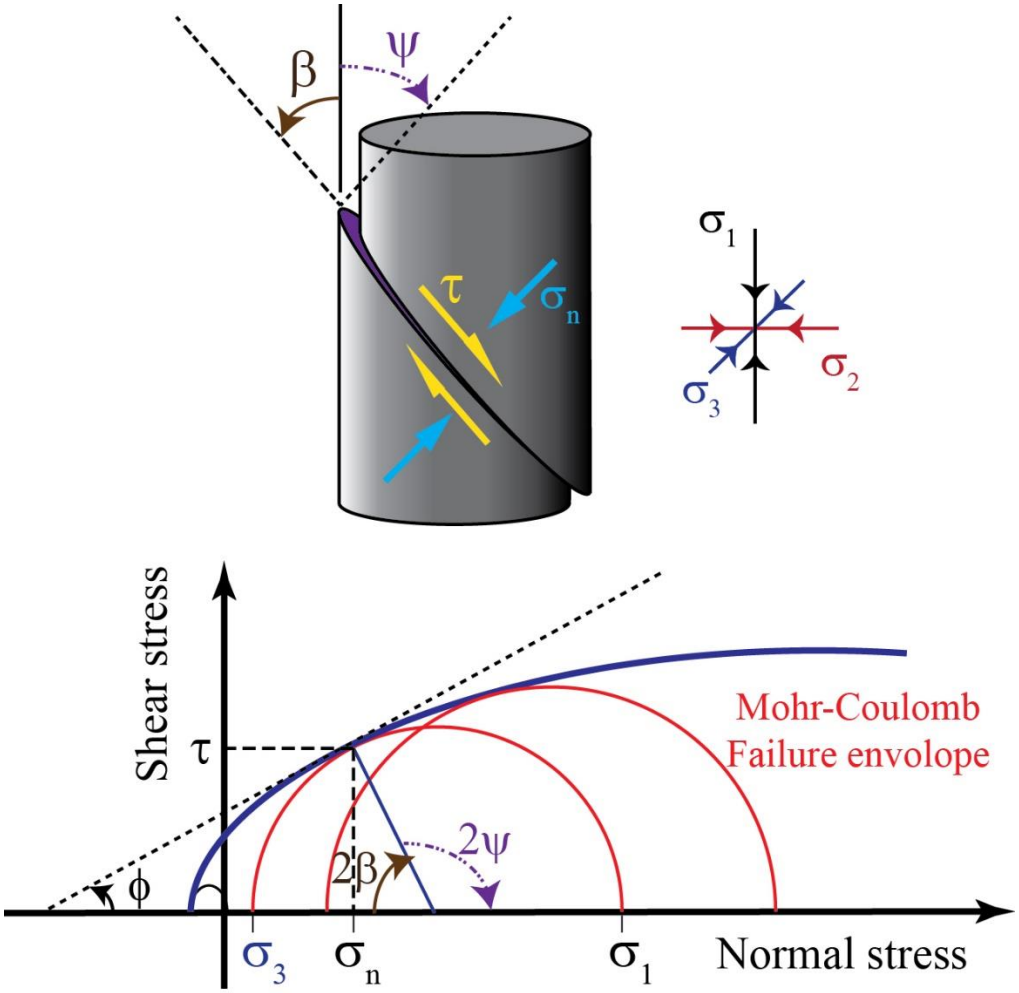

Figure 2.5: Top: Brittle failure in a triaxial setting in rock physics experiments. Bottom: Mohr-Coulomb failure envelope for triaxial compression showing the relation between principal stresses and failure parameters as adapted from Lockner and Beeler (2002). ϕ is the internal frictional angle, β and ψ are the orientation angles of fault plane and fault normal with the maximum compressive stress.

2.2.2 Statistical models of failure

Failure in rocks can be addressed from the perspective of material fracture or failure, when studied at the scale of grains, grain boundaries, pores and pre-existing flaws. These microscale heterogeneities represent the disorder and drive the micro fracture development in heterogeneous solids such as rocks of Earth's crust. A population of micro fractures nucleate randomly in the material and interact through long-range elastic interactions (e.g., Paterson and Wong, 2005). Two factors, disorder and long-range elastic interactions among the population of micro fractures, control failure in heterogeneous solids according to theories of statistical mechanics. Fracture properties such as clustering and precursory activity (Garcimartin et al., 1997) are governed by laws of statistical mechanics and show similarities mean field percolation (Herrmann and Roux, 2014). Therefore, in the context of statistical mechanics, failure is resulting from the interplay between disorder and long-range elastic interactions (Alava et al., 2006).

In order to explain failure in heterogeneous materials, researchers have used numerical simulation of lattice models, which provide a relatively simple description of elasticity and disorder. Random spring model (RSM) (Hansen et al., 1989; Nukala et al., 2005a), a lattice model, assumes that the elastic medium is represented by a network of elastic springs. Disorder is modeled by imposing a random failure threshold on the springs such that they break when a threshold is exceeded in a quasi-static loading condition. Local displacements within the lattice are computed by solving a set of coupled linear equations. Another model consider an elastic medium as a random fuse networks (RFM, e.g., De Arcangelis et al., 1985) and the elastic interactions are scalar. Both models account for disorder and long-range interactions as associated with failure in solids. Another numerical model (Amitrano et al., 1999; Girard et al., 2010; Girard et al., 2012) accounts for progressive damage observed in brittle materials subjected to laboratory tests (Katz et al., 2004), primarily under compression (Vu et al., 2018). This progressive damage model can mimic several properties of brittle compressive failure in rocks such as fracture growth and localization. Material is modeled as discretized triangular elements using finite element method, and applied stress and strain fields are considered to be continuum (tensorial). Each triangular element is large enough compared to the initial phase of microfracture nucleation. With the nucleation of progressive isotropic damage, increased microfracture density results in a decrease of elastic moduli. Damage threshold at the element scale is calculated using a tensorial Mohr-Coulomb criterion, which is valid

for geomaterials. In stress driven simulations, with application of constant increments in stress, instantaneous stress redistributions result in an event of damage, as expected also in real materials. Due to the presence of elastic interactions, stress redistribution around a damaged element can initiate a series of damage in the neighboring elements, resulting in an avalanche of damage. Avalanche proceeds only until the damage criterion is no more fulfilled by any of the elements. Starting with an undamaged material, when macroscopic deformation is linear, damage is homogeneously scattered in the system. With increase in avalanche activity, the material shows elastic softening and the macroscopic behavior deviates from linearity. The catastrophic avalanche that grows indefinitely, spanning across the system, marks the failure stage. A variety of mechanical behaviors can be controlled by the internal friction and therefore can control the brittle-ductile transition (Amitrano et al., 1999; Amitrano, 2003). Features of brittle compressive failure in low-porosity rocks (Lockner et al., 1991) are effectively captured by this model and hence considered for triaxial tests in this thesis.

2.2.3 Scaling laws

When heterogeneous solids are subjected to slow external driving, cracking events occur, spanning a broad range of sizes (Sethna et al., 2001). These fracture events are called crackling noise and can be recorded using a non-destructive technique called acoustic emission (AE) (e.g., Lockner et al., 1991). Population of energies (E) released during these cracking events show power law distributions (with an exponent, β) for various loading conditions (Scholz, 1968; Deschanel et al., 2009),

$$P(E) \sim E^{-\beta} \tag{2.4}$$

At the laboratory scale, failure is characterized by an increased AE activity as approaching failure. Therefore, large events are more likely to occur when approaching failure. This is true for laboratory experiments (Lockner et al., 1991, Vu et al. 2019), collapse of rocky cliffs (Amitrano et al., 2005) and more controversially for earthquakes (Scholz, 1968). In stress controlled experiments, rate of energy release (δE) shows power-law divergence as a function of applied stress,

$$\delta E = \left(\frac{\sigma_c - \sigma}{\sigma_c}\right)^{\kappa} \tag{2.5}$$

where, σ_c is the maximum sustainable stress/ failure stress, κ is the scaling exponent. When applied stress (σ) reaches σ_c, δE diverges.

The precursory activity before failure and scaling laws are characteristic features of critical phenomena as described by statistical models of failure (Alava et al., 2006). However, the interpretation of fracture/failure as a critical phase transition (Sornette and Andersen, 1998) is still controversial (Alava et al., 2006). In lattice models of RFM, RSM and FBM (fiber bundle model), avalanche of failure events precede macroscopic failure. These failure events are defined as broken bonds or fibers, in each model. Distributions of avalanche sizes and energies show power-laws with exponents dependent on the choice of the model (Picallo and Lopez, 2008). These distributions also show finite size scaling (Zapperi et al., 2005; Picallo and Lopez, 2008) and therefore argue for critical interpretation of failure. In case of RFM, size distributions of avalanches showed truncated power-laws, with an exponential cut-off size that is diverging when failure occurred (Zapperi et al., 2005, Vu et al. 2019). Divergence of the cut-off size indicates an increase in the avalanche size that is analogous to an increase in the energy release rate in experiments (Nechad et al., 2005; Amitrano, 2006).

Progressive damage model tracks the proximity to failure in terms of a control parameter Δ, which is defined in stress driven simulations as,

$$\Delta = \frac{\sigma_{mp} - \sigma_m}{\sigma_{mp}} \tag{2.6}$$

where σ_m represent macroscopic stress that reaches σ_{mp} at peak load or failure. Therefore, point of peak load is the critical point. σ_m for initial loading step is equal to zero when the first damage event occurs. Consequently, the control parameters varies from $\Delta = 1$ at initial loading step to $\Delta = 0$ at macroscopic failure. Avalanche sizes (S) and energies (E) are sorted out according to the log spaced bins of Δ and their distributions are computed with respect to each bin. Their probability density functions follow power-laws with exponential cut-off at large sizes/energies, stated as gamma law (Sornette and Andersen, 1998):

$$P(x, \Delta) \sim x^{-\beta_x} \exp(-x/x^*) \tag{2.7}$$

where $x = S \; or \; E$. The cut-off size x^* scales with Δ and system size L, $x^* \sim L^{\delta_x}$. β_x is estimated by the linear fit of equation 2.7 at peak load, $\Delta = 0$.

Moment analysis is used to test the scaling relationships and extract exponents, β_x and δ_x (Chessa et al., 1999). The q-moment of x on a system of size L is defined as

$$\langle x^q \rangle = \int x^q \, P(x, \Delta) dx \tag{2.8}$$

In the asymptotic limit, for infinitely large system sizes, finite size scaling (FSS) becomes valid. Therefore, for $x \to \infty$, $z = {}^{x}/_{L^{\delta_x}}$ and

$$\langle x^q \rangle_L = L^{\delta_x(q+1-\beta_x)} \int z^{q+\beta_x} \exp(-z)\, dz \tag{2.9a}$$

which is approximated as,

$$\langle x^q \rangle_L \sim L^{\theta_x(q)} \tag{2.9b}$$

Exponent $\theta_x(q)$ is estimated as the slope of log-log plot of $\langle x^q \rangle$ versus L, whereas β_x and δ_x are computed from $\theta_x(q) = \delta_x(q + 1 - \beta_x)$.

Again considering finite size scaling (Zapperi et al., 2005),

$$x^* \sim \Delta^{-\gamma_x} \tag{2.10}$$

To validate the results, a data collapse is performed using the estimated exponents and plotting $P(x, \Delta) L^{(\beta_x - 1)\delta_x}$ as a function of ${}^{x}/_{L^{\delta_x}}$.

Integrating equation 2.7, over Δ, is described as sweeping of the control parameter Δ towards an instability (Sornette and Andersen, 1998). This gives a theoretical relation among exponents,

$$\alpha_x = \beta_x + {}^{1}/_{\gamma_x} \tag{2.11}$$

where the exponent α_x is obtained by integrating equation 2.7. Scaling relations for spatial correlation of damage events can be obtained in the similar fashion. Divergence of correlation length is observed when approaching system-size failure, $\Delta = 0$. This model facilitates tracking of either the avalanche events or resulting strain fields, when approaching failure. Progressive damage model have produced results in 1D and 2D simulations (Amitrano et al., 1999; Girard et al., 2010; Girard et al., 2012) which are in agreement with the statistical lattice models and mean field theories (Zapperi et al., 2005; Alava et al., 2006). This analysis has been used for triaxial experiments on Carrara marble (in this thesis), a low porosity rock specimen, to test failure as a critical phenomenon.

2.2.4 Pore-emanated crack model and wing crack model

Unlike compact rocks, porous sedimentary rocks have a more complex microstructure. In rocks of porosity less than 1%, heterogeneities correspond to grain boundaries and in some cases

very small fraction of microscale fractures and flaws. On the other hand, in sedimentary rocks, deformation and strain localization is impacted significantly by the pore structure and geometry. This complex microstructure has to be resolved to understand mechanical compaction, strain localization and fluid transport within the rock. In some of the rock types, voids are classified as equant pores that correspond to macro porosity and elongated cracks that correspond to micro porosity which sometimes is a result of deformation (Ji et al., 2012). Therefore, pore space largely guides the mechanisms of strain localization and wing-crack and pore-emanated crack models are two such microscale mechanisms that I describe below (Jaeger et al., 2009; Nemat-Nasser and Horii, 1982; Sammis and Ashby, 1986; Ashby and Hallam, 1986).

In brittle solids, small pores and cracks are the phases with elastic moduli or stiffness that is nearly zero compared to rock matrix and thus act as nucleating sites for new cracks. A mechanism of initiation of microscopic cracks (referred in this thesis and manuscripts as microfractures) from the periphery of pores was proposed by Sammis and Ashby (1986), as the pore-emanated crack model (Figure 2.6 a). The mechanism for microfractures that initiate from the tip of pre-existing flaws was proposed by Nemat-Nasser and Horii (1982), and Ashby and Hallam (1986), and is named the wing-crack model (Figure 2.6 b). Both models are conceptual and represent useful simplifications of the complexity of micromechanisms of brittle deformation in rocks. The criterion for microfracture initiation under axisymmetric loading has the form,

$$\sigma_1 = c_1\sigma_3 - \sigma_0 \tag{2.12}$$

where c_1 and σ_0 are material properties, σ_1 is the axial stress and $\sigma_2 = \sigma_3$ is the radial stress. Further, an expression for the microfracture nucleation was proposed by Nemat-Nasser and Horii (1982), Ashby and Hallam (1986), and Ashby and Sammis (1990), which is given as,

$$\sigma_1 = \left(\frac{\left(1+\mu^2\right)^{1/2}+\mu}{(1+\mu^2)^{1/2}-\mu}\right)\sigma_3 - \left(\frac{\sqrt{3}}{(1+\mu^2)^{1/2}-\mu}\right)\frac{k_{Ic}}{\sqrt{\pi a}} \tag{2.13}$$

where μ is the coefficient of friction acting across the microfracture opening, k_{Ic} is the fracture toughness of the rock through which microfractures grow and propagate, $2a$ is size of the pore or length of pre-existing flaw. Explanations of these terms are given in Figure 2.6. Once initiated, microfractures propagate parallel to σ_1. The stress intensity factor, k_I is defined at the tip of each wing crack. When k_I becomes equal or higher than a threshold, k_{Ic} i.e., $k_I \geq k_{Ic}$ a tensile microfracture would initiate either from the periphery of the pores or tip of pre-existing flaw, and

propagate parallel to σ_1 (Jaeger et al., 2009). Microfractures emanating from pores interact with their neighboring ones and at peak stress their coalescence leads to instability, resulting in a macroscopic stress drop. Pore-emanating crack model is defined only for conditions of unconfined compression (Wong, 1990). In the wing crack model, at peak stress the instability is caused by coalescence of wing cracks under confinement, as shown in Figure 2.6 b-i,ii.

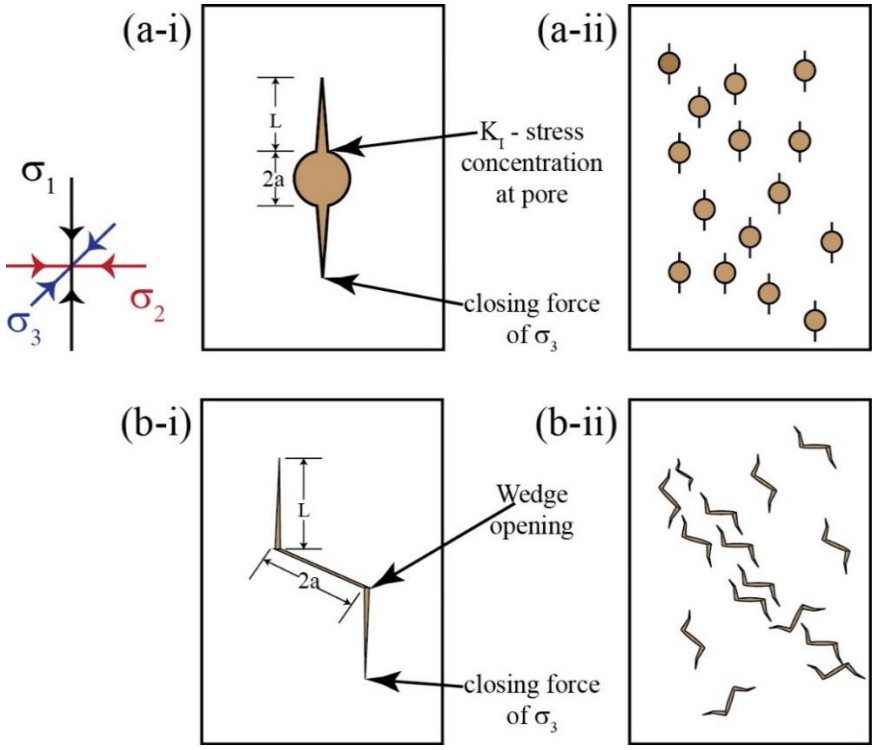

Figure 2.6: Top: Sketch of pore emanated cracks showing stress concentration at the periphery of the pore (a-i). Elastic medium permeated by pores of uniform size '$2a$' (a-ii). Bottom: Wing crack model showing stress concentration at the tip of inclined flaws and wedge opening (b-i). Coalescence of wing cracks giving rise to an instability that results in macroscopic failure at peak stress under triaxial confinement (b-ii). This figure is inspired from Ashby and Sammis (1990) and Zhu et al. (2010).

The pore-emanated crack model has been proposed to explain the microstructural changes resulting from uniaxial compression of porous sandstones and limestones (Zhu et al., 2010; Wong and Baud 2012). However, pore-emanated cracks were observed also in triaxial compression in recent experiments on sandstones and limestones (Vajdova et al., 2010; Renard et al., 2019a).

2.2.5 Pore collapse model

The compressibility of sedimentary rocks that undergo volumetric yield is characterized by the evolution of porosity, and therefore volumetric strain, which is essentially elastic prior to yield and plastic afterwards. This deformation mechanism is called 'pore collapse' (Zhu et al., 2010; Ji et al., 2012). With the increase in applied stress, equant pore space of the rock gets compacted. This results in an irreversible decrease in porosity with increase of elongated cracks and internal collapse of pores.

The plastic pore collapse model (Bhatt et al., 1975; Gurson, 1977; Curran and Carroll, 1979) has been used to describe compaction in porous material. This model assumes a pore to be spherical and collapse of the pore is induced at the pore surface by crystal plasticity. Dislocation slip and twinning are the mechanisms through which the pore collapses. As a result, a concentric shell of plastic deformation sets and the pore geometry is transformed to an ellipsoid with overall decrease in volume. This model is effective in relatively compact porous rocks (Baud et al., 2000) but limited for more porous limestones (Vajdova 2004). In carbonate rocks such as limestones, pore geometry is often more complex than in silicate rocks because porosity shows often a bimodal distribution of pore sizes (Zhu et al., 2010; Ji et al., 2012; Lion et al., 2004). Some limestones are characterized by presence of voids that have porosity at nano meter scale (Lion et al., 2004). Hence, porosity in carbonates is divided into macroporosity and micro- to nano- porosity. Some experimental observations on carbonate rocks deviate from the predictions of plastic pore collapse (Vajdova et al., 2004, 2010). Firstly, the mechanism of pore collapse initiates at the largest pores in contrary to the plastic pore collapse model, which assumes the initiation is equally likely among the large and small pores. Secondly, a concentric halo of cataclasis with micro cracking surround the pores rather than crystal plastic mechanisms. Comminuted fragments from the halo break and fall into the pore resulting in a collapse. In order to explain these processes, Zhu et al. (2010) proposed a micromechanical model of cataclastic pore collapse.

Mechanical compaction in the cataclastic pore collapse model was investigated using a representative volume element in a dual porosity medium consisting of a macro pore embedded in an effective medium of micro pores as shown in Figure 2.7 a. When subjected to an external stress field, stress concentration is induced at the periphery of the macropore as shown in Figure 2.7 b. Yielding occurs in the vicinity of the macropore when the maximum principal stress equals the

uniaxial compressive strength of the effective medium containing micropores alone. Brittle failure in the effective medium proceeds through production of pore-emanated cracks originating from numerous micropores (Sammis and Ashby, 1986). When pressure within the volume element reaches pore collapse pressure, damage accumulates as a halo of cataclasis around the macropore (Figure 2.7 c) and fragments from the effective medium fall in the macropore resulting in collapse. Pore collapse pressure is directly proportional to fracture toughness of the material, k_{Ic} and inversely proportional to effective porosity of the medium.

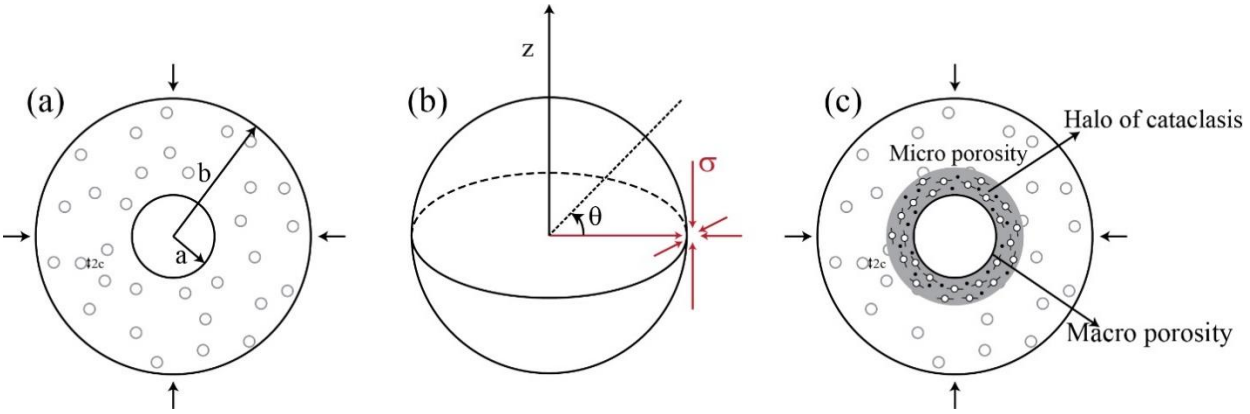

Figure 2.7: Cataclastic pore collapse model – (a) Schematic representation of volume element, with a macropore of radius b embedded into an effective medium that contain numerous micropores of radius a. Externally applied principal stresses are $\sigma_1, \sigma_2 = \sigma_3$. (b) Local stress field at the periphery of the macropore inducing stress concentration. (c) Halo of cataclasis made up of pore-emanated cracks surrounding the macropore. This figure is modified from Zhu et al. (2010) and Wong and Baud (2012).

Pore collapse is often associated with mechanisms of grain crushing and grain size reduction. Experimental results in this thesis show an interplay of the mechanisms described in sections §2.2.2 and §2.2.4, which depend on confinement, quantitative measure of porosity and rock type.

2.3 Triaxial deformation experiments in laboratory rock specimen

Brittle fracture in a rock is sometimes referred to the amounts of inelastic strain that are smaller compared with the elastic range. For example, Heard (1960) had defined brittle fracture as when strain did not exceed 3% prior to the fracture. Many types of experimental tests have been employed to study brittle fracture in rocks (Paterson and Wong 2005). However, results using

uniaxial (Hawkes and Mellor, 1970; Vutukuri et al., 1974; Walsh and Brace, 1972; Spiers et al., 1990), biaxial (Maso and Lerau, 1980; Vardoulakis and Aifantis, 1991) and triaxial (Griggs, 1936; Robertson, 1955; Paterson, 1964, 1970; Smith et al., 1969; Ohnaka, 1973; Jaeger et al., 2009; Main et al., 1989; Gueguen et al., 1990; Wong et al., 1992; Hoek and Brown, 1997; Main et al., 2000; Ojala et al., 2004) tests have the advantage of being the simplest to interpret as they involve only homogeneous stresses along principle axes.

The common procedure for achieving a triaxial state of loading conditions in a laboratory setting is to superimpose a hydrostatic pressure (confining pressure) and a uniaxial stress (axial stress). Such a test is usually called as a "triaxial test". Therefore, the test involves three principal stresses along the principal axes. For cylindrical sample geometries, axial stress is applied along axis of the cylinder while intermediate principal stresses are applied radially and are equal to one another and held constant. Two types of measurements are made at constant confinement, axial force that is stress driven and axial displacement that is strain driven. For over a range of combinations of confining and axial stresses, extensile fracturing was observed to occur when confinement was equal to uniaxial tensile strength of the rock (Murrell, 1965; Hoek and Franklin, 1968). In triaxial compression tests, brittle failure is proceeded through shear fracture which is usually inclined less than 45^o to the maximum compressive stress (Griggs and Miller, 1951).

Triaxial studies on brittle rocks have explored various mechanisms including, increase in fracture stress with strain rate (Brace and Martin, 1968), decrease of strength with increase in temperature (Murrell, 1965), precursors to faulting (Renard et al., 2018), strain localization (Baud et al., 2017), effect of fluid on localization of deformation (Holcomb and Olsson, 2003) and attempted to relate mechanisms responsible for deformation in the crust to material failure properties of rocks (e.g. Paterson and Wong, 2005). Laboratory experiments were aimed to either study geological phenomena like earthquakes (Brace, 1972) or to explore microstructural changes during brittle deformation in crustal rocks (Ji et al., 2015; Vajdova et al., 2004; Renard et al., 2019b). This thesis corresponds to the later case.

Using in situ triaxial tests some of the fundamental problems are also addressed such as, influence of specimen size on strength (Pratt et al., 1970). Size dependencies on strength correspond to the statistical distributions of flaws described by 'weakest link theory' (Weibull, 1952). Fracture of rock under general states of stress was tested using statistical theories that define failure as when

volumetric strain had reached a critical value (Wiebols and Cook, 1968). Acoustic emission (AE) measurements on rocks under triaxial compression (e.g. Lockner et al., 1991; Stanchits et al., 2006; Vu et al., 2018) were used to obtain catalogues of seismic fracturing events that were considered as precursors to failure in brittle rocks. AE rate with time, sometimes called avalanche, is a used as a signal for system-size failure. This technique is effective in capturing the seismic precursors and can be considered analogous to seismic activity before earthquakes. AE can also map the spatial correlation of the events within the volume of the sample, which can be related to the spatial distribution of seismicity around the hypocenter. However, strain localization sometimes results in aseismic deformation and cannot be recorded in the AE catalogue. Also, AE is an indirect measurement for nucleation of damage.

On the other hand, strain localization observed in porous reservoir rocks were explained using theoretical and numerical models (Vajdova et al., 2004; Wong and Baud, 2012; Baud et al., 2017). These models are based on the complex pore geometries in the rocks. Experimental studies using optical (Moore and Lockner, 1995), scanning electron (Brace et al., 1972), and laser scanning confocal microscopy (Fredrich et al., 1995) have been used to characterize the microstructure of brittle material such as microfracture clustering and pore space.

The 4D microtomography experimental techniques described in this thesis, can record dynamical microstructural changes in rock specimen approaching brittle failure and thus underlying strain localization mechanisms can be explored. Considering the versatility and effectiveness of this experimental technique, I aim to address the following goals. I test, for the first time, theoretical and computational models that describe brittle failure in heterogeneous material, in rocks at microscale. I utilize the results to interpret the precursors to fault localization and occurrence of earthquakes. Using the computational technique of DVC, I link the evolution of porosity in rock specimen approaching brittle failure to the accumulation of strain, for the first time. Finally, I explore the factors guiding strain localization mechanisms in rocks of varying porosities and dissimilar microstructure.

3 Experimental approach

3.1 Triaxial deformation and 4D X-ray micro tomography

X-ray microtomography (Flannery et al., 1987) is a non-destructive technique for imaging inside materials. In the thesis, I used the triaxial deformation apparatus, HADES (Renard et al., 2016) that can produce deformation in rocks at crustal loading conditions. This apparatus is installed on beamline ID19 at the European Synchrotron Radiation Facility (ESRF) and is employed to image the microstructure of cylindrical rock specimen in situ under triaxial loading. Results can unravel the microstructural changes during brittle compressive failure in crustal rocks. X-ray microtomography images are acquired using the full white beam of the synchrotron. Due to the adsorption of X-rays by the titanium walls of the HADES rig, the actual energy passing through the rock sample is in the range 60-100 keV. Two-dimensional radiographies, corresponding to cross-section of transmitted X-rays across the sample are acquired from a stationary detector (scintillator) at a sampling resolution of 6.5 micrometers. The HADES triaxial cell is rotated across 180^{o} with an axis of rotation perpendicular to the incoming X-ray beam. A set of 2500 2D radiographs are acquired. A three-dimensional tomogram is reconstructed with this set of projections using a back-projection algorithm (Mirone et al., 2014). The HADES rig can reproduce the temperature and pressure conditions similar to that in the Earth's crust : confining pressure up to 100 MPa, axial stress to 200 MPa, temperature up to 200°C and controlled aqueous fluid flow.

The triaxial cell is composed of a main body (Figure 3.1a) which is machined from a single piece of titanium. Wall thickness surrounding the sample is 5mm, which can sustain a confinement up to 100 MPa and a temperature up to 250°C. In the thesis, all experiments were performed at room temperature. Axial load and confining pressure are controlled by two silicone oil operating micro pumps, each with a capacity of 200ml. They can be operated either in mode of constant pressure or constant flow rate. A predefined ramp can be used to control the flow rate. Under room temperature, the confining pressure within the cell can be varied from 0.1 ± 0.05 MPa to 100 ± 0.05 MPa. A compensation chamber connected to the sample assembly ensures an equilibrium differential stress such that axial stress can reach a maximum of 200 MPa. Two Stigma pumps controlling inlet and outlet pore fluid have a capacity of 300 ml. They are operated in either

constant pressure or constant flow rate modes. At room temperature, pore fluid pressure can be varied from $0.1 \pm 0.01 MPa$ to $100 \pm 0.01 MPa$, and flow rate can be varied from $10 \pm 0.05\ ml\ min^{-1}$ to $100 \pm 0.05\ ml\ min^{-1}$. Temperature within the cell is monitored using a J-type thermocouple ($-40^o\ C$ to $+750^o\ C$), which is placed in contact with the jacket and 8 mm below the sample.

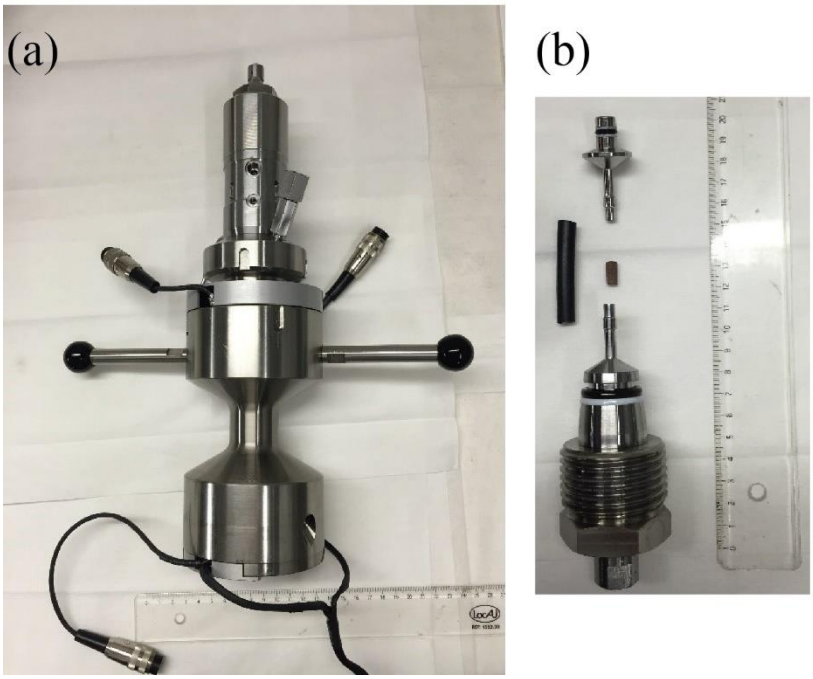

Figure 3.1: (a) Triaxial cell, HADES, (b) upper and lower pistons, silicone jacket and sample. Credit: F. Renard.

The internal sample assembly (Figure 3.1 b) of the cell consists of upper and lower pistons with channels in the center, for circulation of pore fluid. Samples of 10 mm length and 5 mm diameter are inserted into a Viton rubber jacket of 50 mm length and 1.5 mm thickness. Both pistons are then inserted into the jacket, below and above the sample. This ensures a perfect sealing of sample from confining fluid. This assembly is inserted into the triaxial cell and then closed using a nut. Chambers for confining pressure and axial load are separated using a set of O-rings that need to be changed every 2-3 experiments.

The pumps for axial load, confining pressure and pore fluid are attached to the base plate connected to the rotating table of the microtomography table at the synchrotron beamline. To

ensure rotation of the triaxial cell, connectors for pressure sensors, temperature probes, heating elements and power supply are connected to two slip rings, each on top and bottom of the cell.

3.1.1 Elements of micro tomography

The word tomography derives its meaning from the Greek words '*tomos*' and '*graphia*', meaning 'slice' and 'writing' respectively. The technique of X-ray microtomography is based on interaction of X-rays with matter. X-rays are electromagnetic radiation with wavelength in the range $0.01 - 10$ nanometers and energies in the range $10^2 - 10^5 eV$ (Cierniak, 2011). Interaction of these X-rays with matter results in loss of photons from incident flux and this process is called attenuation or adsorption. The relation between incident X-ray intensity (I_0) and attenuated intensity (I) after X-rays have passed through a material of thickness 'x' is given by Lambert-Beer's law:

$$I(x, y, z; E) = I_0(E)\ exp\left[-\int_0^l \mu(x, y, z; E)dz\right] \quad (3.1)$$

where, $\mu(x, y, z; E)$ is the linear attenuation coefficient (e.g., Ketcham and Carlson, 2001; Kyle and Ketcham, 2015) of the material, that depends on the energy E of the X-rays. Samples are most likely to be multi-phase materials and thus equation 3.1 should be modified including the contributions from all the phases

$$I = I_0 exp[-\textstyle\sum_i \mu_i X_i] \quad (3.2)$$

where, $\mu_i$is the attenuation coefficient for the ith phase, X_i is the thickness or path length for each phase.

The fraction of attenuated intensity is collected on a scintillator, which is a two-dimensional detector that transforms X-rays into visible light. A camera then takes a picture, which is called a radiograph, and is coded into a 32 bits gray scale image. A set of such radiographs is obtained by rotating the sample over 180° or 360°, along an axis of rotation perpendicular to the incident X-ray beam (Figure 3.2). The intensity image in the projections are dependent of the phases present in the material. Through a process of reconstruction, a virtual image of the material can be recreated in three dimension. This is a typical setup for obtaining tomographic scanning from synchrotron sources, where source and detector are fixed and sample is rotated perpendicular to incident beam. Conversely, in medical imaging and several laboratory settings, source and detector are rotated while sample is held stationary.

In synchrotron facilities, X-rays are produced using circular storage rings (Figure 3.2). Electrons are deviated in circular paths using bending magnets and accelerated to near-relativistic speeds to produce X-rays. These radiation beams are then directed tangential to the storage ring into the hutch of the beamline and can further be used for experimental studies. Experiments discussed in this thesis are performed at beamline ID19, ESRF, with a rectangular beam configuration. Figure 3.2 shows a schematic of the µCT scanner used during triaxial deformation experiments. Using a wiggler gap of 60mm, the incident polychromatic beam is partially coherent and photon flux density is higher than 10^{10} photons $mm^{-2}s^{-1}$ (Sanchez et al., 2013). To cut-off the lower range of the incident X-ray spectrum, a 2.8 mm-thick aluminium plate as well as the triaxial cell itself are used as filters (Renard et al., 2016).

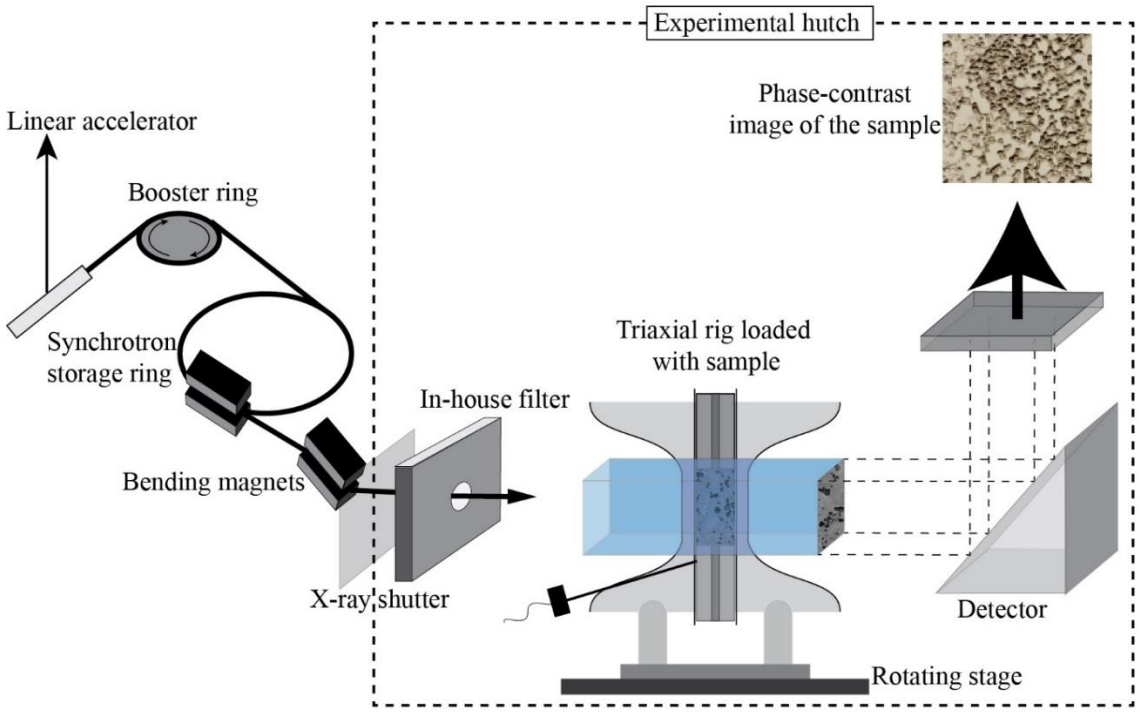

Figure 3.2: Schematic of a synchrotron facility with storage ring, booster, beamline, and µCT scanner utilized for imaging rock microstructure. In-house filter setting comprise of aluminum plates and titanium triaxial cell, which itself acts as a filter. Modified from Dubsky et al. (2012).

3.1.2 Experimental protocol

This thesis present triaxial compression tests on six types of rocks, Carrara marble, monzonite, Westerly granite, Adamswiller sandstone, Bentheim sandstone and Anstrude

limestone. Three rock types are crystalline with porosity less than 1% (Carrara marble, monzonite, granite) and the three other rock types are porous sedimentary rocks with reservoir properties and porosity in the range 20-23%. Each sample is loaded axially between the stainless steel pistons of the triaxial cell. The interfaces between the pistons and the sample were not lubricated. Axial load is increased in steps and tomography scans are acquired at each stress step such that the stress in the sample remains constant for the duration of 1-2 minutes of a 3D scan. During tomographic acquisition, the rotating stage is synchronized with the camera and sample is rotated continuously. At every step increase in stress, the stage of the beamline was rotated from 0^o to $+180^o$ and back to 0^o and that corresponds to one tomography scan. Exposure time for every rotation is $0.036\ s$ and each scan lasted around 90 seconds, producing a series of 2500 two-dimensional projections/radiographs of the three-dimensional sample. Axial stress is increased in incremental steps and tomography scans are acquired until one step before the peak stress. Sample fails with a rapid stress drop and a tomographic scan cannot be recorded during failure. A final scan is obtained after the sample has failed, and then the experiments is ended. The number of 3D scans acquired during one experiment varied depending on the loading rate and when the sample reached failure. The radiographs acquired at beamline ID19 were reconstructed in three-dimensions ($1600\ x\ 1600\ x\ 1600\ voxel^3$) using plain filtered back-projection (Mirone et al., 2014), which is employed in the program PyHST2 and coupled with a single-distance phase-retrieval algorithm adapted from Paganin et al. (2004). Image reconstruction process using filtered back-projection is detailed in Figure 3.3.

After the experiments, the samples were recovered and those that were not pulverized were consolidated with epoxy glue. Then, the samples were cut in two pieces along their cylindrical axis. The surface was polished and then carbon-coated and observed with a Hitachi SU5000 scanning electron microscope at the University of Oslo, with a voltage of 15 kV.

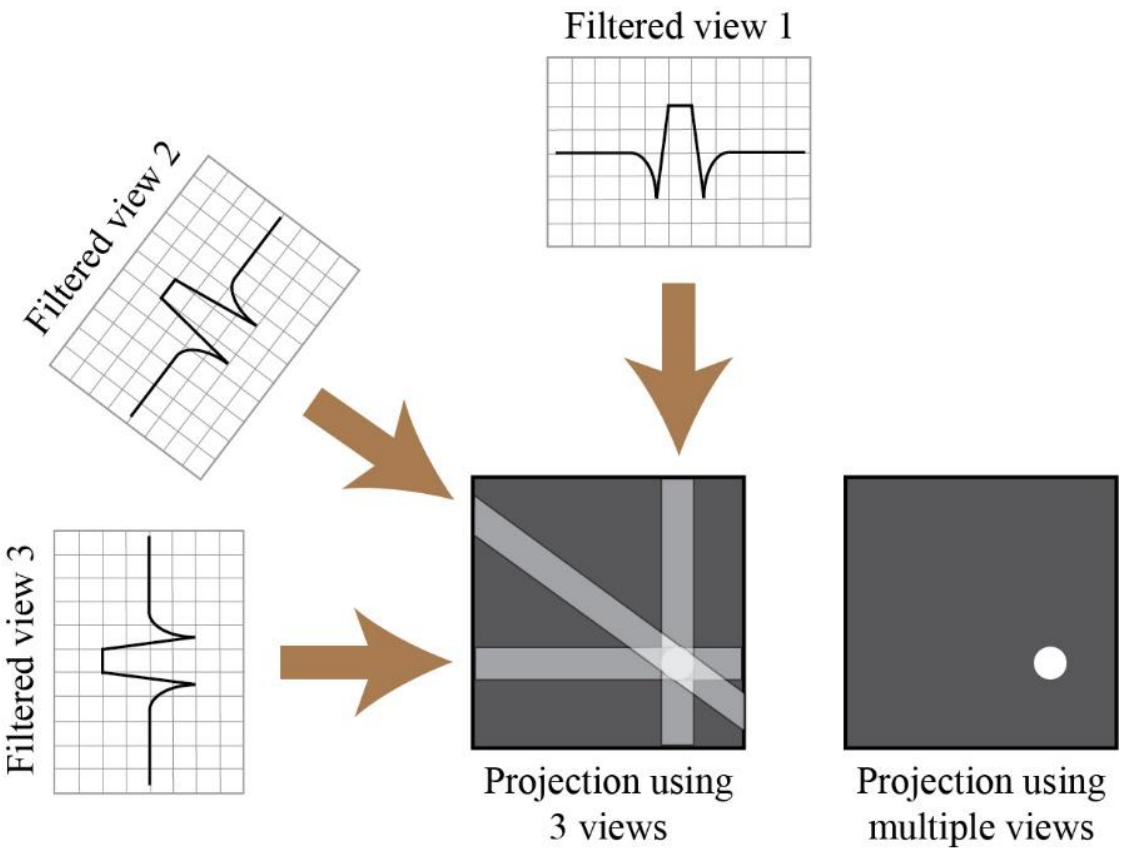

Figure 3.3: Sketch describing the image reconstruction process with a back projection algorithm. Projections obtained for each rotation are filtered and back-projected as shown. Filtering removes the blurring that would result from simple back-projection. Figure adapted from Qiu et al. (2016).

3.1.3 Tomogram segmentation protocol

Three-dimensional digital volumes of rock contain microstructural information of damage accumulation in terms of microfractures and collapsed pores. Series of reconstructed tomograms for each experiment were segmented to extract these damage elements and uncover the damaged rock at microscale. I developed the following workflow to extract the microfractures and damage evolution in the samples. I have used Matlab and the image processing softwares AvizoFire and ImageJ, for segmentation.

(1) During the initial stage, the digital volumes are corrected for artifacts that include, periodic stripes, ring artifacts and beam hardening. Periodic stripes were observed on every 2D slice and correspond to the noise from the scintillator. They are corrected by removing higher

intensities in their Fourier spectrum. Correction for periodic stripes is shown in Figure 3.4. Ring artifacts are corrected using a Matlab lab script developed by Jha et al. (2014). An example for this correction is shown in Figure 3.5.

(2) Intensity gray values are then normalized and the level of noise is reduced using a non-local means filter (Buades et al., 2005) applied to average out the speckle noise.

(3) For, Carrara marble, a background subtraction algorithm (Sternberg, 1983) in ImageJ and AvizoFire is used to remove a smooth continuous background. Images are then thresholded to extract microfractures. Microfractures with a volume less than 100 voxels are limited by the resolution of the segmented images and were removed. Therefore, smallest microfracture is 100 voxels. Using the label analysis module in AvizoFire, geometric and shape parameters of all the microfractures are calculated.

(4) In case of porous rocks, microfractures or micro pore space is extracted based on intensity histogram of each tomogram. Peaks in the gray level histograms of 32 bit images correspond to the various minerals, the void space, and the upper and lower pistons. Peak in the low intensity regime correspond to the regions of low X-ray absorption and signify fractures and pores at microscale. Segmentation based on intensity histogram is shown in Figure 3.6.

(5) For Carrara marble samples, a dilation-erosion filter was used on segmented microfractures to connect any missing voxels that constitute the same microfracture. First, microfractures are dilated by one voxel to connect to the close neighbours, and then they are eroded by one voxel to recover their original volume.

(6) As a result of segmentation, 3D digital volumes of the rock are characterized by associating binary zero, to the fracture/pore space and binary one, to the rock matrix.

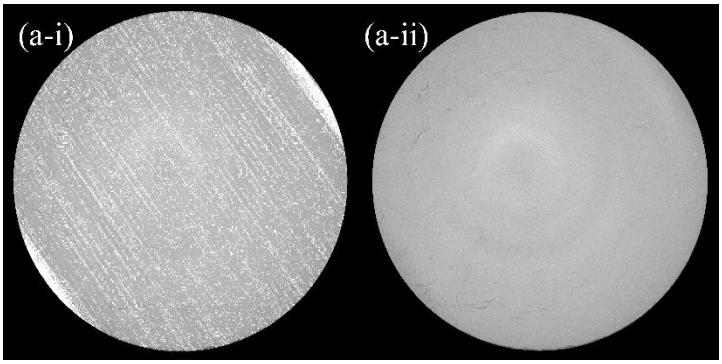

Figure 3.4: Demonstration of correction for periodic stripes. (a) Periodic stripes appear at $\sim 45^{o}$ to the image. (b) Image after filtering out higher intensities in Fourier spectrum and corrected for the stripes. Ring artifacts are also visible from the images.

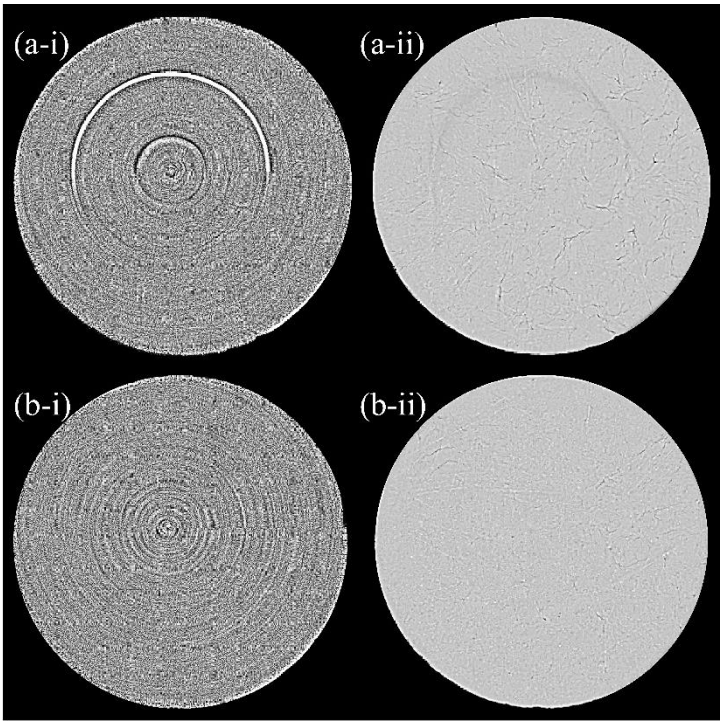

Figure 3.5: Illustration of ring artifact correction. (a-i) and (a-ii) show the two kinds of ring artifacts. (b-i) and (b-ii) are the output images from the ring correction.

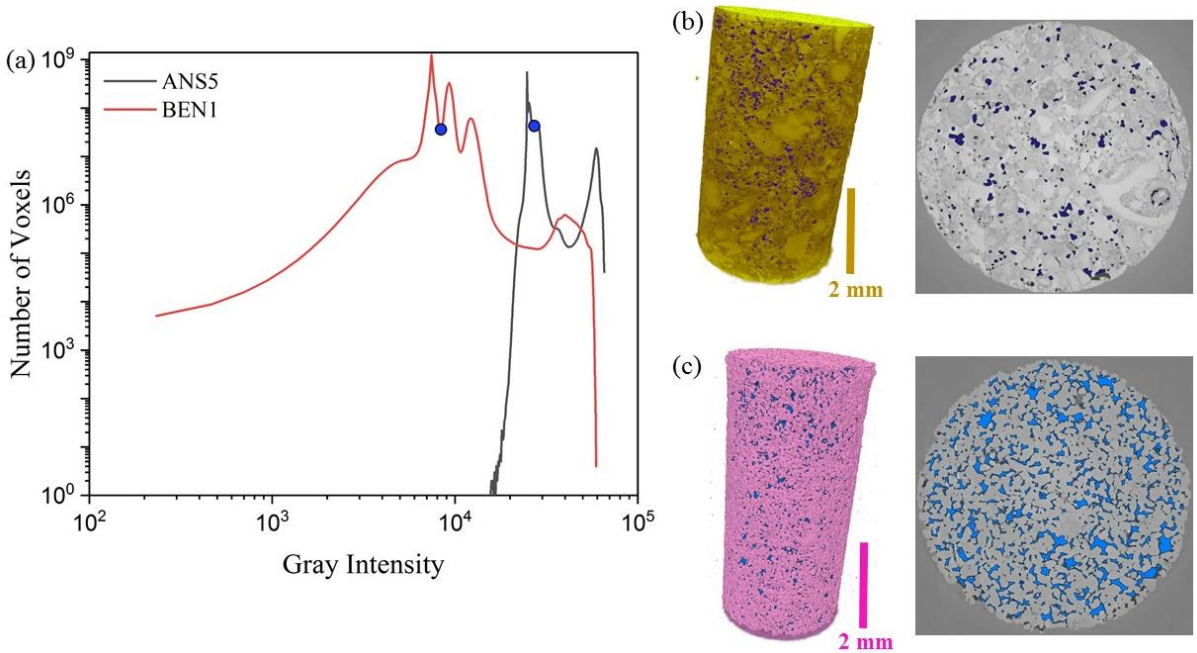

Figure 3.6: X-ray attenuation histograms and snapshots for samples Anstrude limestone 5 (b) and Bentheim sandstone (c). a) Gray level histograms contain several peaks that correspond to the various minerals, the void space, and the upper and lower pistons. The green circles separate the gray level corresponding to the pore space (on the left) from the rock matrix and pistons (on the right). b-c) Three-dimensional views and two dimensional sections of samples Anstrude limestone 5 (b) and Bentheim sandstone (c) with void space rendered in blue color.

3.2 Digital Volume Correlation

A set of 3D digital tomograms, obtained from triaxial loading at incremental stress steps, can be utilized for computation of strain localization during deformation. Gray level functions between two consecutive tomograms are compared to compute displacement field between stress steps. For a given voxel 'x', let $f(x)$ and $g(x)$ represent scalar gray value functions of two consecutive tomograms. The digital volume correlation (DVC) technique (Sutton et al., 1983; Pan et al., 2009; Tudisco et al., 2015, 2017; Buljac et al., 2018) considers that the displacement of voxel 'x' from $f \rightarrow g$ is defined by a displacement field, $u(x)$ and the two images are correlated such that,

$$g\big(x + u(x)\big) = f(x) \tag{3.3}$$

The computation of the displacement is affected by many factors including the discreteness of images, gray level resulting from convolution function and noise in the images (Buljac et al., 2018).

In the theses, I used the software TomoWarp2 (Tudisco et al., 2017; Van Der Walt et al., 2011) to compute localized strain fields between successive tomograms for triaxial tests on porous rock specimen. This computational tool calculates the vector displacement field between 3D image sets based on digital volume correlation and facilitates computation of incremental strain tensor using continuum mechanics. This software has been previously used to study deformation response in heterogeneous material under triaxial compression (Lenoir et al., 2007; Hall et al., 2010; Charalampidou et al., 2011; Tagliaferri et al., 2011; McBeck et al., 2018; Renard et al., 2019b) and is employed to explore strain localization mechanisms in porous rock specimen considered in this thesis.

Each experiment is grouped into pairs of tomograms of nearly equal intervals of axial strain as shown in Figure 3.7. Tomograms (3D images) are divided into subvolumes that distribute over a regular grid that covers the entire sample volume. Subvolumes in one 3D image are mapped onto subvolumes in another image by TomoWarp2, which identifies similar patterns within these subvolumes by translations and rotations (Hall et al., 2006, 2010; Tudisco et al., 2015, 2017). Division of subvolumes requires a node space and mapping subvolumes requires a correlation window size, which are user-defined input parameters. The search window size determines the maximum detected displacement magnitudes, and so larger changes in the macroscopic axial strain require larger search window sizes. We choose a Cartesian coordinate system with the z-axis defining the direction of the maximum compression. Once the parameters are set, TomoWarp2 computes vector displacement fields ($\vec{u}$) (Hild and Roux, 2008), which consecutively calculates displacement gradient tensor ($\overleftrightarrow{u}$) and 3D incremental strain tensor between successive tomograms separated by a strain interval.

Throughout the sub-volumes, components of strain tensor are computed by taking derivatives of the displacement gradient tensor ($\overleftrightarrow{u}$). Negative divergence ($\nabla.\overleftrightarrow{u} < 0$), positive divergence ($\nabla.\overleftrightarrow{u} > 0$), negative rotation (also called curl, $\nabla x\overleftrightarrow{u} < 0$) and positive rotation ($\nabla x\overleftrightarrow{u} > 0$) indicate contractive strain, dilatative strain, left-lateral shear strain and right-lateral shear strain, respectively. Statistics on populations of strain components within the rock volume is required to predict the trends in strain localization mechanisms when approaching macroscopic failure. Mean values of strain components are computed between successive tomograms and normalized by respective strain intervals. Cumulative mean of strain values is necessary to compare these incremental strain values to the porosity evolutions.

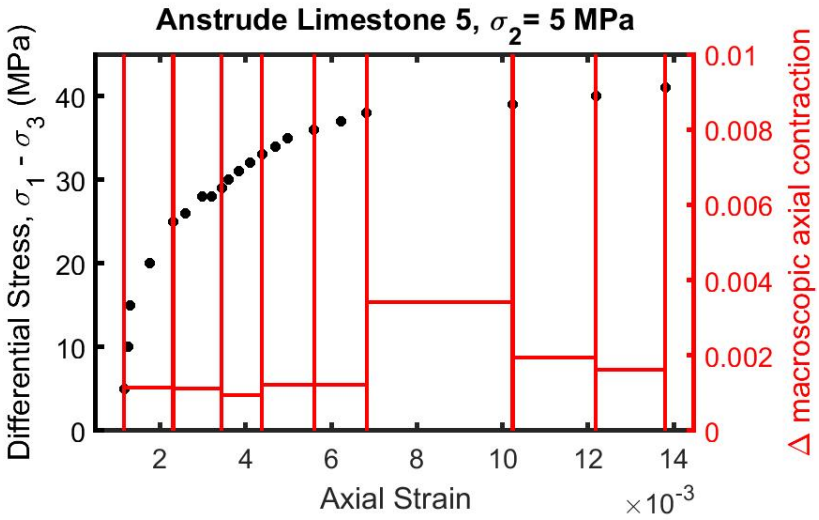

Figure 3.7: Deformation curves for Anstrude limestone experiment #5. Each black dot corresponds to a 3D X-ray tomogram. Stress-strain curve is divided into nearly equal intervals of strain marked by the red vertical lines. The length of each horizontal red line is a measure of strain interval, as given in the right vertical axis.

4 Fracture Tracking Algorithm

During my PhD, I have developed an algorithm to track the nucleation and growth of microfracture in rocks under triaxial deformation condition leading to brittle failure. This algorithm has been used in three publications that are part of the present thesis (Kandula et al., 2019; Renard, McBeck, Kandula, et al., 2019; McBeck, Kandula, et al., 2020). Measured foreshocks before the mainshock of an earthquake, acoustic emission (AE) activity in rocks prior to failure and microfracture avalanches before material failure, all these three observations are based on the instantaneous measurement of damage. However, the X-ray tomography data provide a quantification of the amount of microfractures inside a sample under a given stress state. Therefore, there is a need for an algorithm that computes microfracture increments between two stress steps (an instantaneous measure of damage) for the experiments described in § 3.1. The quantification of incremental microfracture growth facilitates testing the theories of material failure (§2.3.2) and associate them to the rocks of Earth's crust. The algorithm accounts for quasi-static loading conditions (i.e. before the dynamic propagation of a system-size fracture) and is applicable for rocks of very low porosity. It is developed using a Matlab script and contains three main stages (10 steps in total) described in the following.

Stage 1: Identification of individual microfractures

1) The computation begins with the result of tomogram segmentation by considering the set of binary 3D digital volumes of the rock, for a given experiment. Microfractures are represented by binary numbers (zero for the fractures, one for the solid). A Cartesian coordinate system is considered and the direction of maximum compressive stress is along the z-direction (i.e. the axis of the cylindrical sample), whereas the x- and y-directions represent radial directions. Two digital volumes at consecutive stress steps are identified as V_{j-1} and V_j (Figure 4.1a), where $j = [2, n]$ such that $n =$ number of stress steps/scans or scan number at failure. We define also:
   - the number of microfractures in $V_{j-1} = m$
   - the number of microfractures in $V_j = n$

2) Geometric characteristics of microfractures such as, position of their centroid, volume, surface area, and shape parameters are calculated for both the volumes. Voxels that belong to one single microfracture are grouped such that each of them are connected through face, edge or corner, in 3D. The centroids are computed for each cluster of voxels that are considered to correspond to a single microfracture.
   - centroid of each microfracture m in volume $V_{j-1} \rightarrow C_{j-1}^{m}$
   - centroid of each microfracture n in volume $V_j \rightarrow C_j^{n}$

Stage 2: Tracking of microfractures

3) Microfractures with their unique centroids, C_{j-1}^{m} and C_j^{n} in both the volumes can be tracked between stress steps by using a matching criterion. First, distance between C_{j-1}^{m} and C_j^{n} is obtained. If this distance is below a radius threshold, these two are matched and counted as same fracture in the two tomograms. All the other fractures that do not match this criterion are counted as new ones.
4) A tracking identification number (ID) is assigned to each microfracture in V_j. At the initial step, which starts by considering the first 3D tomogram, i.e., V_1, tracking IDs are assigned as a series of integer numbers. From the second step, microfracture in V_j that match the distance criterion are given the same IDs as in V_{j-1}, i.e., IDs for C_{j-1}^{m} translates to C_j^{n}. All other microfractures in V_j are given new IDs.
5) In the data sets the radius threshold for matching centroids is chosen equal to $0.625\ mm$, which is 30% of the largest microfracture length and 6% of sample length. Correction for axial contraction of the sample along the z-direction (Figure 4.2) is also added to the radius threshold. At this stage, microfractures are segregated as growing, nucleating and closing ones. Microfractures that are identified with same IDs in V_{j-1} and V_j shows growth in their volume. This growth corresponds to either increase in number of voxels within the same microfracture or coalescence with neighboring microfractures or partial closing of the microfracture. Nucleation of new microfractures corresponds to those with new IDs in V_j. Also, some of the microfractures in V_{j-1} tend to close completely in V_j and therefore do not show any corresponding IDs. An example of output from this tracking is shown in Figure 4.3.

Stage 3: Computation of microfracture increments

6) Microfracture increments between two successive stress steps were extracted by mapping the segmented volume V_{j-1} at the (j-1)th stress step with the consecutive volume V_j at the jth stress step such that the *position of every voxel in volume* V_j has a *corresponding position in the volume* V_{j-1}, with a procedure described in steps 7 to 9 below. This mapping is necessary due to axial contraction and radial dilation between successive stress steps, so that a simple difference between successive three-dimensional tomograms cannot be used to extract damage increments.
7) Volumes are considered as 2D radial slices stacked along z-axis, $z_{j-1} = [1\ N_{j-1}]$ and $z_j = [1\ \ N_j]$, where N_{j-1} and N_j are number of 2D slices in V_{j-1} and V_j respectively. First, the geometric centers of volumes V_{j-1} and V_j are identified as s_{j-1} and s_j. Volume V_{j-1} is divided into two halves about the center and across the z-axis, i.e., $z_{j-1} = [1\ s_{j-1}]$ represent first half and $z_{j-1} = [s_{j-1} + 1\ N_{j-1}]$ represent the second half. First half in V_{j-1} is projected on to V_j from above i.e., $z_{j-1} = [1\ s_{j-1}] \rightarrow z_j = [1\ s_{j-1}]$. Second half in V_{j-1} is projected on to V_j from below i.e., $z_{j-1} = [s_{j-1} + 1\ N_{j-1}] \rightarrow z_j = [s_{j-1} + 1\ N_j]$. Thus, volumes are mapped along the z-direction as shown in Figure 4.1b. Due to axial contraction, $N_{j-1} > N_j$ by 1-10 voxels for the entire duration of the experiment.
8) Now to map along the x- and y-direction, each of the 2D radial slices mapped previously, are considered. Due to radial dilation, radial lengths along x- and y-direction in V_{j-1} are always less than those in V_j. Therefore, each 2D slice in V_j is now divided into two halves about the center and along the y-direction (Figure 4.1c). Each row in V_j is then mapped on to V_{j-1} following the same logic as in case of mapping along the z-direction.
9) Further, mapping along the x-direction rolls down to single voxel. Using the logic to map along the z- and x-directions, every voxel in each row is mapped between V_{j-1} and V_j. Now, V_{j-1} and V_j are mapped such that every voxel in V_j has a corresponding voxel in V_{j-1}. If L_{j-1} and L_j are representatives of voxels in V_{j-1} and V_j respectively, $L_{j-1} = \{0,1\}$ and $L_j = \{0,1\}$ i.e., voxels can be either '0'- microfracture or '1'-rock matrix. When $L_{j-1} = \{0\} \rightarrow L_j = \{0\}$ condition occurs, i.e., when mapped voxels belong to microfractures, L_j in V_j is removed ($L_j = 1$) (Figure 4.1d). Therefore, as a result of mapping and deleting

common voxels between V_{j-1} and V_j, volume V_j is left with only increments, which can then be classified as either growth, nucleation, or closing of microfractures.

10) Increments are tracked to separate those belong to growing, nucleating and closing microfractures, using the tracking described previously and the statistics of number and volume of microfracture increments are calculated.

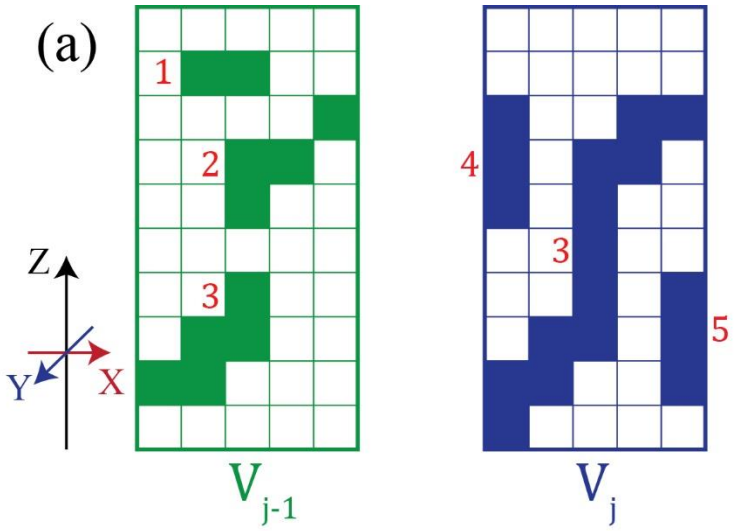

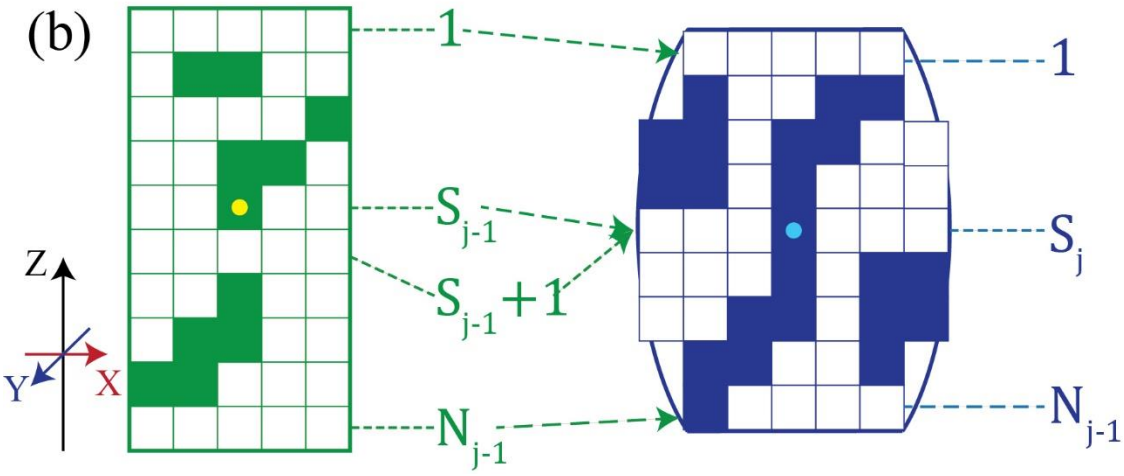

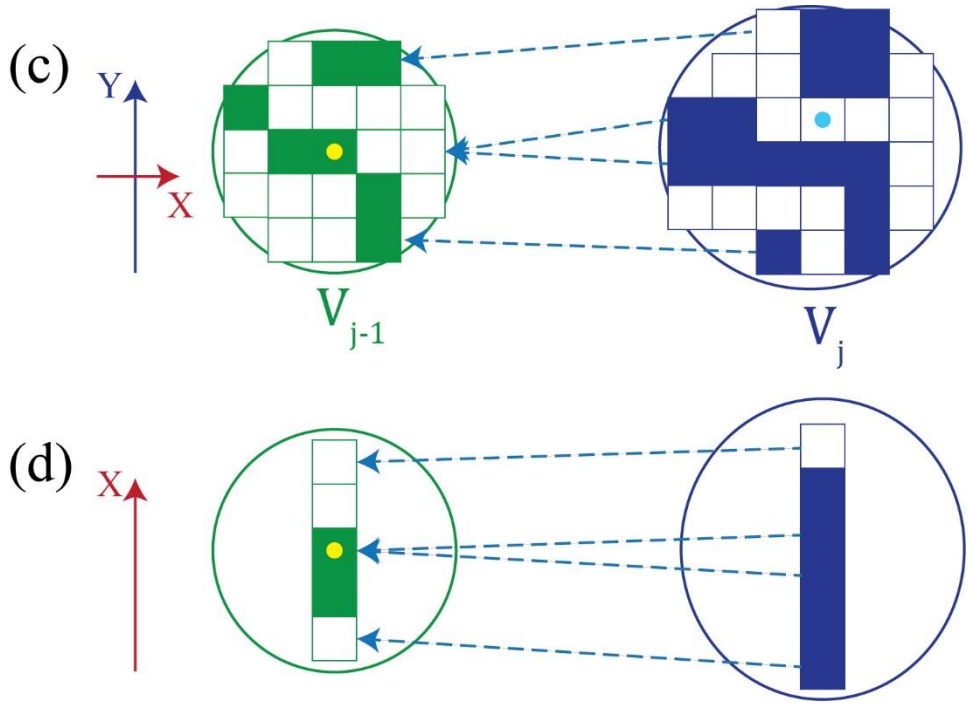

Figure 4.1: Illustration of the microfracture tracking algorithm. For convenience of understanding, the algorithm is shown in 2D. However, it is developed in 3D to track microfractures in tomograms. (a) Representation of digital volumes, V_{j-1} and V_j at (j-1)th and jth stress steps respectively. Microfractures are assigned with tracking numbers and the sketch shows the growth, nucleation and closure mechanisms. Fractures 2 and 3 in V_{j-1} grow and coalesce to form one single fracture, 3 in V_j. Fractures 4, 5 are new fractures that appear in V_j and 1 is representative of a closing fracture. (b) Mapping of digital volumes along the z-direction. Individual volumes are considered as 2D slices stacked along the z-direction. Yellow and blue circles represent geometric centers, and S_{j-1} and S_j represent center slices in V_{j-1} and V_j respectively. Mapping, $z_{j-1} = [1\ s_{j-1}] \rightarrow z_j = [1\ s_{j-1}]$ and $z_{j-1} = [s_{j-1} + 1\ N_{j-1}] \rightarrow z_j = [s_{j-1} + 1\ N_j]$ is shown using arrows directing from V_{j-1} to V_j. (c) Mapping of digital volumes along the y-direction is shown by arrows directing from V_j to V_{j-1}. Rows parallel to the x-direction direction are projected from V_j onto V_{j-1}. (d) Mapping along the x-direction is shown by arrows directing from V_j to V_{j-1}. At this stage, individual voxels are mapped onto each other. Mapping is directed from V_{j-1} to V_j along the z-direction and V_j to V_{j-1} along the x- and y-directions due to axial contraction and radial dilation.

In three rock types namely, Carrara marble, monzonite and Westerly granite, the algorithm identifies the following mechanisms as a result of increasing stress: (1) growth of pre-existing microfractures, (2) nucleation of new microfractures, (3) growth resulting from coalescence of pre-existing microfractures, (4) closing of pre-existing microfractures. Statistics on number and

volume of microfractures corresponding to respective mechanisms in Carrara marble are plotted as a function of applied differential stress, in Figure 4.3. Growth volume of microfractures shows a continuous increase while nucleating volume shows a plateau when failure is approached. Therefore, this algorithm can separate different mechanisms involved in accumulation of damage and can help reveal the dynamics of precursory activity before macroscopic failure.

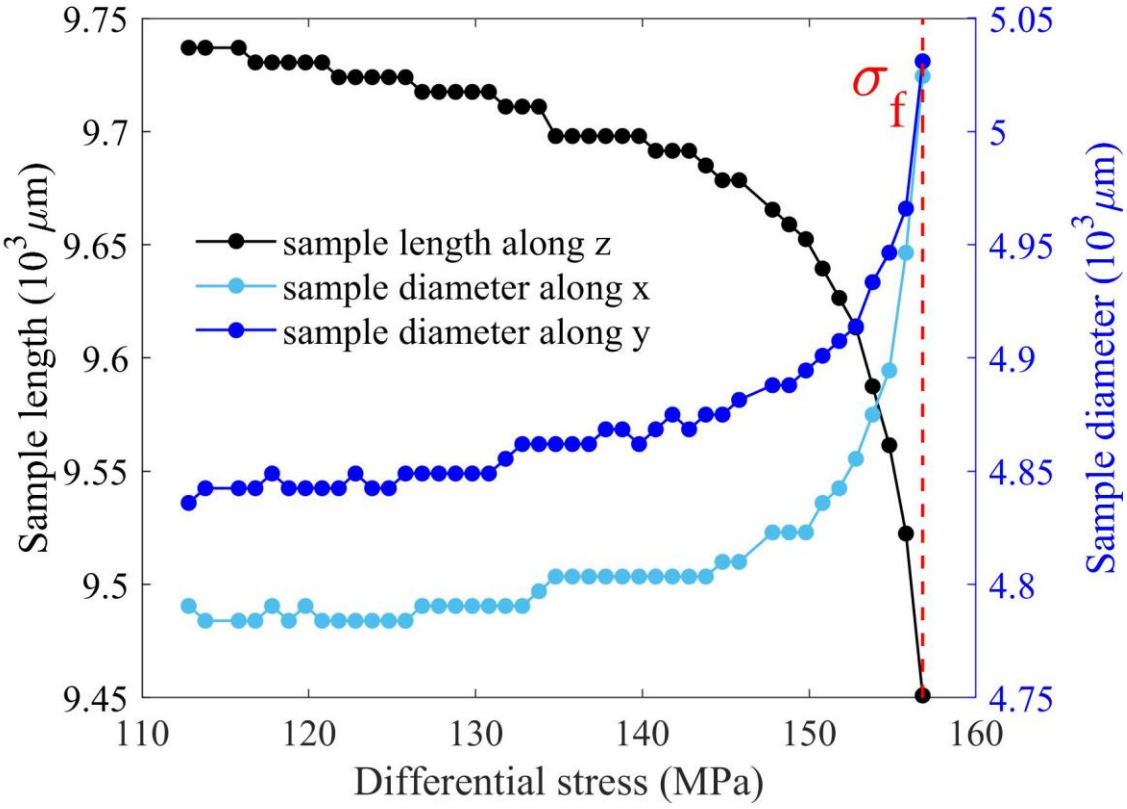

Figure 4.2: Axial length and sample radius along the principle axes for an experiment with a Carrara marble sample (Kandula et al., 2019). The red dashed line marks failure at differential stress, σ_f.

Microfracture increments computed from this procedure gives instantaneous measurement of damage at a given (j^{th}) stress step. Increments are computed for three types of non-porous rock specimen and following observations are made. (1) Growth observed in a microfracture (in V_j) at two different positions, after deletion of voxels (from V_{j-1}), are counted as two different increments. (2) This resulted in numerous increments of sizes below $100\,\mu m^3$ and are cut-off while plotting distributions of size increments. Statistics on increments can facilitate testing theories of brittle failure and correlate my experimental results, with, for example, the b-value

obtained of the Gutenberg-Richter law. Volume of microfracture increments is plotted as a function of applied differential stress for Carrara marble, Monzonite and Westerly granite in Figure 4.4. Volume and differential stress are parameterized as defined in theoretical and computational models (Alava et al., 2006, Girard et al., 2010) to identify power-law scaling and compute scaling exponents. Volume of the increments show power-law scaling in the vicinity of failure in monzonite and granite samples. However, the power-law scaling for Carrara marble differs significantly from that of monzonite and Westerly granite. Increments in Carrara marble are also tracked to separate the increments that are part of growing fractures and nucleating fractures (Figure 4.5). This tracking algorithm identifies a variety of processes involved in accumulation of damage prior to system-size failure. Therefore, it provides new ways of quantifying damage in tomography data, which could not be performed in previous studies (Renard et al., 2017, 2018). An example of the tracking algorithm in Carrara marble is shown in Figure 4.4 and supporting information of Manuscript 1, Figure S1.

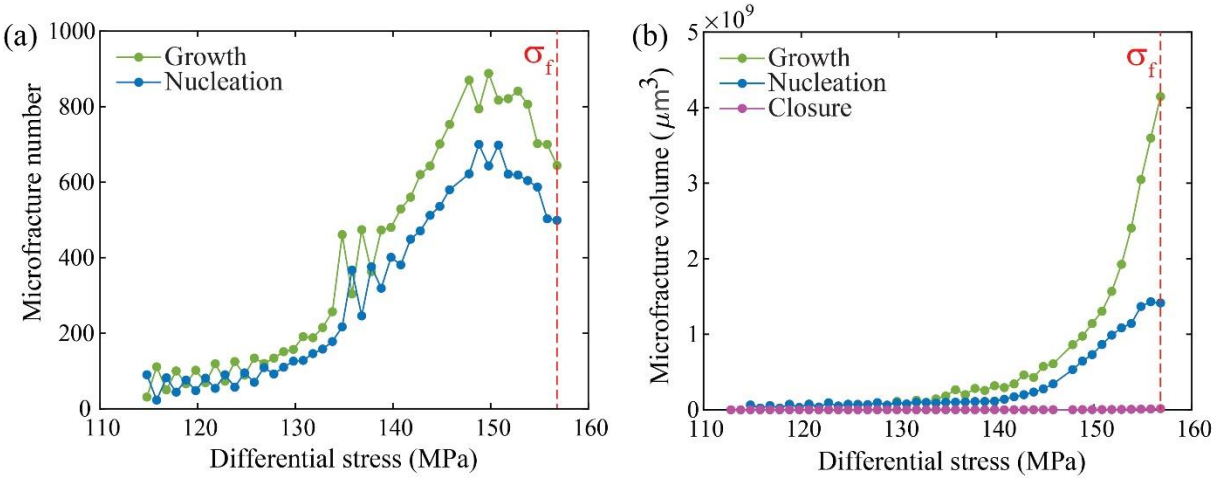

Figure 4.3: Results of tracking algorithm: Growing, nucleating and closing microfractures in Carrara marble (Kandula et al., 2019). Microfracture number (a) and volume (b) as a function of differential stress, for respective mechanisms. Red dashed line marks failure differential stress, σ_f.

Potential errors may originate from the segmentation procedure (especially due to dilation erosion filtering), and the choice of the radius threshold for tracking and mapping of voxels between V_{j-1} and V_j. For example, in Carrara marble, sample length (along z) is ~1500 voxels and width (along x and y) is 740 voxels, for the first scan. The difference in number of voxels along the x-, y- and z-directions between the volumes V_{j-1} and V_j (due to axial contraction and radial

dilation) account to 1-2 voxels in the beginning of the experiment and up to 10 voxels (0.006% of sample length, 0.01% of sample width) for the last stress step before failure. Therefore, mapping between volumes V_{j-1} and V_j is nearly precise. Segmentation errors are observed to be below a size of 100 μm^3 and therefore, this microfracture increment was chosen as a cut-off volume for further analysis.

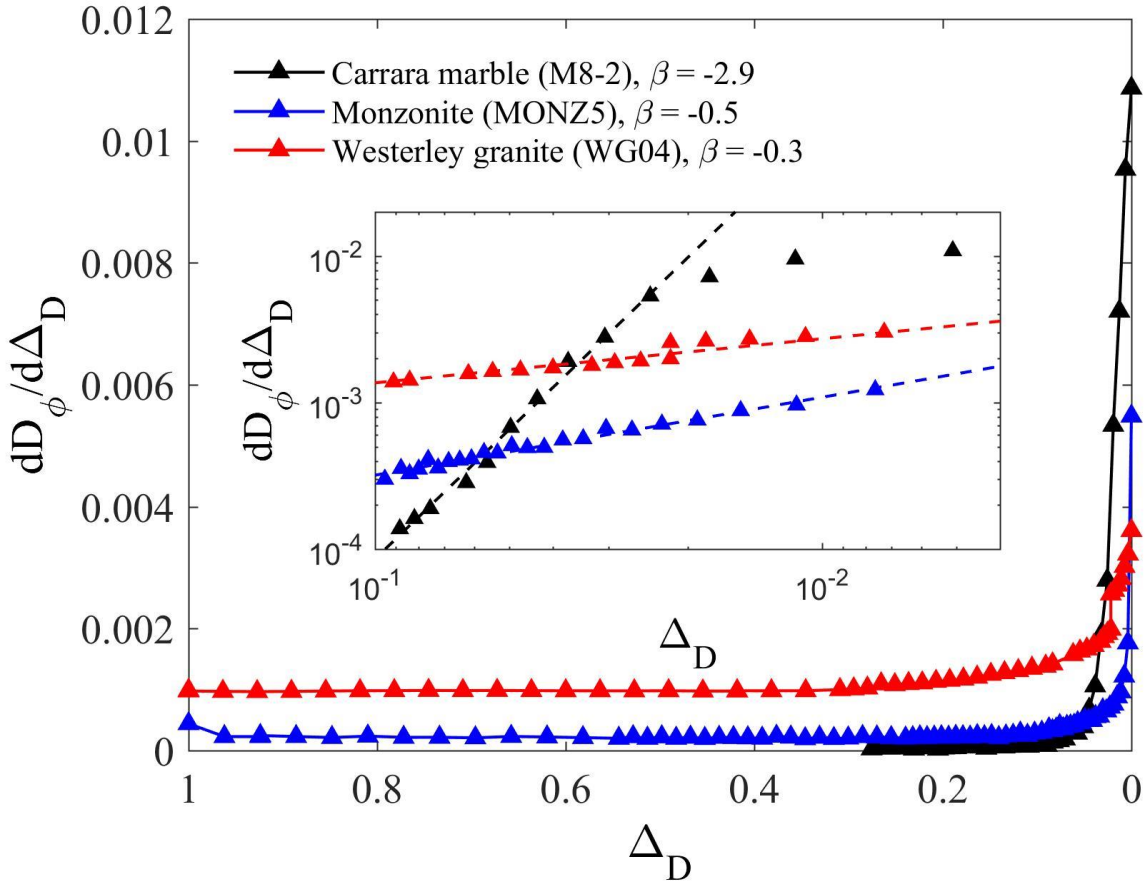

Figure 4.4: Incremental volume as a function of differential stress for Carrara marble (Kandula et al., 2019), monzonite (Renard, McBeck and Kandula, 2019) and Westerly granite (McBeck, Kandula et al., 2019). Incremental volume and differential stress are normalized for comparison of trends among different experiments. $\Delta_D = 1 - \frac{\sigma}{\sigma_f}$, σ = differential stress, σ_f = differential stress at failure. $\frac{dD_\phi}{d\Delta_D}$ = incremental volume, dD_ϕ between the successive stress steps, $d\Delta_D$. Parameterization is used to extract scaling for the trends, which are power-laws. The trend observed in Carrara marble differs significantly from monzonite and Westerly granite and shows a deviation from a power law near failure, which could be due to the final localization before system-size failure.

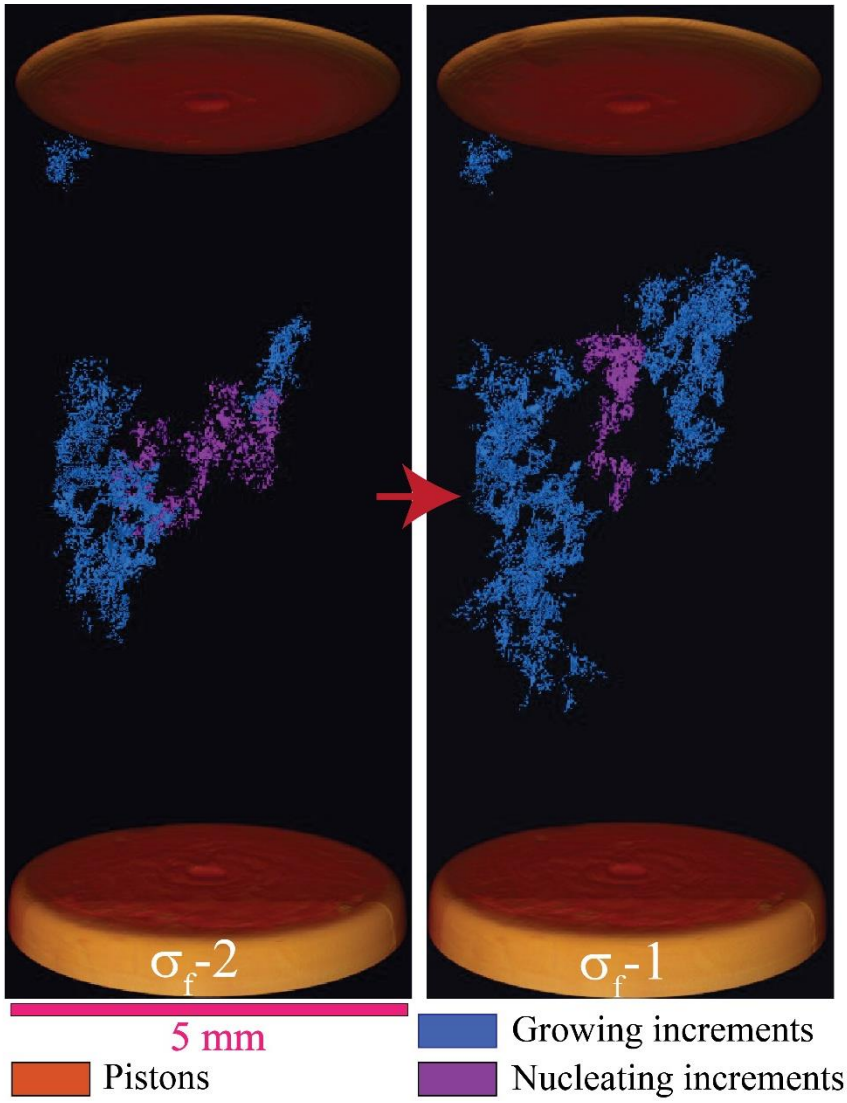

Figure 4.5: Visualization of the tracking algorithm to compute and track microfracture increments in Carrara marble. Three-dimensional illustrations of randomly picked microfracture increments at stress state $\sigma_f - 2$ that grow (dull blue) when the system is driven to a stress state $\sigma_f - 1$ (red arrow). σ_f defines stress at failure. Microfracture increments in purple color nucleate independently at respective stress states.

5 Manuscript Summaries

5.1 Dynamics of microscale precursors during brittle compressive failure in Carrara marble (Journal of Geophysical Research, 2019)

Contribution: I have performed the experiments, analyzed the data, and written the manuscript.

Summary: Failure mechanisms in the crust have microstructural origins, which has motivated the research presented in this manuscript. Using a novel experimental technique of triaxial deformation coupled with time-lapse X-ray microtomography we have imaged the microstructure of Carrara marble under brittle compressive failure at micrometer resolution. We have characterized the damage as opening of new fractures and their coalescence, and closing of pre-existing fractures at incremental loading steps of axial stress. We were able to track all the microfractures as a function of increasing stress. We have computed change in volume of each microfracture using a tracking algorithm that maps 3D digital tomograms between successive stress steps. These incremental change of volume, which we called microfracture increments, show specific power-law statistics that we identified using a maximum likelihood method. Our method allows also the total measurement of strain (both seismic and aseismic, without separating these two components,) and can characterize all deformation events and fracture geometries unlike previous studies using for example acoustic emission monitoring.

Detailed tracking of microfracturing events have revealed that several observables such as incremental damage volume, largest microfracture, distribution of size increments evolve following power law scaling towards system-size failure until 98% of failure stress. Power-law exponents for these observables are in good agreement with theoretical models such as mean-field depinning and progressive damage model, and argue for an interpretation of compressive failure as a critical phase transition from an intact to a failed state. While the assumptions of depinning model does not account for localization of strain, the progressive damage model incorporates microstructural disorder, long-range elastic stress redistributions, local Coulomb damage criterion, and strain localization. Therefore, the progressive damage model successfully captures the characteristics of brittle compressive failure for Carrara marble.

Near-failure dynamics corresponding to greater than 98% of failure stress shows a deviation from a power-law for the incremental damage. Breaking of scaling prior to failure is interpreted to be facilitated by the mechanisms of subcritical (slow aseismic) crack growth and sustained growth of largest damage clusters either through propagation of the largest cluster or the coalescence of damage clusters to form the largest cluster. Therefore, the point at which a deviation from power-law is observed in incremental damage could be a signal that rock volume is approaching system-size failure. Similar analyses on other rock specimen are required to confirm this important observation.

5.2 Synchrotron 4D X-ray imaging reveals strain localization at the onset of system-size failure in porous reservoir rocks (Pure and Applied Geophysics, submitted)

Contribution: I have performed the experiments, analyzed the data, and written the manuscript.

Summary: Porous rocks are characterized by complex microstructure that may control their mechanisms of deformation under crustal conditions. As a result of strain localization, deformation bands form and contain components of dilation, compaction and shear. These deformation bands have been observed in several major geological reservoirs in basins. A systematic characterization of their microstructure is required to provide a consistent description of the multiscale mechanics leading to strain localization. This strain localization process has fundamental implications in geomechanical challenges such as porosity and permeability evolution, induced seismicity, fracturing and subsidence in geological reservoirs. This manuscript focuses on the microstructural evolution in sandstones and limestones subjected to triaxial compression until system-size failure. Dynamic synchrotron X-ray tomography laboratory experiments allowed the direct measurement of pore and microfracture geometries. By mapping the digital tomograms in 3D, incremental strain components are computed between the successive stress steps using a technique of digital volume correlation and dominant localization mechanisms are identified.

Localization of damage occurred through formation of shear bands. Evolutions of porosity with applied load are closely linked to the evolutions of incremental strain components of dilation, compaction and shear. Applied confinement is a guiding parameter in defining the dominant microscale mechanisms and strain localization in porous rocks. Sandstones under low confinement (5 MPa) deform through dilation of pore space and localization of dominant dilatative strain. Under higher confinement of 30 MPa, pore space decreases with applied load facilitated by localization of contractive strain. On the other hand, strain localization in limestones is mixed-mode, with significant contributions from shear along with either dilation or contraction, associated with a decrease in porosity as a function of applied load. Microstructural mechanisms guiding strain localization in sandstones correspond to pore space dilation, pore collapse and grain crushing, and in limestones they correspond to pore collapse, grain crushing with cataclasis and pore-emanating fractures.

5.3 Volumetric and shear processes in crystalline rock approaching faulting (Proceedings of National Academy of Sciences, 2019)

Contribution: I have participated to the experiments, performed data analysis using the fracture tracking algorithm, and contributed to the preparation of the manuscript.

Summary: Experimentally reproducing failure in continental rocks can contribute towards understanding fracturing in geomaterials and preparation processes of large earthquakes. Evolution of microstructure in a crystalline rock under triaxial compression is captured using in-situ dynamic X-ray tomography and cumulative and incremental strain field are computed from digital volume correlation analysis. Experiments performed on a quartz-rich monzonite specimen show damage accumulation through initiation, growth and coalescence of microfractures, leading to macroscopic failure. These processes are accompanied by opening of new microfractures, propagation and closing of existing microfractures, which are revealed by the tracking analysis.

Strain localization in the microscale zones of the rock specimen shows correlation between large positive and negative volumetric strains, shear strain of opposite senses and high volumetric

and shear strains. Evolution of spatial distributions of strain components produced by microfracture development reveals four phases of deformation preceding macroscopic shear failure. (1) Small variation in incremental strain components correspond to initial elastic phase. (2) Volume of rock experiencing positive volumetric strain and negative shear strain increase to 30% following yield. (3) Phase 3 shows a further 10% increase in these volumes. (4) Magnitudes of positive volumetric strain and negative shear strain show a significant 400% increase toward failure while their respective volumes remain roughly constant.

Fracture tracking algorithm is applied to the segmented binary digital volumes as detailed in Chapter 4 of this thesis. Cumulative distributions of microfracture volume increments corresponding to growth, plotted using maximum likelihood method show power-laws. For the last tomogram, this power-law scaling breaks down, which correspond to the last phase of deformation where volumetric and shear strains attain peak values. Accumulation of microfracture increments is therefore facilitated by the volume increasing/decreasing volumetric strain events and positive/ negative shear strain events, which are distributed throughout the rock volume. These events correspond to off-fault seismic and aseismic processes, and can possible occur in the form of conjugate microseismicity. Therefore, these events can play crucial role in preparation processes leading to system-size shear faulting.

5.4 Isolating the factors that govern fracture development in rocks throughout dynamic in situ X-ray tomography experiments (Geophysical Research Letters, 2019)

Contribution: I have performed some of the experiments, the data analysis using the fracture tracking algorithm, and contributed to the preparation of the manuscript.

Summary: Predicting the factors governing fault propagation is a fundamental challenge in geoscience. Several factors that affect fracture propagation have been identified over the past decade. However, the characteristics that determine the likelihood of fracture propagation are still

unclear. This article aims to predict, using a machine learning technique based on logistic regression analysis, characteristics that are most likely to be considered for fracture propagation. We developed and trained logistic regression models for 4 triaxial compression tests on centimeter scale crystalline rock specimen, imaged in situ using X-ray micro tomography. 14 different characteristics that quantify geometry, size, orientation and proximity of a fracture with respect to its neighbors in a network are tested to predict whether a fracture grows or closes. The model produce a logical binary output (true/false) for each parameter based on the input data. Using the tracking algorithm detailed in §4, individual fractures are tracked and labeled with unique identifiers such that growing and closing fractures are separated. Fracture growth is best predicted by the characteristics of length, thickness, volume and orientation with respect to maximum principle stress and distance to the closest neighbor in a network. Growing fractures are clustered, thinner, shorter and oriented $30 - 60^{o}$ to the maximum principle stress. While closing fractures are isolated, thicker, longer and oriented vertically along the maximum principle stress. Our results when exported to crustal faults networks, field analysis should focus on fault length, orientation and clustering for best prediction of their likelihood of propagation.

Manuscript 1

Dynamics of microscale precursors during brittle compressive failure in Carrara marble

Neelima Kandula, Benoît Cordonnier, Elodie Boller, Jérôme Weiss, Dag Kristian Dysthe and François Renard.

Journal of Geophysical Research: Solid Earth, 124(6), 6121-6139 (2019).

AGU100 ADVANCING EARTH AND SPACE SCIENCE

JGR Solid Earth

RESEARCH ARTICLE
10.1029/2019JB017381

Special Section:
Physical Properties of Rocks, Friction and Fracturing: the Walsh Volume

Dynamics of Microscale Precursors During Brittle Compressive Failure in Carrara Marble

Neelima Kandula[1], Benoît Cordonnier[1,2], Elodie Boller[2], Jérôme Weiss[3], Dag Kristian Dysthe[1], and François Renard[1,3]

[1]The Njord Centre, PGP, Departments of Geosciences and Physics, University of Oslo, Oslo, Norway, [2]The European Synchrotron, ESRF, Grenoble, France, [3]University Grenoble Alpes, University Savoie Mont Blanc, CNRS, IRD, IFSTTAR, ISTerre, Grenoble, France

Key Points:
- Microfracture dynamics explains complex physical processes guiding the macroscopic failure in Carrara marble
- Statistical parameters measuring microfracture volume, growth, and spatial organization showed power law scaling with applied stress
- Evolution of several microstructural parameters is in agreement with models that establish compressive failure as a critical phase transition

Supporting Information:
- Supporting Information S1
- Movie S1
- Movie S2
- Movie S3
- Movie S4

Correspondence to:
N. Kandula,
neelima.kandula@geo.uio.no

Citation:
Kandula, N., Cordonnier, B., Boller, E., Weiss, J., Dysthe, D. K., & Renard, F. (2019). Dynamics of microscale precursors during brittle compressive failure in Carrara marble. *Journal of Geophysical Research: Solid Earth*, *124*, 6121–6139. https://doi.org/10.1029/2019JB017381

Received 17 JAN 2019
Accepted 30 MAY 2019
Accepted article online 6 JUN 2019
Published online 26 JUN 2019

Abstract Microscale heterogeneities influence failure mechanisms in the crust. To track the microstructural changes in rock samples when loaded until failure, we employed a novel experimental technique that couples dynamic X-ray microtomography imaging with a triaxial deformation apparatus. We studied the brittle failure of Carrara marble under triaxial compression. Dynamic tomographic data revealed the spatial organization of microfractures and damage increments characterizing the precursory activity toward catastrophic failure. We quantified the emergence of scaling relationships between microstructural parameters, including total damage volume, incremental damage volume, the largest connected microfracture, and the applied differential stress. The total volume of microfractures accumulated from the beginning of the experiment as well as the incremental damage showed power law increase. The growth of the largest connected microfracture was related to differential stress as a power law with divergence at failure. The microfracture volume increments were distributed according to a power law with an upper cutoff that itself spanned the entire volume toward failure. These characteristic features of brittle failure in Carrara marble under compression are in agreement with theoretical models that consider failure as a critical phase transition. We also observed that, very close to failure, several power law relationships broke down, which we interpret to be related to the coalescence of the largest microfractures in a finite size volume. Scaling laws and associated exponents computed from our data are compared with predictions made from theoretical and numerical models. Our results show that precursors of macroscopic brittle failure in Carrara marble follow predictable trends.

1. Introduction

Disorder and long-range stress interactions drive the failure of heterogeneous materials (e.g., Alava et al., 2006). Macroscopic failure arises from the nucleation and growth of fractures and faults that are influenced by heterogeneities at various scales (e.g., Lockner et al., 1991; Paterson & Wong, 2005; Peng & Johnson, 1972). In rocks, structural heterogeneities arise from grains, grain boundaries, pores, joints, and preexisting microfractures. Understanding the microscale physical laws governing the failure of crustal rocks provides fundamental insights into the characterization of precursory signals to brittle compressive failure, including microfracture propagation and arrest, and interaction of microfracture populations.

Preceding some large earthquakes, small earthquakes (foreshocks) often develop in the nucleation zone of the main shock (e.g., Bouchon et al., 2011; Jaumé & Sykes, 1999; Kato et al., 2012). However, earthquake foreshocks are not always observed (Wu et al., 2013; Zaliapin & Ben-Zion, 2013). Experimental and theoretical studies have suggested that the progressive growth of these precursors develop into unstable slip along a fault (Ohnaka, 1992).

Macroscopic brittle deformation in rocks is preceded by the propagation of precursory microfractures (Lockner et al., 1992; Wong et al., 2006). In triaxial compression laboratory experiments, microfractures tend to nucleate and localize along planar faults oriented at ~30° to the direction of the main compressive stress (Lockner et al., 1991). Optical microscopy (Moore & Lockner, 1995; Tapponnier & Brace, 1976), scanning electron microscopy (Brace et al., 1972), laser scanning confocal microscopy (Fredrich et al., 1995), and acoustic emissions (Lockner et al., 1992) have revealed some of the microstructural origins of precursors prior to macroscopic failure. Complementary to these techniques, dynamic X-ray microtomography coupled with triaxial load cell is a unique tool for imaging the microstructure of crustal rocks that are subjected to

deformation (e.g., Renard et al., 2017; Renard, Mcbeck, et al., 2019; Renard, Weiss, et al., 2018; Iglauer & Lebedev, 2017). This technique provides three-dimensional microstructural information on damage distribution as failure is approached and is complementary to other imaging techniques such as acoustic emissions (e.g., Renard, McBeck, et al., 2019).

In the present study, we analyzed in situ time-resolved three-dimensional X-ray microtomography data acquired on centimeter-scale samples of Carrara marble subjected to triaxial compression tests under stress conditions relevant for earthquake nucleation. This imaging technique produced a 3-D digital map of the spatial distribution of microfracture populations and their evolution toward failure. We developed a novel tracking algorithm to image not only the cumulated microfracture network but also the dynamics of increments of fracture growth, allowing quantifying tomography data beyond what has been previously achieved for other rocks (Renard, McBeck, et al., 2019; Renard, Weiss, et al., 2018). Our data sets provide high-resolution quantification of the dynamics of precursors prior to system-size brittle failure. Increments of fracture growth at a given stress step are related to the acoustic energies measured in some laboratory experiments and avalanches described in theoretical and numerical models of rock failure. Hence, our experimental results can test the theoretical predictions on physical laws explaining evolution of microfractures and damage (e.g., Alava et al., 2006) and explore possible deviations from scenarios of the evolution of precursor activity prior to system-size failure.

2. Background

2.1. The Microscale Origin of Rupture in Rocks: The Classical View

When low porosity rocks are loaded, microfractures may initiate from grain boundaries and internal weak zones such as fluid inclusions or healed cracks (Kranz, 1983; Paterson & Wong, 2005; Tapponnier & Brace, 1976). The Griffith's theory of fracture propagation explains failure through the propagation of cracks from preexisting defects (Griffith, 1921). Under compressive loading, it is classically considered that damage and deformation follow two phases: a first phase in which microfractures nucleate stochastically from preexisting heterogeneities in the volume and a second phase where these microfractures start interacting and grow until macroscopic failure leading to the development of roughly two-dimensional faults (Jaeger & Cook, 1969; Kuksenko et al., 1996).

At low axial stresses, rock volume variations are mostly elastic in nonporous rocks. For axial stresses above 40% to 60% of the failure stress, sample volume increases inelastically as the result of the opening of microfractures, a process called dilation (Brace et al., 1966; Hoek & Martin, 2014). Brace and Bombolakis (1963) and Hoek and Bieniawski (1965) have shown that microfractures tend to become parallel to the direction of principal stress and propagate out of their initial plane under uniaxial loading. Uniaxial and triaxial compression tests on granite showed fault surfaces with steps arranged as a staircase, and the surfaces of steps were nearly perpendicular to the direction of principal stress (Peng & Johnson, 1972). This observation was interpreted as the linkage of microfractures with orientations parallel to the main compressive stress, leading to the formation of a shear plane.

2.2. Deformation of Carrara Marble

Deformation of Carrara marble, a rock made of more than 99% calcite and composed of interlocking calcite grains, has been studied extensively. Experimental and field studies on Carrara marble in various settings have shown that macroscopic deformation is guided by microstructural changes during loading. When samples of Carrara marble were deformed near the brittle-plastic limit (Fredrich et al., 1989), a transition from localized brittle fracture to nonlocalized semibrittle flow was observed. In the semibrittle field, the stress-induced crack density and anisotropy decreased with increasing confining pressure. Crack density and anisotropy in samples deformed in the semibrittle field are comparable to those in the prefailure brittle samples. Crack density and anisotropy alone are not sufficient to characterize the damage structure that leads to localization. Fredrich et al. (1989) suggested a quantitative characterization of damage volume and its spatial correlation. Any further increase in confining pressure drove the system to the plastic domain, which inhibited microfracture growth and localization. This inhibition was interpreted by the blunting of fracture tips.

Triaxial deformation tests were performed on Carrara marble across the brittle-ductile transition (Schubnel et al., 2006), and damage growth was observed to be guided by the microstructure and rheological properties

of the rock. The same conclusion was emphasized by acoustic emission measurements (Schubnel et al., 2006). At high confining pressure, plastic strain dominated the deformation until cataclastic flow was observed (Schubnel et al., 2006). During this phase, twinning and dislocations piled up such that cracks were required to accommodate local plastic strain. When the normal stress was decreased, driving the system to a brittle regime, transient creep events was observed along with sudden growth of destabilized microcracks. Oesterling et al. (2007) analyzed the microstructures and textures of a natural shear zone in Carrara marble sampled in the upper part of the Frigido valley in the central Alpi Apuane, Italy. They observed that deformation in this natural shear zone showed strain-dependent variations in microstructure. In the present study, we consider deformation of Carrara marble in the brittle regime and present microstructural changes during deformation, which may provide insights in understanding deformation in this natural shear zone.

2.3. Fracture and Damage Models of Failure

Heterogeneities and disorder guide fracture nucleation and propagation in rocks and other heterogeneous brittle materials. Prior to macroscopic failure, precursory activity was observed as the progressive nucleation of microfractures and their stable growth (Lockner et al., 1992; Renard, Weiss, et al., 2018; Vu et al., 2019; Wong et al., 2006).

Empirical failure criteria, such as the Mohr-Coulomb criterion, quantify rock strength (e.g., Paterson & Wong, 2005). However, by construction, these approaches do not consider the existence of precursors. More recently, theoretical models were developed to describe failure in heterogeneous media, such as rocks, using concepts from out-of-equilibrium statistical physics. These models consider long-range stress interactions and disorder and history effects during loading (e.g., Alava et al., 2006). In these models, heterogeneities in the system are described by a spatial distribution of local stress threshold or initial defects with varying elastic parameters. During loading, damage evolution is inferred from the spatial organization of damage events and energy dissipation that accounts for the complex interplay between disorder and elastic interaction of microfractures. In such models, failure can be described as a phase transition from an initial unbroken stage to a final broken stage (e.g., Alava et al., 2006; Dahmen et al., 2009; Girard et al., 2012; Vu et al., 2019). Evolution of damage is tracked in terms of a control parameter, which is a measure of the applied load.

In the present study, we imaged and measured the total damage volume, the increments of damage, and the volume of the largest microfracture cluster as Carrara marble specimens approached failure. Our main goal is to quantify the relationships between these parameters and the applied stress by using the reduced control parameter, $\Delta_D = \left(\sigma_D^f - \sigma_D\right)/\sigma_D^f$, where σ_D is the differential stress applied on the sample and σ_D^f is the differential stress at failure, considered here as the critical point where the failure transition occurs.

In Figure 1, we summarize the various parameters used in the present study and represent how microfracturing controls the road to failure. Numerical simulations that consider rock failure as a critical phase transition predict that these parameters should follow power law behavior with well-defined exponents when approaching failure (Girard et al., 2012). We compare the scaling exponents measured in our experiments with theoretical predictions and experimentally test the critical nature of the failure process, providing new insights into the failure of geomaterials. We quantify how long-range interactions and disorder present in the system guide the route to brittle compressive failure in Carrara marble.

3. Material and Methods

3.1. Experimental Procedure

Carrara marble, a rock made of 99.6% of calcite, with very low porosity close to ~0.2% and grain sizes in the range 100–200 μm (Rutter, 1972; Malaga-Starzec et al., 2002), was deformed. Two cylindrical samples, 10-mm height and 5-mm diameter, were cored from the same $10 \times 10 \times 10$-cm block. We used an experimental technique that couples high-resolution synchrotron X-ray microtomography and the Hades triaxial deformation apparatus (Renard et al., 2016), enabling time-lapse three-dimensional imaging of rocks at in situ conditions of stress during deformation. We tracked the evolution of fractures in two specimens of Carrara marble (labeled M8-1 and M8-2) that were deformed until brittle failure (Table 1). Each specimen was mounted in the triaxial deformation apparatus ($\sigma_1 > \sigma_2 = \sigma_3$) as shown in the inset of Figure 2. The Hades apparatus is installed on the rotating stage of the X-ray microtomography beamline ID19 at the

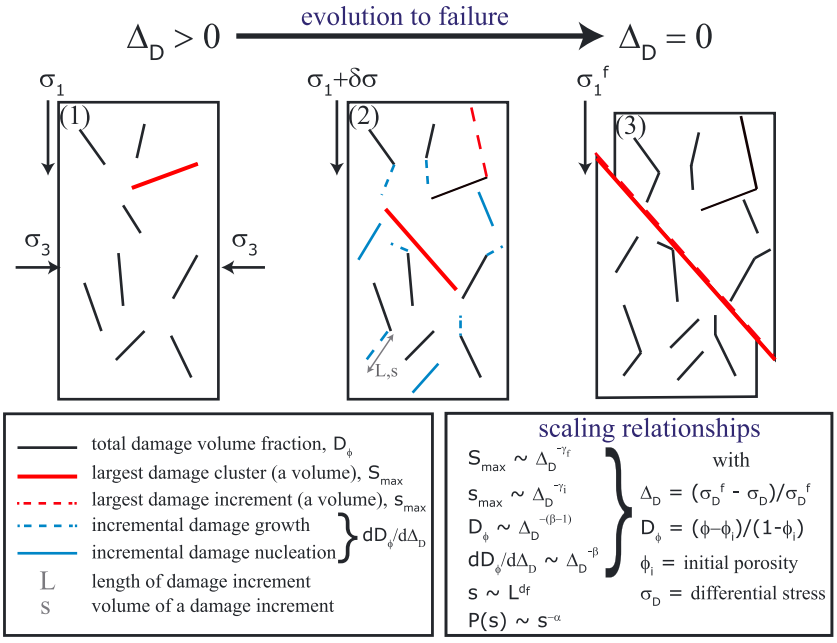

Figure 1. Sketch showing the evolution of Carrara marble toward macroscopic failure in three stages of deformation: (1) random nucleation of microfractures; (2) nucleation, growth, and localization of damage increments; and (3) development of a shear fault at failure. σ_1: axial stress, $\sigma_3 = \sigma_2$: confining pressure, $\sigma_D = (\sigma_1 - \sigma_3)$: differential stress, σ_D^f: differential stress at failure, $_D$: stress control parameter. If failure is considered as a critical phenomenon (Girard et al., 2012; Vu et al., 2019), several power law scaling relationships should emerge among stress control parameter, $_D$; the cumulative microfracture (black line) volume fraction quantified by the damage parameter, D_φ; the volume fraction of the largest microfracture cluster, S_{max} (red line); the volume fraction of damage increments (blue dotted and solid lines); the volume fraction of the largest damage increment, s_{max} (red dotted line), dD_φ/d_D; the size (volume), s, and length, L, of a given microfracture increment; and the probability distribution of damage increments, $P(s)$. γ_f, γ_i, d_f, β, and α are the power law scaling exponents. d_f is the fractal dimension of microfracture increments.

European Synchrotron Radiation Facility (Grenoble, France). Each sample was loaded axially between stainless steel pistons. The interfaces between the pistons and the sample were not lubricated. The sample was inserted into a polymer jacket, and silicon oil applied a constant confining pressure to the sample. Experiments were performed at 25 °C, without pore fluid. The presence of a high flux of X-rays during the scans did not modify the internal temperature in the rig, which was monitored with a thermocouple.

During the experiments, the axial stress was increased in successive steps of either 2 MPa (sample M8-1) or 1 MPa (sample M8-2), until failure. At every step increase in stress, a three-dimensional X-ray microtomography volume was recorded with 2,500 radiographs per scan, with a rotation of 180 degrees. Radiographs were acquired with a polychromatic X-ray beam (Wiggler gap of 68 mm with 5.6 mm of Al filter), given an equivalent energy of 85 keV that crossed the sample. The pixel size was 6.5 μm. Each scan lasted 90 s during which the applied stress was held constant. At this resolution, we did not detect any blurring artifact indicating movement of the sample or fracture growth during scan acquisition. During a single-stress increase, microfractures nucleated, coalesced, or closed by a single growth event or by successive events of growth that occurred during this stress step increase.

Table 1
Experimental Conditions for the Deformation of the Two Carrara Marble Samples

Sample	Confining pressure	Differential stress at yield	Differential stress at failure	Temperature	Rate of increase in differential stress	Number of 3-D scans
M8-1	20 MPa	88 MPa	100.7 MPa	25 °C	2 MPa/step	44
M8-2	25 MPa	126 MPa	156.8 MPa	25 °C	1 MPa/step	97

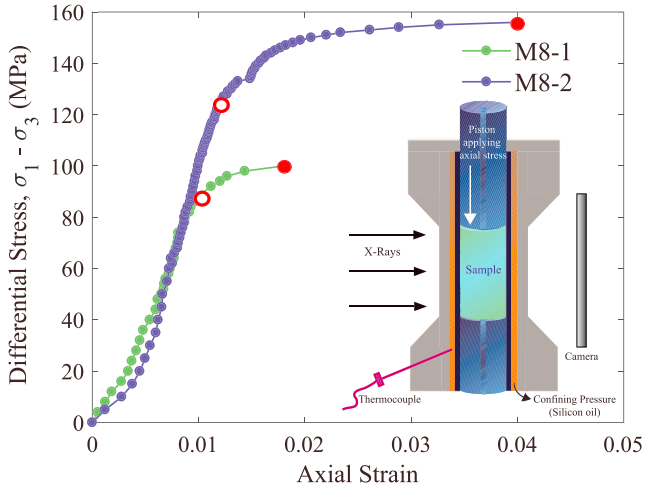

Figure 2. Axial strain versus differential stress for Carrara marble samples M8-1 (confining pressure of 20 MPa) and M8-2 (confining pressure of 25 MPa). Both samples exhibited a quasi-brittle failure behavior. Each circle corresponds to the acquisition of a three-dimensional X-ray tomography volume. Open red circle: macroscopic yield point. Full red circle: last X-ray tomography scan before failure. Inset: sketch of the Hades rig.

Series of 44 and 97 dynamic X-ray microtomography volumes were acquired for samples M8-1 and M8-2, respectively. The radiographs were reconstructed in three dimensions using plain filtered back projection (Mirone et al., 2014), coupled with a single-distance phase retrieval algorithm adapted from Paganin et al. (2004). After experiments, the specimens were impregnated with liquid epoxy resin and then cut along the axial plane after the liquid epoxy had solidified. The exposed surface was polished, coated with 10-nm gold, and imaged using a Hitachi SU5000 scanning electron microscope at the University of Oslo, with a voltage of 15 kV.

3.2. Segmentation of the Tomograms

As the specimens deformed toward failure, damage accumulated in their volume as nucleating and propagating microfractures. The series of three-dimensional digital volumes obtained at every stress step until deformation were postprocessed to extract this damage. The 3-D tomograms were 16-bit images that included artifacts such as rings, periodic stripes, and speckle noise. Seven steps were followed to extract the evolution of damage with increasing stress:

1. Periodic stripes on every 2-D slice appeared due to the noise from the scintillator. A Fourier transform of each original 2-D slice was calculated, and the part of the spectrum that corresponded to higher intensities was cut off to remove these stripes. The inverse Fourier transform of the image was then calculated to recover the original slice (Figure 3a).

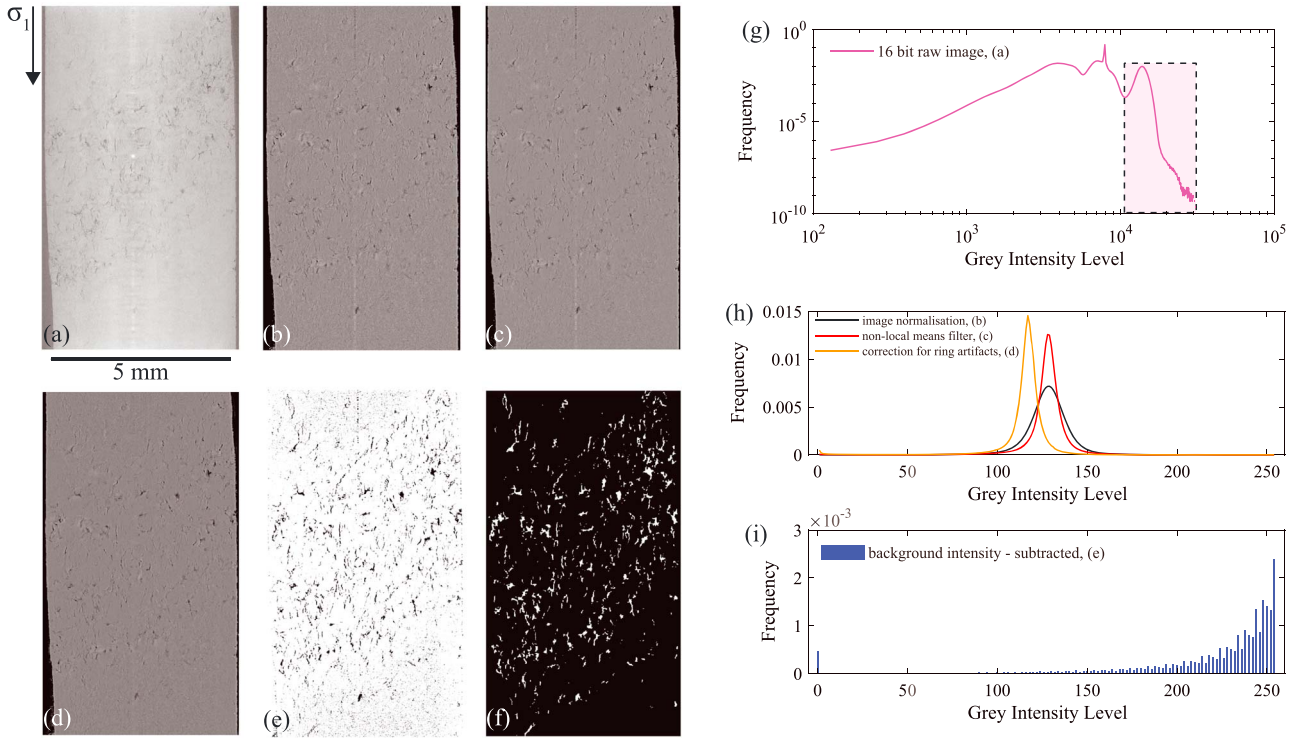

Figure 3. Two-dimensional sections of a three-dimensional volume at various steps of the data segmentation process used to extract the microfractures. (a) Initial reconstructed 16-bit image and (g) corresponding grayscale histogram. Region shaded in pink corresponds to the rock, while the rest of the histogram corresponds to the jacket and oil used for confining the sample. (b) Normalization of the grayscale histogram and transformation into 8-bit image. (c) Image after applying a nonlocal means filter. (d) Image corrected for ring artifacts and corresponding histograms shown in (h). (e) Image after background intensity was subtracted and (i) corresponding histogram. (f) Segmented image with the microfractures in white.

2. The gray level in each volume was normalized to enhance the details of the microfractures (Figure 3b) and saved into 8 bit.
3. A nonlocal means filter (Buades et al., 2005) was applied to average out the speckle noise and sharpen the microfractures (Figure 3c).
4. We used a Matlab package for ring artifact correction (Jha et al., 2014) to remove these artifacts in the three-dimensional volumes. A resulting image is shown in Figure 3d.
5. We employed a background subtraction algorithm (Sternberg, 1983) to remove a smooth continuous background across the image (Figure 3e). This step is performed by choosing a "rolling ball" radius for each image. At every voxel is assigned a local background value by averaging around the voxel over of the rolling ball. This averaged intensity is subtracted from the original image. To remove large spatial variations in the background intensity, we have used the background subtraction filter of the software AvizoFire.
6. Each image was then thresholded to select microfractures. Varying slightly this threshold did not change quantitatively the results (Figure S2 in the supporting information). Microfractures with a volume less than 100 voxels were limited by the resolution of the segmented images and were removed. Therefore, the value of 100 voxels is the lower limit of microfracture size considered here. At the end of this last segmentation step, we obtained a binary image with microfractures quantified as intensity value 1 and the rock with intensity value 0 (Figure 3f).
7. Finally, we have used dilation-erosion filtering to connect voxels that belong to the same microfracture. The procedure we used was to dilate the microfractures by one voxel to connect close neighbors and then erode these microfractures by one voxel to recover their original volume.

3.3. Microfracture Statistics

Geometric characteristics of microfractures such as position, volume, surface area, and shape parameters were calculated from the segmented binary three-dimensional data. Because microfractures accumulated at every axial stress step increase, σ_j, each microfracture or microfracture network at this stress step resulted from the cumulative growth of preexisting microfractures or nucleation of new microfractures that formed during the stress steps $\sigma_{j=1}$ to σ_j (Figure 1). We observed that the incremental damage volume at step σ_j results from a balance between the growth of preexisting fractures, the nucleation of new ones, and the possible closing of some of the preexisting microfractures, whose total volume is negligible (Figure S5). We distinguished between the cumulated damage, D_φ, defined as the total microfracture volume fraction at a given stress step σ_j, and the incremental damage, $\mathrm{d}D_\varphi/\mathrm{d}\Delta_D$, between each stress step σ_{j-1} to σ_j. In order to obtain an instantaneous measurement of the progressive growth of damage, we computed the dynamic variable, the damage increments s that formed only between stress steps σ_{j-1} and σ_j. The sum of these increments s normalized by the sample volume gives the incremental damage, $\mathrm{d}D_\varphi/\mathrm{d}\Delta_D = \frac{\sum_{\sigma_j} s}{V_j^{\mathrm{sample}}}$ for a given stress step σ_j, and sample volume V_j^{sample}. These damage increments, s, between two successive stress steps were extracted by mapping the segmented volume V_{j-1} at the $(j-1)$th stress step with the consecutive volume V_j at the next stress step such that the position of every voxel in volume V_j has a corresponding position in the volume V_{j-1}. We could then select voxels that corresponded to new increments of damage in the volume V_j compared to the volume V_{j-1}. This mapping was necessary because the sample may have compacted or dilated between successive stress steps, so that a simple difference between successive three-dimensional tomograms cannot be used to extract damage increments. This procedure provides new ways of quantifying damage in tomography data, which could not be performed in previous studies (Renard, McBeck, et al., 2019; Renard, Weiss, et al., 2018).

The centroids and volumes of damage increments at every step were tracked until failure and sorted into three categories: (1) damage increments that grew and propagated between stress steps $(j-1)$ and j (blue dashed lines in Figure 1), (2) nucleation of new microfractures at stress step j (full blue lines in Figure 1), and (3) closing or coalescence of microfractures from steps $(j-1)$ and j (Figure S1). The large numbers of microfractures and microfracture increments enable robust statistical analysis on the damage and damage increments. In the analysis, the stress step σ_j is translated in terms of the control parameter, Δ_D. An example of the results obtained using this algorithm is shown in Figure S1.

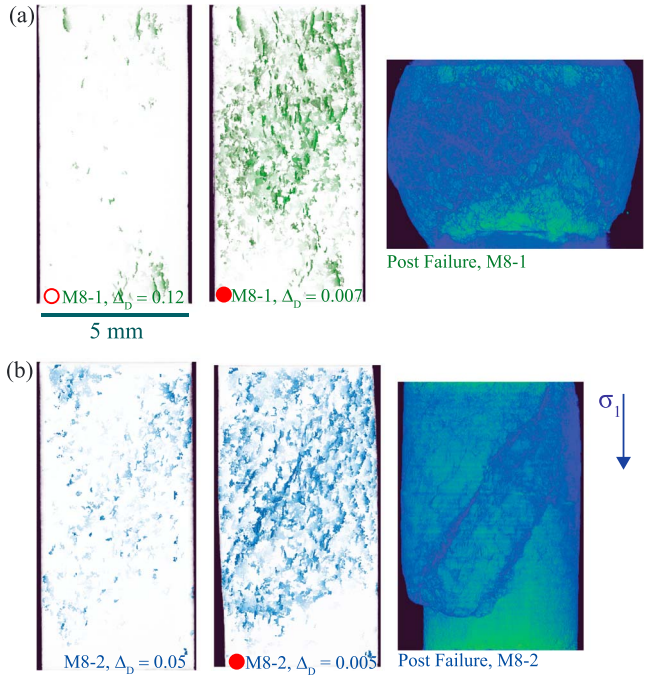

Figure 4. View of segmented damage (i.e., microfractures) in samples M8-1 (a) and M8-2 (b). The left image displays the damage at the macroscopic yield point. The middle image shows the damage at the onset of failure, and the right image shows a three-dimensional rendering of sample after failure and slip along shear planes. Open red circle shows the macroscopic yield point; full red circle shows the last scan acquired before failure for which the corresponding distance to failure $_D$ is indicated. Animations of the evolution of damage are provided in the supporting information (Movies S1–S3).

3.4. Advantages and Limitations of the Experimental Technique

A crucial advantage of the present experimental technique is that all damage can be detected within the spatial resolution, independently of how this damage was produced by a dynamic crack propagation (i.e., seismic) or by a slow crack propagation (i.e., aseismic). Moreover, the exact spatial location of the damage in the sample is unambiguous in our data, which also give access to the shape and orientation of the microcracks (see section 4.3 below and Renard, McBeck, et al., 2019; Renard, Weiss, et al., 2018). These are important differences with experimental studies that monitor damage evolution using acoustic emissions.

On the other hand, the X-ray microtomography experimental technique employed in the present study has several limitations. First, because each scan must be performed on a sample that does not deform, the stress must be maintained constant during each acquisition. The consequence is that despite the loading path is performed at an average constant strain rate, stress is increased step by step. In average, the strain rate was low enough to avoid subcritical crack propagation; therefore, we consider that this experimental constraint did not affect the overall brittle behavior of the samples.

Another limitation is the spatial resolution of 6.5 μm that does not allow detecting microfractures smaller than this resolution. Because our study is based on the detection of voids (i.e., volumetric damage), we cannot detect preexisting microfractures that would have slid during a given stress step increase, without producing additional damage or local dilation. Such situation would happen likely for slips below the spatial resolution of the data.

4. Results

As the differential stress was increased, the deformation of the Carrara marble samples can be qualitatively characterized by the progressive accumulation of damage, which finally localized along a shear plane resulting in a macroscopic fault (Figures 1, 2, and 4). Damage accumulated by an increase in the number and size of microfractures, which dilated the volume. Because we could extract the microfractures visible at the resolution of the tomograms, we were able to quantify the statistical evolution of six parameters as a function of the control parameter, $\Delta_D = \left(\sigma_D^f - \sigma_D\right)/\sigma_D^f$, at failure (Figure 1), as mentioned in section 2.3. We tracked the following:

1. the total damage volume fraction defined as $D_\varphi = \frac{\phi-\phi_i}{1-\phi_i}$, where ϕ is the volume fraction of all open microfractures and voids at a given stress step and ϕ_i is the volume fraction corresponding to the initial porosity of the sample before loading ($\phi_i \approx 0.2\%$);
2. the new volumes of voids and microfractures, also called incremental damage, with increasing differential stress, $dD_\varphi/d\Delta_D$, computed as explained in section 3.3.
3. the volume fraction of the largest microfracture cluster, S_{max};
4. the volume fraction of the largest damage increment s_{max};
5. the size (volume) s and the largest eigenvalue of microfracturing increments, considered as their lengths L; and
6. the probability distribution of microfracture increments, $P(s)$.

All these parameters are sketched in Figure 1. Their evolution toward the peak stress should show power law scaling if brittle failure is a critical phenomenon (Girard et al., 2012). Two procedures may be used to obtain the scaling exponents (Stanley, 1999). We present the first method in section 4.2 by calculating scaling laws. We present the second method in section 4.3 by performing a data collapse analysis.

4.1. Macroscopic Mechanical Behavior and Microstructure

Here, we analyze the macroscopic failure in Carrara marble along with the microstructural changes. Figure 2 displays the macroscopic mechanical behavior of the two specimens. The differential stress-axial strain response was nonlinear for differential stresses below 40 MPa. We interpret this behavior to arise from the closure of voids during initial loading. A quasi-linear regime was observed above 40 MPa until a significant departure from elastic behavior occurred, here defined as the macroscopic yield stress, σ_D^y. The position of this yield stress occurs at a deviation of linearity in the effective stress versus volumetric strain curve (Brace et al., 1966). This point nearly occurs at 90% and 80% of the differential stress at failure, σ_D^f, for samples M8-1 and M8-2, respectively (Table 1). After this point, additional increases in differential stress resulted in irreversible macroscopic strain deformation until σ_D^f was reached, where an abrupt transition to macroscopic brittle failure was observed. Within one-step increase in applied differential stress, the rocks failed and a stress drop larger than 10 MPa occurred. Figure 4 shows views of the total damage, D_φ, at the yield point and near failure, as well as 3-D renderings of the failed samples, and indicates that damage started well before the macroscopic yield.

Tomography data show that damage clusters initially nucleated in spatially disperse, apparently random, locations in the initial stage of deformation (Movie S1), similar to acoustic emissions locations in granite (Lockner et al., 1991). With increasing differential stress, microfractures localized near the largest damage clusters (Movie S1), growing into larger clusters (Movie S2), until one or few quasi two-dimensional system-spanning shear planes developed (Movie S3). The shear planes were oriented at $30° \pm 3°$ to the direction of the main compressive stress, σ_1, as shown in Movies S1 and S3. Figure 4 shows snapshots of segmented microfractures in both samples (Movie S1) and the sample configuration after failure, which corresponds to the last snapshot in the Movie S3.

Figure 5 shows scanning electron microscopy images of the samples after deformation. The mean grain size was in the range 100–200 μm, in agreement with other studies (Rutter, 1972; Malaga-Starzec et al., 2002). A larger number of microfractures grew within grains rather than along grain boundaries (Figure 5e). Their general orientation tended to be roughly parallel to the main compressive stress direction (Figure 5b). Some microfractures also propagated across grain boundaries. After failure, damage localization resulted in several shear planes (Figures 5c and 5d), which were oriented at an angle of ~30° to the main compressive stress. Shear sliding resulted in cataclasis and reduction in grain size along with the formation of a gouge (Movies S1 and S3).

4.2. Damage Scaling Laws

Data allow computing geometrical parameters of microfractures. The dynamics of microfractures toward system-size failure was tracked as a function of the control parameter, Δ_D, which measures the distance to failure through the applied differential stress. We also represent the evolution of the damage parameter, D_φ, as a function of normalized differential stress σ_D/σ_D^f (Figure 6). Microfractures nucleated and grew, producing macroscopic irreversible strain (Figure 2). An accelerated growth of D_φ toward failure was observed (Figure 6). For sample M8-1, a sharp increase of D_φ was observed when approaching failure. However, due to the limited number of tomograms near failure, a robust fit could not be estimated for this sample. For sample M8-2, for which more three-dimensional volumes were acquired when approaching failure, the growth of D_φ was progressive and accelerated toward failure. In the range $0.02 < \Delta_D < 0.2$, this acceleration followed a power law $D_\varphi \sim {\Delta_D}^{-(\beta - 1)}$ with an exponent $(\beta - 1) = 1.5$ (inset of Figures 6 and S3). Here the exponent $(\beta - 1)$ comes from the fact that the exponent β is defined for the incremental damage, $dD_\varphi/d\Delta_D$, for which we expect a power law acceleration $\mathrm{d}D_\varphi/\mathrm{d}\Delta_D \sim {\Delta_D}^{-\beta}$ (see Renard, McBeck, et al., 2019; Renard, Weiss, et al., 2018, and below), while the total damage, D_φ, is the integral of this quantity (Figure 1). For this sample, D_φ tapered at small values of the control parameter and showed an exponential evolution for $\Delta_D < 0.02$.

Microtomography data provide information on the volume of microfractures from the beginning of the experiment. In order to compare our results with existing theoretical and numerical studies on brittle failure, we have computed the change in the volume of pores and microfractures, $\mathrm{d}D_\varphi/\mathrm{d}\Delta_D$, between two successive stress steps (see section 3.3). The evolution of $\mathrm{d}D_\varphi/\mathrm{d}\Delta_D$ during loading is relevant to compare our experimental results with theoretical models of damage progression toward failure (Alava et al., 2006; Girard et al., 2012).

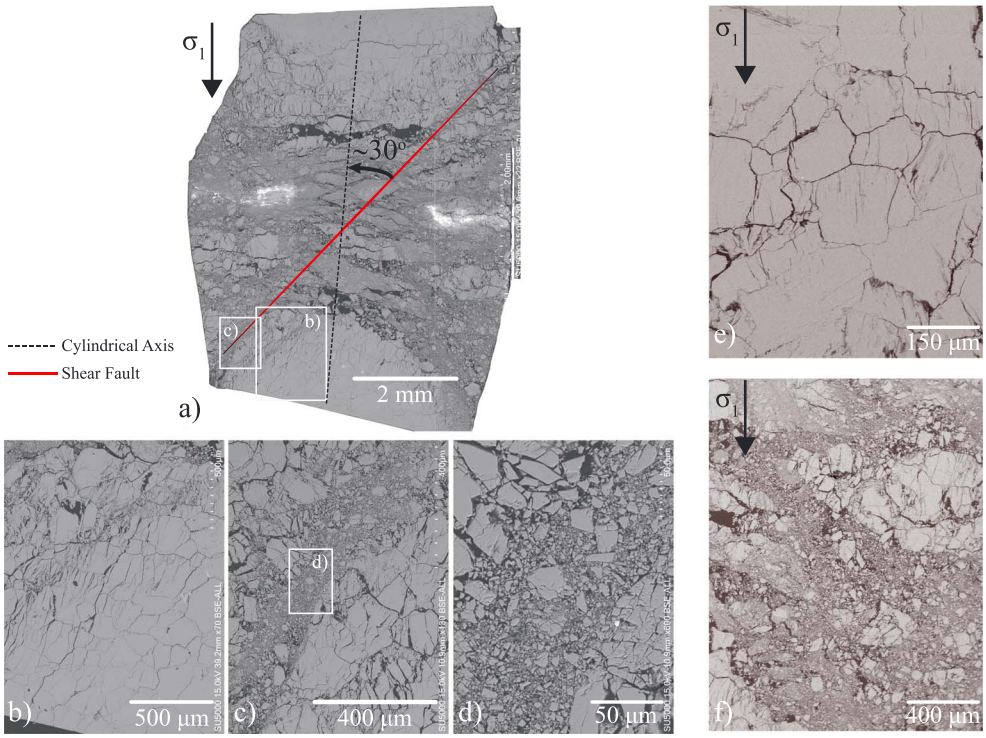

Figure 5. Scanning electron microscopy images of samples M8-1 (a–d) and M8-2 (e, f) recovered after failure. (a) Vertical cross section in the middle of the entire sample. (b–d) Zooms showing microfractures in grains (b) and zoom on one shear zone with intense grain comminution (c, d). (e) Development of microfractures inside grains and opening of grain boundaries. Many intragranular microfractures are pinned at grain boundaries. (f) Shear zone in sample M8-2 with intense grain comminution. In all images, the main compressive stress is oriented vertical.

These theoretical models have predictions for volume fractions of $dD_\varphi/d\Delta_D$ produced by the damage nucleation and growth and are plotted as a function of Δ_D in Figure 7a for sample M8-2. These data show that the growth of existing microfractures in the neighborhood of large microfractures is dominant in number and volume compared to the nucleation of new microfractures when approaching failure. For sample M8-2, $dD_\varphi/d\Delta_D$ shows a power law scaling $dD_\varphi/d\Delta_D \sim \Delta_D^{-\beta}$ up to the vicinity of failure ($\Delta_D \approx 2 \times 10^{-2}$) with an exponent $\beta = 2.6$ fully consistent with the results of Figure 6 for cumulated damage ($\beta - 1 = 1.5$) (inset in Figure 7a). A tapering of the power law behavior of $dD_\varphi/d\Delta_D$ for $\Delta_D < 0.02$ is observed, similar to the flattening or exponential increase observed in the behavior of D_φ (Figure 6).

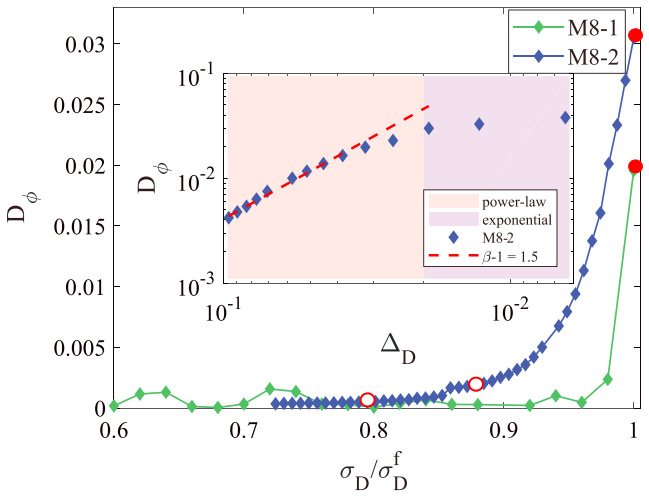

Figure 6. The damage index, D_φ, increases with increasing differential stress for samples M8-1 (green) and M8-2 (blue). Inset: log-log plot of D_φ as a function of $_D$ for sample M8-2. A linear trend in the range $0.02 < _D < 0.1$ demonstrates a power law relationship $D_\varphi \sim _D{}^{-(\beta - 1)}$ with a scaling exponent $(\beta - 1) = 1.5$. Open red circle shows the macroscopic yield point; full red circle shows the last scan acquired before failure.

We also computed the number of damage increments between two successive stress steps, $dN/d\Delta_D$, also called damage event rate. In seismology, it has been proposed, for example, that volcanic eruptions could be preceded by an accelerating foreshock sequence following a so-called inverse Omori's law, $dN/dt \propto (t_f - t)^{-p}$ (e.g., Bell et al., 2013), with N the number of earthquakes. In our system, we consider an equivalent inverse Omori's law, $dN/d\Delta_D \propto \Delta_D{}^{-p}$, where time is replaced by the control parameter Δ_D. The number of damage increments plotted as a function of Δ_D for sample M8-2 (Figure 7b) follows such inverse Omori law until $\Delta_D \approx 0.02$ with a scaling exponent $p = 1.9 \pm 0.05$. Breaking down of this inverse Omori scaling close to failure, for $\Delta_D < 0.02$, could possibly be connected to the tapering of the power law behavior of $dD_\varphi/d\Delta_D$ shown in Figure 7a.

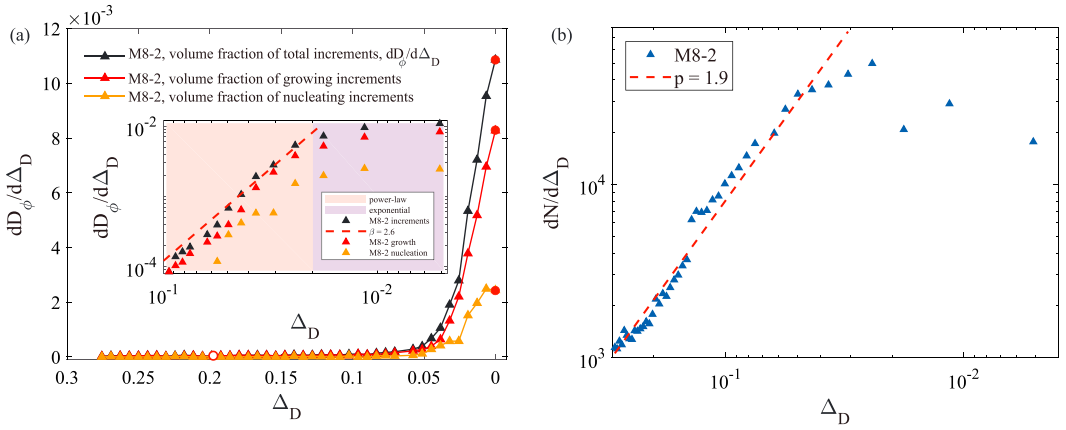

Figure 7. (a) Evolution of incremental damage, dD_{φ}/d_D as a function of control parameter, $_D$ in sample M8-2. Damage increments are tracked as incremental events of growth and nucleation (see Figure 1), and the respective volume fractions are plotted as a function of $_D$. Inset: Rate of damage growth and nucleation plotted against control parameter for sample M8-2, showing a scaling $dD_{\varphi}/d_D \sim {}_D^{-\beta}$ with an exponent $\beta = 2.6$ for $0.02 < {}_D < 0.1$ (red dashed straight line). For $_D < 0.02$, an exponential evolution is observed. Open red circle shows the yield point; full red circle shows the last scan acquired before failure. (b) Number of damage increments (damage event rate), dN/d_D plotted as a function of control parameter, $_D$, shows a power law scaling, $dN/d_D \sim {}_D^{-p}$ with exponent $p = 1.9 \pm 0.06$ for $_D > 0.02$ and a fluctuating decrease for $_D < 0.02$.

When approaching failure, the dynamics of microfractures was dominated by the growth of the largest microfracture, S_{max}, defined as the volume fraction of the largest microfracture cluster. Figure 8 shows the growth of the largest cluster, S_{max} and of largest increment, s_{max}, as a function of Δ_D. The volume fraction of the largest cluster in sample M8-1 remained very small prior to failure and increased abruptly at failure. Once again, the number of scans before failure is too limited for this sample to precisely track the evolution of S_{max} or s_{max}. For sample M8-2, where the rate of loading was slower, it was possible to track the growth of the largest cluster prior to the peak load in more details (inset in Figure 8). It showed a power law scaling, $S_{max} \sim \Delta_D^{-\gamma_f}$, with an exponent $\gamma_f = 2.4 \pm 0.1$. At failure, the largest cluster occupied 1.5% and 1.9% of the total microfracture volume in M8-1 and M8-2, respectively, and connected the two opposite boundaries of the sample. The volume fraction of the largest damage increment, s_{max}, plotted against the control parameter showed a similar power law scaling, $s_{max} \sim \Delta_D^{-\gamma_i}$, with a smaller exponent $\gamma_i = 1.1 \pm 0.1$ for sample M8-2 (inset in Figures 8 and S4). Within the inherent fluctuations in the evolutions of S_{max} and s_{max} (see inset of Figure 8), we did not detect a significant breaking of scaling near final failure in this case.

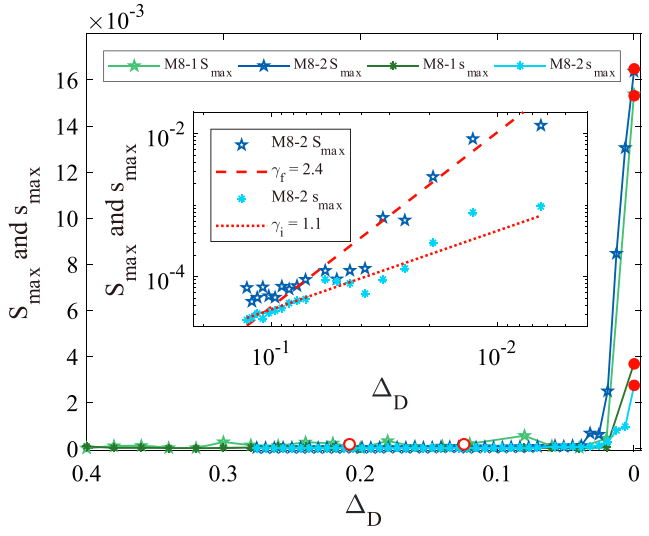

Figure 8. Volume fractions of the largest microfracture, S_{max}, and of largest increment, s_{max},plotted against the control parameter, $_D$, for both samples, M8-1 (green) and M8-2 (blue). Inset: log-log plot of S_{max} and s_{max} as a function of $_D$ showing a power law scaling, $S_{max} \sim {}_D^{-\gamma_f}$ and $s_{max} \sim {}_D^{-\gamma_i}$ for sample M8-2, with exponents, $\gamma_f = 2.4 \pm 0.1$ and $\gamma_i = 1.1 \pm 0.1$ (Figure S4). Open red circle shows the macroscopic yield point; full red circle shows the last scan acquired before failure.

4.3. Shape and Size Distribution of Damage Increments

To characterize the shape of the fracture increments, we calculated their size (volume), s, and maximum length, L, computed as the largest eigenvalue of the covariance matrix. This eigenvalue may interpreted as representing the largest axis of the best fit ellipsoid of a given microfracture. A power law scaling, $s \sim L^{-d_f}$, where d_f is the fractal dimension characterizing their shape, was observed with d_f=2.3 and 2.1 for samples M8-1 and M8-2, respectively (Figure 9). The value of these exponents, close to 2, indicates that the fracture increments are quasi-two-dimensional objects, as expected for microfractures.

Figure 10 shows the cumulative density functions (CDF) of damage increment sizes occurring at different stress steps, corresponding to different

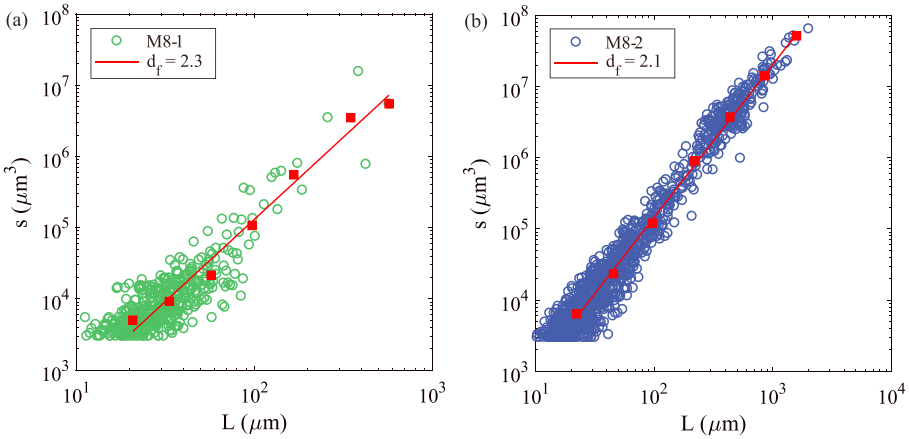

Figure 9. Size (volume) of damage increments, s, plotted against their lengths L for samples M8-1 (a) and M8-2 (b). Red squares represent average sizes of binned data. The fractal dimension d_f in both cases is 2.2 ± 0.8, showing that damage growth increments were quasi-planar two-dimensional objects, corresponding to microfractures.

values of the control parameter Δ_D, for samples M8-1 (Figure 10a) and M8-2 (Figure 10b). Several important features can be identified as follows:

1. For sizes (volumes) larger than ~10^5 μm^3, the CDFs progressively evolve toward a power law distribution, $P(\geq s) \sim s^{-\alpha+1}$, as one approaches the failure stress.
2. This power law scaling is clearly broken down at a lower cutoff, $s_{inf} \approx 10^5$ μm^3. As $s \sim L^{-d_f}$ (Figure 9), this translates into a cutoff length scale $L_{inf} \approx 10^{5/2.2} \approx 180$ μm. This value, which fits very well with the range of grain sizes of Carrara marble (100–200 μm), illustrates the role of grain boundaries as barriers to microfracture extension. Microfractures confined within individual grains clearly differ from the damage dynamics and interactions at larger scales.
3. At the ultimate stress steps before final failure, some outliers are visible in the tail of the distributions, corresponding to anomalously large damage increments. The physical interpretation of these outliers is discussed in section 5.3.

From the results of point (1), we conjecture (for scales larger than the average grain size, see point [2]), an evolution of the probability density function (PDF) of damage increment sizes of the form, $p(s) \sim s^{-\alpha} f(s/s^*)$, where $f(x)$ is a rapidly vanishing function for $x > 1$ and the upper cutoff, s^*, grows toward the failure stress as $s^* \sim \Delta_D^{-\gamma}$. This conjecture is consistent with a nontruncated PDF near failure, $P(s) \sim s^{-\alpha}$ (or equivalently

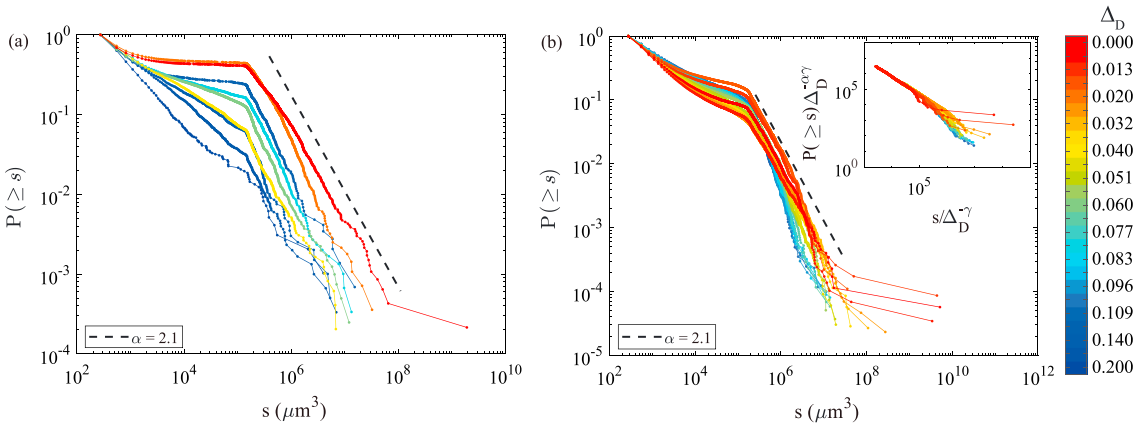

Figure 10. Cumulative density functions of the sizes of damage increments, $P(\geq s)$, for (a) samples M8-1 and (b) sample M8-2, for different stress steps, that is, different values of $_D$. Inset: Data collapse of the data of sample M8-2. The slope breaking in the data around microfractures sizes of 10^5 μm^3 corresponds to the average grain size of the rock (see text for details).

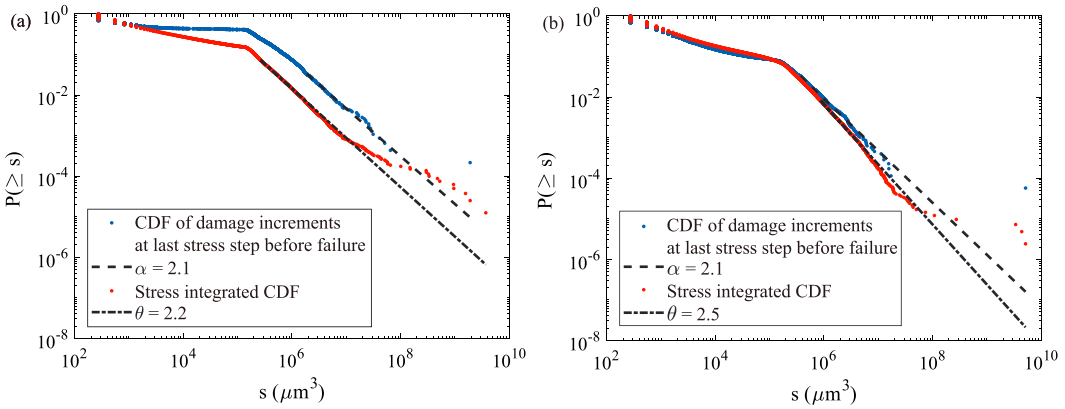

Figure 11. Cumulative density functions (CDF) of the sizes of damage increments at the last stress step before failure and CDF of stress-integrated (damage increments recorder over the entire loading up to peak stress) distributions for (a) samples M8-1 and (b) sample M8-2.

$P(\geq s) \sim s^{-\alpha+1}$ for the CDF); see Figure 10, as the cutoff volume, s^*, spans the entire volume of the system. In addition, the stress-integrated (damage increments recorder over the entire loading up to peak stress) PDF should follow another nontruncated power law, $P(s) \sim s^{-\theta}$, with $\theta = \alpha + 1/\gamma$ (Sornette, 1994). Our results for the sample M8-2 support this conjecture with $\alpha = 2.1 \pm 0.4$ and $\theta = 2.5 \pm 0.07$; hence, $\gamma = 2.5 \pm 2.5$ (Figure 11b). We have used a robust maximum likelihood method (Clauset et al., 2009) to estimate the power law exponents. Because of the propagation of errors, the uncertainty on γ is large. This value can however be confirmed from a data collapse analysis. Using the values of α and γ, the CDFs of Figure 10b can be collapsed by plotting $P(\geq s) \sim \Delta_D^{-\alpha\gamma}$ as a function of $s/\Delta_D^{-\gamma}$, as shown in the inset of Figure 10b. From this scaling of the upper cutoff, s^*, the evolution of the correlation length of damage dynamics, ξ, can be obtained from the fractal scaling of damage increments (Figure 9), that is, $\xi \sim \left(s^*\right)^{1/d_f} \sim \Delta_D^{-\nu}$, with $\nu = \frac{\gamma}{d_f} = 1.15$.

Note that, for sample M8-1, although we observed a reasonable power law distribution for the last scan before failure as well as for the stress-integrated distribution (Figure 11a), with $\theta > \alpha$, the estimation of γ was not reliable, most likely because of the limited number of scans before failure (last scan too far from failure).

Finally, we would like to stress that we compare in the present study two experiments, performed at two different stress and strain rate resolutions (value of stress steps and number of scans to failure). Although the experiment M8-1 does not allow a precise characterization of the acceleration of damage as approaching failure, the two experiments (M8-1 and M8-2) are consistent in terms of largest microfracture and largest increment (Figure 8), shape of damage increments (Figure 9), and distribution of damage increment sizes (Figure 11). Therefore, we consider that, despite a different resolution in the two experiments, results on the evolution of the microstructure prior to failure show the same quantitative behavior.

5. Discussion

5.1. Microstructural Changes as Approaching Failure

In our experiments, we observed sample compaction at the very early stages of deformation (Figures 5c, 5d, and 5f). Above the yield point, the samples dilated with increasing load. Our results allow linking this macroscopic process to the nucleation and growth of microfractures. The samples deformed through the formation of microfractures that increased in number and volume. When approaching failure, the number of fracture clusters decreased due to microfracture coalescence, while the volume of the largest cluster and the total damage increased (Figure 6). Therefore, in the last stages of deformation, the growth of preexisting microfractures dominated the nucleation of new ones (Figure 7). We observed the development of intragranular microfractures parallel to the axial stress direction (Figure 5). After failure, sliding occurred along system-spanning faults (Figure 4 and Movie S3). A further increase of the differential stress promoted further

frictional sliding and considerable decrease in sample height (last frame of Movie S3). This frictional sliding induced a reduction of grain size (grain crushing) along the shear faults (Figure 5).

Our results are consistent with other studies on the deformation of Carrara marble under uniaxial or triaxial compressive stress conditions (Tal et al., 2016; Wawersik & Fairhurst, 1970; Wong & Einstein, 2009). Two-dimensional strain maps obtained from uniaxial tests on marble (Tal et al., 2016) were decomposed into shear and normal components. The normal and shear components of strain were localized along narrow and diagonal features interpreted as microfractures. These shear and dilatant features coalesced with increasing load, increasing in density. Near yield, dilatant vertical microfractures initiate along the grain boundaries that result in a decreasing slope of the stress-strain curve (Schubnel et al., 2006). In this nonlinear regime, grain boundary geometry limits the propagation of intergranular microfractures, and intragranular microfractures propagated instead (Richter et al., 1976). The impact of grain boundaries on microfracture propagation is illustrated in our results by a lower cutoff in the power law distribution of increment sizes (Figure 10).

5.2. Interpreting Failure in Carrara Marble as a Critical Phase Transition

Our detailed tracking of microfracturing during compressive failure revealed that several observables such as the incremental damage, $dD_\varphi/d\Delta_D$, the largest microfracture, $S_{\max}$, or the distribution of fracture increment sizes evolve toward failure following specific scaling laws, up to at least $\Delta_D \approx 10^{-2}$. These scaling laws argue for an interpretation of compressive failure as a critical phase transition from an intact to a failed state (Alava et al., 2006; Girard et al., 2010; Vu et al., 2019). Different theoretical models can be proposed to interpret such critical transition, yielding specific scaling laws and critical exponents (Renard, Weiss, et al., 2018). A comparison of these predictions with our results is detailed below.

The simplest possible scenario would be a percolation of microfractures to form a system-spanning fault. It is known that the problem of failure of heterogeneous media can be mapped onto the percolation problem in case of infinite disorder (Roux et al., 1988). In that case, microfractures nucleate randomly and do not mechanically interact. If classical percolation predicts a power law divergence of the largest cluster, $S_{\max}$, as approaching the critical transition (the percolation threshold), the control parameter of this transition is the total damage itself, not the stress. In addition, percolation theory does not account for an evolution of the incremental damage or of the damage increments. Therefore, the compressive failure of Carrara marble cannot be mapped onto this theoretical framework.

This result points out to the crucial role of mechanical interactions between microfractures during the compressive failure process and suggests an analogy with another class of critical phenomena. Namely, the depinning transition (Ertaş & Kardar, 1994; Fisher, 1998) and the yielding transition (Lin et al., 2015; Nicolas et al., 2018) both share three fundamental ingredients with our problem: a local threshold mechanics, disorder, and elastic long-ranged interactions. In our experiments, the initial disorder in the rock arises from local strength heterogeneities related to pores, joints, and grain boundaries. The progressive clustering of microfracturing events toward sample failure results from long-ranged elastic interactions between cracks. Another prerequisite to observe such critical transition is a slow-driving condition. In our experiments, the loading (stress) rate was well below the rate of elastic stress relaxation after microfracturing events or the mean duration of avalanches of microfracturing events, both having time scales comparable to the propagation of elastic waves in the solid. Here, we compare the power law exponents obtained from the data with those predicted by theoretical frameworks or obtained by numerical models of damage in nonporous solids (Table 2) and discuss the quantitative deviations from predicted values.

Fisher et al. (1997) and Fisher (1998) have interpreted fault slip initiation as a depinning transition. These studies considered that during the initiation phase, the faults progressively unpin from the rock matrix before generalized frictional sliding takes place at the depinning transition. Brittle compressive failure of heterogeneous materials was also recently mapped to the depinning transition (Vu et al., 2019; Weiss et al., 2014), and associated predictions for system size effects on failure strength were proposed (Vu et al., 2018). The scaling predictions of the depinning framework are qualitatively consistent with our observations, in terms of incremental damage evolution, largest damage increment, or distribution of damage increments (see Table 2). The mean field description of the depinning transition provides predictions for the

Table 2
List of Scaling Exponents Calculated in Models of Compressive Failure in Heterogeneous Materials and Comparison With our Data on Carrara Marble

Scaling property (row) Models (column)	Incremental damage $dD_\varphi/d_{D\sim D}^{-\beta}$	Distribution of damage increment volumes at the critical point $P(s)\sim s^{-\alpha}$	Distribution of damage increment volumes (potency) at the critical point	Upper cut-off $s^{*}\sim^{-\gamma}$ (damage increment volume), or $P_0^{*}\sim^{-\gamma_P}$ (potency)	Correlation length $\xi\sim^{-\nu}$
Classical percolation (Stauffer, 1979)	No	No	No	No	$\nu \approx 0.8$ in 3-D
Depinning (mean field; LeBlanc et al., 2013; Weiss et al., 2014)	$\beta = \gamma(2-\alpha) = 1$	—	α=1.5	γ=2.0	$\nu = 1.0$
Yielding transition (Lin et al., 2015; Nicolas et al., 2018)	$\beta = \gamma(2-\alpha) \approx 1.1$	—	$\alpha_P \approx 1.5$ in 3-D	$\gamma_P \approx 2.3$ in 3-D	$\nu \approx 0.7$
Progressive damage model (Girard et al., 2010; Girard et al., 2012)	$\beta = \gamma(2-\alpha) \approx 0.4$	—	α=1.8 in 2-D	γ2.0 in 2-D	$\nu = 1.0 \pm 0.1$
The present study	$\beta = 2.6$	$\alpha = 2.1$	α=1.75	$\gamma = 2.5$ γ=3.6	$\nu = \frac{\gamma}{d_f} = 1.15$

critical exponents (LeBlanc et al., 2013), which were found to be in remarkable agreement with exponents obtained from an acoustic emission analysis of the compressive failure of concrete (Vu et al., 2019).

To compare our results with this theoretical framework, one must first clarify the definition of the size of a damage event. In the measurements detailed above, the size, s, of a damage increment is defined as the volume of the associated porosity. As this volume scales as $s\sim L^{d_f}$ with $d_f \approx 2.2$ (Figure 9), the so-defined "size" actually measures essentially the rupture area. In the interpretation of fault slip initiation (Fisher et al., 1997) or of compressive failure as a depinning transition (Vu et al., 2019), the damage avalanche size is defined instead as the integral of slip or displacement u over this rupture area A, that is, scales as a seismic potency, $P_0 = \int_A du$. Therefore, in order to link our measure of the size s of the damage increment with the avalanche size (or potency), a hypothesis has to be done about the average slip $\langle u \rangle$ over the rupture area. The classical assumption is $\langle u \rangle \sim L$ (Scholz & Cowie, 1990), which would give $P_0 \sim \langle u \rangle s \sim L^{3.2} \sim s^{1.45}$. Hence, the scaling $P(s)\sim s^{-\alpha} f(s/s^{*})$ with $s^{*}\sim\Delta^{-\gamma}$ (see section 4.3) can be translated into an avalanche size scaling $P(P_0)\sim P_0^{-\alpha_P} f\left(P_0/P_0^{*}\right)$, with $P_0^{*}\sim\Delta^{-\gamma_P}$, and the corresponding exponents given by $\alpha_P = \frac{\alpha+0.45}{1.45} \approx 1.75$ and $\gamma_P = 1.45\gamma \approx 3.6$. If the value of α_P compares relatively well with the mean field depinning exponent (1.5; see Table 2), γ_P is significantly larger than the depinning value (2.0). On the other hand, the correlation length exponent $\nu = 1.15$, whose estimation does not rely on an assumption about the average slip (see section 4.3), is in close agreement with the depinning prediction ($\nu = 1.0$).

However, when comparing the compressive failure of rocks with the depinning transition, one important point should be kept in mind regarding the nature of the elastic interaction kernel. In classical depinning, this kernel is assumed to be convex, meaning that stress (or force) redistribution after a depinning event occurs equally in all directions. This precludes a progressive localization of damage toward an incipient shear fault. This assumption represents a significant shortcoming to explain our observations. The yielding transition, describing the onset of plastic flow in amorphous media, integrates a nonconvex elastic interaction kernel, allowing strain localization along plastic shear bands (Lin et al., 2015; Nicolas et al., 2018). In terms of avalanches statistics, the yielding transition is similar to the depinning transition, with slightly different exponents (see Table 2). The agreement with our values is correct for α_P and ν but not for γ_P (see Table 2). As the yielding transition does not, in its classical formulation, incorporate friction (i.e., a role of pressure on microfracture nucleation or growth), the orientation of the macroscopic faults in our experiments, at 30° of the maximum principal stress, is not captured by this theoretical framework.

To circumvent the simplifying assumptions of these theoretical frameworks, progressive damage models have been developed (Amitrano et al., 1999; Tang, 1997). These models incorporate microstructural disorder from a distribution of local damage thresholds, internal friction in the form of a local Coulomb damage criterion, long-range elastic stress redistributions following damage events, and, more recently, a partition between elastic (small) and permanent (large) deformations, as well as healing mechanisms (Weiss &

Dansereau, 2017). They successfully capture the characteristics of brittle compressive failure for low-porosity rocks. Damage and strain localization arise naturally because the elastic kernel is nonconvex. The 2-D simulations have shown power law distributions of damage avalanche sizes with an upper cutoff becoming system spanning as approaching the maximum (failure) stress (Girard et al., 2010; Girard et al., 2012), which is analogous to microfracture increments distributions computed from our results. Similarly, the results of Figure 8 for the largest microfracture are qualitatively consistent with the growth of the largest damage cluster in this progressive damage model (Girard et al., 2012). Overall, the agreement between our results and the progressive damage model in terms of incremental damage, distributions of microfracture increments, or of the largest fracture/damage cluster, including in terms of exponents for α_P and ν (see Table 2), suggests an interpretation of the compressive failure of Carrara marble as a critical transition.

Concerning the scaling of the incremental damage, dD_φ/Δ_D (Figure 7a), it is worth stressing that the above-mentioned models do not predict an increasing damage event rate $dN/d\Delta_D$ when approaching the critical point. Therefore, our observations strongly differ from these models on this specific point but are in agreement with the acoustic emission monitoring of the compressive failure of nonporous heterogeneous materials (Vu et al., 2019). In our case, the incremental damage evolution results from both the evolution of the distribution of damage avalanche sizes and the evolution of the damage event rate. This might explain the difference between these modeling frameworks and our results in terms of exponent β; as in the case of the compressive failure of marble, the changing distribution combines with an increasing event rate. In addition, acoustic emissions measurements have shown that the p-exponent of the inverse Omori's scaling can vary with the material considered (e.g., Ojala et al., 2004; Vasseur et al., 2015). Hence, the variability of β, when compared with previous studies on quartz-monzonite (Renard, McBeck, et al., 2019; Renard, Weiss, et al., 2018), might come from the nature of the rock itself, through the variability on p.

Beyond this critical interpretation of compressive failure, we have shown on Figure 7 that the power law scaling of the incremental damage seems to break off very close to the failure stress ($\Delta_D < 0.02$), which is associated with a decreasing event rate. This is accompanied by few outliers in the tail of the distribution of increments (Figure 10). These observations indicate a possible departure from the critical scenario just before macroscopic faulting. The possible mechanisms associated with this breaking of scaling are discussed in the following.

5.3. Breaking of Scaling Near the Critical Point

Different mechanisms, or a combination of them, can be tentatively proposed to explain this breaking of scaling near the critical point. Note first that the two observations mentioned above might appear contradictory at first sight: whereas the near-failure dynamics is characterized by few, anomalously large damage increments (outliers on Figure 10), the global incremental damage itself does not accelerate as a power law in the vicinity of failure. We also stress that such breaking on the incremental damage scaling was not observed for quartz-monzonite (Renard, McBeck, et al., 2019; Renard, Weiss, et al., 2018), while damage increments were not analyzed in this material and less 3-D tomography data were acquired near failure.

The first possible mechanism is a subcritical growth of an incipient fault, corresponding to a slow (aseismic) crack growth under a stress intensity factor below the toughness of the material (Atkinson, 1982). In this case, one (or few) large damage cluster(s) could grow even during the constant stress conditions prevailing during the final 90-s stress steps needed to scan the sample (see section 3.1), whereas smaller clusters would remain unchanged. However, as mentioned in section 3.1, we did not detect a blurring of the radiographs, suggesting that fracture growth during scan acquisition is probably limited.

Another possibility would be a coalescence of some damage clusters to form the final fault by bridging of the gaps and taking place through anomalously large fracture increments. The signs of fracture coalescence in our experiment are the outliers in the distribution of increments (Figures 10 and 11). The breaking of scaling near failure, visible in Figures 6 and 7, appears more as a consequence of such coalescence. In a progressive damage model, similar outliers in the tail of the damage cluster sizes distributions were reported after the peak load, accompanying the coalescence of preexisting clusters into a major fault (Girard et al., 2012). This is consistent with our results, although such coalescence seems to be triggered slightly before peak stress in the present case. Girard et al. (2012) also mentioned that, once the largest cluster becomes system spanning, further damage and deformation accumulate along this fault, inhibiting additional damage

elsewhere. This is also consistent with the AE monitoring of fracturing of granite under multiaxial compression (Lockner et al., 1991). Such inhibition could explain the breaking of scaling of the incremental damage dD_{φ}/Δ_D (Figure 7). Whatever the mechanisms involved, the point at which the incremental damage deviates from a power law evolution could therefore represent a signal that a rock volume is approaching system-size failure. Additional observations on other rocks would be needed to confirm this observation.

5.4. Implications for Fault Mechanics

The scaling laws associated with progressive damage/microfracturing in our experiments shed light on the evolution of acoustic emissions prior to failure in laboratory experiments (Lockner et al., 1991; Vu et al., 2019) and possibly on foreshock activity before large earthquakes (Jaumé & Sykes, 1999). In the present discussion, we are aware of the huge scale gap between the laboratory experiments and natural faults. Several studies have attempted to export the concept of a critical point and precursory phenomena to predict large earthquakes (Main, 1996 and references therein). The stress released by earthquakes into the surrounding volume drives the system away from criticality. Conversely, progressive tectonic loading drives it toward a future critical state (Jaumé & Sykes, 1999), increasing the probability of the next large earthquake. The onset of slip along a 2-D heterogeneous fault in a 3-D elastic solid, that is, earthquake nucleation, has been interpreted as a critical depinning transition and mean field exponents derived (Fisher, 1998; Fisher et al., 1997). A two-phase diagram was proposed for the behavior of such fault: the Gutenberg-Richter phase characterized by a power law distribution of slip event sizes with an exponential cutoff and a runaway phase characterized by small events as well as quasiperiodic occurrence of system-size earthquakes (Dahmen et al., 1998). This might be reminiscent of our observations. The Gutenberg-Richter phase would be analogous to the prefailure, damage development phase in a rock, controlled by elastic long-range stress interactions and characterized by the emergence of power laws. The runaway phase would be equivalent to the system-size failure resulting from the formation of a percolating cluster leading to frictional sliding. Hence, the dynamics of precursory microfracturing activity before faulting observed in our experiments may be used to interpret a possible precursory activity before large earthquakes on geological faults. In this context, a breaking of power law scaling (see section 5.3), signing the transition from the Gutenberg-Richter phase to the runaway phase, could be the ultimate precursory signal before large earthquakes.

However, the possible prediction of large earthquakes on such basis remains an unsolved problem. If many large earthquakes seem to be preceded by foreshocks as well as a divergence of the seismic moment release rate (Jaumé & Sykes, 1999), these precursory phenomena are far to be ubiquitous (Bouchon et al., 2013; de Arcangelis et al., 2016; Zaliapin & Ben-Zion, 2013). Foreshocks could actually result from cascades of triggered seismicity implying that earthquakes are "predictable" to the same degree whatever their size (Helmstetter & Sornette, 2003). The use of these potential precursors as an earthquake forecasting tool remains therefore elusive so far. This raises important questions, such as the difference between the compressive failure of initially unfaulted rocks (this work) and the earthquake nucleation along a preexisting crustal fault, and calls for further theoretical and experimental work as well as geophysical data analysis.

6. Conclusions

We describe 3-D experimental data that reveal the spatial distribution of nucleating, propagating, and coalescing microfractures during the brittle compressive failure of Carrara marble rock samples. Our novel experimental setup allows in situ imaging of the sample during deformation and so enables the computation of statistical properties of the volume of microfractures and the derivation of scaling laws through which we quantify the critical nature of the failure process. We quantified the behavior of precursory microfracture events preceding macroscopic failure. The incremental damage showed power law acceleration with increasing stress up to ~98% of the failure stress and then transitioned to an exponential evolution in the vicinity of system-size failure. This evolution from power law to exponential appears therefore as the ultimate precursory signal of material failure.

Scaling laws pertaining to prepeak phase described the evolution of damage increments. The distribution of the sizes of microfracture increments showed power law scaling with exponential cutoff at large sizes. This cutoff itself is related to the correlation length of the damage process and increases toward failure, possibly through a power law divergence. The volume of the percolating largest fracture network diverged as well toward failure and could serve as an order parameter for failure interpreted as a critical phase transition

(Girard et al., 2012). Thus, brittle compressive failure in Carrara marble is a complex process that involves long-range elastic interactions, growth, nucleation, and coalescence of microfractures, leading to clustering, faulting, frictional sliding along faults, grain size reduction, and elastic softening. Scaling laws obtained from our data are in agreement with the damage models listed in Table 2. However, substantial differences in terms of the scaling exponents, their ranges, and a breaking of power law scaling very close to failure for the incremental damage are observed in our experimental data. Although the existence of power laws argues for a critical interpretation of failure (e.g., LeBlanc et al., 2013; Weiss et al., 2014; Girard et al., 2010; Girard et al., 2012), a complete micromechanical model that explains brittle failure under compression and that reproduces all these microstructural evolutions is still lacking. Breaking of scaling just before failure is understood as a complex interplay between microstructural phenomena such as subcritical crack growth and coalescence of large damage clusters.

Acknowledgments
The deformation apparatus was built by Sanchez Technology. Paul Tafforeau and Alexander Rack provided advice on the design of the tomography setup. This study received funding from the Norwegian Research Council (project HADES, Grant 250661). Beamtime was allocated at the European Synchrotron Radiation Facility (Long-Term Proposal ES-295). Data storage was provided by UNINETT Sigma2—the National Infrastructure for High Performance Computing and Data Storage in Norway (project NS9073K), and the experimental data can be obtained from the archive (https://doi.org/10.11582/2019.00001). The dynamic 3-D microtomography of the two Carrara marble samples is available freely through the UNINETT Sigma2 repository (https://doi.org/10.11582/2019.00001). The authors thank Jess McBeck for a careful review of an early draft of this manuscript.

References

Alava, M. J., Nukala, P. K., & Zapperi, S. (2006). Statistical models of fracture. *Advances in Physics*, *55*(3–4), 349–476. https://doi.org/10.1080/00018730300741518

Amitrano, D., Grasso, J. R., & Hantz, D. (1999). From diffuse to localised damage through elastic interaction. *Geophysical Research Letters*, *26*(14), 2109–2112. https://doi.org/10.1029/1999GL900388

Atkinson, B. K. (1982). Subcritical crack propagation in rocks: Theory, experimental results and applications. *Journal of Structural Geology*, *4*(1), 41–56. https://doi.org/10.1016/0191-8141(82)90005-0

Bell, A. F., Naylor, M., & Main, I. G. (2013). The limits of predictability of volcanic eruptions from accelerating rates of earthquakes. *Geophysical Journal International*, *194*(3), 1541–1553. https://doi.org/10.1093/gji/ggt191

Bouchon, M., Durand, V., Marsan, D., Karabulut, H., & Schmittbuhl, J. (2013). The long precursory phase of most large interplate earthquakes. *Nature Geoscience*, *6*(4), 299–302. https://doi.org/10.1038/ngeo1770

Bouchon, M., Karabulut, H., Aktar, M., Özalaybey, S., Schmittbuhl, J., & Bouin, M. P. (2011). Extended nucleation of the 1999 Mw 7.6 Izmit earthquake. *Science*, *331*(6019), 877–880. https://doi.org/10.1126/science.1197341

Brace, W. F., & Bombolakis, E. G. (1963). A note on brittle crack growth in compression. *Journal of Geophysical Research*, *68*(12), 3709–3713. https://doi.org/10.1029/JZ068i012p03709

Brace, W. F., Paulding, B. W. Jr., & Scholz, C. H. (1966). Dilatancy in the fracture of crystalline rocks. *Journal of Geophysical Research*, *71*(16), 3939–3953. https://doi.org/10.1029/JZ071i016p03939

Brace, W. F., Silver, E., Hadley, K., & Goetze, C. (1972). Cracks and pores: A closer look. *Science*, *178*(4057), 162–164. https://doi.org/10.1126/science.178.4057.162

Buades, A., Coll, B., & Morel, J. M. (2005). A review of image denoising algorithms, with a new one. *Multiscale Modeling & Simulation*, *4*(2), 490–530.

Clauset, A., Shalizi, C. R., & Newman, M. E. (2009). Power-law distributions in empirical data. *SIAM Review*, *51*(4), 661–703. https://doi.org/10.1137/070710111

Dahmen, K., Ertaş, D., & Ben-Zion, Y. (1998). Gutenberg-Richter and characteristic earthquake behavior in simple mean-field models of heterogeneous faults. *Physical Review E*, *58*(2), 1494–1501. https://doi.org/10.1103/PhysRevE.58.1494

Dahmen, K. A., Ben-Zion, Y., & Uhl, J. T. (2009). Micromechanical model for deformation in solids with universal predictions for stress-strain curves and slip avalanches. *Physical Review Letters*, *102*(17), 175501. https://doi.org/10.1103/PhysRevLett.102.175501

de Arcangelis, L., Godano, C., Grasso, J. R., & Lippiello, E. (2016). Statistical physics approach to earthquake occurrence and forecasting. *Physics Reports*, *628*, 1–91. https://doi.org/10.1016/j.physrep.2016.03.002

Ertaş, D., & Kardar, M. (1994). Critical dynamics of contact line depinning. *Physical Review E*, *49*(4), R2532–R2535. https://doi.org/10.1103/PhysRevE.49.R2532

Fisher, D. S. (1998). Collective transport in random media: From superconductors to earthquakes. *Physics Reports*, *301*(1–3), 113–150. https://doi.org/10.1016/S0370-1573(98)00008-8

Fisher, D. S., Dahmen, K., Ramanathan, S., & Ben-Zion, Y. (1997). Statistics of earthquakes in simple models of heterogeneous faults. *Physical Review Letters*, *78*(25), 4885–4888. https://doi.org/10.1103/PhysRevLett.78.4885

Fredrich, J. T., Evans, B., & Wong, T. F. (1989). Micromechanics of the brittle to plastic transition in Carrara marble. *Journal of Geophysical Research*, *94*(B4), 4129–4145. https://doi.org/10.1029/JB094iB04p04129

Fredrich, J. T., Menendez, B., & Wong, T. F. (1995). Imaging the pore structure of geomaterials. *Science*, *268*(5208), 276–279. https://doi.org/10.1126/science.268.5208.276

Girard, L., Amitrano, D., & Weiss, J. (2010). Failure as a critical phenomenon in a progressive damage model. *Journal of Statistical Mechanics: Theory and Experiment*, *2010*(01), P01013. https://doi.org/10.1088/1742-5468/2010/p01013

Girard, L., Weiss, J., & Amitrano, D. (2012). Damage-cluster distributions and size effect on strength in compressive failure. *Physical Review Letters*, *108*(22), 225502. https://doi.org/10.1103/PhysRevLett.108.225502

Griffith, A. A. (1921). VI. The phenomena of rupture and flow in solids. *Philosophical Transactions of the Royal Society of London Series A*, *221*(582–593), 163–198. https://doi.org/10.1098/rsta.1921.0006

Helmstetter, A., & Sornette, D. (2003). Foreshocks explained by cascades of triggered seismicity. *Journal of Geophysical Research*, *108*(B10), 2457. https://doi.org/10.1029/2003JB002409

Hoek, E., & Bieniawski, Z. T. (1965). Brittle fracture propagation in rock under compression. *International Journal of Fracture Mechanics*, *1*(3), 137–155.

Hoek, E., & Martin, C. D. (2014). Fracture initiation and propagation in intact rock—A review. *Journal of Rock Mechanics and Geotechnical Engineering*, *6*(4), 287–300. https://doi.org/10.1016/j.jrmge.2014.06.001

Iglauer, S., & Lebedev, M. (2017). High pressure-elevated temperature x-ray micro-computed tomography for subsurface applications. *Advances in Colloid and Interface Science*, *256*, 393–410.

Jaeger, J. C., & Cook, N. G. (1969). *Fundamentals of Rock Mechanics* (Vol. 513). London: Methuen & Co. Ltd.

Jaumé, S. C., & Sykes, L. R. (1999). Evolving towards a critical point: A review of accelerating seismic moment/energy release prior to large and great earthquakes. In *Seismicity patterns, their statistical significance and physical meaning* (pp. 279–305). Basel: Birkhäuser. https://doi.org/10.1007/978-3-0348-8677-2_5

Jha, D., Sørensen, H. O., Dobberschütz, S., Feidenhans'l, R., & Stipp, S. L. S. (2014). Adaptive center determination for effective suppression of ring artifacts in tomography images. *Applied Physics Letters*, *105*(14), 143107. https://doi.org/10.1063/1.4897441

Kato, A., Obara, K., Igarashi, T., Tsuruoka, H., Nakagawa, S., & Hirata, N. (2012). Propagation of slow slip leading up to the 2011 Mw 9.0 Tohoku-Oki earthquake. *Science*, *335*, 705–708. https://doi.org/10.1126/science.1215141

Kranz, R. L. (1983). Microcracks in rocks: A review. *Tectonophysics*, *100*(1–3), 449–480. https://doi.org/10.1016/0040-1951(83)90198-1

Kuksenko, V., Tomilin, N., Damaskinskaya, E., & Lockner, D. (1996). A two-stage model of fracture of rocks. *Pure and Applied Geophysics*, *146*(2), 253–263. https://doi.org/10.1007/BF00876492

LeBlanc, M., Angheluta, L., Dahmen, K., & Goldenfeld, N. (2013). Universal fluctuations and extreme statistics of avalanches near the depinning transition. *Physical Review E*, *87*(2), 022126. https://doi.org/10.1103/PhysRevE.87.022126

Lin, J., Gueudré, T., Rosso, A., & Wyart, M. (2015). Criticality in the approach to failure in amorphous solids. *Physical Review Letters*, *115*(16), 168001. https://doi.org/10.1103/PhysRevLett.115.168001

Lockner, D., Byerlee, J. D., Kuksenko, V., Ponomarev, A., & Sidorin, A. (1991). Quasi-static fault growth and shear fracture energy in granite. *Nature*, *350*(6313), 39–42. https://doi.org/10.1038/350039a0

Lockner, D. A., Byerlee, J. D., Kuksenko, V., Ponomarev, A., & Sidorin, A. (1992). Observations of quasistatic fault growth from acoustic emissions. *International Geophysics*, *51*, 3–31. https://doi.org/10.1016/S0074-6142(08)62813-2

Main, I. (1996). Statistical physics, seismogenesis, and seismic hazard. *Reviews of Geophysics*, *34*(4), 433–462. https://doi.org/10.1029/96RG02808

Malaga-Starzec, K., Lindqvist, J. E., & Schouenborg, B. (2002). Experimental study on the variation in porosity of marble as a function of temperature. *Geological Society, London, Special Publications*, *205*(1), 81–88. https://doi.org/10.1144/GSL.SP.2002.205.01.07

Mirone, A., Brun, E., Gouillart, E., Tafforeau, P., & Kieffer, J. (2014). The PyHST2 hybrid distributed code for high speed tomographic reconstruction with iterative reconstruction and a priori knowledge capabilities. *Nuclear Instruments and Methods in Physics Research Section B: Beam Interactions with Materials and Atoms*, *324*, 41–48. https://doi.org/10.1016/j.nimb.2013.09.030

Moore, D. E., & Lockner, D. A. (1995). The role of microcracking in shear-fracture propagation in granite. *Journal of Structural Geology*, *17*(1), 95–114. https://doi.org/10.1016/0191-8141(94)E0018-T

Nicolas, A., Ferrero, E. E., Martens, K., & Barrat, J. L. (2018). Deformation and flow of amorphous solids: Insights from elastoplastic models. *Reviews of Modern Physics*, *90*(4), 045006. https://doi.org/10.1103/RevModPhys.90.045006

Ojala, I. O., Main, I. G., & Ngwenya, B. T. (2004). Strain rate and temperature dependence of Omori law scaling constants of AE data: Implications for earthquake foreshock-aftershock sequences, *Geophysical Research Letters*, *31*, L24617. https://doi.org/10.1029/2004GL020781

Oesterling, N., Heilbronner, R., Stünitz, H., Barnhoorn, A., & Molli, G. (2007). Strain dependent variation of microstructure and texture in naturally deformed Carrara marble. *Journal of Structural Geology*, *29*(4), 681–696. https://doi.org/10.1016/j.jsg.2006.10.007

Ohnaka, M. (1992). Earthquake source nucleation: A physical model for short-term precursors. *Tectonophysics*, *211*(1–4), 149–178. https://doi.org/10.1016/0040-1951(92)90057-D

Paganin, D., Gureyev, T. E., Pavlov, K. M., Lewis, R. A., & Kitchen, M. (2004). Phase retrieval using coherent imaging systems with linear transfer functions. *Optics Communications*, *234*(1-6), 87–105. https://doi.org/10.1016/j.optcom.2004.02.015

Paterson, M. S., & Wong, T. F. (2005). *Experimental rock deformation-the brittle field*. Heidelberg: Springer Science & Business Media.

Peng, S., & Johnson, A. M. (1972). Crack growth and faulting in cylindrical specimens of Chelmsford granite. *International Journal of Rock Mechanics and Mining Sciences & Geomechanics Abstracts*, *9*(1), 37–86). Pergamon. https://doi.org/10.1016/0148-9062(72)90050-2

Renard, F., Cordonnier, B., Dysthe, D. K., Boller, E., Tafforeau, P., & Rack, A. (2016). A deformation rig for synchrotron microtomography studies of geomaterials under conditions down to 10 km depth in the earth. *Journal of Synchrotron Radiation*, *23*(4), 1030–1034. https://doi.org/10.1107/S1600577516008730

Renard, F., Cordonnier, B., Kobchenko, M., Kandula, N., Weiss, J., & Zhu, W. (2017). Microscale characterization of rupture nucleation unravels precursors to faulting in rocks. *Earth and Planetary Science Letters*, *476*, 69–78. https://doi.org/10.1016/j.epsl.2017.08.002

Renard, F., McBeck, J., Cordonnier, B., Zheng, X., Kandula, N., Sanchez, J. R., et al. (2019). Dynamic in situ three-dimensional imaging and digital volume correlation analysis quantify strain localization and fracture coalescence in sandstone. *Pure and Applied Geophysics*, *176*(3), 1083–1115. https://doi.org/10.1007/s00024-018-2003-x

Renard, F., Weiss, J., Mathiesen, J., Ben-Zion, Y., Kandula, N., & Cordonnier, B. (2018). Critical evolution of damage toward system-size failure in crystalline rock. *Journal of Geophysical Research: Solid Earth*, *123*(2), 1969–1986. https://doi.org/10.1002/2017JB014964

Richter, D., Simmons, G., & Siegfried, R. (1976). Microcracks, micropores, and their petrologic interpretation for 72415 and 15418. In *Lunar and Planetary Science Conference Proceedings* (Vol. 7, pp. 1901–1923). New York: Pergamon Press.

Roux, S., Hansen, A., Herrmann, H., & Guyon, E. (1988). Rupture of heterogeneous media in the limit of infinite disorder. *Journal of Statistical Physics*, *52*(1–2), 237–244. https://doi.org/10.1007/BF01016411

Rutter, E. H. (1972). The influence of interstitial water on the rheological behaviour of calcite rocks. *Tectonophysics*, *14*(1), 13–33. https://doi.org/10.1016/0040-1951(72)90003-0

Scholz, C. H., & Cowie, P. A. (1990). Determination of total strain from faulting using slip measurements. *Nature*, *346*(6287), 837.

Schubnel, A., Walker, E., Thompson, B. D., Fortin, J., Guéguen, Y., & Young, R. P. (2006). Transient creep, aseismic damage and slow failure in Carrara marble deformed across the brittle-ductile transition. *Geophysical Research Letters*, *33*, L17301. https://doi.org/10.1029/2006GL026619

Sornette, D. (1994). Sweeping of an instability: An alternative to self-organized criticality to get power laws without parameter tuning. *Journal de Physique I*, *4*(2), 209–221. https://doi.org/10.1051/jp1:1994133

Stanley, H. E. (1999). Scaling, universality, and renormalization: Three pillars of modern critical phenomena. *Reviews of Modern Physics*, *71*(2), S358. https://doi.org/10.1103/RevModPhys.71.S358

Stauffer, D. (1979). Scaling theory of percolation clusters. *Physics Reports*, *54*(1), 1–74. https://doi.org/10.1016/0370-1573(79)90060-7

Sternberg, S. (1983). Biomedical image processing. *Computer*, *16*(1), 22–34. https://doi.org/10.1109/MC.1983.1654163

Tal, Y., Evans, B., & Mok, U. (2016). Direct observations of damage during unconfined brittle failure of Carrara marble. *Journal of Geophysical Research: Solid Earth*, *121*, 1584–1609. https://doi.org/10.1002/2015JB012749

Tang, C. A. (1997). Numerical simulation of progressive rock failure and associated seismicity. *International Journal of Rock Mechanics and Mining Sciences*, *34*(2), 249–261. https://doi.org/10.1016/S0148-9062(96)00039-3

Tapponnier, P., & Brace, W. F. (1976). Development of stress-induced microcracks in westerly granite. *International Journal of Rock Mechanics and Mining Science & Geomechanical Abstracts*, *13*(4), 103–112. https://doi.org/10.1016/0148-9062(76)91937-9

Vasseur, J., Wadsworth, F. B., Lavallée, Y., Bell, A. F., Main, I. G., & Dingwell, D. B. (2015). Heterogeneity: the key to failure forecasting. *Scientific Reports*, *5*, 13259.

Vu, C. C., Amitrano, D., Plé, O., & Weiss, J. (2019). Compressive failure as a critical transition: Experimental evidence and mapping onto the universality class of depinning. *Physical Review Letters*, *122*(1), 015502. https://doi.org/10.1103/PhysRevLett.122.015502

Vu, C. C., Weiss, J., Plé, O., Amitrano, D., & Vandembroucq, D. (2018). Revisiting statistical size effects on compressive failure of heterogeneous materials, with a special focus on concrete. *Journal of the Mechanics and Physics of Solids*, *121*, 47–70. https://doi.org/10.1016/j.jmps.2018.07.022

Wawersik, W. R., & Fairhurst, C. (1970). A study of brittle rock fracture in laboratory compression experiments. *International Journal of Rock Mechanics and Mining Sciences & Geomechanics Abstracts*, *7*(5), 561–575). Pergamon. https://doi.org/10.1016/0148-9062(70)90007-0

Weiss, J., & Dansereau, V. (2017). Linking scales in sea ice mechanics. *Philosophical Transactions of the Royal Society A*, *375*(2086), 20150352. https://doi.org/10.1098/rsta.2015.0352

Weiss, J., Girard, L., Gimbert, F., Amitrano, D., & Vandembroucq, D. (2014). (Finite) statistical size effects on compressive strength. *Proceedings of the National Academy of Sciences*, *111*(17), 6231–6236. https://doi.org/10.1073/pnas.1403500111

Wong, L. N. Y., & Einstein, H. H. (2009). Crack coalescence in molded gypsum and Carrara marble: Part 1. Macroscopic observations and interpretation. *Rock Mechanics and Rock Engineering*, *42*(3), 475–511. https://doi.org/10.1007/s00603-008-0002-4

Wong, T. F., Wong, R. H., Chau, K. T., & Tang, C. A. (2006). Microfracture statistics, Weibull distribution and micromechanical modeling of compressive failure in rock. *Mechanics of Materials*, *38*(7), 664–681. https://doi.org/10.1016/j.mechmat.2005.12.002

Wu, C., Meng, X., Peng, Z., & Ben-Zion, Y. (2013). Lack of spatiotemporal localization of foreshocks before the 1999 M w 7.1 Düzce, Turkey, earthquake. *Bulletin of the Seismological Society of America*, *104*(1), 560–566. https://doi.org/10.1785/0120130140

Zaliapin, I., & Ben-Zion, Y. (2013). Earthquake clusters in southern California I: Identification and stability. *Journal of Geophysical Research: Solid Earth*, *118*, 2847–2864. https://doi.org/10.1002/jgrb.50179

Journal of Geophysical Research: Solid Earth

Supporting Information for

Dynamics of microscale precursors during brittle compressive failure in Carrara marble

Neelima Kandula [1], Benoit Cordonnier[1,2], Elodie Boller[2], Jérôme Weiss[3], Dag Kristian Dysthe[1] & François Renard[1,3]

[1]The Njord Centre, PGP, Departments of Geosciences & Physics, University of Oslo, Norway.

[2]The European Synchrotron, ESRF, beamline ID19, Grenoble, France.

[3]Université Grenoble Alpes, Université Savoie Mont Blanc, CNRS, IRD, IFSTTAR, IsTerre, 38000 Grenoble, France.

Contents of this file

Figures S1 to S5

Additional Supporting Information (Files uploaded separately)

Captions for Movies S1 to S4

Introduction

The Supporting Information contains five figures and four movies. The figures provide additional information on 1) the tracking algorithm used to extract damage increments in the tomography data, 2) how the various power-law relationships were calculated.

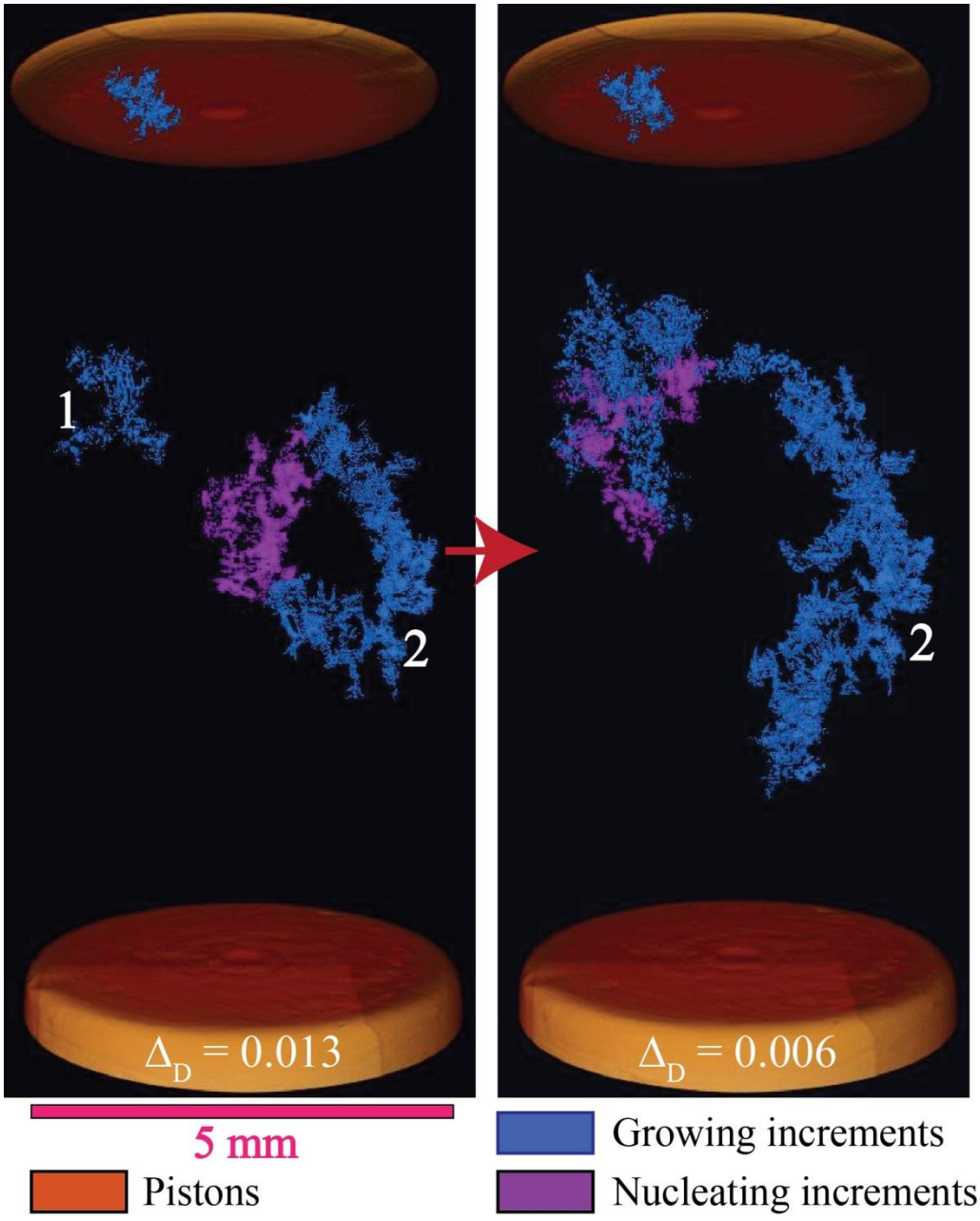

Figure S1. Demonstration of tracking algorithm described in section 3.3 to compute and track microfracture increments. Three-dimensional illustrations of randomly picked microfracture increments at stress state $\Delta_D = \mathbf{0.013}$ that grow (dull blue) when system is driven to a stress state $\Delta_D = \mathbf{0.006}$ (red arrow). Microfracture increments in purple color nucleate independently at respective stress states, Δ_D. Microfracture increments (in blue color), '1' and '2' at $\Delta_D = \mathbf{0.013}$ grow and merge as '2' when system is loaded to $\Delta_D = \mathbf{0.006}$.

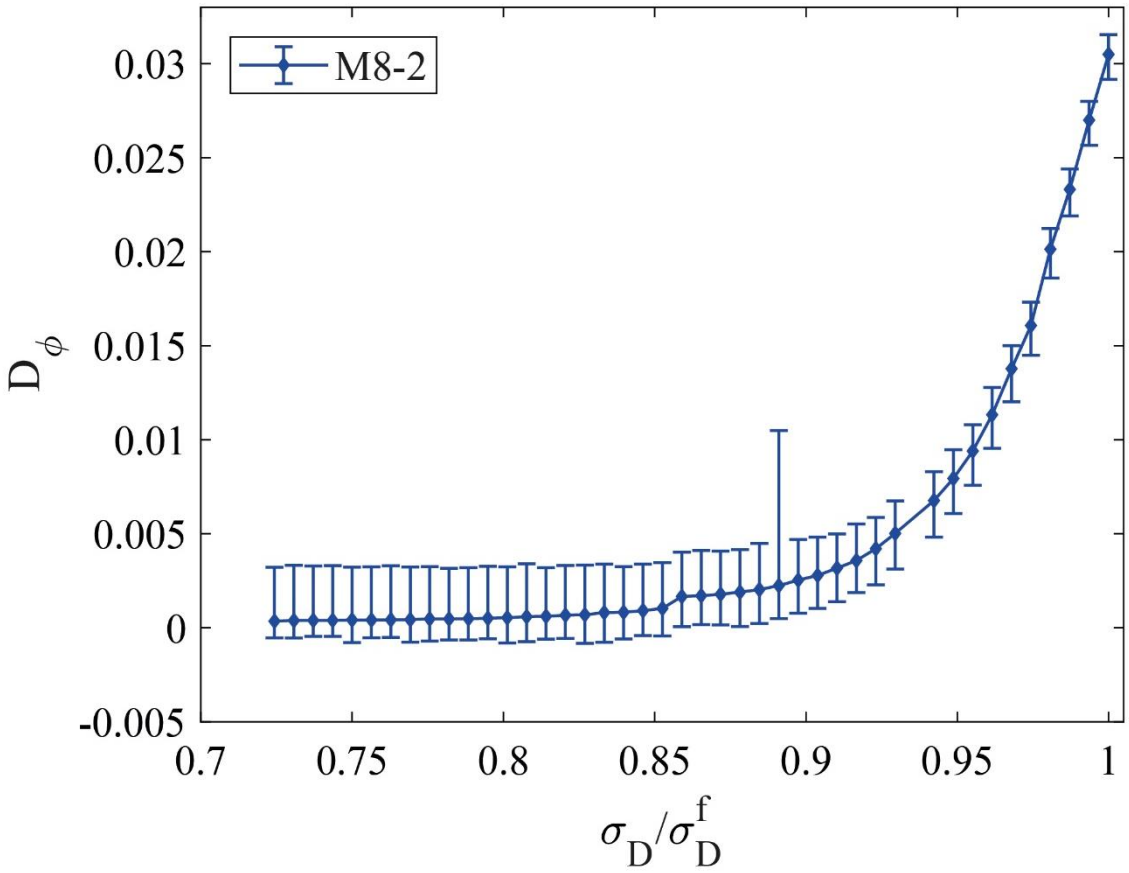

Figure S2. Evolution of damage with increasing differential stress in sample M82 (same representation as Figure 6), where the error bars indicate the range of variations of damage volume when the gray level threshold used to extract microfractures in the tomography data is increased or decreased.

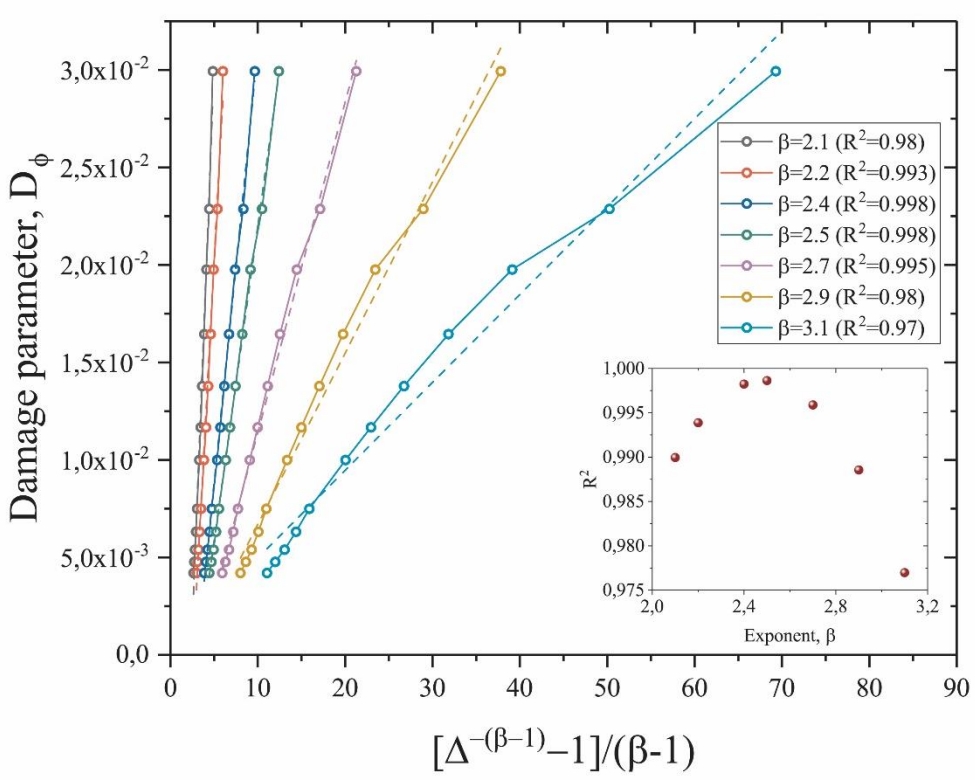

Figure S3. Plot of damage parameter, D_φ against $\frac{\left(\Delta_D{}^{-(\beta-1)}-1\right)}{(\beta-1)}$, for different values of β for sample, M8-2. The best fit corresponds to a value of the exponent $\beta = 2.5$. Inset: R^2 fit for every β.

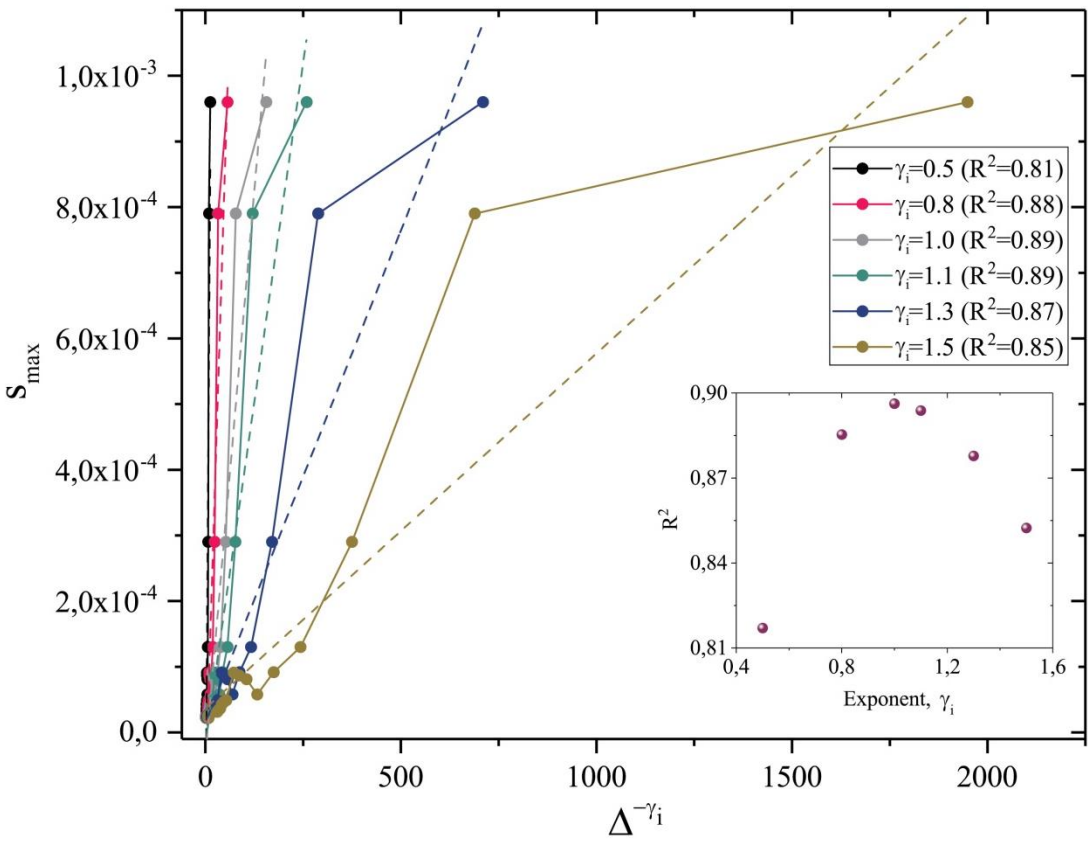

Figure S4. Plot of largest damage increment, s_{max} against $\Delta_D^{-\gamma_i}$, for different values of γ_i for sample M8-2. The best fit corresponds to the value $\gamma_i = 1.0$. Inset: R^2 fit for every value of γ_i.

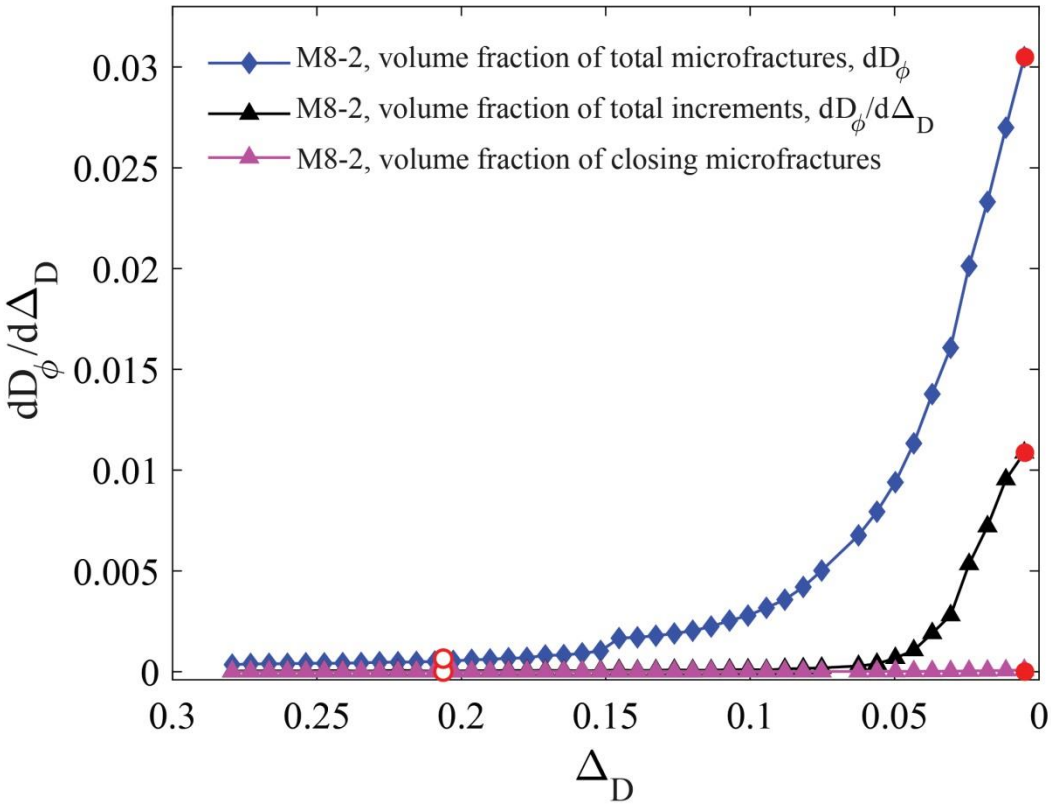

Figure S5. Evolution of total damage, $\boldsymbol{D_{\varphi}}$, incremental damage, $\boldsymbol{dD_{\varphi}/d\Delta_D}$, and closing microfracture volume fraction as a function of control parameter, Δ_D in sample M8-2.

Movie Captions

Movie S1. Evolution of microfractures in samples M8-1 and M8-2, towards failure. $\boldsymbol{\Delta_D = 0}$, represents the failure point, $\boldsymbol{\Delta_D > 0}$ indicates the pre-failure phase and $\boldsymbol{\Delta_D = 0.12}$ corresponds to the yield point. Microfractures grow randomly in the entire sample in the initial stages of deformation and start to localize along a plane oriented at ~30° to the axial load. Further increase in load favors growth of damage clusters, which evolve into two dimensional shear bands near failure.

Movie S2. Growth of the largest cluster in samples M8-1 and M8-2, towards failure. $\boldsymbol{\Delta_D = 0}$ represents the failure point, $\boldsymbol{\Delta_D > 0}$ indicates the pre-failure phase and $\boldsymbol{\Delta_D = 0.12}$ corresponds to the yield point. At failure, the largest cluster spans the sample resulting in a shear fault.

Movie S3. Development of macroscopic shear band on approaching failure in samples M8-1 and M8-2. $\boldsymbol{\Delta_D = 0}$ represents the failure point, $\boldsymbol{\Delta_D > 0}$ indicates the pre-failure phase and $\boldsymbol{\Delta_D = 0.12}$ corresponds to the yield point.

Movie S4. Localization of microfractures on approaching failure in sample M8-2. $\boldsymbol{\Delta_D = 0}$ represents the failure point, $\boldsymbol{\Delta_D > 0}$ indicates the pre-failure phase. Microfractures are indicated as red volumes.

Manuscript 2

Synchrotron 4D X-ray imaging reveals strain localization at the onset of system-size failure in porous reservoir rocks

Neelima Kandula, Jessica McBeck, Benoît Cordonnier, Jérôme Weiss, Dag Kristian Dysthe and François Renard

Submitted to *Pure and Applied Geophysics* (2021).

Synchrotron 4D X-ray imaging reveals strain localization at the onset of system-size failure in porous reservoir rocks

Neelima Kandula[1,*], Jessica McBeck[1], Benoît Cordonnier[1,2], Jérôme Weiss[3], Dag Kristian Dysthe[1], François Renard[1,3,*]

[1] PGP, The Njord Centre, Departments of Geosciences & Physics, University of Oslo, Norway

[2] The European Synchrotron, ESRF, beamline ID19, Grenoble, France

[3] Université Grenoble Alpes, Université Savoie Mont Blanc, CNRS, IRD, IFSTTAR, ISTerre, 38000 Grenoble, France

[*] e-mail: 91neelimak@gmail.com; francois.renard@fys.uio.no

Highlights:

1. In situ dynamic X-ray micro tomography imaging during triaxial compression provides detailed quantitative microstructural characterization during deformation of porous rocks.

2. The trends in porosity are closely linked to the evolution of the incremental strain components, dilation, contraction and shear.

3. Strain localization in reservoir rocks are strongly influenced by the microstructure of the rock, complexity of pore space and applied confinement.

Abstract

Understanding the mechanisms of strain localization leading to brittle failure in reservoir rocks can help addressing geomechanical challenges like porosity and permeability evolution, induced seismicity, fracturing and subsidence in geological reservoirs. We perform triaxial compression tests on three types of porous reservoir rocks to reveal the local deformation mechanisms that control system-size failure. We deformed cylindrical samples of Adamswiller sandstone (23% porosity), Bentheim sandstone (22% porosity), and Anstrude limestone (20% porosity), using an X-ray transparent triaxial deformation apparatus. This apparatus enables the acquisition of three-dimensional synchrotron X-ray images, under in situ stress conditions. Analysis of the tomograms provide 3D distributions of the deformation that include the microfractures and dilatant pores from which we calculated the evolving porosity. Digital Volume Correlation analysis reveals the dominant strain localization mechanisms through computation of incremental strain components from digital tomograms. Damage localized as a single shear band or by the formation of conjugate bands in the three rock types. The porosity evolutions closely match the evolution of the incremental strain components of dilation, compaction and shear. With increase in confinement, strain localization in sandstones shifts from dominant dilatative strain (Bentheim sandstone) to contractive strain (Adamswiller sandstone). SEM images indicate that the microscale mechanisms guiding strain localization in sandstones are pore collapse and grain crushing and in limestones are pore collapse, pore-emanated fractures and cataclasis. Our dynamic X-ray microtomography data brings unique insights on the correlations between the evolutions of rock microstructure and macroscopic strain during the approach to brittle failure in reservoir rocks.

Keywords: X-ray tomography; porous rocks; brittle failure

1. Introduction

Strain localization in rocks and geomaterials (e.g., cement) is observed over a broad range of length scales, varying from centimeter-sized laboratory rock specimens (e.g., Lockner et al., 1991; Paterson and Wong, 2005; Renard et al., 2019a) to crustal fault zones stretching over several kilometers (e.g., Fossen et al., 2007; Fossen et al., 2018; Cilona et al., 2012; Rotevatn et al., 2016). Strain localization within reservoir rocks can occur as deformation bands (e.g. Aydin & Johnson 1978; Shipton & Cowie 2001). These features influence permeability and thus fluid flow in sedimentary basins (e.g. Bjørlykke 1993), and reservoir compaction and subsidence (e.g. Nagel 2001). In sandstone and carbonate reservoirs, open and subsequently cemented fracture networks and deformation bands are the structures resulting from strain localization, which have contributions from aseismic deformation.

1.1 Deformation bands in sandstone and limestone

Deformation bands in sandstones may form by a combination of shear and compaction. A kinematic classification system of deformation bands depends on the competition between these two end-members. Bands of localization where shear displacement exceeds compaction are categorized as compaction shear bands (Zuluaga et al., 2014; Fossen et al., 2018). Bands where compaction and shear are of comparable magnitude are described as shear-enhanced compaction bands (e.g, Ballas et al. 2013) and those dominated by compaction are pure compaction bands (e.g, Fossen et al., 2011). Shear-enhanced compaction bands are characterized by high dihedral angles (47^{o} in Entrada Sandstone, Utah, Fossen et al., 2018; dihedral angle is the angle measured between the conjugate deformation bands) and pure compaction bands are formed perpendicular to maximum principle stress (Fossen et al., 2011). Dilatational bands with a higher porosity than the host rock also occur in Nubian Sandstone in Sinai (Fossen et al., 2007). Dilatational bands may increase the permeability while the compaction bands decrease it (Zuluaga et al., 2014).

Due to complexity in the pore space, grain assemblage and mineralogy, carbonate rocks are in many aspects different from sandstones. Although 50-60% of hydrocarbons are produced in conventional carbonate reservoirs, only recently significant attention has focused on localization mechanisms in carbonate rocks. Knowledge about the evolution of deformation bands and their

corresponding effect on the petrophysical properties of the host rock is thus less established in carbonate rocks. Similar to sandstones, localization is sensitive to the pore geometry and grain size distribution (Rustichelli et al., 2012; Cilona et al., 2014), and can reduce the porosity and permeability (Rath et al., 2011; Tondi et al., 2016). Four main strain localization types have been identified in carbonate rocks within contractional and extensional tectonic settings: pure compaction bands (Rotevatn et al., 2016), narrow bands of compaction and shear described as compactional shear bands (e.g., Aydin, 1978; Rath et al., 2011), pressure solution at the grain contacts (Croize et al., 2013) leading to the formation of solution-dominated compactional shear bands (Rutter, 1983), and cataclasis within the compactional shear bands forms cataclasis-dominant compactional shear bands (Rotevatn et al., 2016).

1.2 Laboratory experiments of sandstone and limestone brittle deformation

Many studies have analyzed inelastic deformation and strain localization in sandstones and limestones with varying porosities and under a range of confining pressures in the laboratory (e.g. Scott & Nielsen, 1991; Wong et al., 1997; Baud et al., 2000; Olsson & Holcomb 2000; Fortin et al., 2009; Vajdova et al., 2010; Wong & Baud 2012; Brantut et al., 2014; Ji et al., 2015; Baud et al., 2017a; Baud et al., 2017b). Brittle faulting in a porous rock under compressive loading is generally accompanied by shear localization. However, field and laboratory studies have documented that the failure mode in porous rocks is highly dependent of the confinement. With increasing confining pressure, the failure mode in both sandstones (Menéndez et al., 1996; Zhu & Wong 1997) and limestones (Vajdova et al., 2010; Baud et al., 2017c) shows a transition from brittle faulting to cataclastic flow and then ductile deformation, which is an universal behavior in compressive failure (Renshaw and Schulson, 2001). Under low confinement (5 MPa), dilatancy leads to shear localization at macroscopic failure whereas at higher confinement, cataclasis results in shear-enhanced compaction and strain hardening. Thin sections of failed limestone samples deformed under intermediate confinement did not show evidence of high-angle shear bands or diffusive compaction bands, indicative of higher confinement. However, triaxially compressed Leitha limestone formed discrete compaction bands at intermediate confinement (Huang, 2019). Therefore, questions about the microstructural origins of strain localization in this transitional regime of 20-40MPa confining pressure remain open.

Strain localization and porosity evolution are closely connected with the failure mode, and vary depending on the initial porosities and pore geometries of individual rock. Recent triaxial tests on porous carbonate rocks (Baud et al., 2017a) have classified failure modes based on the initial porosity and applied confinement. The failure mode at low confinement in carbonate rock cores with high initial porosity is dominated by compaction and tend to form compaction bands. The failure mode in lower porosity carbonates includes a combination of compaction and shear resulting in compaction shear bands and conjugate shear bands.

Strain localization in rocks is resulting from the elastic interaction kernel, which is anisotropic (Dansereau et al., 2019). Microscale heterogeneities guide the nucleation and perseverance of damage (Brace, 1978). In the crust, these heterogeneities correspond to pores, grains, grain boundaries, and the cement between the grains. Pore space can be comprised of numerous equant pores connected through narrow passages (pore throats). When an external stress field is applied, damage may nucleate on the grain scale heterogeneities and develop by growth of microfractures and collapse of the pore space (Paterson & Wong, 2005; McBeck et al., 2019), through the redistribution of stress field as force chains. When the rock is driven to larger stresses, fractures may coalesce to form localized zones of intense deformation. These localized zones extend over multiple grains and cut across the sample length (Brace, 1978).

Fracture nucleation and the characteristics of localized zones are sensitive to rock type, initial porosity, complexity of the pore geometry and loading conditions (Paterson & Wong, 2005). Sandstones are comprised of angular grains with narrow grain size distributions and uniform pore space. Conversely, limestones may exhibit a more complex pore geometry because the pore size may span a broad range, and is often characterized by a bimodal distribution (Ji et al., 2015). Large pores between the grains may be surrounded by a myriad of small pores located inside the grains or in the cement. These two categories of pores may form two parallel networks, 1) macroporosity, which can be identified by optical microscopy and moderate resolution X-ray microtomography, 2) microporosity with submicron features not readily resolved by these standard techniques (Pittman 1971), but may be identified by scanning electron microscopy or submicrometer X-ray microtomography (Ji et al., 2015). Previous analyses have identified and characterized the microscale mechanisms of grain crushing, pore collapse and pore-emanated fractures in the brittle failure mode under low confining pressures (Zhu & Wong 1997; Wong & Baud 2012; Baud et al.,

2017a; Vajdova et al., 2010). Conversely, under higher confinement, larger amounts of cataclasis may lead to failure (reference). But an ambiguity exists about the microscale mechanisms associated with intermediate confining pressures (20-40MPa).

Acoustic emission (AE) measurements provide an alternative technique for quantifying grain-scale damage localization related to faulting. AE activity measured in Westerly granite (Lockner et al., 1992), a rock with <1 % porosity, revealed the spatiotemporal development of strain localization. For porous sandstones and limestones, AE data have revealed microfracturing events that were inferred to occur at grain interfaces (Olsson et al., 2002; Baud et al., 2004; Vajdova et al., 2004; Fortin et al., 2009; Baud et al., 2017b). These analyses have led to the conclusion that the spatial distribution of AE arises from 1) the formation of extensional fractures or 2) transgranular fractures due to grain breakage. From microstructural observations of the samples after the experiments, the dominant microscale mechanisms giving rise to compaction was identified as pore collapse (resulting from sliding between the grains), which does not generate significant amount of AE and therefore appeared aseismic in these experiment. This dominance of pore collapse was observed in diffusive compaction bands and high-angle shear bands in carbonate rocks (Wong & Baud 2012; Ji et al., 2015), and compactional shear bands in sandstones (Vajdova et al., 2004; Louis et al., 2007).

1.3 Motivations for the present study

Recent studies (Louis et al., 2007; Wong & Baud 2012; Ji et al., 2015; Baud et al., 2017b) have argued for a systematic microstructural characterization including X-ray computed tomography (μCT) and Digital Volume Correlation (DVC) to provide a consistent description of the multiscale mechanics of strain localization in porous reservoir rocks. With this motivation, we present here triaxial deformation tests on Adamswiller sandstone, Bentheim sandstone and Anstrude limestone (of comparable porosities 20-23%) subjected to low and intermediate confining pressures (5-30 MPa). We employ synchrotron X-ray microcomputed tomography imaging (μCT) and scanning electron microscopy imaging (SEM) for microstructural characterization. We also perform digital volume correlation (DVC) to compute the incremental strain accumulated toward system-size failure. Recent experiments have elucidated strain localization mechanisms in sandstones (Renard et al., 2019a) and limestone (Huang et al., 2019) using the same experimental

technique. Our experimental technique quantifies the combination of aseismic and seismic deformation components, which cannot be gained through other experimental techniques. Computing the local strain tensors provides close constraints on the dominant deformation mechanism that defines the failure mode. Recent studies using DVC (Renard et al., 2019a, 2019b, Zheng et al., 2019; McBeck et al., 2020) have shown that the distribution and localization of damage in a range of rock types are mixed-mode, involving contributions from both tensile and shear components of strain. The effectiveness of the technique enables the present study to address the following questions: What are the differences in the failure modes and strain localization mechanisms between two classes of reservoir rocks (sandstones and limestones)? How does the interplay of dilatancy, compaction and shear affect the variation in porosity? How does confining pressure influence porosity variations and in turn damage localization? What are the microscale mechanisms underlying the strain localization in respective rock types? Through the elaborate discussion following the later part of this article, we show that the strain localization mechanisms in sandstones and limestones are defined by the underlying microstructure and pore geometry in these respective rock types. In sandstones, brittle deformation is dominated by either dilatative or contractive strain components while in limestones it is more of a mixed-mode. Microscale mechanisms guiding strain localization in sandstones are pore space dilation or pore collapse along with grain crushing. On the other hand, pore collapse, grain crushing with cataclasis and pore-emanating fractures constitute the microscale processes in limestones. Applied confinement also plays a major role in determining microscale mechanisms and strain localization in porous rocks.

2. Methods

Table 1 Symbols and parameters

Parameters	**Definition, units**
σ_1	axial stress, MPa
$\sigma_2 = \sigma_3$	confining stress (i.e. confining pressure), MPa
p_0	pore fluid pressure, MPa
σ_d	differential stress, $\sigma_1 - \sigma_3$, with $\sigma_2 = \sigma_3$, MPa
σ_d^y	differential stress at yield, MPa

σ_d^f	differential stress at the failure, MPa
ε_{zz}	macroscopic axial strain, no unit
ε_{zz}^f	macroscopic axial strain at failure, no unit
$\varepsilon_{zz}/\varepsilon_{zz}^f$	normalized axial strain (in the range [0 1]), no unit
ϕ	porosity of the sample measured using segmented 3D tomograms, no unit
ϕ_0	Initial porosity of the sample measured using segmented 3D tomograms
ϕ/ϕ_0	normalized porosity, no unit
$\langle\phi\rangle$	mean porosity in the sample, no unit
$D_\phi = \frac{\phi - \phi_0}{1 - \phi_0}$	porosity parameter, no unit
$\vec{u}$	incremental displacement, m
$\Delta\varepsilon_{zz}$	difference of macroscopic axial strain between two tomograms used for each digital volume calculation, no unit
$\lvert mean/\Delta\varepsilon_{zz}\rvert$	mean of the absolute values of the incremental strain components, normalized by $\Delta\varepsilon_{zz}$, no unit
$\sum \lvert mean/\Delta\varepsilon_{zz}\rvert$	cumulative mean of the absolute values of the incremental strain components, normalized by $\Delta\varepsilon_{zz}$, no unit

2.1. Triaxial compression X-ray tomography experiment

We imaged in 4D under in situ stress conditions the microstructural evolution of porous rocks subjected to triaxial compression until system-size (macroscopic) failure. We deformed samples using the X-ray transparent triaxial compression apparatus Hades (Renard et al., 2016), and acquired time series of images of the rock microstructure using time-lapse synchrotron X-ray microtomography. We performed seven experiments on porous reservoir rock samples, including one Adamswiller sandstone core (Rimmelé et al., 2010), one Bentheim sandstone core (Klein et al., 2001) and five Anstrude limestone cores (Lion et al., 2004, Renard et al., 2017). All the Anstrude samples were cored from the same block. These three rock types constitute a set of sandstones and limestones of comparable initial porosities (20-23%) and are ideal for studying the

relative variations in porosities, microstructural changes and strain localization mechanisms among them.

Adamswiller sandstone is a Triassic (Bundsandstein) sandstone from a quarry in Bas-Rhin. It is composed of 71% quartz, 9% feldspar, 11% clay, 5% mica, traces of apatite, and oxides of iron and titanium (Rimmelé et al., 2010). It has an average porosity of 23%, mean grain size in the range $120\ \mu m$ (Heap et al., 2017) to $90\ \mu m$ (Wong et al., 1997). Bentheim sandstone comes from an outcrop at Gildehausen quarry, near Bentheim, Germany (Klein et al., 2001). This sandstone is relatively homogeneous and composed of 95% quartz, 3% kaolinite and 2% orthoclase. The size of the quartz grains varies between $200 - 400\ \mu m$ (Van Baaren et al., 1990; Schutjens et al., 1995), with a mean grain size of $300\ \mu m$ (Ma et al., 2016). The average porosity of this sandstone is 22.8% (Klein et al., 2001). Anstrude limestone is obtained from a quarry in Bierry-les-Belles-Fontaines, Burgundy, France. The limestone is an assemblage of $100 - 1000\ \mu m$ sized ooids (concentric spheres of calcite). Each ooid is made of micro-crystalline calcite with grain size finer than $4\ \mu m$, and in turn contains numerous small pores at micro to nano meter scale, making it highly porous (Lion et al., 2004). Sparite crystalline calcite makes the cement between the ooids. Mean porosity of this limestone is 19.9%, close to 20% (Lion et al., 2004). Thus the porosity of our rocks range from 20% (Anstrude limestone), 22% (Bentheim sandstone), to 23% (Adamswiller sandstone).

Table 1 indicates the various parameters used in the present study, and Table 2 shows the experimental conditions. The core samples had a height (~10 mm) to diameter (~5 mm) ratio of 2:1. For each experiment, we inserted the specimen into a jacket made of Viton fluoropolymer elastomer and then inserted this assembly into the triaxial deformation apparatus. Experiments were performed at ambient temperature (20-23 °C), under a constant confining pressure ($\sigma_2 = \sigma_3$) applied by silicon oil on the jacket that surrounded the sample. Each sample was placed axially between two stainless steel pistons and the interface contacts were not lubricated. The lower piston was held fixed and samples were loaded axially (σ_1) in steps of 1-5 MPa applied on the upper piston, until failure occurred. For experiment #6, we injected water as a pore fluid with a constant fluid pressure of 10 MPa (Table 2). The porosity of each sample was not measured before the experiments. Segmentation of the tomograms provides an estimate of the initial and evolving porosity at the spatial resolution of the images (Table 2).

The Hades apparatus is installed on the rotating stage of the X-ray microtomography beamline ID19 at the European Synchrotron Radiation Facility (Grenoble, France). A synchrotron polychromatic X-ray beam with a maximum energy of 200 keV was sent through the apparatus. Due to X-ray attenuation from the walls of the Hades apparatus made of titanium, the average X-ray energy absorbed by the sample was around 89 keV. During each scan, the stage of the beamline was rotated from 0^o to $+180^o$ and back to 0^o while stress was maintained constant. Each scan lasted around 90 seconds and a series of 2500 two-dimensional radiographs of the three-dimensional sample were recorded. Each experiment was stopped when a significant stress drop was measured, corresponding to the brittle failure of the sample. Between 26 and 144 tomograms were acquired for each sample.

Table 2 Experimental conditions for dynamic in-situ X-ray synchrotron imaging of triaxial compression tests on porous rocks

Rock type	**Initial porosity (μCT)** ϕ_0	**Confining pressure** $\sigma_2 = \sigma_3$	**Pore pressure** p_0	**Differential stress at yield** σ_d^y	**Differential stress at failure** σ_d^f	**Temperature**	**Rate of increase in differential stress**	**Number of 3D scans**
Adamswiller sandstone	13.2%	30 MPa	0	80 MPa	102 MPa	20 °C	2 MPa/step (5MPa for final step)	54
Bentheim sandstone	16.7%	5 MPa	0	66 MPa	76 MPa	23 °C	1 MPa/step	56
Anstrude limestone 2	7.8%	20 MPa	0	40 MPa	59 MPa	22 °C	5 MPa/step	43
Anstrude limestone 3	6.8%	5 MPa	0	32 MPa	40 MPa	22 °C	2 MPa/step	26
Anstrude limestone 4	15.6%	20 MPa	0	51 MPa	66 MPa	23 °C	1 MPa/step	55
Anstrude limestone 5	3.5%	5 MPa	0	36 MPa	42 MPa	23 °C	1 MPa/step	43
Anstrude limestone 6	6.3%	30 MPa	10 MPa	56 MPa	125 MPa	22 °C	1 MPa/step	114

2.2. Tomogram reconstruction and segmentation

The radiographs acquired at beamline ID19 were processed to reconstruct three-dimensional tomograms (1600 x 1600 x 1600 voxel) using the plain filtered back-projection method employed in the program PyHST2 (Mirone et al., 2014), with a single-distance phase-retrieval algorithm adapted from Paganin et al. (2004). The voxel size in the tomograms was 6.5 micrometers. The spatial resolution was not measured here but, on beamline ID17 with similar optical systems as beamline ID19, a spatial resolution of the order of 20 micrometers was measured (Mittone et al. 2017). After reconstructing the volumes, we did not observe blurring that would indicate movements of the sample or fracture growth during scan acquisition. We computed the axial strain as a function of applied stress by measuring the axial length of the sample directly on the three-dimensional X-ray tomograms (e.g., Renard et al., 2018, 2019a). Segmentation of tomograms incorporate corrections for 1) the fluctuations in synchrotron X-ray intensity, 2) beam hardening, 3) ring artifacts and 4) other false projections. We reduced the noise in the data by using non-local means filter (Buades et al., 2005). Then, based on the intensity of the histogram of each tomogram, we separated the voxels into two classes: the rock matrix, and pore space/fractures (Renard et al., 2019a). The same grey level threshold was applied in all the tomograms of a given experiment. Because the samples are heterogeneous and may contain a bimodal porosity (Anstrude limestone), and because the porosity extracted on the tomograms is limited by the spatial resolution, the initial micro-computed tomography porosities reported in Table 2 are smaller than the actual porosities of the rock samples.

To calculate the mean porosity from the segmented tomograms, we divided the rock volume into sub-volumes of size equivalent to twice the grain size of the respective rock. The mean grain size of Adamswiller sandstone is near $120\ \mu m$ (Heap et al., 2017) and Bentheim sandstone is $300\ \mu m$ (Ma et al., 2016). Anstrude limestone grain size is approximated to $100 \mu m$, which is the size of smallest ooid (Lion et al., 2004). We then computed the volume of the pore space in each sub-volume and found the mean of these local porosity values at every strain step in the experiment. We performed this calculation to compare the calculated porosity to the local strain computed from digital volume correlation (DVC, see below). The DVC algorithm divides each tomogram into sub-volumes (of ~ 130 micrometers in the present study) and calculates incremental strain values for each of the sub-volume, providing a local measurement. To conclude,

using these subvolumes, one can compares the local strain increments in the sample with the local porosity evolution.

2.3. Digital volume correlation analysis

Digital volume correlation (DVC) analysis calculates fields of local 3D incremental strain tensors between two 3D volumes. We applied this technique to quantify incremental strain evolution between pairs of 3D tomograms acquired in the experiments. We employed the software TomoWarp2 (Tudisco et al. 2017), following procedures described in McBeck et al. (2018) and Renard et al. (2019a, 2019b). We divided each experiment into eight to ten nearly equal intervals of macroscopic axial strain ($\Delta\varepsilon_{zz}$), as shown in Figure S2 and then calculated DVC on the pairs of tomograms acquired at those equally-spaced macroscopic axial strains. The DVC algorithm divides each 3D tomogram into sub-volumes, with a node spacing of 20 voxels, producing a spatial sampling of 130 micrometers. We used search window sizes of ± 10, ± 15 or ± 50 voxels, depending on the magnitude of the macroscopic axial strain obtained between the tomogram pair. The search window size determines the maximum detected displacement magnitudes, and so larger changes in the macroscopic axial strain require larger search window sizes. We choose the coordinate system such that the direction of the maximum compression is along z-axis.

For each experiment, we first computed the three-dimensional incremental displacement field between each pair of tomograms. From the displacement fields, we calculated the displacement gradient tensor ($\vec{u}$), from which we calculated the components of the incremental strain tensor. Throughout the sub-volumes, we computed the components of incremental strain tensor following continuum mechanics, such that negative divergence ($\nabla.\vec{u} < 0$), positive divergence ($\nabla.\vec{u} > 0$), negative rotation (also called curl, $\nabla x\vec{u} < 0$) and positive rotation ($\nabla x\vec{u} > 0$) indicate the contractive strain, dilatative strain, left-lateral shear strain and right-lateral shear strain, respectively. From the population of strain components (Figure S3) within each rock volume, we computed the mean of the local strain values normalized by the amount of axial strain increment ($\Delta\varepsilon_{zz}$) at every DVC step, $|mean/\Delta\varepsilon_{zz}|$. These calculated strains are incremental measurements of the strain accumulated between the acquisitions of the two tomogram pairs used in the analysis. In order to compare these incremental strain values to the porosity, which is a

cumulative measure, we also computed a cumulative measure of the incremental strain components, $\sum |mean/\Delta\varepsilon_{zz}|$.

2.4. Scanning electron microscopy imaging

Most samples, when removed from the rig, were highly damaged and mostly in powder form. However, for the Adamswiller sandstone and Anstrude limestone #2, #4, #5 samples, the cores could be recovered after the experiment for post-mortem observations. Two samples (Adamswiller sandstone and Anstrude limestone #4) were impregnated with epoxy resin to consolidate them and then cut along the vertical axis of the cylinder. The surfaces were polished with several sandpapers with increasing grit, from #320 to #4000, and then carbon coated. SEM backscatter images of two samples were acquired on a Hitachi SU5000 field-emission scanning electron microscope (FE-SEM) at the Department of Geosciences, University of Oslo.

3. Results

3.1 Macroscopic mechanical deformation

We observed two modes of brittle compressive failure in porous rocks in this study. The sandstones (experiments #1, #2) and limestones at low confinement (experiments #4, #6) failed with a short yielding phase and small amount of accumulated macroscopic axial strain (Figure 1). In contrast, the limestones under higher confinement (experiment #5) and with pore pressure (experiment #7) failed with longer yielding phases. At low differential stress, $\sigma_d = \sigma_1 - \sigma_2 = \sigma_1 - \sigma_3$, the axial strain increased quasi-linearly with increasing differential stress, in the macroscopic linear regime. We identified the differential stress at the yield point, σ_d^y, when the differential stress versus strain curve deviated by 3% from linearity (e.g., Brace et al., 1966). The yield point occurred at 70 - 80% of the differential stress at failure, σ_d^f, for all the samples except for Anstrude limestone #6, where it was 40-45% of σ_d^f (Table 2). Further increase in the differential stress resulted in irreversible accumulation of macroscopic contraction in the core until σ_d^f, when the sample failed with a sudden stress drop, and slip along several faults.

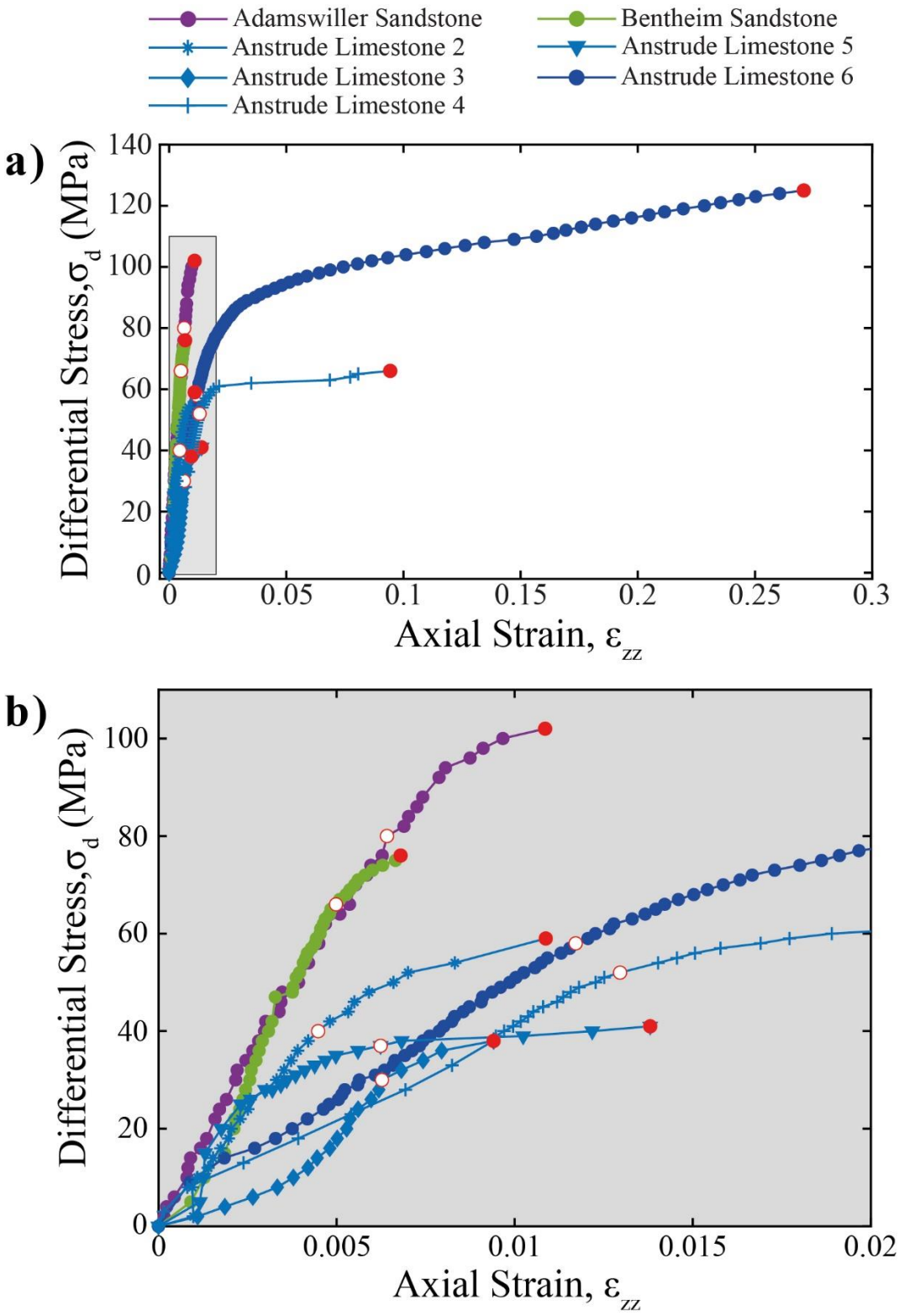

Figure 1. Relationships between differential stress and axial strain in seven experiments on porous rocks: Adamswiller sandstone, Bentheim sandstone, and Anstrude limestone (2, 3, 4, 5, 6). Table 2 shows the

experimental conditions. a) The complete differential stress versus axial strain relationships. b) Close up of relationships for the domain shown in the gray rectangle in (a). Open and closed red circles indicate the yield point and last scan before sample-size failure, respectively. Each circle shows the mechanical conditions of a 3D microtomography scan.

The total accumulated axial strain at failure in the sandstone experiments (0.006-0.011%) was less than the Anstrude limestone experiments (0.011-0.27%). The Bentheim sandstone accumulated the least macroscopic axial contraction of all the experiments (0.006%). This sandstone subjected to $\sigma_3 = 5\,MPa$ may have hosted less contraction than the Adamswiller sandstone ($\sigma_3 = 30\,MPa$) due to the lower applied confining stress. The five experiments on Anstrude limestone host a wider range of cumulative axial strain than the two sandstone experiments. The application of 10 MPa water fluid pressure in one of the limestone experiments, and the resulting large accumulation of axial contraction relative to the other experiments, produce this wider range in the limestone experiments.

3.2. Microstructural changes and evolution of porosity towards failure

Macroscopic deformation in each rock core occurs by deformation of pores and grains at microscopic scale, giving rise to a change in microstructure. Our experimental setup provides access to the deformation microstructure with 6.5 μm sampling distance. We segmented the pore space and rock matrix in each individual tomogram for each experiment until sample-size failure. Figures 2 and 3 show the microstructural changes including porosity variation in Adamswiller sandstone and Anstrude limestone #6, respectively. In the Adamswiller sandstone experiment, the x-z (vertical) cross-sections of the tomograms show a reduction in pore space at the yield stress (Figure 2b). The density of pore space post-yield (Figure 2b-iii) appears larger than that at yield (Figure 2b-ii). In the Anstrude limestone #6 experiment, the rock core compacted as the pore space decreased. Then, fracture coalescence characterized macroscopic failure (Figure 3f).

To quantify the porosity evolution that resulted in the observed sample compaction, we computed the volume of pore space in each rock core throughout loading (Figure S1). To compare the variation in porosity from the beginning to the end of each experiment, we calculate a measure of the relative variation in porosity. We computed the porosity parameter, $D_\phi = \frac{\phi - \phi_0}{1 - \phi_0}$, similar to

previous studies (Renard et al., 2018; Kandula et al., 2019). This parameter allows comparing samples with different initial porosities, where ϕ_0 is the initial porosity and ϕ is the porosity of the current scan. Positive D_ϕ indicates sample dilation and negative D_ϕ indicates compaction. On Figure 4b where the vertical axis is logarithmic, we report $-D_\phi$, because most samples compacted, as a function of normalized axial strain, $\varepsilon_{zz}/\varepsilon_{zz}^f$.

The porosity of all the rock cores decreases towards failure, indicating compaction. This decrease is rapid for Anstrude limestones 2, 4 and 6, which are subjected to higher confining pressures. Anstrude limestone 3 and 5 are subjected to low confining stresses ($\sigma_3 = 5\ MPa$) and show a linearly decreasing trend in porosity. For Anstrude 2, the slope of the axial strain-porosity curve changes at yield, i.e. $\varepsilon_{zz}/\varepsilon_{zz}^f = 0.65$. For Anstrude 5, a sharp peak and drop is observed at $\varepsilon_{zz}/\varepsilon_{zz}^f = 0.1$. When subjected to higher confining stress (20 MPa for Anstrude 3 and 5, 30 MPa for Anstrude 7), this limestone shows a non-linear decrease in porosity. Anstrude 2 shows a sharp drop at $\varepsilon_{zz}/\varepsilon_{zz}^f = 0.5$, post yield while Anstrude 4 shows a sharp drop at $\varepsilon_{zz}/\varepsilon_{zz}^f = 0.1$, before yield. Anstrude 6, which was subjected to pore fluid pressure, shows a smooth continuous decrease in porosity with a small peak near yield ($\varepsilon_{zz}/\varepsilon_{zz}^f = 0.1$). Similar to the limestone experiments, the Adamswiller sandstone shows a continuous non-linear decrease in porosity. In contrast, the Bentheim sandstone shows increasing porosity post yield. Thus, for this sample, the porosity first decreased until the yield point at $\varepsilon_{zz}/\varepsilon_{zz}^f = 0.75$, and then increased until failure.

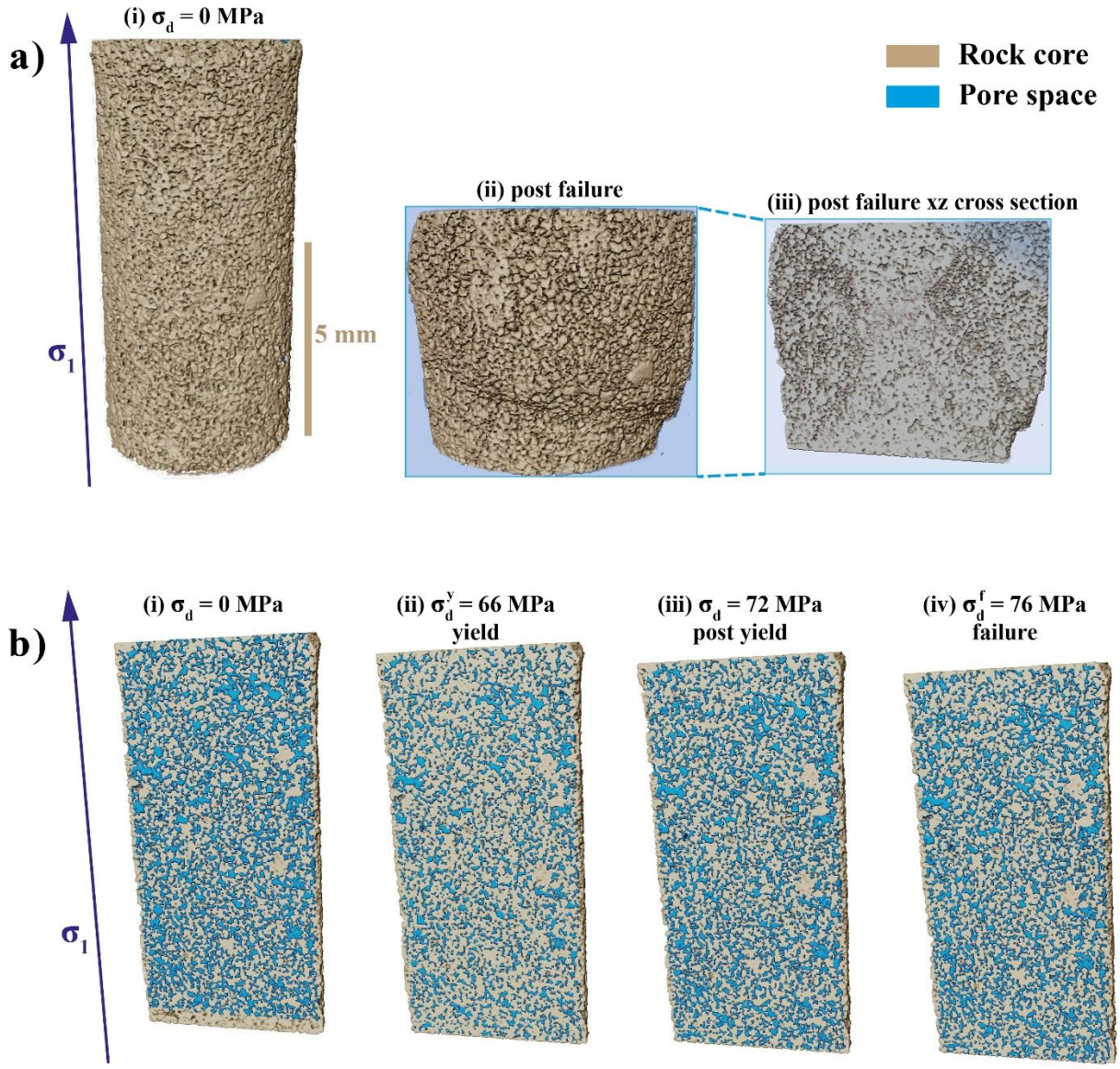

Figure 2. Rendering of the microstructural evolution of pore space in Adamswiller sandstone imaged by X-ray microtomography. a) Rock microstructure at the initial (i) and final stage (ii) of the experiment. iii) Axial cross-section of post-failure rock core. b) Cross-sections of pore space for an x-z cross section at (i) initial, (ii) yield, (iii) post yield and (iv) just before failure stages, where the porosity is represented in blue.

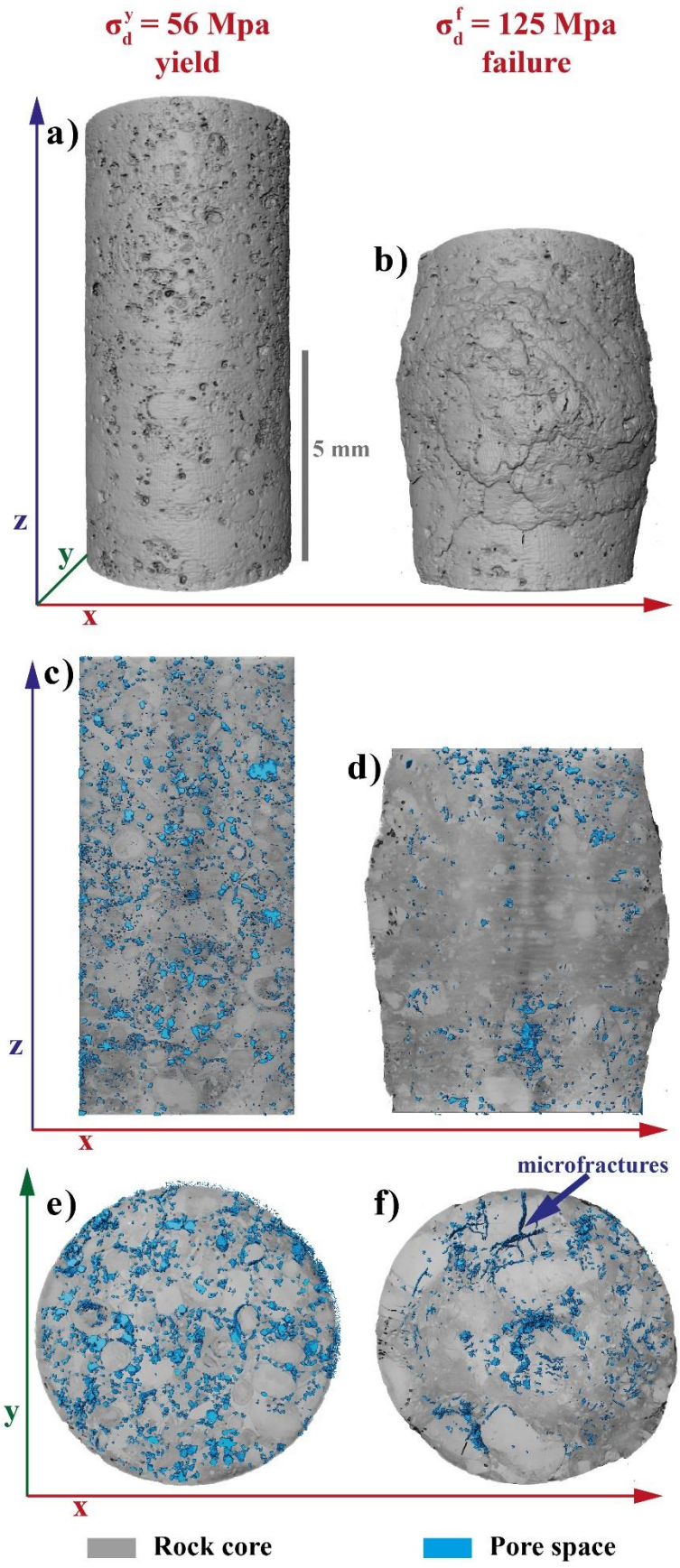
σ_d^y = 56 Mpa
yield
σ_d^f = 125 Mpa
failure
a)
b)
5 mm
z
y
x
c)
d)
z
x
microfractures
e)
f)
y
x
Rock core
Pore space

Figure 3. 3D pore microstructure at yield and just before the final failure in Anstrude limestone 6 sample. a-b) 3D rock core surface. c-f) Cross sections. The pore space is shown in blue.

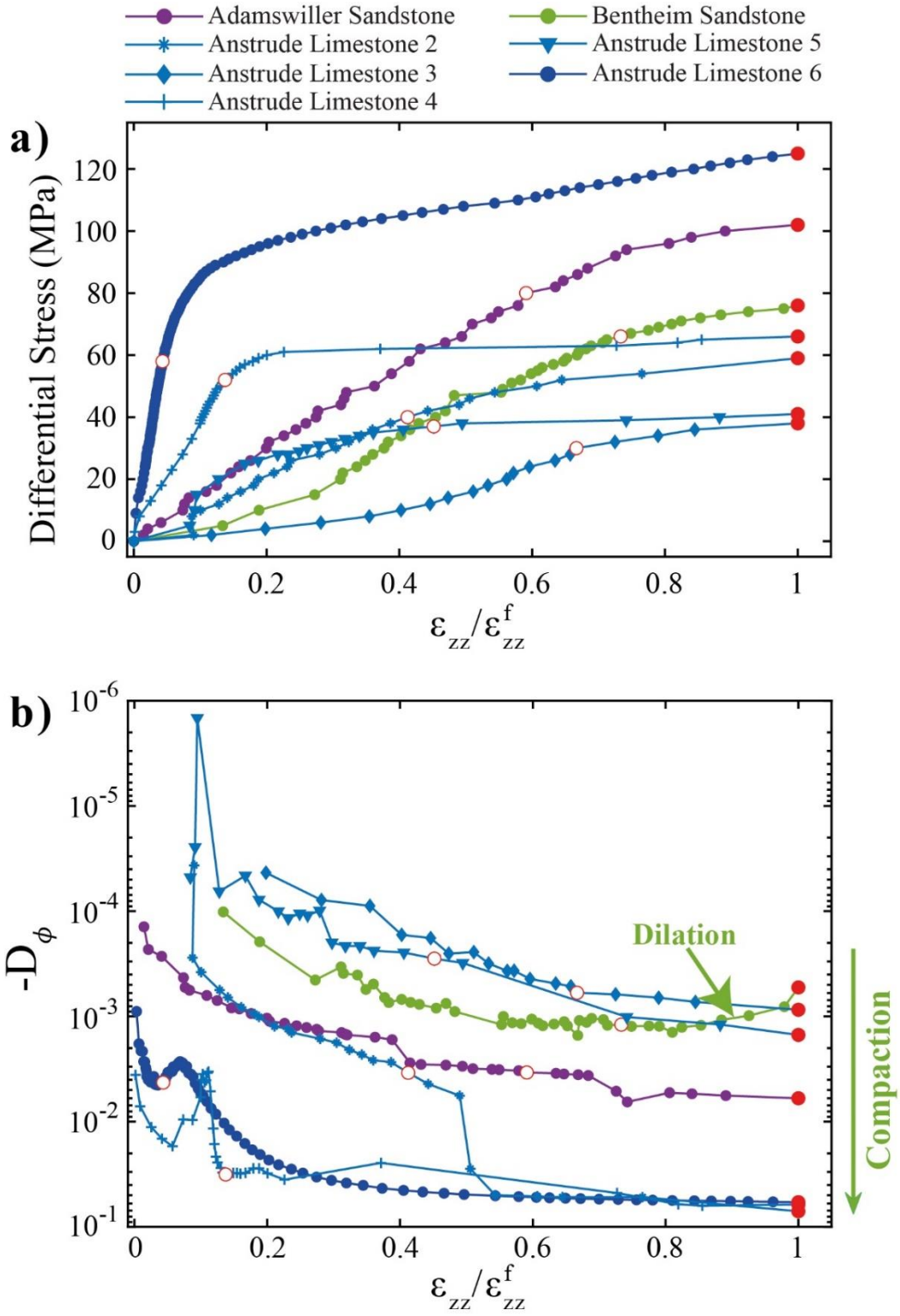

Figure 4. a) Differential stress versus macroscopic axial strain, ε_{zz}, normalized by the axial strain at failure, ε_{zz}^{f}. b) Dimensionless porosity parameter, $D_{\phi} = (\phi - \phi_0)/(1 - \phi_0)$ relative to $\varepsilon_{zz}/\varepsilon_{zz}^{f}$ shown in semi-log scale and reversed axis. Increasingly negative values indicate increasing compaction. The open and filled circles show the yield point and last scan before failure, respectively. The arrow points to the increase of dilation in the Bentheim sandstone when approaching failure.

3.3. Computation of accumulated strain toward failure

Using the digital volume correlation (DVC) method detailed in section §2.3, we have computed the incremental strain components. We display three-dimensional views of the variations of these components as a function of applied axial strain, which facilitates the evaluation of the dominant failure mechanism guiding the deformation for each sample. Figures 5 and 6 show the 95th percentile of the incremental strain component populations at low and high $\varepsilon_{zz}/\varepsilon_{zz}^{f}$ for two samples: Bentheim sandstone and Anstrude limestone 6. These DVC calculations show that the high values of incremental strain population tend to localize near failure (Figures 5 and 6). For example, conjugate bands of higher magnitude strain formed in the Anstrude limestone 6 near failure (Figure 6 e-h). When $\varepsilon_{zz}/\varepsilon_{zz}^{f}$ is close to zero, the higher strain values are spread throughout the rock. When approaching $\varepsilon_{zz}/\varepsilon_{zz}^{f} = 1$, the high strain values appear more localized. In all of the experiments, the strain components indicate localization of damage towards failure (Figures 5 and 6; Movies V1-V7). In Bentheim sandstone (Figure 5), the contractive strain is diffusely spread throughout the rock core at $\varepsilon_{zz}/\varepsilon_{zz}^{f} = 0.18$ and at failure ($\varepsilon_{zz}/\varepsilon_{zz}^{f} = 1$). Conversely, the dilatative strain is spread at $\varepsilon_{zz}/\varepsilon_{zz}^{f} = 0.18$ and then localizes at failure. Similar to the dilatative strain, the shear strain components show localization towards failure. In the 3D incremental strain components, the zones of high dilation and compaction do not exactly match the zones of high shear in all the experiments.

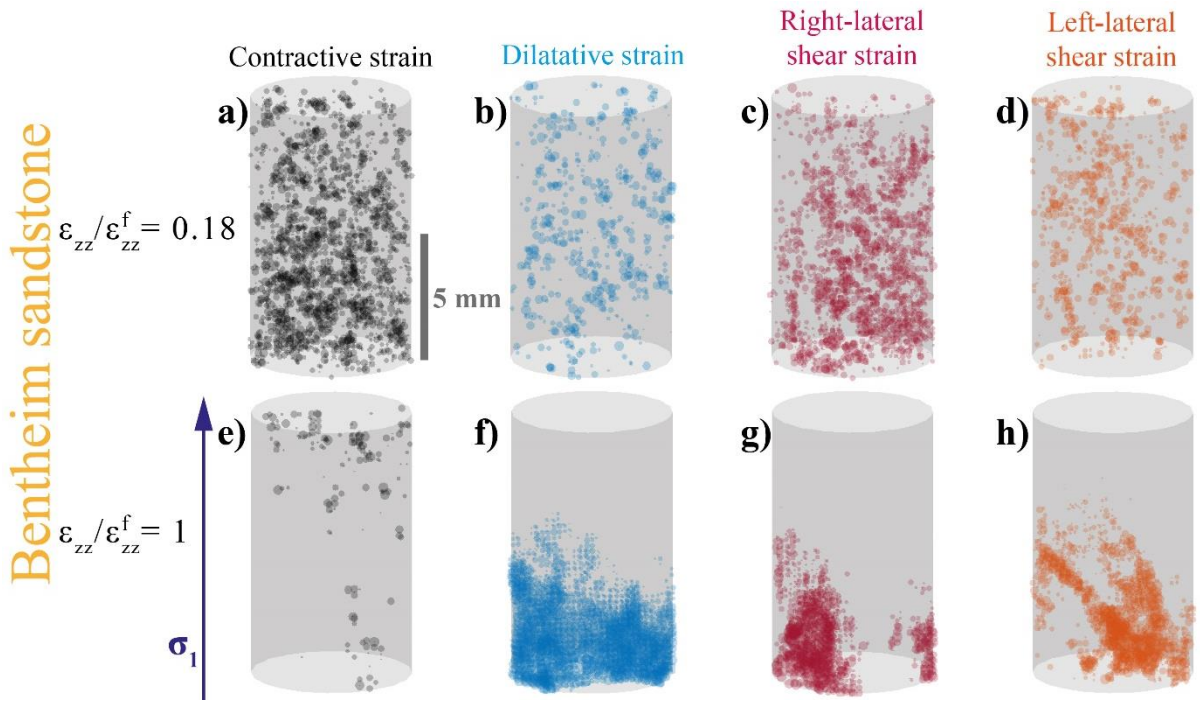

Figure 5. High values of 3D incremental strain components at low and high macroscopic strains for the experiment on Bentheim sandstone. Circles show the strain values > 95th percentile of each strain population. The columns show the contractive (a, e), dilatative (b, f), right-lateral shear strain (c, g) and left-lateral shear strain (d, h). Top and bottom rows show the strain fields when $\varepsilon_{zz}/\varepsilon^f_{zz} = 0.18$ and $\varepsilon_{zz}/\varepsilon^f_{zz} = 1$, respectively. The size of each marker is proportional to the magnitude of strain.

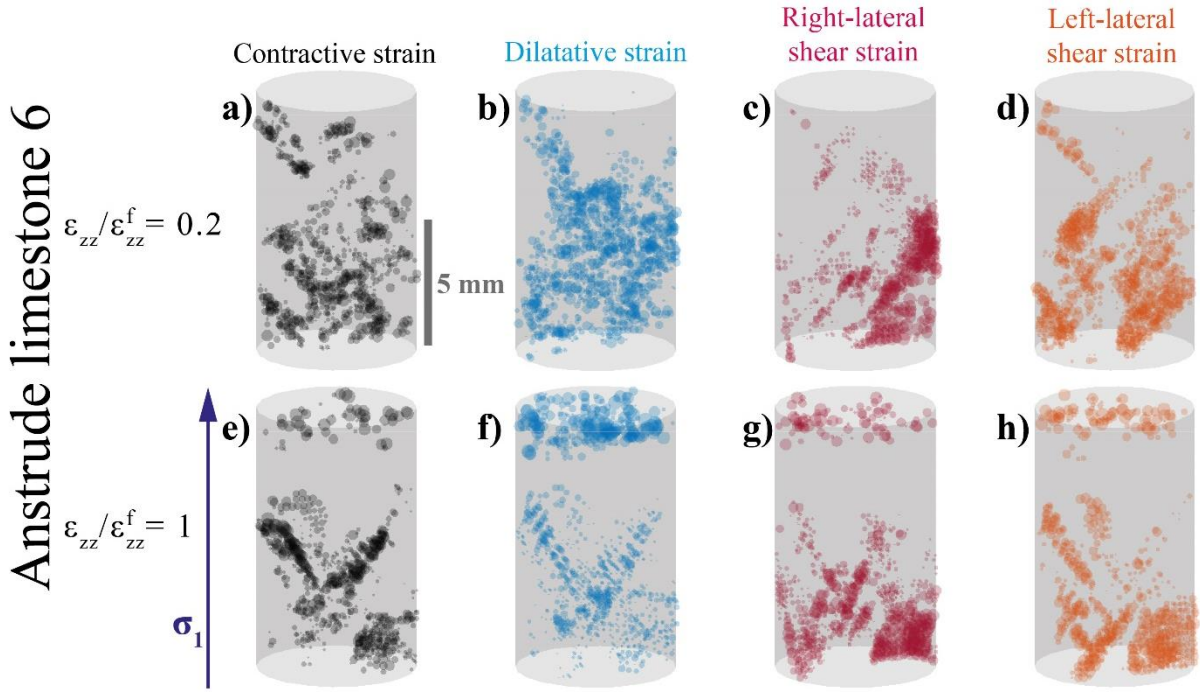

Figure 6. High values of 3D incremental strain components at low and high macroscopic strains for the experiment on Anstrude limestone 6. Circles show the strain values > 95th percentile of each strain population. The columns show the contractive (a, e), dilatative (b, f), right-lateral shear strain (c, g) and left-lateral shear strain (d, h). Top and bottom rows show the strain fields when $\varepsilon_{zz}/\varepsilon_{zz}^{f} = 0.18$ and $\varepsilon_{zz}/\varepsilon_{zz}^{f} = 1$, respectively. The size of each marker is proportional to the magnitude of strain.

To compare the dominance of the various strain components when approaching failure, we show the magnitude of the mean incremental contraction, dilation and shear strain throughout loading in each experiment. We divide each incremental component by the amount of macroscopic axial contraction, $\Delta\varepsilon_{zz}$, that occurs between pairs of tomograms used in the DVC calculations to ensure that the magnitude of $\Delta\varepsilon_{zz}$ does not strongly influence the relative magnitudes of the means. Figure 7 thus shows the mean of each component divided by $\Delta\varepsilon_{zz}$, $|mean/\Delta\varepsilon_{zz}|$. For the sandstone experiments, the mean of the incremental strains indicates that the micromechanisms guiding deformation shift from contraction to dilation post yield (Adamswiller) or near yield (Bentheim). In contrast, the five cores of Anstrude limestone show three different behaviors. The dominant failure mechanism guiding Anstrude 2 is contraction. For Anstrude 3 and 4, contraction dominates deformation until close to failure, when dilation dominates. For Anstrude 5 and 6, dilation dominates deformation throughout the experiment.

For Adamswiller sandstone, the dominant mechanism guiding deformation shifts from contraction to dilation at $\varepsilon_{zz}/\varepsilon_{zz}^{f} = 0.7$ (post yield), and continues until failure (Figure 7a). For Bentheim sandstone (Figure 7b), the dilatative incremental strain accelerates between the yield point and failure. At $\varepsilon_{zz}/\varepsilon_{zz}^{f} = 0.9$ near failure, the shear strain dominates contraction. For Anstrude 2, all three components of incremental strain show a continuous increase up to failure (Figure 7c). Contraction dominates throughout loading. Deformation in Anstrude 3 and 4 (Figures 7d and 7e) is dominated by contraction until $\varepsilon_{zz}/\varepsilon_{zz}^{f} = 0.9$, when dilation exceeds contraction. For Anstrude 4, the mean values of all the three incremental strain components show a peak at $\varepsilon_{zz}/\varepsilon_{zz}^{f} = 0.7$ (Figure 7e). Similarly, in Anstrude 5, a peak in strain occurs at $\varepsilon_{zz}/\varepsilon_{zz}^{f} = 0.75$ (Figure 7f), as dilation dominates deformation. In general, three of the limestone experiments are dominated by contraction throughout the majority of the loading (Anstrude 2, 3, 4), while two are

dominated by dilation (Anstrude 5, 6). Both sandstones are dominated by dilation following yielding and near failure.

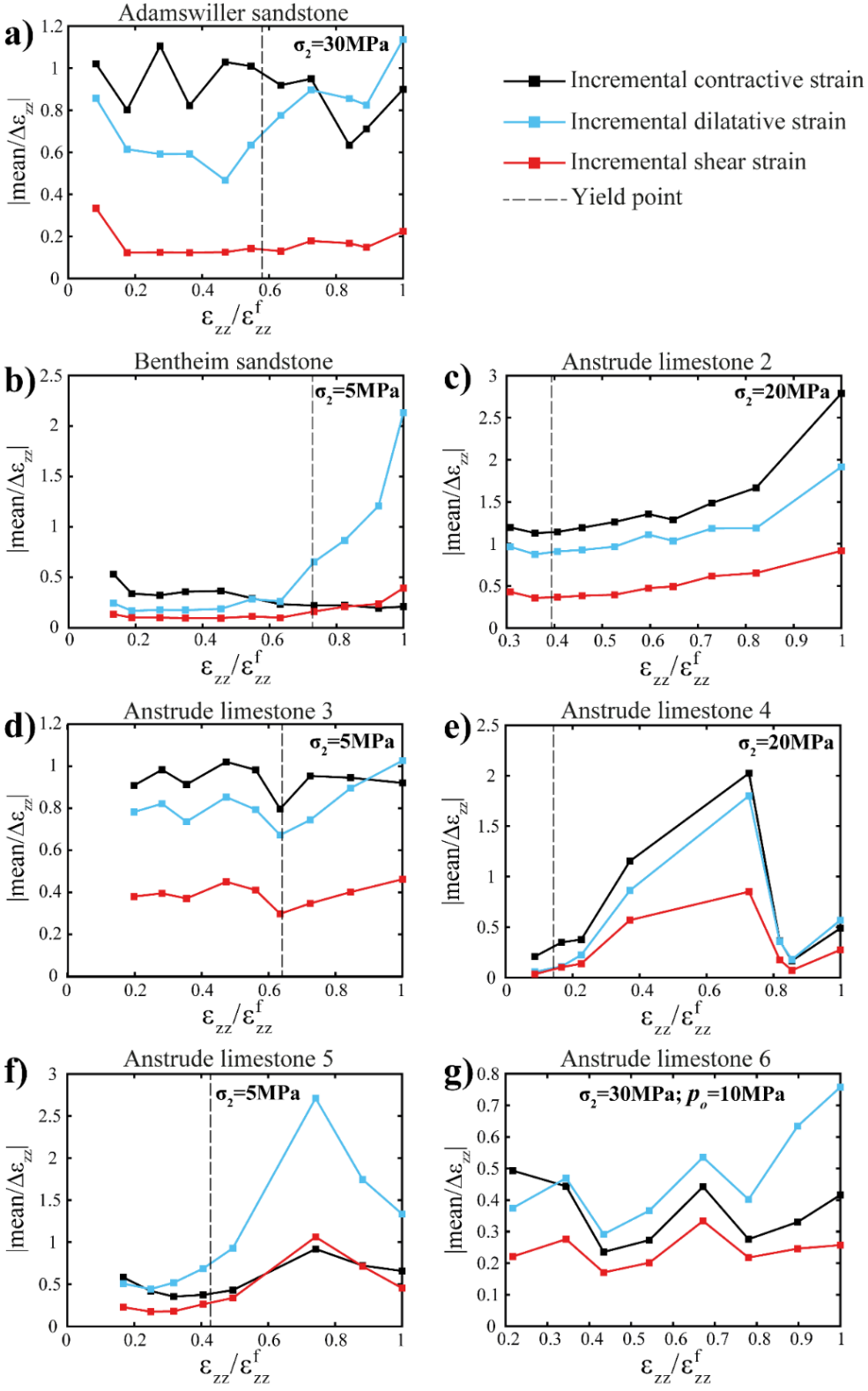

Figure 7. a-g) Mean of the absolute values of the incremental strain components. Mean value of each component is normalized by the amount of macroscopic axial contraction, $\Delta\varepsilon_{zz}$, that occurs between scans used in the DVC calculations.

3.4. Linking porosity variation with incremental strain evolution

Our X-ray tomography data enable tracking the porosity and local strain field simultaneously. In order to characterize the strain localization mechanisms guiding the porosity evolution, we compare the bulk porosity calculated from the tomograms and the local strain components calculated from DVC. In Figure 8, we show the cumulative means of respective strain components as a function of scaled axial strain, $\varepsilon_{zz}/\varepsilon_{zz}^{f}$, for all experiments, $\sum|mean/\Delta\varepsilon_{zz}|$. The mean value of porosity is obtained from image segmentation at every step of axial step increase, as described in Section 2.2.

For all the experiments except the Bentheim sandstone, the mean porosity decreases while the cumulative incremental strain components increase towards failure (Figure 8). In the Adamswiller sandstone experiment, the mean porosity decreases in steps and then falls quickly following the yield point, at $\varepsilon_{zz}/\varepsilon_{zz}^{f} = 0.75$ (Figure 8a). All the strain components show an approximately linear increasing trend, indicating constant rates of strain accumulation. The contraction tends to increase the fastest, while the dilation and strain components increase at slower rates. This dominance of local contraction agrees with the decreasing porosity with loading. In the Bentheim sandstone experiment (Figure 8b), the mean porosity decreases non-linearly and then stays at similar levels near the yield point. Then, above $\varepsilon_{zz}/\varepsilon_{zz}^{f} = 0.8$, the porosity increases rapidly up to failure. These trends in the porosity agree with the evolution of the strain fields: the dilation remains below the contraction until $\varepsilon_{zz}/\varepsilon_{zz}^{f} = 0.8$ and then the dilation increases rapidly preceding failure (Figure 8). The samples of Anstrude limestone 2, 3, and 4 (Figures 8c-e) show similar trends in the evolution of cumulative strain components. All of the three cumulative strain components increase non-linearly. Contraction dominates deformation rather than dilation or shear strain. Consistent with these strain evolutions, porosity decreases with loading in all three experiments.

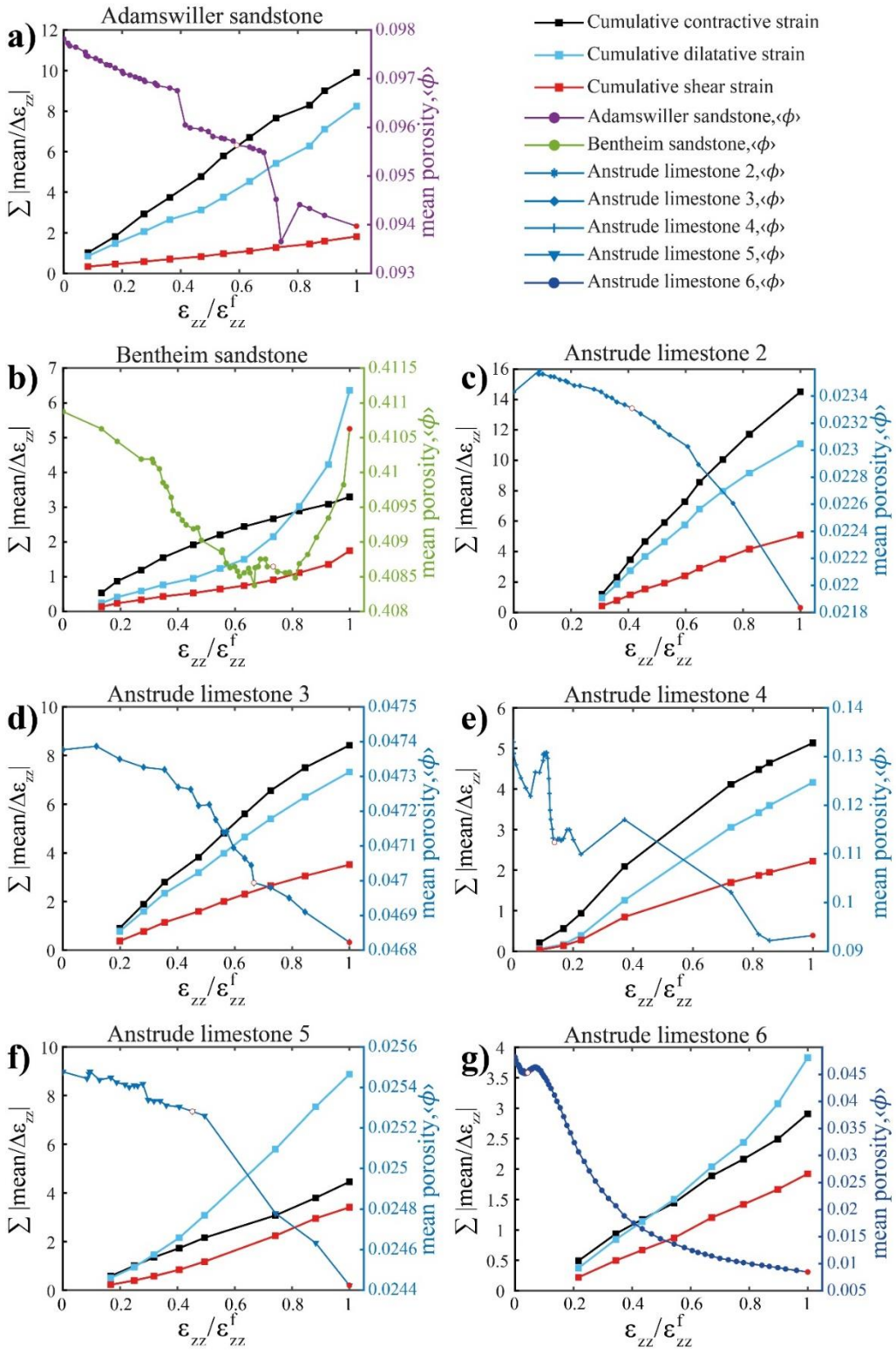

Figure 8. Evolution of the cumulative local strain components and porosity. The cumulative local strain components are shown as the sum of the $|\text{mean}/\Delta\varepsilon_{zz}|$ from previous DVC calculations, i.e., the cumulative

mean. In general, porosity decreases as the magnitudes of the strain components increase. The exception to this trend is the Bentheim sandstone experiment, which hosts an increase of porosity (i.e. dilation) from the yield point until failure.

The relationships between the porosity and cumulative strain evolutions differ between the Anstrude limestone 5 and 6 (Figure 8f-g) and the other Anstrude limestone experiments. The porosity of the Anstrude limestone 5 and 6 decrease with loading, similar to the other experiments. However, these experiments differ from the others because the mean cumulative dilation tends to be slightly higher than the mean cumulative contraction throughout loading in these experiments. While the decreasing porosity indicates that contraction should dominate deformation, the DVC data indicate that dilation barely dominates deformation in these two limestone experiments. Figure S4 provides a summary of evolutions of the differential stress, mean porosity, and cumulative and incremental strain means for three different rock types subjected to low and high confinement.

3.5. Post failure microstructure

In order to provide further insights into the deformation mechanisms operating within these porous rocks, we imaged the microstructure of two samples post failure using scanning electron microscopy. Electron backscatter images of Adamswiller sandstone (Figure 9) and Anstrude limestone 4 (Figure 10) show compaction shear bands, with pore collapse, grain crushing and formation of transgranular microfractures.

In Adamswiller sandstone, damage localization occurs along compaction shear bands located near one end of the sample. These regions (Figures 9b, 9c) host grain comminution and pore space reduction. This observation is in agreement with the observed overall reduction of total porosity (Figure 4) and dominance of compaction rather than dilation (Figure 8). The total porosity decreases towards failure. The cumulative mean of the contractive strain (Figure 8a) is higher than cumulative dilation and shear strains throughout the experiment. The porosity evolution, strain fields, and microstructures indicate that this sandstone sample failed via porosity reduction and diffuse compaction at lower differential stress, and then more localized compaction and shear with grain crushing, grain comminution, and transgranular fractures at higher differential stress.

All the limestone samples show regions of localization in the form of shear bands characterized by significant amount of grain crushing leading to intense fragmentation of the rock. When samples were unloaded from the triaxial rig, regions of powered rock formed cavities, which were filled by epoxy during the impregnation step, as shown in Figure S6. Shear zones display complex features that are reminiscent of various microscale mechanisms. Dilatantional microfractures originated from macro pores and propagated either along grain boundaries as intergranular microfractures or coalesced with transgranular fractures within ooids and grains. Shear zone of Anstrude 2 (Figure S5) contains microfractures that are oriented at $> 30^o$ to σ_1. Also, the multiple fracture strands within the shear band propagated across the sample length spanning the entire rock volume. Regions outside the shear zone are relatively intact (right section of Figure S6-a, top section of Figure 10a) and host transgranular fractures (top section of Figure 10a). In the sample Anstrude 5 (Figure S6), a fault oriented $\sim 30^o$ to σ_1 separates the highly crushed shear zone and the intact rock matrix. Shear zones in all the limestones host some intact ooids with transgranular microfractures.

For the Anstrude limestone 4 sample (Figure 10), compaction is accommodated by grain size reduction and the formation of transgranular fractures (Figures 10a, 10b). Our results show that the overall porosity decreased while contraction increased in this experiment (Figures 8c, 8d and 8e). The formation and opening of micro fractures may prompt locally high dilation. In samples Anstrude 5 and 6 (Figures 8f and 8g), dilation dominates deformation at failure, consistent with the formation of transgranular microfractures. The 3D tomograms of Anstrude limestone 6 also show evidence of transgranular fractures (Figure 3f).

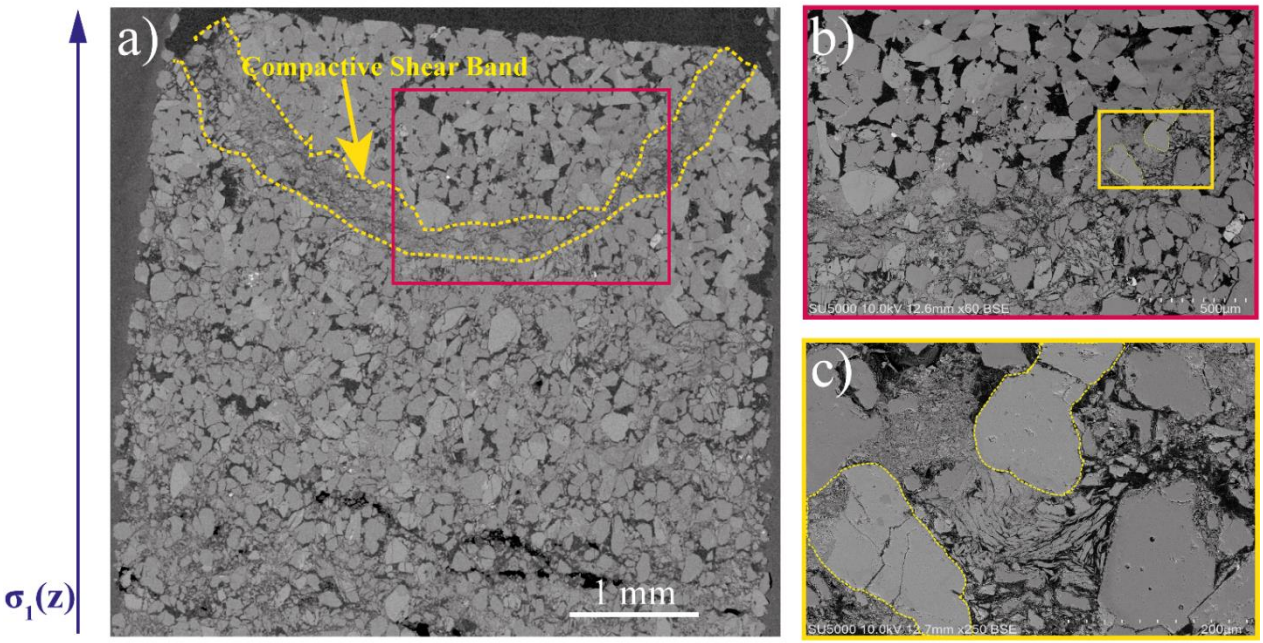

Figure 9. Scanning electron micrograph of a thin section of the Adamswiller sandstone sample after failure. a) Compaction shear bands. b) Close up of area in (a). c) Close up of area in (b). Grains appear comminuted and crushed. Development of intra granular fractures is evident in (c).

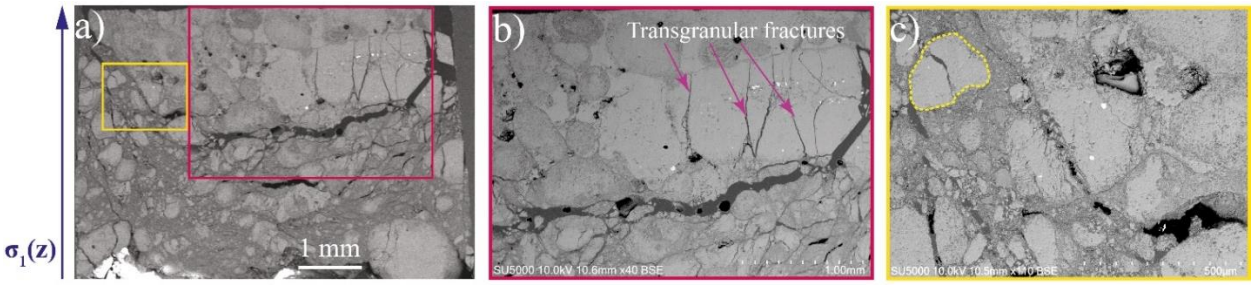

Figure 10. Scanning electron micrograph of sample Anstrude limestone 4 after failure. b) Close up of area in (a). c) Close up of area in (b). Some grains appear crushed and others host transgranular fractures parallel to σ_1.

4. Discussion

Our results present a detailed analysis of strain localization observed in three kinds of porous rocks deformed in the brittle regime under in-situ conditions with dynamic synchrotron X-ray tomography. For the first time, the 4D evolution of incremental strain components of dilation,

contraction and shear is compared to the evolutions of the bulk porosity and microstructure. In the brittle regime, porous rocks subjected to compressive loading may fail by shear localization, compaction localization, or cataclastic flow (e.g. Paterson & Wong, 2005). Dilatancy is a precursory phenomenon for the inception of shear localization observed at low confining stresses (Brace, 1978; Wong & Baud 2012; Renard et al., 2019a, 2019b). A recent machine learning analysis identified dilation as a key predictor of the proximity of macroscopic failure (McBeck et al., 2020). Conversely, localized compaction (with localized planes at $\sim 90^o$ to σ_1) is observed at higher confining stresses, resulting in cataclasis (Olsson, 1999; Klein et al., 2001). At intermediate confining stresses, a transitional regime occurs with complex localized features such as conjugate shear bands (Klein et al., 2001; Paterson & Wong, 2005).

Strain localization mechanisms are influenced by several parameters such as porosity, grain size distribution, pore fluid and confining pressure (Scott & Nielsen, 1991; Wong et al., 1997; Baud et al., 2000). Our study involves a broad range of values for these parameters; 1) three rock types with different grain size distributions, 2) variations in porosity, 3) variations in pore fluid for one of the Anstrude limestone experiments, and 4) confining pressures of 5-30 MPa.

DVC reveals that all of the rock cores attained brittle failure by shear localization. The regions that host the largest local strains align at an angle close to 30^o to the maximum stress direction at the onset of failure. We are using a qualitative visual assessment to describe localization, rather than a quantitative statistical metric. We did not perform any quantitative measurement on angles of localized zones in both tomograms and 3D strain components.

For the Bentheim sandstone, the left-lateral shear strain show this alignment (Figure 5 and Movie V2), whereas the dilatative strain in Anstrude limestone #5 shows this alignment (Movie V6). For Anstrude limestone #6, conjugate shear bands are observed within all of the strain components (Figure 6 and Movie V7). SEM images reveal grain crushing and comminution, and transgranular fractures in post-failure microstructures (Figures 9, 10, S5, S6). However, the SEM images do not show large amounts of cataclasis in any of the rock cores. Thus, the porous rocks in our study show micromechanisms corresponding to the conditions of low/intermediate confinement, resulting in either localization along a single shear band or the formation of conjugate shear bands.

4.1. Mechanisms of brittle deformation in Adamswiller and Bentheim sandstones

4.1.1 Strain localization and its link to bulk porosity variations

Strain localization in sandstones at low confinement (Bentheim sandstone) proceeds by accumulation of dilatative strain, which results in increasing pore volume. Conversely, at increased confinement (Adamswiller sandstone) accumulation of contractive strain guides the strain localization that results in porosity reduction. Both the sandstones in our study have nearly equal porosities, Bentheim sandstone (22%) and Adamswiller sandstone (23%). They are subjected to low/intermediate confinement (5-30MPa) and deformed through shear localization. Sandstones, deformed under dry conditions in the present study, have failed after a period of strain hardening (Figure 1). The same behavior was observed in discrete element models for porous rocks presented by Wang et al., (2008). The observed relation between strain localization and porosity variation is a step further to the previous studies on Adamswiller sandstone (Wong et al., 1997; Zhu et al., 1997) and Bentheim sandstone (Vajdova et al., 2004). These studies have shown that the evolution of porosity and stress state are coupled; porosity controls strain localization and subsequently the failure mode. But, through our current study, we can separate the total accumulated strain into dilatative, contractive and shear (left-lateral and right-lateral) components unlike previous experiments. Independent of the initial porosity variations, the DVC reveals that deformation occurs through the interplay of dilation, contraction and shear (Figures 7, 8). Deformation in Adamswiller sandstone is dominated by contractive strain (Figures 7a, 8a) and reduction of porosity (Figures 4b, 8a). Dilation increases near yield, at 0.75% of normalized macroscopic axial strain, becoming dominant over the contractive strain when failure is approached (Figure 7a). This strain evolution is accompanied by a brief increase in mean porosity (Figure 8a). Porosity in Bentheim sandstone decreased during the initial phase of deformation, consistent with the observed dominance of contractive strain. From the yield point and until failure, dilation dominates (Figures 7b, 8b), and porosity increases (Figures 4b, 8b).

In our sandstones with porosity 22-23%, the SEM images show the development of compacted zones of localization characterized by grain crushing and transgranular fractures, and

the DVC data indicate that this development produced local dilation (Figure 9). Thus, the increase of dilatative strain corresponds to the accumulation of transgranular fractures, along with collapse of the pore space. These processes control the initiation of shear localization near macroscopic failure. Therefore, we conclude that the variations in dilatative strain components strongly guide the strain localization in both sandstones in the present study. The onset of strain localization (visual observation of tomograms and post-failure SEM images) in sandstones occurred at the onset of failure, which corresponds to the peak stress. Dilation increased significantly in magnitude near macroscopic yield (Figure 7). In Bentheim sandstone, deformation is dominated by dilation and further characterized by the porosity increase. In Adamswiller sandstone, although dilation strongly influence the observed strain localization, the dominant mechanism of failure is compaction accompanied by porosity reduction.

4.1.2 Micromechanisms of strain localization

Microscale mechanisms of grain crushing and pore space dilation produce local dilatation and increase in porosity, when subjected to low confinement (Bentheim sandstone). Mechanism of pore collapse does not compensate for local dilation, hence the evolution of dilatative strain. At intermediate confinement (Adamswiller sandstone), pore collapse with extensive grain crushing results in porosity decrease, which increased contractive strain accumulation. To elucidate the microscale mechanisms resulting in strain localization in Adamswiller and Bentheim sandstones (22-23%), we compare the results of present study with experiments on Fontainebleau sandstone done in our group (Renard et al., 2019a). These Fontainebleau sandstones were deformed in the Hades rig, at confining pressures of 10-20 MPa, and we employed the same segmentation procedure and computational analysis as the present study. The porosity of Fontainebleau sandstone was measured to be in the range of 5.5-7%, which is lower than the Adamswiller and Bentheim sandstones (22-23%). Profiles of the incremental strain components of Bentheim sandstone show similarities to that of Fontainebleau sandstone (Figure 7 here, and Figure 11 in Renard et al., 2019a). In both experiments, the dilatative incremental strain increases near yield. However, the corresponding microstructural changes in each rock differ from each other. In Fontainebleau, increasing dilatative strain signifies nucleation and coalescence of microfractures, while in Bentheim, it is linked to dilation of pore space.

Sandstones of lower porosities (5.5-7%; Renard et al., 2019a) have higher amounts of cementation between the grains and nucleation of damage involve the following microscale mechanisms. (i) Pore-emanated mode I cracks (Sammis and Ashby, 1986)) initiated along grain boundaries. (ii) Following the development of intergranular fractures, transgranular fracturing occurred at higher differential stresses, as explained by the Hertzian fracture concept (Johnson 1982). (iii) Strain Localization occurred by the coalescence of these microfractures either at failure (samples F1 and F3 in Renard et al., 2019) or at yield (sample F2 in Renard et al., 2019) that grew as core-spanning fault at failure. On the other hand, in Adamswiller and Bentheim sandstones of relatively higher porosities (22-23%) in the current study, failure is dominated by pore collapse and grain crushing (resulting in the reduction of grain size) via the spread of transgranular fractures (Figure 9). In Bentheim sandstone subjected low confinement (5 MPa), compaction is observed in the initial stages of deformation (contractive strain in Figures 7b, 8b; porosity in Figures 4b, 8b, S1), which corresponds to the collapse of pore space. Later, near yield, an increase in dilatative strain is linked with an increase in bulk porosity (Figure 8b). This phase can be attributed to the initiation of intergranular and transgranular microfractures, resulting in grain crushing and sliding along the shear fault. At failure, the microstructure evolved into a localized shear zone with grain comminution. The post-failure tomograms show significant macroscopic contraction along the axial direction and dilation along the radial direction (e.g. Figure 2a). On the contrary, Adamswiller sandstone, which is subjected to relatively high confinement (30 MPa), the dominant contractive incremental strain and the bulk porosity reduction suggest that the dominant deformation mechanism is pore collapse. The increase of dilatative strain near the yield suggest considerable amounts of fracture opening, and perhaps grain crushing via transgranular fracture development. Transgranular fractures are signatures of grain crushing and are observed in post-failure microstructure (Figure 9) of Adamswiller sandstone. This grain crushing and collapse of pore space resulted in the localization of a compaction shear band at failure.

Thus, we infer that the microstructural mechanisms guiding strain localization in both Adamswiller and Bentheim sandstones were pore collapse and grain crushing. These micromechanical processes were observed to play a crucial role in the development of shear deformation bands in other porous sandstones (Menéndez et al., 1996; Mair et al., 2000) as well. A discrete element model for damage localization in porous rock captures the microstructural

changes during brittle faulting (Wang et al., 2008; McBeck et al., 2019) similar to those observed in our sandstone experiments. This model explains the initiation of intergranular and transgranular damage leading to grain crushing and pore collapse as possible microscopic mechanisms for strain localization. The rock matrix is modeled as an assemblage of super-particles made up of clusters of bonded smaller particles. The bond strength among the small particles is larger than at the contact between super-particles. The super-particles represent the grains of the rocks and the contacts between super-particles represent grain contacts. Thus, transgranular damage develop within a grain if loading continues to increase after intergranular contacts have ruptured. Transgranular damage produces grain crushing and the relative movements of the smaller particles contribute to pore collapse. A conceptual model describes the microstructural changes associated with pore collapse and grain crushing observed in Adamswiller and Bentheim sandstones (Fortin et al., 2009). In order for a pore to collapse, grains and parts of the cement need to be broken. Grain breakage occurs by transgranular microfractures and shear sliding along them. The collapse of a pore occurs through a mixed mode that involve both grain breakage (as mode II cracks, a shear type event) and the breakage of the cement. These numerical and conceptual models elucidate the mechanisms of pore collapse and grain crushing observed in both sandstones in the present study.

4.2 Mechanisms of brittle deformation in Anstrude limestone

4.2.1 Strain localization and its link to porosity variations

Anstrude limestone rock cores considered in this study have micro-computed tomography porosities varying between 3.5-15.6%. These core samples contain ooids and shell fragments with grain size varying between $100 - 1000\,\mu m$ (Lion et al., 2004), making the microstructure complex compared to the sandstones. During deformation towards brittle failure, we observe macroscopic sample compaction. Nevertheless, the tomograms do not provide clear indicators of the microstructural features of strain localization. One explanation is that grain crushing tends to homogenize the spatial distribution of X-ray attenuation (Otani et al. 2005), and strain localization mechanisms produce relative dispersion in the X-ray intensity, masking the microstructural features for visual observations. However, the SEM images and DVC analysis on the digital

tomograms provide further facts on the strain localization mechanisms guiding failure (Figures 10, S5, S6). These results show that damage has localized into shear bands.

Localization of strain in Anstrude limestone (20% actual porosity) occurs through an interplay of compaction, dilation and shear, as observed in the 3D strain distributions (Movies V3-V7, Figures 6, 7). This observation is in contrast to sandstones (Movies V1 & V2, Figures 5, 7), where either dilation of compaction is dominant and shear strain contributions are very low. Independent of dominant strain localization mechanisms, in each of the five experiments, porosity reduction (Figure 4b) resulted in overall macroscopic sample contraction (see tomograms at failure in Figures 2 & 3). However, trends in porosity are dependent on applied confinement. Under low confinement (5 MPa), porosity as measured in the microtomography data shows a nearly linear decreasing trend until localization occurred near failure. Whereas under relatively higher confinement (20-30 MPa), porosity decreased rapidly after the yield stress (Figure 4b), associated with strain localization post yield.

At the onset of strain localization, DVC data shows the formation of compacting shear bands oriented at an oblique angle to σ_1. However, the angle of these deformation bands vary with applied confinement. At a higher confinement (Anstrude #2, #4 and #6, $\sigma_2 - p_0 = 20\text{MPa}$) compacting shear bands are resulting from accumulation of dominant contractive strain and have a higher angle than those deformed at lower confinement (Anstrude #3 and #5, $\sigma_2 - p_0 = 5\text{MPa}$), where localization is dominated by dilatative strain component. This is in agreement with the study of Wong & Baud (2012), who have shown that the angle between shear bands and the maximum compression direction is higher at intermediate confining pressures compared to those at low confinement. However, we provide an explanation with the corresponding dominant strain localization mechanism.

Characteristics of deformation bands and their orientation is strongly dependent on the initial porosity (Baud et al., 2017a). A complex pore network defines the microstructure of limestone, characterized by a bimodal distribution of pores. As a result, deformation bands in limestones were classified based on their initial porosities and a range of confining pressures (Olsson & Holcomb, 2000;Vajdova et al., 2010; Ji et al., 2015; Baud et al., 2017a, 2017b; Huang et al., 2019). Our study contributes to this by understanding deformation bands in Anstrude

limestone with an initial porosity of 20%. Limestones with porosities lower than or comparable to 20% show strain localization similar to our Anstrude samples. Compaction shear bands are observed in the brittle regime for Leitha limestone of 21% porosity (Baud et al., 2017a) and localization occurs through coalescence of microfractures growing sub-parallel to σ_1 such as, for example in the Tavel limestone with 10-14% porosity (Vajdova et al., 2010) and Figures 10 and S5 in the present article. Leitha limestone with 31% porosity (Baud et al., 2017a) to 26% porosity (Huang et al., 2019) and Saint-Maximin limestone with 37% porosity (Baud et al., 2017b) have porosities higher than Anstrude limestone (present study) and show strain localization through formation of compaction bands perpendicular to σ_1. In one study, they are discrete compaction bands (Huang et al., 2019) while in another, the width of the compaction bands grow (thickening) in the direction of σ_1(Olsson & Holcomb, 2000). Majella limestone with porosity of 32-33% (Ji et al., 2015) at low confinement shows compacting shear bands but, they are at high-angle compared to Anstrude (post-failure SEM images of Anstrude 2 in Figure S5).

4.2.2 Micromechanisms of strain localization

Owing to the complexity in the pore geometry (Choquette and Pray 1970; Folk 1980), porosity in carbonate rocks may host a bimodal distribution. The rocks may contain large macropores and numerous micropores (Lion et al., 2004) that cannot be resolved under optical microscope (Pittman 1971). Ji et al. (2015) have shown a bimodal distribution of pore sizes using microtomography data of Majella limestone. SEM images of post-failure microstructure show evidence for such bimodal porosity in our Anstrude limestone. The macroporosity is the visible pore space with large voids within the deformed rock matrix. The microporosity occurs in 1) ooids/grains (speckle pattern in Figure S5-c), 2) cemented regions in Figure 10b and, 10c) and in the periphery of macropores (fractures in Figure S6). This observation is supported by the microstructure study of Anstrude limestone by Lion et al. (2004). Thus, the presence of macropores and micropores gives rise to a complex pore geometry, which may have a strong influence in defining microstructural mechanisms of strain localization in Anstrude limestone.

Microstructural features associated with strain localization in Anstrude limestone depend on the confining pressure. Experiments performed with higher confinement have shear zones oriented $> 30^o$ to σ_1 (Figure S5), while those at lower confinement are $\sim 30^o$ to σ_1 (Figure S6).

The experiment Anstrude 5, with a confining pressure of 5 MPa (Figure S6), hosted grain crushing, pore collapse and intense comminution within the shear band. In contrast, experiments Anstrude 2 and 4, with 20 MPa confining stress (Figures S5 and 10 respectively) additionally hosted dilatant fracture networks within the shear band.

Possible microscale mechanisms giving rise to strain localization in Anstrude limestone are 1) pore collapse, 2) grain crushing with cataclasis and 3) pore-emanating fractures. Zones of shear localization show pore collapse and intense cataclasis in the SEM images of Anstrude limestone subjected to a low confinement (5 MPa, Figure S6). Shear bands hosting dilatant fracture networks at higher confinement (20 MPa, Figure S6) may show the signatures of pore-eminent fractures. During mechanical compaction, anisotropy in the spatial distribution of damage around the macropores (Vajdova et al., 2004) results in pore collapse (Zhu et al., 2010). In previous studies on triaxial deformation in Tavel limestone (Vajdova et al., 2010), brittle failure was primarily observed to be associated with cataclastic damage. An event of cataclastic pore collapse is highlighted in SEM of Anstrude 5 (Figure S6), which is subjected to low confinement (5 MPa). A collapsed macropore is surrounded by an asymmetrical fracture network and result in dispersed damage within the shear zone. In contrast, in experiments Anstrude 2 and 4, performed with 20 MPa confinement (Figures S5 and 10, respectively), the shear zones host dilatant fractures. In our experiments, inelastic compaction of the pore space resulted in the nucleation of dilatant fractures localized 1) at the interface of a macropore and rock (as shown in the post-failure SEM microstructures), and 2) within the micropores (transgranular fractures). Coalescence and propagation of dilatant fractures originating from macro- and micropores as pore-eminent cracks, result in the microstructural mechanism of grain crushing.

The pore-emanated crack model proposed by Sammis and Ashby (1986) accounts for the evolution of such dilatant microfractures in the brittle failure regime. The model considers a 2D elastic medium permeated by circular pores of uniform radius. When subjected to loading, cracks emanate parallel to σ_1, at the periphery of circular pores. As the applied differential stress increases, stress at the crack tips increases, and then reaches a critical value, which results in their propagation. The interaction of these cracks induce an additional tensile stress and ultimately their coalescence with neighboring cracks leads to an instability that creates a macroscopic stress drop. This model is defined for conditions of unconfined compression (Wong, 1990). Application of

confinement of only 1 MPa can inhibit the localization of brittle failure (Sammis & Ashby, 1986). However, in our experiments and those of Vajdova et al. (2004), brittle faulting occurs for confining pressures up to 30 MPa. We observed transgranular fractures aligned sub-parallel to σ_1 in relatively intact regions of the post-failure microstructure (Figure 10), consistent with the characteristics expected in the pore-emanated crack model discussed in Sammis & Ashby (1986) and Vajdova et al. (2010).

5. Conclusion

Here, we present a comparative study of inelastic deformation and strain localization in Adamswiller sandstone (23% porosity), Bentheim sandstone (22% porosity) and Anstrude limestone (20% porosity), three kinds of reservoir rocks of comparable porosities at conditions of low and intermediate confining pressures. We show that the 4D evolution of the strain components of dilation, contraction and shear, are closely linked to variations in the bulk porosity and microstructure. Although all of the rock types experience strain localization via shear bands development, the deformation behavior differs depending on the microstructure of the rock, complexity in the pore geometry and applied confinement. These sandstones are characterized by narrow grain size distributions and homogeneous pore geometry. When subjected to low confinement (Bentheim sandstone experiment), deformation is dominated by dilatative strain and an increase in porosity. Grain crushing and pore space dilation produces this local dilatation and increase in porosity. At intermediate confinement (Adamswiller sandstone), deformation proceeds by the accumulation of compaction strain and decreasing porosity. Pore collapse with extensive grain crushing produces local compaction and porosity decrease. Anstrude limestone has a complex microstructure with ooids and bimodal porosity distribution. Due to this bimodal porosity, strain localization mechanisms produce relative dispersion in the X-ray intensity and the formation of deformation bands are hardly discernable from tomograms. Hence, DVC is an effective tool in quantifying and visually mapping strain localization that is not detectable in the tomograms. Under low confinement (Anstrude sample 5), accumulated dilatative strain dominates during the triaxial deformation and porosity decreases with axial strain. At intermediate confinement (Anstrude samples 2, 4), compaction dominates and porosity decreases with axial strain. Presence of pore fluid results in dominant dilation (Anstrude 6). The microstructural deformation mechanisms in Anstrude include (i) pore collapse, (ii) pore-emanated fracturing that

initiate at the periphery of the macropores and propagate as transgranular fractures within the shear zones, and (iii) cataclasis. Under low confinement, shear zones are defined by extended cataclasis with pervasive damage, whereas at intermediate confinement, they are characterized by dilatant fractures that extend across the sample. The experiment with pore fluid and intermediate confinement, sample Anstrude 6, shows localization of conjugate shear bands. Sandstones and Anstrude limestone samples under low confinement are characterized by shorter yielding phases (in terms of axial strain) and the localization of strain is observed at the onset of failure, near the peak stress. Conversely, limestones at intermediate confinement are characterized by long yielding phases and strain localization occurred following yield and before macroscopic failure. Our results demonstrate that dynamic X-ray tomography experiments coupled with digital volume correlation analysis and SEM observations provide invaluable quantitative information about the deformation mechanisms of porous reservoir rocks.

Declarations:

This research does not raise ethical issues. The authors declare no conflict of interest. This study received funding from the Norwegian Research Council (project HADES, grant 250661). Beamtime was allocated at the European Synchrotron Radiation Facility (Long Term Proposal ES-295). Data storage was provided by UNINETT Sigma2 - the National Infrastructure for High Performance Computing and Data Storage in Norway (project NS9073K). The X-ray tomography data (series of 3D volumes, 16 bytes gray scale) supporting the conclusions are available publicly at https://doi.org/10.11582/2020.00058

Acknowledgements:

The deformation apparatus was built by Sanchez Technologies. Elodie Boller, Paul Tafforeau, and Alexander Rack provided advices on the design of the tomography setup.

6. References

Aydin A. (1978) Small Faults Formed as Deformation Bands in Sandstone. In: Byerlee J.D., Wyss M. (eds) *Rock Friction and Earthquake Prediction*. Contributions to Current Research in Geophysics (CCRG), vol 6. Birkhäuser, Basel. https://doi.org/10.1007/978-3-0348-7182-2_22.

Aydin, A., & Johnson, A. M. (1978). Development of faults as zones of deformation bands and as slip surfaces in sandstone. *Pure and Applied Geophysics*, 116(4-5), 931-942.

Ballas, G., Soliva, R., Sizun, J. P., Fossen, H., Benedicto, A., & Skurtveit, E. (2013). Shear-enhanced compaction bands formed at shallow burial conditions; implications for fluid flow (Provence, France). *Journal of Structural Geology*, 47, 3-15.

Baud, P., Schubnel, A., & Wong, T. F. (2000). Dilatancy, compaction, and failure mode in Solnhofen limestone. *Journal of Geophysical Research: Solid Earth*, 105(B8), 19289-19303.

Baud, P., Klein, E., & Wong, T. F. (2004). Compaction localization in porous sandstones: spatial evolution of damage and acoustic emission activity. *Journal of Structural Geology*, 26(4), 603-624.

Baud, P., Exner, U., Lommatzsch, M., Reuschlé, T., & Wong, T. F. (2017a). Mechanical behavior, failure mode, and transport properties in a porous carbonate. *Journal of Geophysical Research: Solid Earth*, 122(9), 7363-7387.

Baud, P., Schubnel, A., Heap, M., & Rolland, A. (2017b). Inelastic compaction in high-porosity limestone monitored using acoustic emissions. *Journal of Geophysical Research: Solid Earth*, 122(12), 9989– 10,008. https://doi.org/10.1002/2017JB014627.

Baud, P., Hall, S., Ji, Y., Wong, T. F., & Heap, M. J. (2017c). The Brittle-Ductile Transition in Porous Limestone Imaged by X-Ray Computed Tomography and Digital Image Correlation. In *Poromechanics VI, Proceedings of the Sixth Biot Conference on Poromechanics* (pp. 1782-1788).

Bjørlykke, K. (1993). Fluid flow in sedimentary basins. *Sedimentary Geology*, 86(1-2), 137-158.

Brace, W. F. (1978). Volume changes during fracture and frictional sliding: A review. *Pure and Applied Geophysics*, 116(4-5), 603-614.

Brantut, N., Heap, M. J., Baud, P., & Meredith, P. G. (2014). Mechanisms of time-dependent deformation in porous limestone. *Journal of Geophysical Research: Solid Earth*, 119(7), 5444-5463.

Buades, A., Coll, B., & Morel, J. M. (2005, June). A non-local algorithm for image denoising. In Computer Society Conference on Computer Vision and Pattern Recognition, 2005, *IEEE* vol. 2, pp. 60-65.

Choquette, P. W., & Pray, L. C. (1970). Geologic nomenclature and classification of porosity in sedimentary carbonates. *AAPG bulletin*, 54(2), 207-250.

Cilona, A., Baud, P., Tondi, E., Agosta, F., Vinciguerra, S., Rustichelli, A., & Spiers, C. J. (2012). Deformation bands in porous carbonate grainstones: Field and laboratory observations. *Journal of Structural Geology*, 45, 137-157.

Cilona, A., Faulkner, D. R., Tondi, E., Agosta, F., Mancini, L., Rustichelli, A.,.Baud, P., & Vinciguerra, S. (2014). The effects of rock heterogeneity on compaction localization in porous carbonates. *Journal of Structural Geology*, 67, 75-93.

Croize, D., Renard, F., & Gratier, J. P. (2013). Compaction and porosity reduction in carbonates: A review of observations, theory, and experiments. In *Advances in Geophysics* (Vol. 54, pp. 181-238). Elsevier.

Dansereau, V., Démery, V., Berthier, E., Weiss, J., & Ponson, L. (2019). Collective damage growth controls fault orientation in quasibrittle compressive failure. *Physical Review Letters*, 122(8), 085501.

Folk, R. L. (1980). *Petrology of sedimentary rocks*. Hemphill publishing company.

Fortin, J., Stanchits, S., Dresen, G., & Gueguen, Y. (2009). Acoustic emissions monitoring during inelastic deformation of porous sandstone: comparison of three modes of deformation. *Pure and Applied Geophysics*, 166(5-7), 823-841.

Fossen, H., Schultz, R. A., Shipton, Z. K., & Mair, K. (2007). Deformation bands in sandstone: a review. *Journal of the Geological Society*, 164(4), 755-769.

Fossen, H., Schultz, R. A., & Torabi, A. (2011). Conditions and implications for compaction band formation in the Navajo Sandstone, Utah. Journal of Structural Geology, 33(10), 1477-1490.

Fossen, H., Soliva, R., Ballas, G., Trzaskos, B., Cavalcante, C., & Schultz, R. A. (2018). A review of deformation bands in reservoir sandstones: geometries, mechanisms and distribution. *Geological Society, London, Special Publications*, 459(1), 9-33.

Girard, L., Amitrano, D., & Weiss, J. (2010). Failure as a critical phenomenon in a progressive damage model. *Journal of Statistical Mechanics: Theory and Experiment*, 2010(01), P01013.

Heap, M. J., Kushnir, A. R., Gilg, H. A., Wadsworth, F. B., Reuschlé, T., & Baud, P. (2017). Microstructural and petrophysical properties of the Permo-Triassic sandstones (Buntsandstein) from the Soultz-sous-Forêts geothermal site (France). *Geothermal Energy*, 5(1), 26, https://doi.org/10.1186/s40517-017-0085-9.

Huang, L., Baud, P., Cordonnier, B., Renard, F., Liu, L., & Wong, T. F. (2019). Synchrotron X-ray imaging in 4D: Multiscale failure and compaction localization in triaxially compressed porous limestone. *Earth and Planetary Science Letters*, 528, 115831.

Ji, Y., Hall, S. A., Baud, P., & Wong, T. F. (2015). Characterization of pore structure and strain localization in Majella limestone by X-ray computed tomography and digital image correlation. *Geophysical Journal International*, 200(2), 701-719.

Johnson, K. L. (1982). One hundred years of Hertz contact. Proceedings of the Institution of Mechanical Engineers, 196(1), 363-378.

Kandula, N., Cordonnier, B., Boller, E., Weiss, J., Dysthe, D. K., & Renard, F. (2019). Dynamics of microscale precursors during brittle compressive failure in Carrara marble. *Journal of Geophysical Research: Solid Earth*, 124(6), 6121-6139.

Klein, E., Baud, P., Reuschlé, T., & Wong, T. F. (2001). Mechanical behaviour and failure mode of Bentheim sandstone under triaxial compression. *Physics and Chemistry of the Earth, Part A: Solid Earth and Geodesy*, 26(1-2), 21-25.

Lion, M., Skoczylas, F., & Ledésert, B. (2004). Determination of the main hydraulic and poro-elastic properties of a limestone from Bourgogne, France. *International Journal of Rock Mechanics and Mining Sciences*, 41(6), 915-925.

Lockner, D., Byerlee, J. D., Kuksenko, V., Ponomarev, A., & Sidorin, A. (1991). Quasi-static fault growth and shear fracture energy in granite. *Nature*, 350(6313), 39-42.

Lockner, D. A., Byerlee, J. D., Kuksenko, V., Ponomarev, A., & Sidorin, A. (1992). Observations of quasistatic fault growth from acoustic emissions. In *International Geophysics* (Vol. 51, pp. 3-31). Academic Press.

Louis, L., Wong, T. F., & Baud, P. (2007). Imaging strain localization by X-ray radiography and digital image correlation: Deformation bands in Rothbach sandstone. *Journal of Structural Geology*, 29(1), 129-140.

Ma, X., & Haimson, B. C. (2016). Failure characteristics of two porous sandstones subjected to true triaxial stresses. *Journal of Geophysical Research: Solid Earth*, 121(9), 6477-6498.

Mair, K., Main, I., & Elphick, S. (2000). Sequential growth of deformation bands in the laboratory. *Journal of Structural Geology*, 22(1), 25-42.

McBeck, J., Kobchenko, M., Hall, S. A., Tudisco, E., Cordonnier, B., Meakin, P., & Renard, F. (2018). Investigating the onset of strain localization within anisotropic shale using digital volume correlation of time-resolved X-ray microtomography images. *Journal of Geophysical Research: Solid Earth*, 123(9), 7509-7528.

McBeck, J., Mair, K., & Renard, F. (2019). How porosity controls macroscopic failure via propagating fractures and percolating force chains in porous granular rocks. *Journal of Geophysical Research: Solid Earth*, 124(9), 9920-9939.

McBeck, J., Ben-Zion, Y., & Renard, F. (2020). The mixology of precursory strain partitioning approaching brittle failure in rocks. *Geophysical Journal International*, 221(3), 1856-1872.

Menéndez, B., Zhu, W., & Wong, T. F. (1996). Micromechanics of brittle faulting and cataclastic flow in Berea sandstone. *Journal of Structural Geology*, 18(1), 1-16.

Mittone, A., Manakov, I., Broche, L., Jarnias, C., Coan, P., & Bravin, A. (2017). Characterization of a sCMOS-based high-resolution imaging system. *Journal of Synchrotron Radiation*, 24(6), 1226-1236.

Mirone, A., Brun, E., Gouillart, E., Tafforeau, P., & Kieffer, J. (2014). The PyHST2 hybrid distributed code for high speed tomographic reconstruction with iterative reconstruction and a priori knowledge capabilities. *Nuclear Instruments and Methods in Physics Research Section B: Beam Interactions with Materials and Atoms*, 324, 41-48.

Nagel, N. B. (2001). Compaction and subsidence issues within the petroleum industry: From Wilmington to Ekofisk and beyond. *Physics and Chemistry of the Earth, Part A: Solid Earth and Geodesy*, 26(1-2), 3-14.

Olsson, W. A. (1999). Theoretical and experimental investigation of compaction bands in porous rock. *Journal of Geophysical Research: Solid Earth*, 104(B4), 7219-7228.

Olsson, W. A., & Holcomb, D. J. (2000). Compaction localization in porous rock. *Geophysical Research Letters*, 27(21), 3537-3540.

Olsson, W. A., Holcomb, D. J., & Rudnicki, J. W. (2002). Compaction localization in porous sandstone: Implications for reservoir mechanics. *Oil & Gas Science and Technology*, 57(5), 591-599.

Otani, J., Mukunoki, T., & Sugawara, K. (2005). Evaluation of particle crushing in soils using X-ray CT data. *Soils and Foundations*, 45(1), 99-108.

Paganin, D., Gureyev, T. E., Pavlov, K. M., Lewis, R. A., & Kitchen, M. (2004). Phase retrieval using coherent imaging systems with linear transfer functions. *Optics Communications*, 234(1-6), 87-105.

Paterson, M. S., & Wong, T. F. (2005). *Experimental rock deformation-the brittle field*. Springer Science & Business Media.

Pittman, E. D. (1971). Microporosity in carbonate rocks. *AAPG Bulletin*, 55(10), 1873-1878.

Rath, A., Exner, U., Tschegg, C., Grasemann, B., Laner, R., & Draganits, E. (2011). Diagenetic control of deformation mechanisms in deformation bands in a carbonate grainstone. *AAPG bulletin*, 95(8), 1369-1381.

Renard, F., Cordonnier, B., Dysthe, D. K., Boller, E., Tafforeau, P. and Rack, A. (2016) A deformation rig for synchrotron microtomography studies of geomaterials under conditions down to 10 km depth in the Earth, *Journal of Synchrotron Radiation*, 23, 1030-1034.

Renard, F., Cordonnier, B., Kobchenko, M., Kandula, N., Weiss, J., & Zhu, W. (2017). Microscale characterization of rupture nucleation unravels precursors to faulting in rocks. *Earth and Planetary Science Letters*, 476, 69-78.

Renard, F., Weiss, J., Mathiesen, J., Ben-Zion, Y., Kandula, N., & Cordonnier, B. (2018). Critical evolution of damage toward system-size failure in crystalline rock. *Journal of Geophysical Research: Solid Earth*, 123(2), 1969-1986.

Renard, F., McBeck, J., Cordonnier, B., Zheng, X., Kandula, N., Sanchez, J. R., Kobchenko, M., Noiriel, C., Zhu, W., Meakin, P., Fusseis, F., & Dysthe, D. K. (2019a) Dynamic in situ three-dimensional imaging and digital volume correlation analysis quantify strain localization and fracture coalescence in sandstone, *Pure and Applied Geophysics*, 176, 1083-1115, https://doi.org/10.1007/s00024-018-2003-x.

Renard, F., McBeck, J., Kandula, N., Cordonnier, B., Meakin, P., Ben-Zion, Y. (2019b). Volumetric and shear processes in crystalline rock approaching faulting, *Proceedings of the National Academy of Sciences*, 116, 16234-16239, doi: 10.1073/pnas.1902994116.

Renshaw, C. E., & Schulson, E. M. (2001). Universal behaviour in compressive failure of brittle materials. *Nature*, 412(6850), 897-900.

Rimmelé, G., Barlet-Gouédard, V., & Renard, F. (2010). Evolution of the petrophysical and mineralogical properties of two reservoir rocks under thermodynamic conditions relevant for CO2 geological storage at 3 km depth. *Oil & Gas Science and Technology–Revue de l'Institut Français du Pétrole*, 65(4), 565-580.

Rotevatn, A., Thorsheim, E., Bastesen, E., Fossmark, H. S., Torabi, A., & Sælen, G. (2016). Sequential growth of deformation bands in carbonate grainstones in the hangingwall of an active growth fault: Implications for deformation mechanisms in different tectonic regimes. *Journal of Structural Geology*, 90, 27-47.

Rustichelli, A., Tondi, E., Agosta, F., Cilona, A., & Giorgioni, M. (2012). Development and distribution of bed-parallel compaction bands and pressure solution seams in carbonates (Bolognano Formation, Majella Mountain, Italy). *Journal of Structural Geology*, 37, 181-199.

Rutter, E. H. (1983). Pressure solution in nature, theory and experiment. *Journal of the Geological Society*, 140(5), 725-740.

Sammis, C. G., & Ashby, M. F. (1986). The failure of brittle porous solids under compressive stress states. *Acta Metallurgica*, 34(3), 511-526.

Schutjens, P. M. T. M., Hausenblas, M., Dijkshoorn, M., & Van Munster, J. G. (1995). The Influence of Intergranular Microcracks on the Petrophysical Properties of Sandstone—Experiments to Quantify effects of core damage. In *Proc. Int. Symp. Soc. Core Analysts* (Vol. 9524, pp. 1-12).

Scott, T. E., & Nielsen, K. C. (1991). The effects of porosity on the brittle-ductile transition in sandstones. *Journal of Geophysical Research: Solid Earth*, 96(B1), 405-414.

Shipton, Z. K., & Cowie, P. A. (2001). Damage zone and slip-surface evolution over μm to km scales in high-porosity Navajo sandstone, Utah. *Journal of Structural Geology*, 23(12), 1825-1844.

Tondi, E., Rustichelli, A., Cilona, A., Balsamo, F., Storti, F., Napoli, G., Agosta, F., Renda, P. & Giorgioni, M. (2016). Hydraulic properties of fault zones in porous carbonates, examples from central and southern Italy. *Italian Journal of Geosciences*, 135(1), 68-79.

Tudisco, E., Andò, E., Cailletaud, R., & Hall, S.A. (2017). TomoWarp2: a local digital volume correlation code. *SoftwareX*, 6, 267–270.

Vajdova, V., Baud, P., & Wong, T. F. (2004). Permeability evolution during localized deformation in Bentheim sandstone. *Journal of Geophysical Research: Solid Earth*, 109, B10406, doi:10.1029/2003JB002942.

Vajdova, V., Zhu, W., Chen, T. M. N., & Wong, T. F. (2010). Micromechanics of brittle faulting and cataclastic flow in Tavel limestone. Journal of Structural Geology, 32(8), 1158-1169.

Van Baaren, J. P., Vos, M. W., & Heller, H. K. J. (1990). Selection of outcrop samples for acoustic measurements on reservoir rocks. Delft University of Technology.

Wang, B., Chen, Y., & Wong, T. F. (2008). A discrete element model for the development of compaction localization in granular rock. *Journal of Geophysical Research: Solid Earth*, 113, B03202, doi:10.1029/2006JB004501.

Wong, T. F. (1990). Mechanical compaction and the brittle—ductile transition in porous sandstones. *Geological Society, London, Special Publications*, 54(1), 111-122.

Wong, T. F., David, C., & Zhu, W. (1997). The transition from brittle faulting to cataclastic flow in porous sandstones: Mechanical deformation. *Journal of Geophysical Research: Solid Earth*, 102(B2), 3009-3025.

Wong, T. F., & Baud, P. (2012). The brittle-ductile transition in porous rock: A review. *Journal of Structural Geology*, 44, 25-53.

Zheng, X., Cordonnier, B., McBeck, J., Boller, E., Jamtveit, B., Zhu, W., & Renard, F. (2019). Mixed-mode strain localization generated by hydration reaction at crustal conditions. *Journal of Geophysical Research: Solid Earth*, 124(5), 4507-4522.

Zhu, W., & Wong, T. F. (1997). The transition from brittle faulting to cataclastic flow: Permeability evolution. *Journal of Geophysical Research: Solid Earth*, 102(B2), 3027-3041.

Zhu, W., Baud, P., & Wong, T. F. (2010). Micromechanics of cataclastic pore collapse in limestone. *Journal of Geophysical Research: Solid Earth*, 115, B04405, doi:10.1029/2009JB006610.

Zuluaga, L. F., Fossen, H., & Rotevatn, A. (2014). Progressive evolution of deformation band populations during Laramide fault-propagation folding: Navajo Sandstone, San Rafael monocline, Utah, USA. *Journal of Structural Geology*, 68, 66-81.

Supplementary information for

Synchrotron 4D X-ray imaging reveals strain localization at the onset of system-size failure of porous reservoir rocks

Neelima Kandula[1,*], Jessica McBeck[1], Benoît Cordonnier[1,2], Jérôme Weiss[3], Dag Kristian Dysthe[1], François Renard[1,3]

[1] PGP, The Njord Centre, Departments of Geosciences & Physics, University of Oslo, Norway

[2] The European Synchrotron, ESRF, beamline ID19, Grenoble, France

[3] Université Grenoble Alpes, Université Savoie Mont Blanc, CNRS, IRD, IFSTTAR, ISTerre, 38000 Grenoble, France

The supplementary information contains 6 figures and 7 movies.

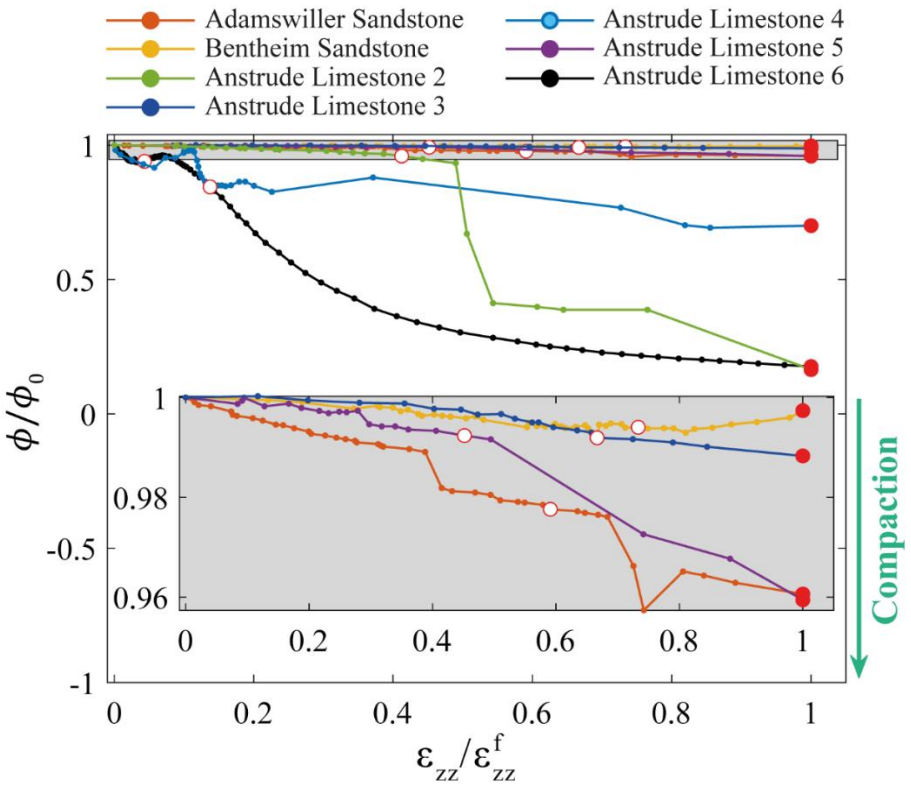

Figure S1. Evolution of normalized porosity, ϕ/ϕ_0, relative to $\varepsilon_{zz}/\varepsilon_{zz}^f$. Inset: Close up of region highlighted by gray rectangle.

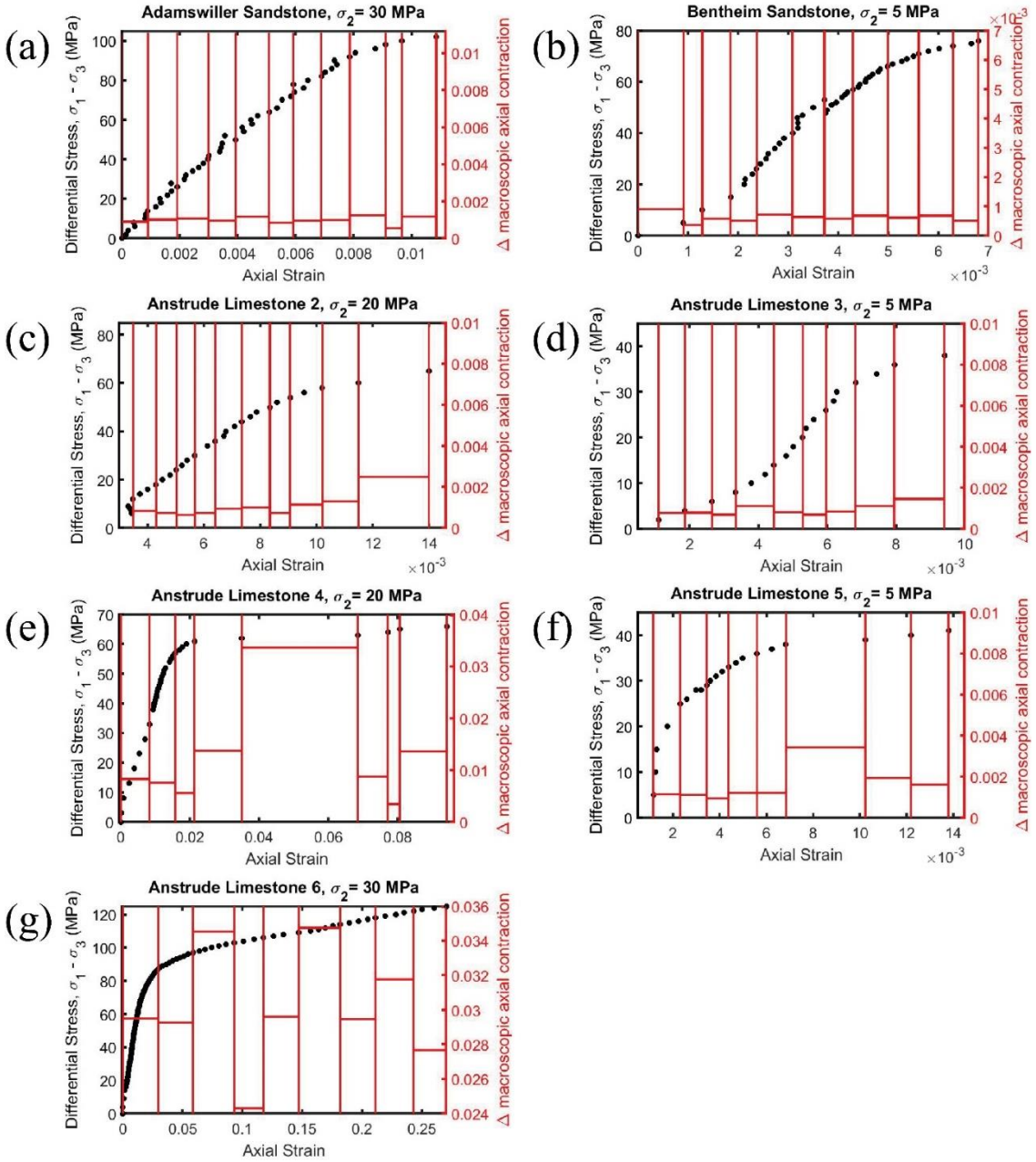

Figure S2. Deformation curves for experiments, Adamswiller sandstone (a), Bentheim sandstone (b), Anstrude limestone 2 (c), 3 (d), 4 (e), 5 (f), and 6 (g) where the differential stress is plotted against the macroscopic axial strain. Each black dot corresponds to a 3D X-ray tomogram. Each stress-strain curve is divided into nearly equal intervals of strain marked by the red vertical lines. The length of each horizontal red line measures $\Delta\varepsilon$, as given in the right vertical axis.

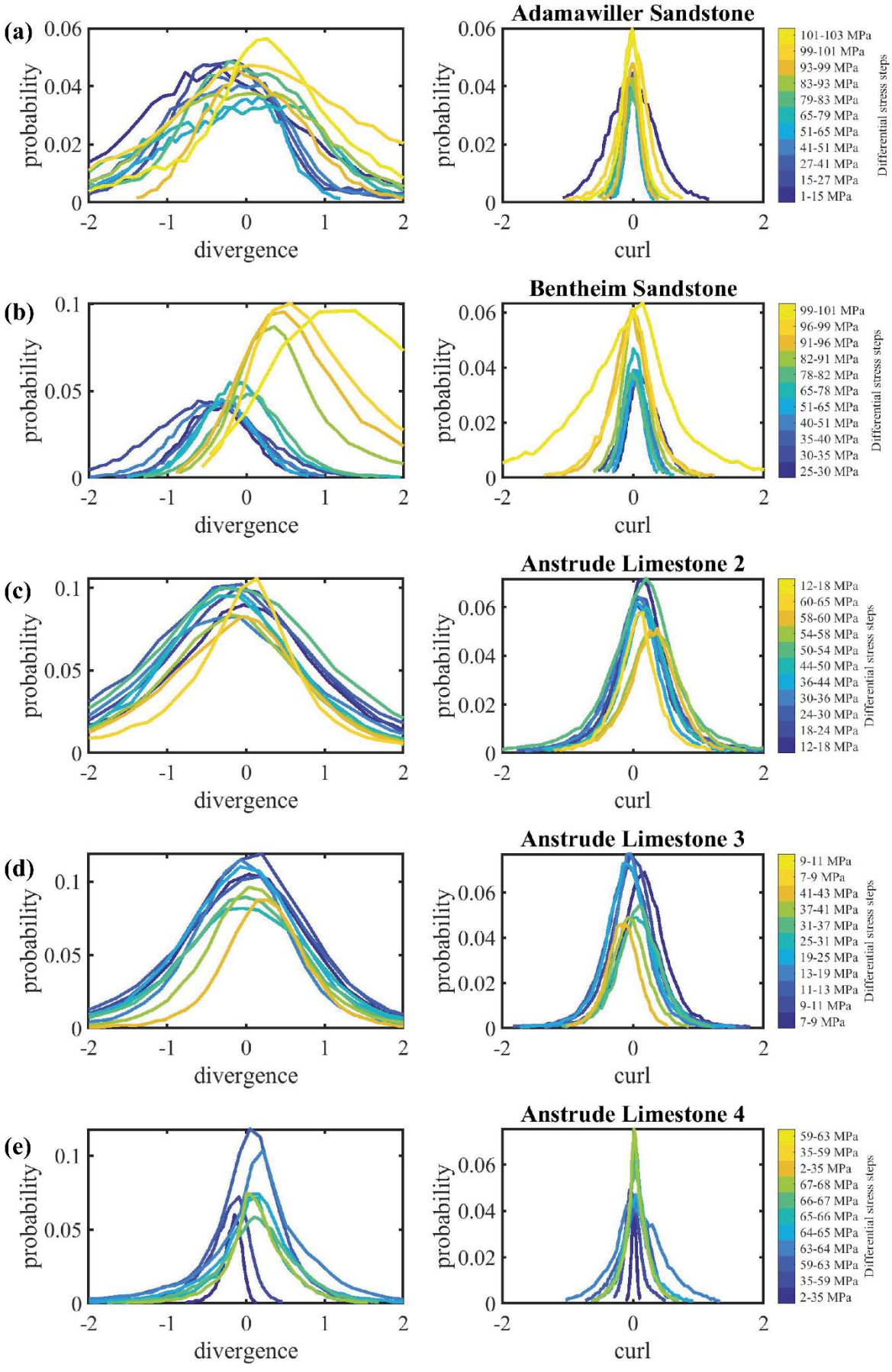
(a)
Adamawiller Sandstone
probability
divergence
curl
101-103 MPa
99-101 MPa
93-99 MPa
83-93 MPa
79-83 MPa
65-79 MPa
51-65 MPa
41-51 MPa
27-41 MPa
15-27 MPa
1-15 MPa
Differential stress steps
(b)
Bentheim Sandstone
99-101 MPa
96-99 MPa
91-96 MPa
82-91 MPa
78-82 MPa
65-78 MPa
51-65 MPa
40-51 MPa
35-40 MPa
30-35 MPa
25-30 MPa
(c)
Anstrude Limestone 2
12-18 MPa
60-65 MPa
58-60 MPa
54-58 MPa
50-54 MPa
44-50 MPa
36-44 MPa
30-36 MPa
24-30 MPa
18-24 MPa
12-18 MPa
(d)
Anstrude Limestone 3
9-11 MPa
7-9 MPa
41-43 MPa
37-41 MPa
31-37 MPa
25-31 MPa
19-25 MPa
13-19 MPa
11-13 MPa
9-11 MPa
7-9 MPa
(e)
Anstrude Limestone 4
59-63 MPa
35-59 MPa
2-35 MPa
67-68 MPa
66-67 MPa
65-66 MPa
64-65 MPa
63-64 MPa
59-63 MPa
35-59 MPa
2-35 MPa

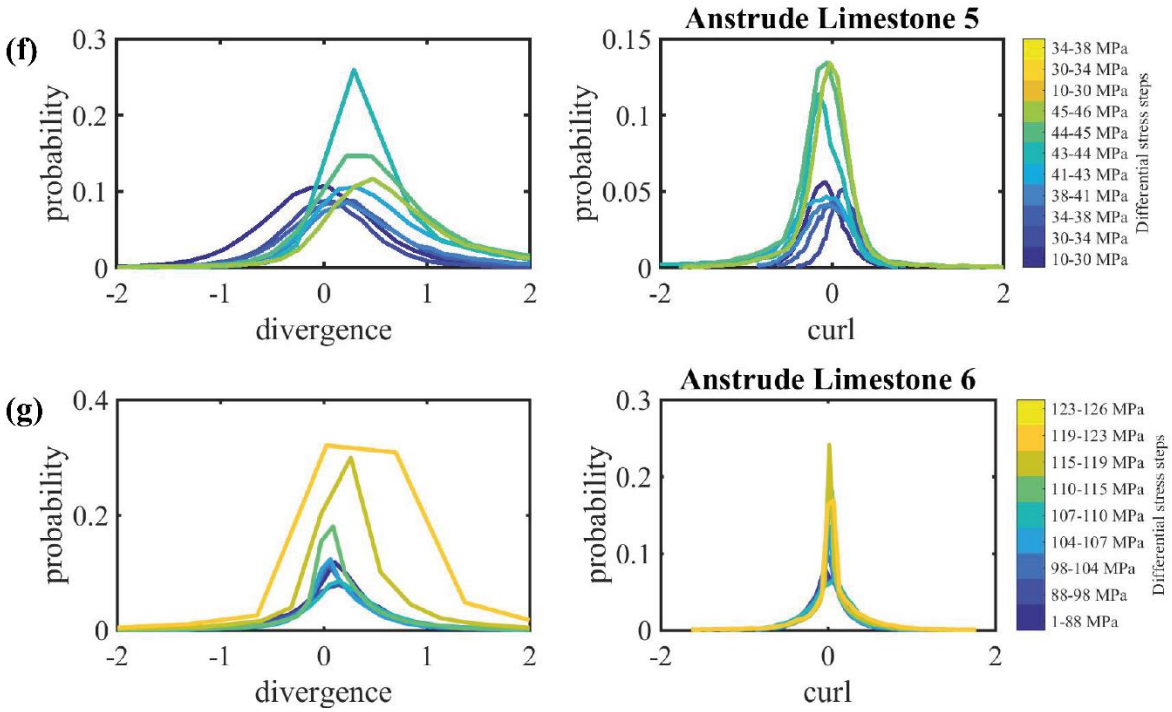

Figure S3. Histograms of divergence and curl of the incremental displacement fields ($\vec{\boldsymbol{u}}$) computed from DVC analysis with 20 voxel node spacing for the Adamswiller sandstone (a), Bentheim sandstone (b), Anstrude limestone 2 (c), Anstrude limestone 3 (d), Anstrude limestone 4 (e), Anstrude limestone 5 (f) and Anstrude limestone 6 (g). Color scale from blue to yellow for each experiment represents the successive experimental increments and corresponds to the differential stress for the pair of tomograms chosen for DVC analysis. Tomograms at nearly equal strain increments are chosen for DVC analysis as given in supplementary Figure S2.

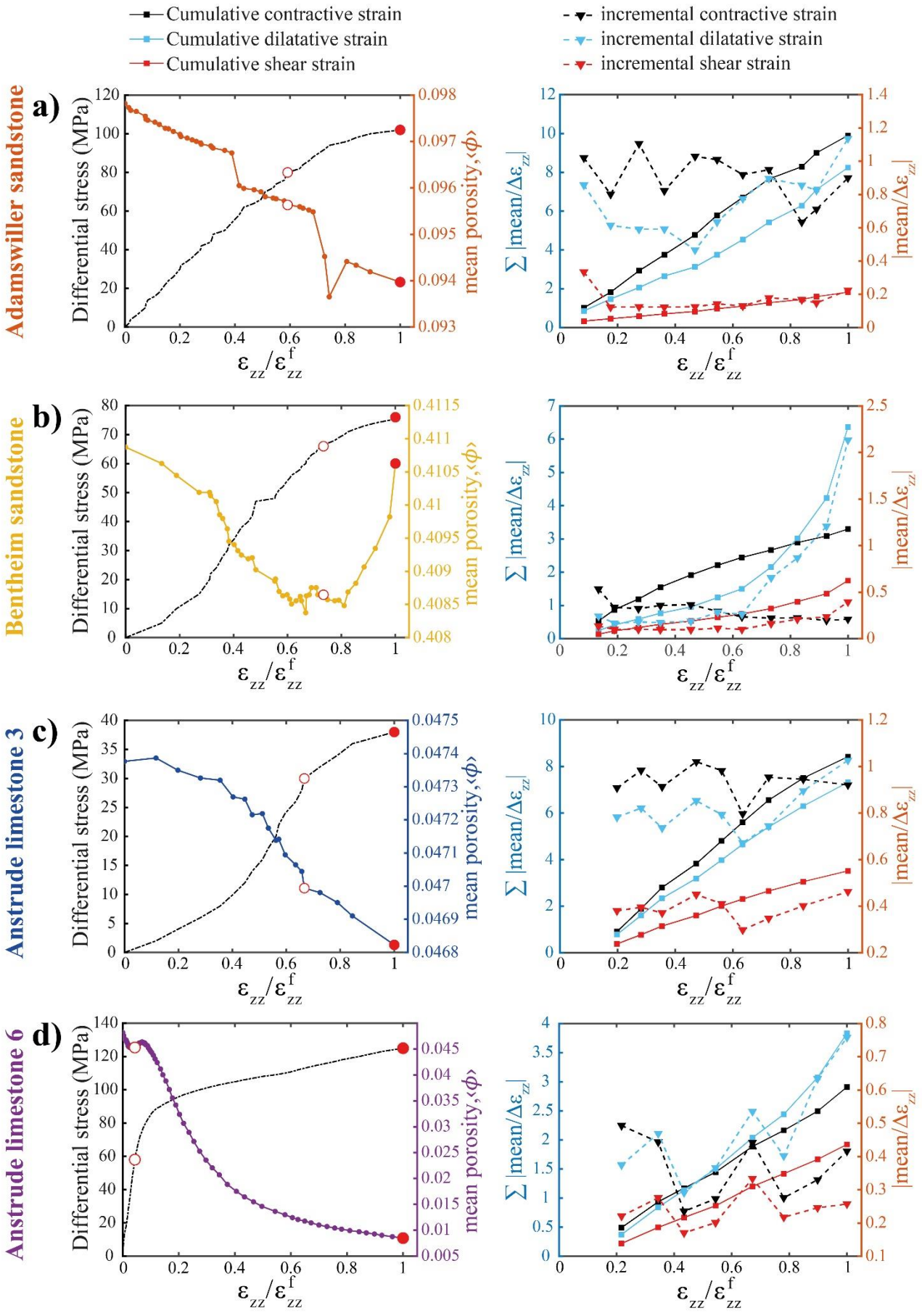
Cumulative contractive strain
Cumulative dilatative strain
Cumulative shear strain
incremental contractive strain
incremental dilatative strain
incremental shear strain
a)
Adamswiller sandstone
b)
Bentheim sandstone
c)
Anstrude limestone 3
d)
Anstrude limestone 6
Differential stress (MPa)
mean porosity,⟨φ⟩
∑ |mean/Δε_zz|
|mean/Δε_zz|
ε_zz/ε^f_zz

Figure S4: Evolutions of the differential stress, mean porosity, and cumulative and incremental strain means. Each row shows a different experiment. Left and right columns show the macroscopic deformation (stress-strain curves) and mean porosity and incremental and cumulative incremental strain components, respectively.

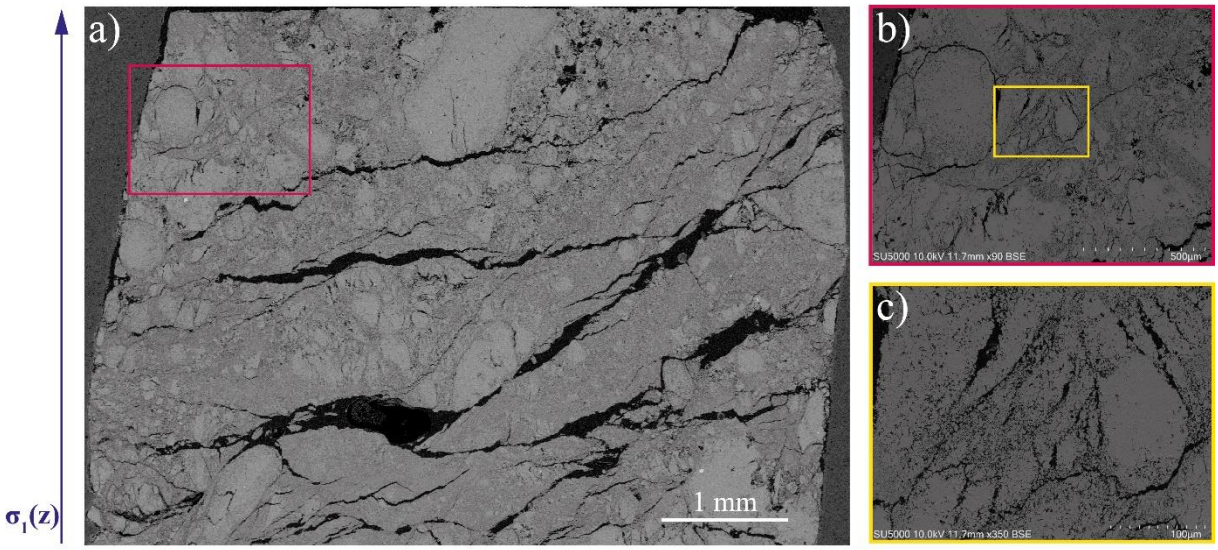

Figure S5. Scanning electron micrograph of the Anstrude limestone 2 showing the microstructure after a brittle compressive failure. a) Whole width of the sample. b-c) Magnified images of highlighted areas in a) and b) respectively. All images show grain crushing and in a-b) transgranular fractures are observed.

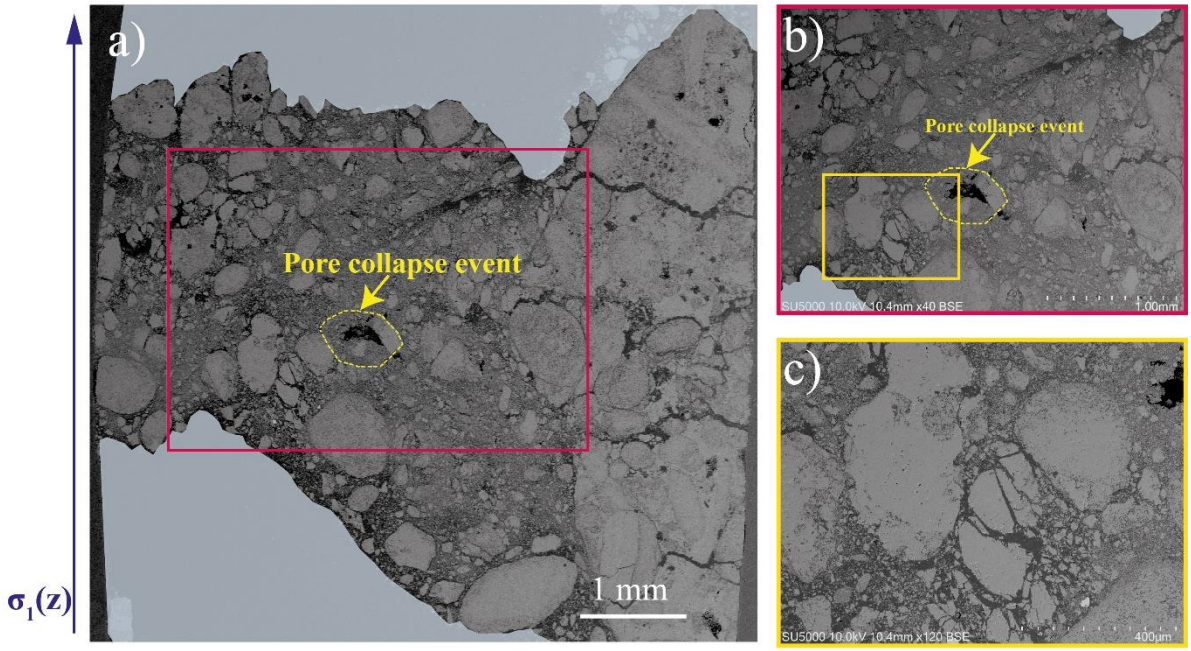

Figure S6. Scanning electron micrograph of the sample of Anstrude limestone 5 showing the microstructure after a brittle compressive failure. a) Whole width of the sample. b-c) Magnified images of highlighted areas in a) and b) respectively. All images show significant grain size reduction and transgranular fractures. Patches in SEM is the cavity formed when sample is removed and is filled with epoxy.

Movie V1: Adamswiller sandstone incremental strains, number

Movie V2: Bentheim sandstone incremental strains, number

Movie V3: Anstrude limestone 2 incremental strains, number

Movie V4: Anstrude limestone 3 incremental strains, number

Movie V5: Anstrude limestone 4 incremental strains, number

Movie V6: Anstrude limestone 5 incremental strains, number

Movie V7: Anstrude limestone 6 incremental strains, number

Manuscript 3

Volumetric and shear processes in crystalline rock approaching faulting

François Renard, Jessica McBeck, **Neelima Kandula**, Benoît Cordonnier, Paul Meakin, & Yehuda Ben-Zion.

Proceedings of the National Academy of Sciences, *116*(33), 16234-16239 (2019).

Volumetric and shear processes in crystalline rock approaching faulting

François Renard[a,b,c,1], Jessica McBeck[a,b], Neelima Kandula[a,b], Benoît Cordonnier[a,b,d], Paul Meakin[e], and Yehuda Ben-Zion[f]

[a]The Njord Centre, Department of Geosciences, University of Oslo, 0316 Oslo, Norway; [b]The Njord Centre, Department of Physics, University of Oslo, 0316 Oslo, Norway; [c]Université Grenoble Alpes, Université Savoie Mont Blanc, CNRS, IRD, IFSTTAR, ISTerre, 38000 Grenoble, France; [d]The European Synchrotron Radiation Facility, 38000 Grenoble, France; [e]Department of Physics, Temple University, Philadelphia, PA 19122; and [f]Department of Earth Sciences, University of Southern California, Los Angeles, CA 90007

Edited by David T. Sandwell, Scripps Institution of Oceanography, La Jolla, CA, and approved July 9, 2019 (received for review February 20, 2019)

Understanding the approach to faulting in continental rocks is critical for identifying processes leading to fracturing in geomaterials and the preparation process of large earthquakes. In situ dynamic X-ray imaging and digital volume correlation analysis of a crystalline rock core, under a constant confining pressure of 25 MPa, are used to elucidate the initiation, growth, and coalescence of microfractures leading to macroscopic failure as the axial compressive stress is increased. Following an initial elastic deformation, microfractures develop in the solid, and with increasing differential stress, the damage pervades the rock volume. The creation of new microfractures is accompanied by propagation, opening, and closing of existing microfractures, leading to the emergence of damage indices that increase as powers of the differential stress when approaching failure. A strong spatial correlation is observed between microscale zones with large positive and negative volumetric strains, microscale zones with shears of opposite senses, and microscale zones with high volumetric and shear strains. These correlations are attributed to microfracture interactions mediated by the heterogeneous stress field. The rock fails macroscopically as the microfractures coalesce and form a geometrically complex 3D volume that spans the rock sample. At the onset of failure, more than 70% of the damage volume is connected in a large fracture cluster that evolves into a fault zone. In the context of crustal faulting dynamics, these results suggest that evolving rock damage around existing locked or future main faults influences the localization process that culminates in large brittle rupture events.

faulting | earthquake | strain localization | X-ray tomography | digital volume correlation

Understanding the route to failure in crystalline rocks is fundamental for developing improved quantitative frameworks for the behavior of faults, the evolution of permeability in the continental crust, and the fracturing of geomaterials. High-resolution earthquake catalogs show abundant microseismicity in the volumes surrounding major faults (1, 2). The interaction between seismicity along faults and in the surrounding rock volume is critical for understanding the spatiotemporal evolution of earthquakes in active areas (3, 4). Laboratory experiments demonstrate that microfracture generation produces macroscopic dilation of rocks before macroscopic shear failure occurs (5–7) and controls the transition from distributed damage to shear localization (8–12). After an initial damage phase of random microfracturing, large fractures and faults nucleate within an array of microfractures oriented more or less parallel to the direction of maximum principle stress. This array is inclined at about 30° relative to the direction of the maximum principle stress (10) and acts as a precursor of the fault formation. The fault and array grow in concert with new microfractures acting as the fault process zone. A model for faulting, based on failure of an array of beams, separated from each other by an array of fractures inclined at about 30° relative to the direction of the maximum principle stress, is presented in ref. 10, but it is not clear whether the array is formed by coalescence of multiple smaller arrays or by the growth of a single array. It is also not clear whether the faults that form within the array propagate from a single nucleation site or propagate from multiple nucleation sites and coalesce.

Determination of the spatial distribution of acoustic emissions in rocks indicates that microfractures initially nucleate and grow at apparently random locations (8, 9) rather than within the future fault zone. However, uncertainties in the locations of acoustic emission sources and inability to monitor aseismic strain release (i.e., failure processes that do not emit acoustic waves) have prevented a more complete quantification of the evolving inelastic strain before failure from these data. In other words, the strain localization processes leading to macroscopic rock failure remain unclear since the experimentalist cannot see how the fracture pattern evolves inside the progressively deformed sample.

Recent analysis of time-lapse 3D X-ray tomograms (13) demonstrated that the total volume of the microfractures, rate of damage growth, and size of the largest microfracture cluster all increase as powers of Δ_D, where $\Delta_D = (\sigma_D^f - \sigma_D)/\sigma_D^f$ is a normalized stress parameter that measures the difference between the differential stress at failure σ_D^f and the evolving differential stress $\sigma_D = \sigma_1 - \sigma_3$, where σ_1 and σ_3 are the largest and smallest compressive principle stress values, respectively (a list of symbols is provided in *SI Appendix*, Table S1). This behavior suggests that

Significance

The dynamics of brittle deformation prior to macroscopic instability is critical to faulting events. This study provides direct high-resolution information on this process obtained using X-ray microtomography and digital volume correlation analysis of evolving microfractures and deformation fields in laboratory fracturing experiments. Brittle failure results from the dynamic coupling between microfracture growth, opening, shear, coalescence, and closing. The evolving microfracture volume and size distributions increase as powers of the differential stress, as the differential stress approached the failure level. The results highlight the key roles that seismic and aseismic off-fault cracking play in the preparation process leading to large brittle shear rupture events.

Author contributions: F.R. and Y.B.-Z. designed research; F.R., J.M., N.K., and B.C. performed research; F.R., J.M., N.K., and P.M. analyzed data; and F.R. and P.M. wrote the paper.

The authors declare no conflict of interest.

This article is a PNAS Direct Submission.

Data deposition: The X-ray tomography data (sample Monzonite 5, series of 3D volumes, 16 bytes gray scale) supporting the conclusions are available at https://doi.org/10.11582/2018.00023.

[1]To whom correspondence may be addressed. Email: francois.renard@geo.uio.no.

This article contains supporting information online at www.pnas.org/lookup/suppl/doi:10.1073/pnas.1902994116/-/DCSupplemental.

Published online August 1, 2019.

fracture growth within low-porosity crystalline rocks under compressional loading is a critical phenomenon, in which acceleration of damage accumulation precedes system-size failure (13, 14). However, in this previous study (13), the precise change in volume due to fracture growth, analogous to microseismicity in the crust, could not be extracted and studied in detail. The present study overcomes this limitation.

Here we present results of an investigation of the evolving microfractures in a brittle crystalline rock representative of the continental crust during the approach to macroscopic failure. This situation applies to the generation of faulting in pristine rocks (5–8) and to the relocalization of deformation in noncreeping faults that have been partially healed during the interseismic period (15–17). The results are obtained by in situ imaging of microfractures during triaxial compression with dynamic X-ray tomography. A combination of direct time-lapse imaging and digital volume correlation analysis is used to track damage accumulation from the onset of loading to macroscopic failure. The digital volume correlation analysis demonstrates that inelastic strain accumulated as dilatant and contractive damage events as well as left-lateral and right-lateral shear events (Fig. 1). These 4 expressions of damage pervade the volume and interact with each other throughout the deformation, beyond the linear elastic regime. Following macroscopic yielding, strain begins to localize and become increasingly asymmetric as dilation and 1 sense of shear become dominant. These results quantify how 1) macroscopic volumetric strain arises from a competition between microscale dilation and compaction, 2) microscopic deformation outside the future fault zone influences the localization of strain into this zone, and 3) the coalescence of the largest microfracture cluster with surrounding smaller fractures triggers macroscopic shear failure.

In Situ Imaging of the Failure of Crystalline Rock and Measurement of Strain Evolution

A centimeter-scale sample of quartz-rich crystalline monzonite rock (13) was deformed under 25 MPa confining pressure and a temperature of 24 °C in the HADES triaxial apparatus (18, 19) installed on X-ray microtomography beamline ID19 at the European Synchrotron Radiation Facility. The experimental conditions are relevant for brittle deformation of rocks at depth up to 2 to 3 km, where rock failure envelopes predict dilatancy and faulting (20). This enabled time-lapse imaging of the sample during compressive deformation. Seventy-seven 3D tomograms were acquired as the differential stress was increased (*Materials and Methods*), with a spatial resolution of 6.5 μm. The last tomogram was acquired at 99.993% of the failure differential stress, allowing detailed characterization of the system-size faulting process. The loading history and the strain measurements are shown in *SI Appendix*, Fig. S1. The sample contained around 2,000 grains (10 × 10 × 20 grains), which is a representative volume of the whole rock. Its centimeter-scale dimensions were similar to the dimension of the fault nucleation zone in granite identified using acoustic emissions (21).

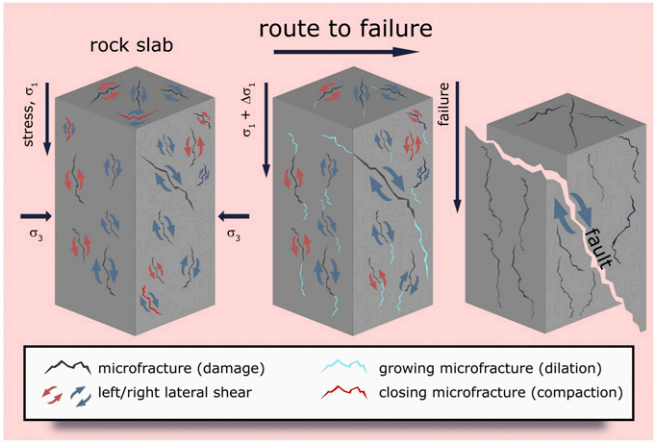

Fig. 1. The route to failure in crystalline rock. Under a state of differential stress $(\sigma_1 - \sigma_3)$, damage accumulates in the form of microfractures that may open, close, and slip in a right-lateral or left-lateral sense. As failure is approached, one slip mode becomes dominant, right-lateral on this sketch, leading to macroscopic faulting.

The axial strain versus differential stress relationship (Fig. 2*A* and Movie S1) shows behavior characteristic of crystalline rocks (e.g., ref. 22). At low differential stresses (40 to 178 MPa), the quasi-linear relationship between macroscopic strain and differential stress is indicative of an elastic regime, with small variations in the slope at stresses below 40 MPa, which we attribute to closing of voids initially present in the rock. Beyond the yield point at 178 MPa, defined here as a deviation of 3% of the experimental volumetric strain from the linear trend in the elastic regime (5), microfractures accumulate progressively in the rock, leading to macroscopic radial dilation, until failure occurs via shear fault development through the growth of the largest microfracture cluster and coalescence with smaller clusters (Fig. 2 *A* and *B*).

The 3D digital volume correlation software TomoWarp2 (23) was used to characterize incremental displacement and strain during deformation. Digital volume correlation analysis provides a discretized displacement field from which a discretized displacement gradient field can be calculated. TomoWarp2 calculates translations and rotations between two 3D datasets, following the same procedure as in reference (19). This digital volume correlation technique produces 3D displacement fields from which the divergence, $\nabla \cdot \Delta\mathbf{u}$, and curl, $\nabla \times \Delta\mathbf{u}$, of the incremental displacement fields, $\Delta\mathbf{u}$, are calculated (Figs. 2 *C* and *D* and 3 and Movie S2). These fields reveal the magnitude of local dilatancy (positive divergence), compaction (negative divergence), left-lateral shear (negative curl), and right-lateral shear (positive curl).

In brittle rocks such as quartz-rich monzonite, large strain cannot occur without fracturing, and we attribute large magnitudes of $\nabla \times \Delta\mathbf{u}$ on the scale of the node spacing used in the digital volume correlation analysis to shear displacement along microfractures. These microfractures may have apertures that are not sufficiently large to produce X-ray attenuation coefficient contrasts that are larger than the noise level, and some of them may remain undetected through segmentation. Some elastic deformation of mineral grains or aggregates of mineral grains may occur without microfracturing, but because of the high stiffness of the mineral grains and the brittleness of the bonding between them this is not expected to contribute significantly to $\nabla \times \Delta\boldsymbol{u}$ on the scale of the digital volume correlation analysis node spacing. Similarly, the opening and closing of microfractures and other voids is expected to be the dominant contribution to volumetric strain on the digital volume correlation analysis node spacing scale. Because of the very low initial porosity of the sample, most of the volumetric compaction occurred in regions that contained voids that were previously dilated and then collapsed.

If the displacements on opposite sides of a microfracture, which cannot always be detected directly in X-ray tomograms, are measured, an effective discretized simple shear strain proportional to d/Δ_n can be determined, where d is the shear displacement and Δ_n is the node spacing used in the digital volume correlation analysis. For continuous displacement fields, $\nabla \times \Delta\mathbf{u}$ measures the magnitude and sense of the simple shear strain, and consequently, high magnitudes of $\nabla \times \Delta\mathbf{u}$ highlight sites of localized shear displacement. We calculated 3D incremental displacement fields between 10 pairs of 3D tomograms at regular

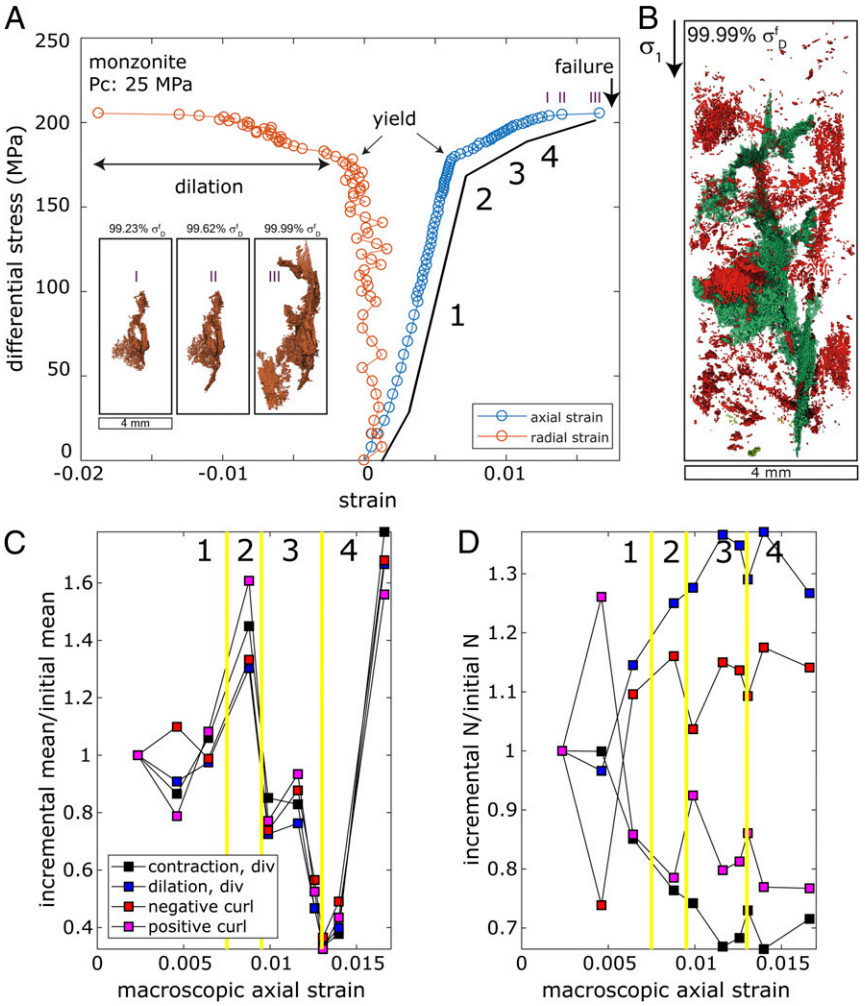

Fig. 2. Evolution of damage before failure. (*A*) Variation of axial and radial strains as the differential stress was increased. A 3D X-ray tomography dataset was acquired under the stress and strain conditions indicated by each circle. The axial strain versus stress curve is divided into 4 stages: 1, elastic; 2, yield; 3, volumetric damage; and 4, localization before failure. (*Inset*) Evolution of the largest microfracture cluster in the last 3 tomography images (labeled I, II, and III) at 99.23, 99.62, and 99.99% of the failure differential stress, σ^f_D. (*B*) A 3D view of the accumulated damage at the onset of failure. The largest microfracture cluster (green) is surrounded by microfractures with smaller volumes (red) that pervade the entire rock volume. (*C*) Relative variation of mean incremental divergence and mean incremental magnitudes of positive and negative curl of the displacement field as failure was approached. (*D*) Relative variation of the number of subvolumes with divergence and incremental curl magnitudes above/below ±0.5 as failure was approached. Digital volume correlation analysis was used to calculate 10 displacement fields from 11 3D tomograms acquired as the differential stress was increased, and the *x* coordinate of each of the 10 sets of 4 data points indicates the macroscopic axial strain when the second of each pair of tomograms used in each digital volume correlation analysis was acquired. In *C*, the mean values of the divergence or curl calculated by digital volume correlation analysis divided by the mean value calculated for the first pair of tomograms are shown. In *D*, the number of subvolumes above a threshold value used in the digital volume correlation calculation normalized by the same value for the first pair of tomograms are shown.

intervals of axial strain that encompassed the experiment (Fig. 2 *C* and *D* and Movie S2). The windows used to perform the digital volume correlations had a cubic shape with 4 faces parallel to the main compressive stress σ_1 and 2 faces perpendicular to it. Following tests performed in a previous study (19), we used a correlation window size of 10 voxels (65 μm) and node spacing size of 20 voxels (130 μm).

Dynamics of Strain Evolution

The digital volume correlation analysis provides quantitative information about cumulative and incremental strain localization. Time series of 3D divergence and curl fields enable quantitative assessment of evolving volumetric and simple shear components of the incremental strain fields (Fig. 2 *C* and *D* and Movie S2). We tracked populations of the increments in positive (dilatational) and negative (contractive) volumetric strain (divergence) and negative (left-lateral) and positive (right-lateral) shear strain (curl) as the differential stress was increased. The results revealed the evolving spatial distribution of left-lateral and right-lateral slip as well as dilation and compaction produced by microfracture development and the final localization of damage onto a sample-spanning fault. The mean magnitudes of the dilation and contraction, and left- and right-lateral shear events, paralleled each other as the differential stress was increased (Fig. 2*C*).

The varying means of the positive and negative incremental $\nabla \cdot \Delta\mathbf{u}$ and $\nabla \times \Delta\mathbf{u}$ populations (Fig. 2*C*), and the volume of material experiencing high absolute values (>0.5) of each of the 4 displacement field measures (Fig. 2*D*), can be used to distinguish between 4 phases of evolving deformation and damage preceding macroscopic shear failure: 1) small changes in the mean values of the divergence and curl of the incremental displacement field, corresponding to the initial linear elastic regime; 2) a 30% increase in the volume of rock experiencing divergence and left-lateral curl following the macroscopic yield point (Fig. 2*D*); 3) a 10% increase of these values from 178 to 190 MPa differential stress (Fig. 2*D*); and 4) a 400% increase of divergence and left-lateral curl in the final 15 MPa preceding failure at 205.5 MPa (Fig. 2*C*), while the volume of material experiencing these large strain field modes ($\nabla \cdot \Delta\mathbf{u}$ and $\nabla \times \Delta\mathbf{u}$) remained essentially constant during this last phase (Fig. 2*D*).

The observed variations of means and volume of material experiencing these large-magnitude strain field components indicate that the path toward failure was dominated by the accumulation of compaction, dilation, left-lateral shear, and right-lateral shear and interactions between them, consistent with previous observations and models (10, 24, 25). The macroscopic dilation of the sample was due to a combination of compaction in the direction parallel to the direction of the largest compressive stress and the concomitant increase in the cross-sectional area in the perpendicular plane, with a total volume increase of 2.1% at the onset of failure. Fig. 3 demonstrates that both dilation and compaction were distributed throughout the rock specimen immediately preceding macroscopic failure. This spatial representation of the compacting and dilating volumes above the 95th percentile of the strain populations further shows that regions of high compaction and high dilation were spatially correlated with

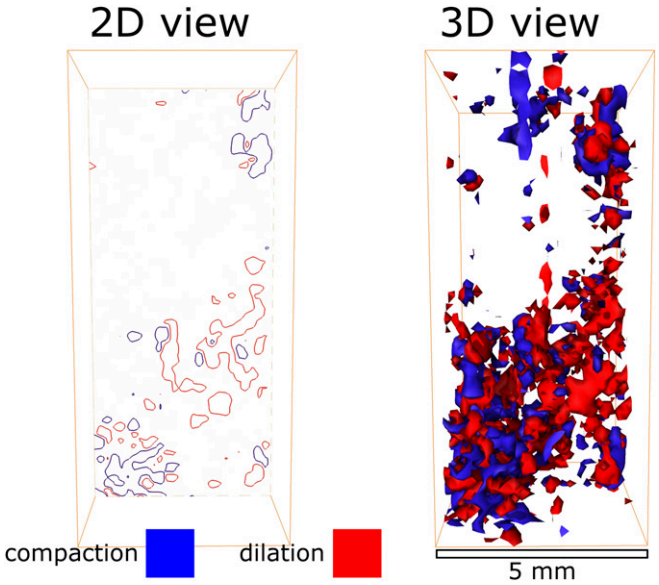

Fig. 3. Spatial correlation between dilation and compaction. The divergence field of the incremental displacement vector field caused by the 0.8 MPa differential stress increase just before failure (calculated by digital volume correlation analysis of the last 2 tomograms before failure). (*Left*) A 2D planar cut along the axis of the cylindrical specimen and (*Right*) 3D view showing the volumes of high positive and high negative divergence (red indicates divergence > 0.5, and blue indicates divergence < −0.5). The $\nabla \cdot \Delta \mathbf{u} = \pm 0.5$ isosurfaces show the combination of compaction and dilation in the sample and the spatial distribution of these quantities.

each other and with the regions of high positive and negative curl (Movie S2). This correlation suggests that regions of high volumetric strain and high shear strain share a common origin, which we attribute to the nucleation, growth, opening, and closing of microfractures and the coupling between them. The postfailure tomogram shows that a higher number of microfractures formed inside grains and propagated across grain boundaries, rather than developing along grain boundaries, in contrast with the behavior observed in Carrara marble (26). The fractures were oriented preferentially toward the direction of the largest compressive stress which is consistent with other studies of similar crystalline rocks (10, 11). Macroscopic shear failure occurred via shear fracture formation that produced a gouge layer with intense grain comminution within a quasi-tabular zone with some variation in thickness (13). This development is similar to field observations of fault zones that contain a gouge layer surrounded by a damage zone (27).

Segmentation of the tomograms into rock matrix and voids (pores and microfractures) provides the volume fraction of voids as a function of increasing differential stress (*SI Appendix*, Fig. S2). We quantify microfracture growth with a damage index, $D_\phi = \frac{\phi - \phi_i}{1 - \phi_i}$, where ϕ_i is the initial void fraction of the sample under the initial confining pressure preceding axial loading ($\phi_i = 0.1\%$) and ϕ is the void fraction measured at a given differential stress (13). The damage index is measured as a function of the normalized deviation of the differential stress from the differential stress at failure $\Delta_D = \left(\frac{\sigma_D^f - \sigma_D}{\sigma_D^f} \right)$, where σ_D^f is the differential stress at which failure occurred and σ_D is the differential stress when each tomogram was acquired. As failure was approached, the total volume of microfractures, the volume of the largest microfracture cluster, and the number of detected microfractures all increased (*SI Appendix*, Fig. S2*A*). During the final 3 differential stress increments, the largest microfracture cluster increased in size (Fig. 2*A*, Inset) until it spanned the entire volume (Fig. 2*B*) and evolved later into the main fault. The volume fraction of microfractures in the specimen at the onset of failure was 1.4%, and the largest microfracture cluster contained 71% of this volume. The generated fault zone was a geometrically complex 3D volume that differs greatly from the concept of fault initiation on a surface that plays a key role in various models, such as those using frictional failure criteria.

Power Law Statistics of Microfracture Growth Events

An increase in microfracture nucleation and growth as failure approached has been observed in previous studies (9, 10, 13). However, the detailed geometry and evolution was challenging to quantify because previous studies only characterized the postfailure sample (10, 11, 22) or because they used acoustic emissions, which are not sensitive to all deformation events and do not accurately determine fracture geometries (8, 9, 28). X-ray microtomography coupled with digital volume correlation analysis allows the total strain (seismic plus aseismic) to be measured. We extracted the change in volume of each microfracture and the volume of each new microfracture that developed between successive tomograms and studied their statistics (Fig. 4). This analysis required tracking of each individual microfracture in space and time and recognition of the geometry of new fractures that opened and preexisting fractures that closed. A maximum likelihood method (29) was used to determine how well the microfracture volume increments of growth, δv^+, can be fit by a power law, with an exponent $\beta \sim 0.5$ (Fig. 4*A*, *Inset*). This power law behavior breaks down for the last tomogram before failure because of the onset of sliding on the future slip surface, indicating that the largest damage cluster has reached a length close to the size of the sample.

The detected volume of fractures is linked to the potential seismic energy release because earthquake potency (moment/rigidity) depends on the volume of rock around a fault that sustains inelastic deformation (30). In analogy to the Gutenberg–Richter frequency–size distribution of earthquakes, we refer to the power law exponent of the frequency–volume distributions of the fractures as the a-value. The distribution of microfracture volume increments is characterized by a constant α value of 1.7 ± 0.3 with 95% confidence. The total number of microfractures increased as failure was approached (*SI Appendix*, Fig. S2), indicating that the property analogous to earthquake productivity (a-value) also increased. These results are consistent with numerical simulations of evolving seismicity and stress along a strongly heterogeneous fault (31).

Implications for Failure in Continental Rocks and Earthquakes Dynamics

Experiments suggest that in crystalline rocks under confinement, macroscopic dilation occurs through the development of microfractures dominated by tensile cracks (5, 7, 8). The nonlinear shape of the failure envelope suggests that fault localization under compression corresponds to an instability that may be described by continuum models (32). By construction, these mechanical models do not take into account the development of damage and so cannot predict its evolution toward system-size failure. Dilatant behavior highlights the limitations and simplifications of failure criteria that do not consider the effect of volume increase on the evolution of mechanical properties during deformation (33). Dilatancy may cause rock stiffness to decrease and pore fluid pressure to vary compared with commonly used constant volume models. Mohr–Coulomb and Griffith failure theories depend on only a small number of parameters. They describe failure as a scale-independent macroscopic process that is independent of local strain dissipation. Furthermore, they do not take into account processes that occur before failure, how they influence the failure stress, and the dynamics and geometry of large-scale strain localization. These results motivated the development of numerical and

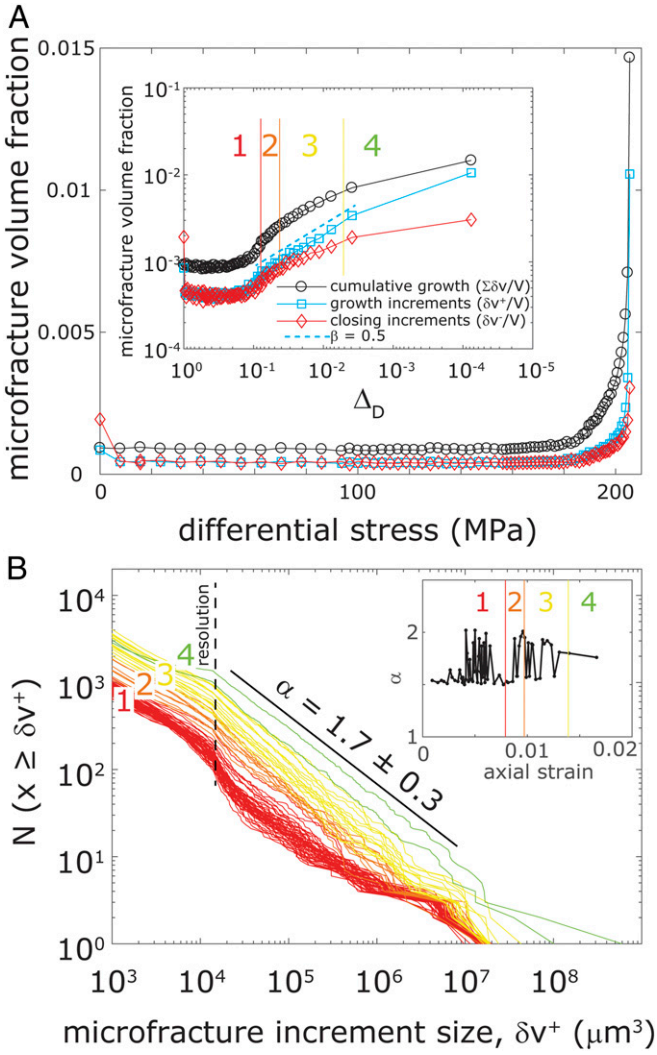

Fig. 4. Evolution of microfractures toward failure. (*A*) The total cumulative normalized volume of microfractures (black curve), $\sum \delta v/V = (|\sum \delta v^+| - |\sum \delta v^-|)/V$, is due to the accumulation of positive volume increments, δv^+, due to microfracture growth (light blue microfractures in Fig. 1) and negative volume increments, δv^-, as some microfractures may close (red microfractures in Fig. 1). Here V is the sample volume. The black curve is equal to the cumulative sum of the light blue curve (positive increments) and red (negative increments) curve. (*Inset*) The same data plotted versus $\Delta_D = \left(\frac{\sigma_D^f - \sigma_D}{\sigma_D^f}\right)$, where σ_D^f is the differential stress at failure. $\beta = 0.5$ is the power law exponent of the damage increment growth until very close to failure. This power law breaks down for the last increment because of system size effect. (*B*) Complementary cumulative distribution of microfracture volume growth increments, δv^+, and power law behavior with $\alpha = 1.7 \pm 0.3$ (SD). The red, orange, yellow, and green colors indicate stages 1 through 4 of the macroscopic strain–differential stress behavior shown in Fig. 2. (*Inset*) The evolution of α toward failure.

mechanical models of rock failure that include damage development preceding macroscopic failure (e.g., refs. 14, 34–36). These models reproduce the dilatant behavior of rocks and the growth of microfractures until their concentration is large enough to enable the development of a macroscopic fault. They also predict the existence of power law behavior, a characteristic of critical phenomena (13, 14), consistent with our experimental observations.

Experiments that detect and quantify energy releasing events before failure, such as those using acoustic emissions (8, 9, 37) or direct visualization of microfractures by X-ray tomography (13), have documented complex behavior between initial yielding and final failure. Such observations cannot be readily reconciled with the Griffith or Mohr–Coulomb failure criteria but can be interpreted in terms of damage mechanics frameworks that describe the acceleration and localization of acoustic emissions before rock failure (9, 37). Damage models that account for the long-range interactions between brittle failure events (14, 35, 37) predict the acceleration of the rate of damage as the stress increases at a constant rate approaching failure, as observed in experiments (13, 28, 37). Such models make several predictions, including the amount of dilatancy, localization, and power law increases in the rate of damage accumulation and the size of the largest microfracture cluster when failure is approached; Renard et al. (13) observed all these predictions experimentally. Our results (Figs. 3 and 4) enable measurements of not only the total damage (i.e., the total volume of all of the fractures as was done in ref. 13) but also the change in volume of each individual microfracture (and the volumes of any new microfractures that formed), as well as the local changes in left-lateral and right-lateral shear for each differential stress increment. This provides 3D maps of the components (dilation, contraction, left-lateral shear, and right-lateral shear) of the incremental damage and how the components of the incremental damage changed with loading. The power law distribution of the increment damage volumes shows an exponent of $\beta \sim 0.5$ (Fig. 4*A*), and the increase of the incremental damage volumes approaching failure exhibits another power law with an exponent of $\alpha \sim 1.7$ (Fig. 4*B*). Both exponents are in agreement with a 2D numerical damage model (35) that predicts power law exponents of $\beta \sim 0.4$ and $\alpha \sim 1.8$.

The results of the present study quantify how macroscopic failure occurs through spatially asymmetric events (Fig. 1) that exhibit power law scaling as failure is approached and how these events pervade the specimen before failure. Crystalline rocks sustain brittle deformation in the seismogenic zone up to about 20 km depth. However, larger stresses, increased temperature, and the presence of fluids may activate additional deformation mechanisms such as subcritical crack growth or pressure solution creep. Therefore, extrapolation of our results to such depths should be done with caution. The spanning of a partially healed fault by the largest damage cluster could explain the occurrence of geochemical signals before earthquakes (38) because new long-range fluid flow pathways connected in 3 dimensions may be formed. The data presented here demonstrate that macroscopic dilation and compaction are coupled processes and that local dilation and compaction are spatially correlated and act in concert (Figs. 2 and 3). This correlation may arise because local dilation or compaction alters the stress field, particularly in neighboring volumes. For example, the growth and concomitant opening of a microfracture with diameter L primarily influences a volume of the order of L^3 surrounding the microfracture, as well as the long-range stress field. The resulting volume of influence produces both tensile stress shielding (an increase in compressive stress) and tensile stress amplification (a decrease in compressive stress) that affect the opening, closing, nucleation, and propagation of neighboring microfractures and pore volumes. When the entire volume (i.e., the core specimen in these experiments) has experienced a certain amount of pervasive damage, additional inelastic deformation drives localization (stage 4 in Fig. 2). These cooperative interactions lead to power law distributions of microfracture growth events at every increase of stress (Fig. 4).

Our data at the microscale quantify how failure depends on asymmetric damage development within the future failure zone and in the surrounding rock. Fig. 2*D* shows that when n_f microfractures open in response to an increment of strain caused by an increment in the differential stress, $\Delta\sigma_D$, close to failure, around $0.5n_f$ microfractures close, and $0.9n_f$ left-lateral shear events and $0.6n_f$ right-lateral shear displacement events occur. In the brittle crust, a balance between volume increasing/decreasing

events and between left-/right-lateral shear events may occur in the form of conjugate microseismicity and faulting or distributed deformation near complex fault geometries, as well as in the surrounding volume (26, 39). High-resolution earthquake catalogs in well-instrumented areas show that ongoing seismicity can occur in zones with width of the order of 10 km around major faults (1, 3). While the largest events occur on the main faults, off-fault seismicity and aseismic processes of the type documented in this study can play key roles in the localization or relocalization of faulting in geomaterials.

Materials and Methods

The experiment was performed at 24 °C on a dry cylindrical monzonite specimen of 10 mm length and 4 mm diameter, using a procedure similar to that of Renard et al. (13). The interfaces between the rock sample and the pistons of the rig were not lubricated. To capture snapshots of deformation, the experiment was conducted by increasing the differential stress (the difference between the axial stress, σ_1, and the confining pressure, σ_3) in steps of 8 MPa far from failure (1 to 140 MPa), then steps of 3 MPa (100 to 160 MPa), steps of 1.5 MPa (160 to 190 MPa), and steps of 0.75 MPa as failure at 205.5 MPa was approached (*SI Appendix*, Fig. S1). This enabled the changes in deformation and damage to be determined in sufficient detail as failure was approached and deformation and damage increased more rapidly with increasing differential stress. We acquired X-ray radiographs at a constant stress after each stress increment. Acquisition of the 2D radiographs required to construct a 3D data set took about 1.5 min. We did not find evidence for significant changes in structure during data acquisition, such as blurring of the distinct edges between void space and grains in the tomograms that would have indicated time-dependent subcritical crack growth in the specimen. A jacket made of Viton fluoropolymer elastomer encased the rock sample, and pressurized silicone oil applied the confining pressure of 25 MPa to this jacket. A series of 77 data sets of 1,600 radiographs were acquired at a voxel size of 6.5 μm, corresponding to the spatial resolution of the images. From the 2D radiographs, 3D volumes of the specimen were reconstructed in 16-bit grayscale following the same procedure as in ref. 19. The details of strain measurements are given in *SI Appendix*. The tomography data are available in ref. 40.

Microfracture shapes and sizes (Figs. 2 *A* and B and 4 and *SI Appendix*, Fig. S2) were imaged and extracted from the tomograms by applying the segmentation procedure described in ref. 12. Every segmented microfracture was identified in each tomogram, and its volume was calculated. Then, by comparing each pair of successive tomograms, the difference between the microfractures in these 2 volumes was extracted to determine the microfracture growth increments (schematically represented in light blue in Fig. 1) and decrements (shown in red in Fig. 1). The contributions of the microfracture volume increments and decrements to the total microfracture volume and the size distribution of the volume increments are shown in (Fig. 4 and *SI Appendix*, Fig. S2).

ACKNOWLEDGMENTS. The deformation apparatus was built by Sanchez Technology. Elodie Boller, Paul Tafforeau, and Alexander Rack provided advice on the design of the tomography setup. This study received funding from the Norwegian Research Council (project HADES, grant 250661). Y.B.-Z. acknowledges support from the US–Israel Bi-national Science Foundation (BSF Grant 2016043). The European Synchrotron Radiation Facility allocated beam time for the experiment (Long Term Proposal ES-295). Data storage was provided by UNINETT Sigma2 - the National Infrastructure for High Performance Computing and Data Storage in Norway (project NS9073K). The authors thank Jérôme Weiss, David Lockner, and Georg Dresen who provided useful suggestions on an early draft of this article.

1. E. Hauksson, W. Yang, P. M. Shearer, Waveform relocated earthquake catalog for southern California (1981 to June 2011). *Bull. Seismol. Soc. Am.* **102**, 2239–2244 (2012).
2. C. Wollin, M. Bohnhoff, P. Martínez-Garzón, L. Küperkoch, C. Raub, A unified earthquake catalogue for the Sea of Marmara Region, Turkey, based on automatized phase picking and travel-time inversion: Seismotectonic implications. *Tectonophysics* **747–748**, 416–444 (2018).
3. Y. Cheng, Z. E. Ross, Y. Ben-Zion, Diverse volumetric faulting patterns in the San Jacinto fault zone. *J. Geophys. Res.* **123**, 5068–5081 (2018).
4. Y. Ben-Zion, I. Zaliapin, Spatial variations of rock damage production by earthquakes in southern California. *Earth Planet. Sci. Lett.* **512**, 184–193 (2019).
5. W. F. Brace, B. W. Paulding, C. H. Scholz, Dilatancy in the fracture of crystalline rocks. *J. Geophys. Res.* **71**, 3939–3953 (1966).
6. C. H. Scholz, Microfracturing and the inelastic deformation of rock in compression. *J. Geophys. Res.* **73**, 1417–1432 (1968).
7. K. Mogi, Fracture and flow of rocks under high triaxial compression. *J. Geophys. Res.* **76**, 1255–1269 (1971).
8. D. Lockner, J. D. Byerlee, V. Kuksenko, A. Ponomarev, A. Sidorin, Quasi-static fault growth and shear fracture energy in granite. *Nature* **350**, 39–42 (1991).
9. S. Stanchits, S. Vinciguerra, G. Dresen, Ultrasonic velocities, acoustic emission characteristics and crack damage of basalt and granite. *Pure Appl. Geophys.* **163**, 975–994 (2006).
10. S. Peng, A. M. Johnson, Crack growth and faulting in cylindrical specimens of Chelmsford granite. *Int. J. Rock Mech. Min. Sci.* **9**, 37–86 (1972).
11. P. Tapponnier, W. F. Brace, Development of stress-induced microcracks in Westerly granite. *Int. J. Rock Mech. Min. Sci. Geomech. Abstr.* **13**, 103–112 (1976).
12. Z. Reches, D. A. Lockner, Nucleation and growth of faults in brittle rocks. *J. Geophys. Res.* **99**, 18159–18173 (1994).
13. F. Renard *et al.*, Critical evolution of damage toward system-size failure in crystalline rock. *J. Geophys. Res.* **123**, 1969–1986 (2018).
14. K. A. Dahmen, Y. Ben-Zion, J. T. Uhl, A micromechanical model for deformation in disordered solids with universal predictions for stress-strain curves and related avalanches. *Phys. Rev. Lett.* **102**, 175501 (2009).
15. R. H. Sibson, Implications of fault-valve behaviour for rupture nucleation and recurrence. *Tectonophysics* **211**, 283–293 (1992).
16. F. Renard, J. P. Gratier, B. Jamtveit, Kinetics of crack-sealing, intergranular pressure solution, and compaction around active faults. *J. Struct. Geol.* **22**, 1395–1407 (2000).
17. E. Tenthorey, S. F. Cox, H. F. Todd, Evolution of strength recovery and permeability during fluid–rock reaction in experimental fault zones. *Earth Planet. Sci. Lett.* **206**, 161–172 (2003).
18. F. Renard *et al.*, A deformation rig for synchrotron microtomography studies of geomaterials under conditions down to 10 km depth in the Earth. *J. Synchrotron Radiat.* **23**, 1030–1034 (2016).
19. F. Renard *et al.*, Dynamic in situ three-dimensional imaging and digital volume correlation analysis quantify strain localization and fracture coalescence in sandstone. *Pure Appl. Geophys.* **176**, 1083–1115 (2019).
20. A. Aydin, R. I. Borja, P. Eichhubl, Geological and mathematical framework for failure modes in granular rock. *J. Struct. Geol.* **28**, 83–98 (2006).
21. D. E. Moore, D. A. Lockner, The role of microcracking in shear-fracture propagation in granite. *J. Struct. Geol.* **17**, 95–114 (1995).
22. M. S. Paterson, T. F. Wong, *Experimental Rock Deformation—The Brittle Field* (Springer Science & Business Media, 2005).
23. E. Tudisco, E. Andò, R. Cailletaud, S. A. Hall, TomoWarp2: A local digital volume correlation code. *SoftwareX* **6**, 267–270 (2017).
24. M. F. Ashby, C. G. Sammis, The damage mechanics of brittle solids in compression. *Pure Appl. Geophys.* **133**, 489–521 (1990).
25. D. Lockner, T. Madden, A multiple-crack model of brittle fracture. 1. Non-time-dependent simulations. *J. Geophys. Res.* **96**, 19623–19642 (1991).
26. Y. Tal, B. Evans, U. Mok, Direct observations of damage during unconfined brittle failure of Carrara marble. *J. Geophys. Res.* **121**, 1584–1609 (2016).
27. J. S. Chester, F. M. Chester, A. K. Kronenberg, Fracture surface energy of the Punchbowl fault, San Andreas system. *Nature* **437**, 133–136 (2005).
28. H. O. Ghaffari, M. H. B. Nasseri, R. P. Young, Faulting of rocks in a three-dimensional stress field by micro-anticracks. *Sci. Rep.* **4**, 5011 (2014).
29. A. Clauset, C. R. Shalizi, M. Newman, Power-law distributions in empirical data. *Soc. Ind. Appl. Math. Rev.* **51**, 661–703 (2009).
30. Y. Ben-Zion, Collective behavior of earthquakes and faults: Continuum-discrete transitions, evolutionary changes, and corresponding dynamic regimes. *Rev. Geophys.* **46**, RG4006 (2008).
31. Y. Ben-Zion, M. Eneva, Y. Liu, Large earthquake cycles and intermittent criticality on heterogeneous faults due to evolving stress and seismicity. *J. Geophys. Res.* **108**, 2307 (2003).
32. J. W. Rudnicki, J. R. Rice, Conditions for the localization of deformation in pressure-sensitive dilatant materials. *J. Mech. Phys. Solids* **23**, 371–394 (1975).
33. W. R. Wawersik, C. Fairhurst, A study of brittle rock fracture in laboratory compression experiments. *Int. J. Rock Mech. Min. Sci. Geomech. Abstr.* **7**, 561–575 (1970).
34. L. Girard, D. Amitrano, J. Weiss, Failure as a critical phenomenon in a progressive damage model. *J. Stat. Mech.* **2010**, P01013 (2010).
35. V. Lyakhovsky, Y. Ben-Zion, A. Agnon, Distributed damage, faulting, and friction. *J. Geophys. Res.* **102**, 27635–27649 (1997).
36. Y. Ben-Zion, V. Lyakhovsky, Accelerated seismic release and related aspects of seismicity patterns on earthquake faults. *Pure Appl. Geophys.* **159**, 2385–2412 (2002).
37. C. C. Vu, D. Amitrano, O. Plé, J. Weiss, Compressive failure as a critical transition: Experimental evidence and mapping onto the universality class of depinning. *Phys. Rev. Lett.* **122**, 015502 (2019).
38. H. Wakita, Geochemical challenge to earthquake prediction. *Proc. Natl. Acad. Sci. U.S.A.* **93**, 3781–3786 (1996).
39. D. R. Faulkner, T. M. Mitchell, D. Healy, M. J. Heap, Slip on 'weak' faults by the rotation of regional stress in the fracture damage zone. *Nature* **444**, 922–925 (2006).
40. F. Renard, Data from "Volumetric and shear processes in crystalline rock during the approach to faulting." Norstore. https://doi.org/10.11582/2018.00023. Deposited 20 August 2018.

PNAS
www.pnas.org

Supplementary Information for

Volumetric and shear processes in crystalline rock approaching faulting

François Renard, Jessica McBeck, Neelima Kandula, Benoît Cordonnier, Paul Meakin, and Yehuda Ben-Zion

Corresponding author: François Renard
Email: francois.renard@geo.uio.no

This PDF file includes:

Text: Strain measurements
Table S1
Figs. S1 to S2
Captions for movies S1 to S2

Other supplementary materials for this manuscript include the following:

Movies S1 to S2

www.pnas.org/cgi/doi/10.1073/pnas.1902994116

Table S1: List of symbols and parameters used in the Figures 4 and S2

Symbol	Description and unit
σ_1	axial stress (MPa)
$\sigma_3 = \sigma_2$	confining pressure (MPa)
$\sigma_D = (\sigma_1 - \sigma_3)$	differential stress (MPa)
σ_D^f	differential stress at failure (MPa)
$\Delta\sigma_D = \sigma_D^f - \sigma_D$	differential stress at failure minus differential stress (MPa)
$\Delta_D = (\sigma_D^f - \sigma_D)/\sigma_D^f$	stress control parameter that measures the distance to failure (without unit)
φ	void fraction (i.e. porosity) of the sample (without unit)
φ_i	initial porosity before deformation (without unit)
D_φ	damage volume fraction equal to $\frac{\varphi-\varphi_i}{1-\varphi_i}$ (without unit)
n_f	number of microfractures that open during a stress step
α, β	exponents of power laws (Figure 4)
$\nabla\cdot\Delta\mathbf{u}$	divergence of the incremental displacement field calculated using digital volume correlation, used as a proxy of the volumetric strain
$\nabla\times\Delta\mathbf{u}$	curl of the incremental displacement field calculated using digital volume correlation, used as a proxy of the shear strain
$\varepsilon_{zz}^M, \varepsilon_r^M$	macroscopic axial and radial strains (without unit)
Δ_n	node spacing in the digital volume correlation calculation (m)
d	incremental shear displacement calculated using the digital volume correlation calculation (m)
δv^+	positive (microfracture opening) volume increment (m^3)
δv^-	negative (microfracture closing) volume increment (m^3)
$\Sigma\delta v$	total microfracture volume increase in the sample at a given state of differential stress, corresponding to $\Sigma\delta v = \lvert\Sigma\delta v^+\rvert - \lvert\Sigma\delta v^-\rvert$ (δv^- is a negative volume change)
V	volume of the sample (m^3)

Text: Strain measurements

Strain in the sample was measured by using three complementary techniques. Measuring the specimen dimensions during deformation from the tomograms quantified macroscopic radial and axial strain (Figs. 2A, SI Appendix, Fig. S1 and Movie S1). We quantified strain heterogeneities in the sample in situ by: 1) calculating three-dimensional displacements fields via digital volume correlation (Figs. 2C-D, 3, SI Appendix, Movie S2); and 2) segmenting the microfractures from the host rock to track the evolving volume of microfractures (Figs. 2A, 2B, 4, SI Appendix, Fig. S2 and Movie S1). The macroscopic axial strain, ε_{zz}^{M}, was calculated from the distance between the two pistons visible in the tomograms inset in SI Appendix, Fig. S1). We verified that the axial strain was equal to the displacement of the piston measured using a displacement sensor installed on the rig, after correction for the deformation of the rig and the pistons (SI Appendix, Fig. S1). The macroscopic radial strain, ε_{r}^{M}, was determined by measuring the diameter of the sample at six different positions on each tomogram and by calculating the average value (SI Appendix, Fig. S1). The macroscopic volumetric strain at the onset of failure, $(\varepsilon_{zz}^{M} + 2\varepsilon_{r}^{M})$, was equal to 2.1%, and the volume fraction of microfractures was 1.4%. The difference between these two quantities is attributed primarily to the presence of microfractures with apertures below the resolution of the X-ray tomography images. The volumes of pre-existing microfractures and other voids present before the differential stress was applied must have changed during the experiment, as the non-linear strain-stress relationship and relatively small effective Young's modulus at differential stresses less than 40 MPa suggests. However, the volumetric strain was very small until yielding commenced at a differential stress of 178 MPa, and this implies that pre-existing voids contributed little to the volumetric strain at the onset of failure.

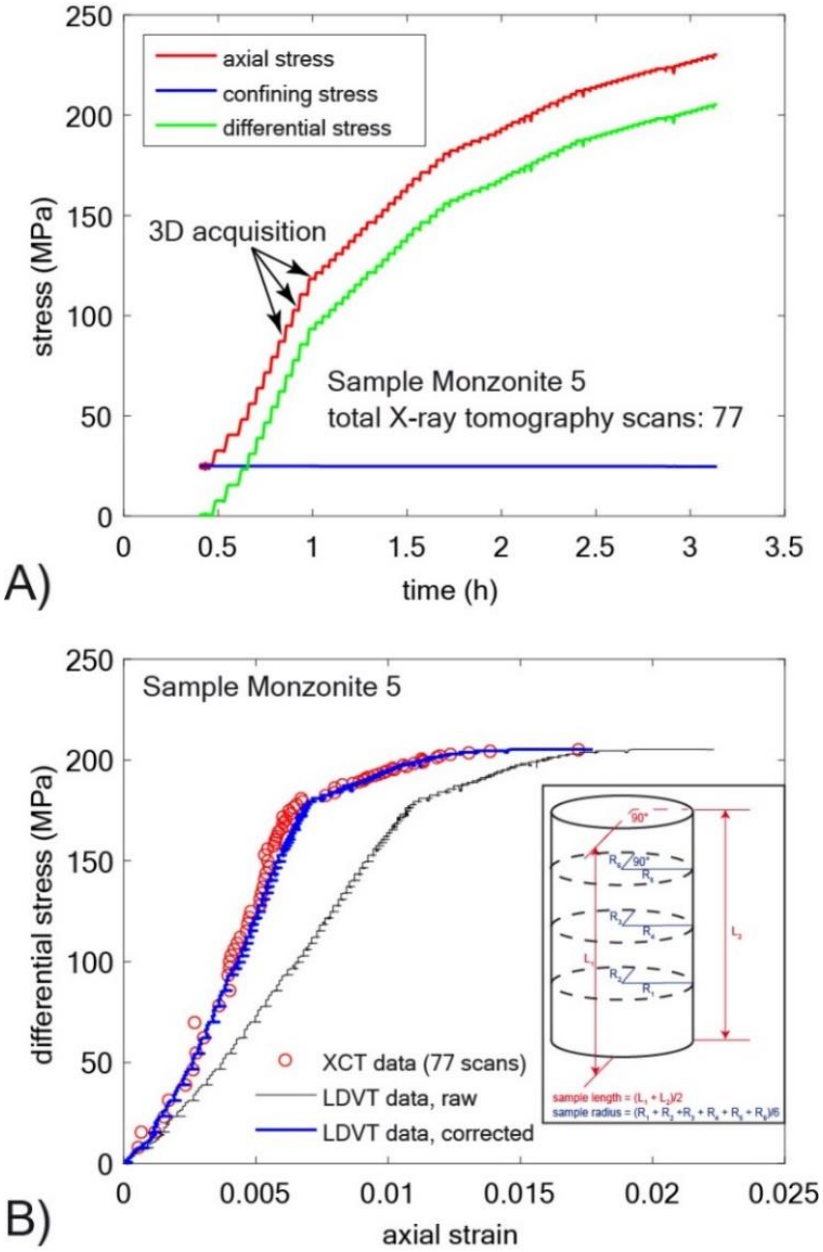

Fig. S1. Stress history and strain measurements. A) Stress history during deformation of the quartz-rich monzonite sample. The top of each step in the axial stress curve corresponds to one of the 77 X-ray tomography acquisitions. B) Comparison of measurement of the axial strain by using: 1) direct measurement of the shortening of the specimen using three-dimensional images (red circles); and 2) the linear variable differential transformer (LVDT) displacement sensor (black curve) installed on the Hades rig (Renard et al., 2016). The LDVT measurements were corrected to account for the elastic deformation of the rig and the pistons (blue curve). Inset: Procedure used to measure the average length and radius of the core sample (the radius was measured in two mutually perpendicular directions within three planes perpendicular to the axial direction).

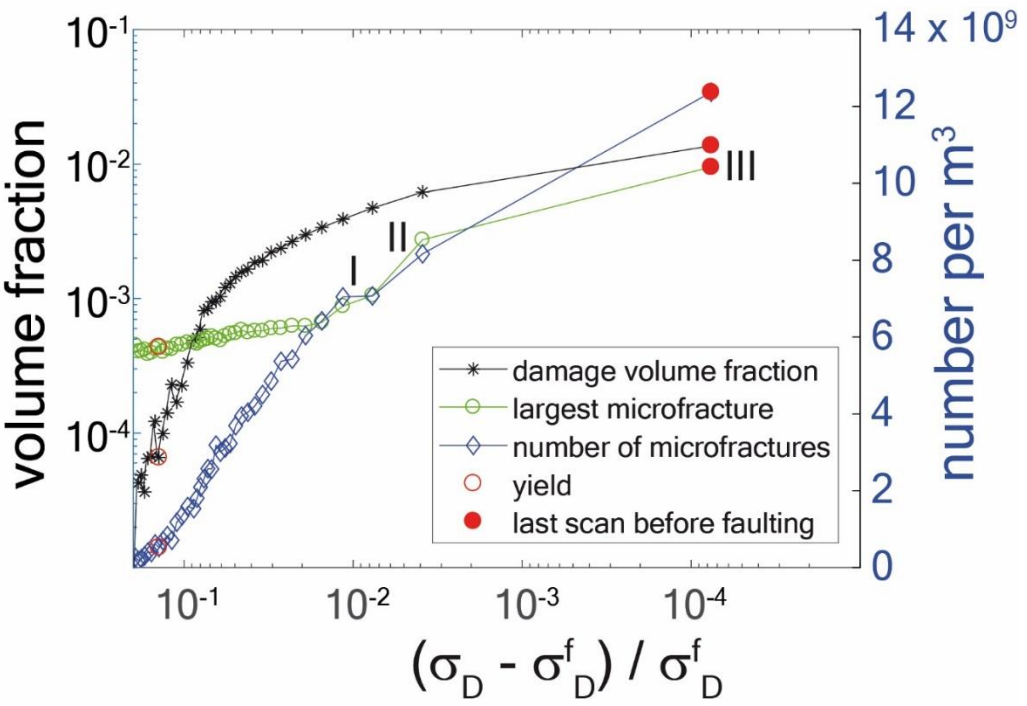

Fig. S2. Microfracture volume evolution prior to failure in crystalline rock. Evolution of the damage volume fraction (i.e. volume of microfractures divided by volume of the sample), number of microfractures per cubic meter and volume fraction of the largest microfracture cluster as failure was approached (σ_D^f: differential stress at failure). The numbers I, II, III correspond to the three differential stresses at which the views of the largest microfracture cluster are shown in the inset of Fig. 2A.

Movie S1. Deformation of the specimen and damage development prior to failure. Left: three-dimensional rendered view of the specimen with the rock matrix shown in gray shades and the microfracture porosity shown in blue. Top right: differential stress versus axial and radial strains. The open red circle shows the yield point and the full red circle shows the stress at failure. Bottom right: Mohr diagram throughout loading. The thick black line shows the Coulomb failure criterion using a cohesion of 49.7 MPa and internal friction of 0.6, which were estimated from the data and from the deformation of two other samples determined in a previous study (Renard et al., 2018).

Movie S2. Spatial distribution of positive and negative divergence and positive and negative curl magnitudes above the 95th percentile of each incremental strain population normalized by the incremental macroscopic axial strain difference, $\Delta\varepsilon_{zz}^{M}$, between the successive pairs of tomograms used to determine the incremental strain population. A-D) The diameters of the spheres are proportional to the magnitudes of $\boldsymbol{\nabla} \cdot \Delta\boldsymbol{u}$ and $\boldsymbol{\nabla} \times \Delta\boldsymbol{u}$, which were calculated at the digital volume correlation analysis nodes. A) Gray spheres show the negative divergence (compaction); B) blue spheres show positive divergence (dilation); C) pink spheres show negative curl, and D) red spheres show positive curl. E) Axial strain versus differential stress with vertical lines showing the differential stress and axial strain of the pair of tomograms used to determine the incremental displacement fields by DVC analysis. Sum (F), mean (G), and number of values (H) within population of incremental strain calculated from digital volume correlation analysis. F-H) The values are normalized by the value of the first digital volume correlation increment of the experiment, and shown as a function of the macroscopic axial strain at which the second scan used in the digital volume correlation analysis was acquired.

References

1. Renard F, et al. (2016) A deformation rig for synchrotron microtomography studies of geomaterials under conditions down to 10 km depth in the Earth. *Journal of Synchrotron Radiation* 23:1030-1034.

2. Renard F, et al. (2018) Critical evolution of damage toward system-size failure in crystalline rock. *Journal of Geophysical Research: Solid Earth* 123. https://doi.org/10.1002/2017JB014964.

Manuscript 4

Isolating the factors that govern fracture development in rocks throughout dynamic in situ X-ray tomography experiments

Jessica McBeck, **Neelima Kandula**, John M. Aiken, Benoît Cordonnier, and François Renard.

Geophysical Research Letters 46, no. 20: 11127-11135 (2019).

AGU100 ADVANCING EARTH AND SPACE SCIENCE

Geophysical Research Letters

RESEARCH LETTER
10.1029/2019GL084613

Isolating the Factors That Govern Fracture Development in Rocks Throughout Dynamic In Situ X-Ray Tomography Experiments

Jessica McBeck[1], Neelima Kandula[1], John M. Aiken[2,3], Benoît Cordonnier[1,4], and François Renard[1,5]

[1]Physics of Geological Processes, The Njord Centre, Department of Geosciences, University of Oslo, Oslo, Norway, [2]Center for Computing in Science Education, Department of Physics, University of Oslo, Oslo, Norway, [3]Department of Physics and Astronomy, Michigan State University, East Lansing, MI, USA, [4]Beamline ID19, The European Synchrotron and Radiation Facility, Grenoble, France, [5]University Grenoble Alpes, University Savoie Mont Blanc, CNRS, IRD, IFSTTAR, ISTerre, Grenoble, France

Key Points:
- We predict fracture growth in four X-ray tomography experiments using the machine learning method of logistic regression
- The best predictors of growth are the fracture size, length, aperture, and orientation and fracture network clustering
- Growing fractures are smaller in volume, shorter, thinner, more obliquely dipping from σ_1, and more clustered than closing fractures

Supporting Information:
- Supporting Information S1

Correspondence to:
J. McBeck,
j.a.mcbeck@geo.uio.no

Citation:
McBeck, J., Kandula, N., Aiken, J. M., Cordonnier, B., & Renard, F. (2019). Isolating the factors that govern fracture development in rocks throughout dynamic in situ X-ray tomography experiments. *Geophysical Research Letters*, *46*, 11,127–11,135. https://doi.org/10.1029/2019GL084613

Received 20 JUL 2019
Accepted 25 SEP 2019
Accepted article online 15 OCT 2019
Published online 29 OCT 2019

Abstract Centuries of work have highlighted the importance of several characteristics on fracture propagation. However, the relative importance of each characteristic on the likelihood of propagation remains elusive. We rank this importance by performing dynamic X-ray microtomography experiments that provide unique access to characteristics of evolving fracture networks as rocks are triaxially compressed toward failure. We employed a machine learning technique based on logistic regression analysis to predict whether or not a fracture grows from 14 fracture geometry and network characteristics identified throughout four experiments on crystalline rocks in which thousands of fractures propagated. The characteristics that best predict fracture growth are the length, thickness, volume, and orientation of fractures with respect to the external stress field and the distance to the closest neighboring fracture. Growing fractures tend to be more clustered, shorter, thinner, volumetrically smaller, and dipping closer to 30–60° from the maximum compression direction than closing fractures.

Plain Language Summary What controls fracture growth in rocks? Previous work highlights the importance of many characteristics on the likelihood of fracture growth but has not ranked the importance of these characteristics. We use triaxial compression experiments of rocks and machine learning to predict fracture growth using measures of the fracture network clustering and fracture size, shape, and orientation. The characteristics that are the best predictors of fracture growth are the fracture length, thickness, volume, and orientation and distance to the nearest fracture. Fractures that grow (increase in volume) during each increase in differential stress are shorter, thinner, smaller in volume, and more clustered than fractures that close (decrease in volume).

1. Introduction

Predicting when and how faults propagate and interact is a fundamental challenge in geosciences. Over the past century, analyses have isolated the importance of several factors on fracture development, including the spatial distribution and orientation of fractures with respect to an external stress field, the proximity to pre-existing weaknesses and neighboring fractures, and the length, aperture, and shape of fractures (e.g., Anderson, 1942; Dahlen, 1984; Griffith, 1921; Hubbert, 1951; Irwin, 1957; Raju & Newman, 1979; Rybicki & Kanninen, 1977; Sih, 1974). However, such analyses were not able to compare the relative importance of these factors on the likelihood of fracture propagation to each other. This gap in knowledge causes scientists to categorize a multitude of properties of fault networks in order to predict fault interaction.

In situ dynamic X-ray microtomography experiments reveal precise details of fracture growth and coalescence within crustal rocks under triaxial compression (e.g., Renard et al., 2017, 2018). Time series of 3-D X-ray attenuation fields, that is, tomograms, captured after loading steps during triaxial compression experiments reveal the geometries of individual opening fractures within evolving fracture networks as the rocks are driven toward macroscopic failure (Figure 1). Algorithms that track each identified fracture indicate how individual fractures interact and grow within the network (Kandula et al., 2019). These experiments and postprocessing techniques provide unprecedented access to factors that control microfracture

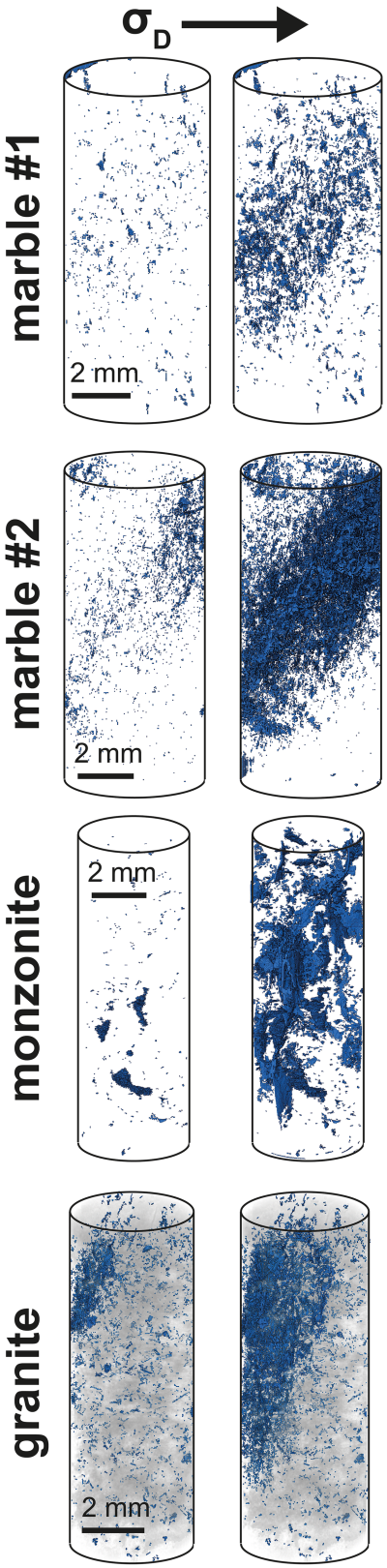

Figure 1. Fracture development within in situ X-ray tomography triaxial compression experiments. Snapshots of fracture networks (blue) at (left) lower and (right) higher differential stresses during four analyzed experiments on marble, monzonite, and granite. With increasing differential stress, some fractures lengthen and open, while others close, and the fracture network becomes increasingly clustered.

development to varying degrees. Machine learning techniques enable quantifying the importance of each factor on fracture development. In recent years, geoscientists have used machine learning to understand and predict earthquakes in the lab and the field (e.g., Asencio-Cortés et al., 2017; Asim et al., 2017; Bergen et al., 2019; Reyes et al., 2013; Rouet-Leduc et al., 2017). However, none of these analyses have yet attempted to predict the likelihood of fracture propagation through intact rock, nor have they rank the importance of recognized controls on fracture development.

Here we aim to determine the importance of a suite of fracture characteristics on the likelihood of fracture propagation (Figure S1 in the supporting information). To achieve this goal, we built and trained logistic regression models (e.g., Cox, 1958; Hosmer et al., 2013) that predict whether an individual fracture will grow using measures of its size (i.e., length, aperture, and volume), shape (i.e., anisotropy and elongation), orientation, and position within the fracture network (i.e., clustering) (Figure S2). Then we used recursive feature elimination (e.g., Guyon et al., 2002) to identify the fracture characteristics that are the best predictors of propagation (Figure S1). Finally, we tracked the statistical properties of these predictors from the onset of loading until macroscopic failure to pinpoint the quantities that characterize fractures that are growing (gaining volume) and those that are closing (losing volume). Determining the criteria that exert the greatest impact on fracture network evolution may improve seismic hazard assessments of natural fault systems. Rather than categorizing many and perhaps insignificant fault network properties, more cost- and time-efficient field studies could focus on the properties that exert the greatest influence on fracture development.

2. Methods

2.1. Experimental Design and Fracture Tracking

We analyze results from four rock deformation experiments that include rock types representative of low-porosity crystalline rocks within the continental crust: two on Carrara marble, one on monzonite, and one on Westerly granite (Table S1). In each experiment, we increased the differential stress, σ_D, applied to a 1-cm-tall and 0.5-cm-wide rock core, with σ_1 parallel to the axis of the core, while the confining stress, $\sigma_2 = \sigma_3$, was held constant until the core macroscopically failed. Under constant confining stress, we increased the axial stress in steps of 0.5–5 MPa, with smaller steps closer to failure, and acquired a time series of X-ray tomograms at a resolution of 6.5 μm per voxel edge, at beamline ID19 at the European Synchrotron Radiation Facility using the Hades deformation apparatus (Renard et al., 2016; Table S1).

We segmented the tomograms into fractures and intact rock using a nonlocal mean filter and several additional image processing techniques developed by Renard et al. (2018). Tracking an individual fracture from the moment when it appears to when it closes or merges with another fracture, or when the rock macroscopically fails, is a nontrivial problem. As the core shortens axially and expands radially, fractures may translate in space in the absence of propagation, opening or closure. Kandula et al. (2019) developed algorithms to solve this nontrivial problem and track individual fractures (labeled with unique identifiers) throughout microtomography experiments. We employed this approach to track fractures here and followed the evolution of thousands of fractures toward failure in each sample.

2.2. Feature Extraction From Fractures and Fracture Networks

In each experiment, we tracked the evolution of every fracture using the voxel locations of the fractures identified with the tracking algorithm (Table S1). For each fracture, we calculated 14 measures that quantify the geometry, size, and orientation of each fracture or its proximity to other fractures within the fracture network. We selected these measures because previous formulations of linear elastic fracture mechanics predict the likelihood of fracture growth using these characteristics (e.g., Anderson, 1942; Dahlen, 1984; Griffith, 1921; Hubbert, 1951; Irwin, 1957; Raju & Newman, 1979; Rybicki & Kanninen, 1977; Sih, 1974).

We quantify the proximity of each fracture to the others in the network by calculating the minimum, mean, and median distances from the centroid of each fracture to all the other fracture centroids in the network. We also calculated these values for each fracture using the 25th percentile of other fractures with centroids nearest to its centroid. Analyzing these two sets of distance measures indicates whether the local or global fracture network is a better predictor of fracture development.

To characterize the geometry of each fracture, we calculated the covariance matrix of the set of voxels that represent each fracture and the corresponding eigenvectors and eigenvalues. The covariance matrix is

equivalent to the inertial moment tensor if each voxel corresponds to a point mass of unity located at its centroid. The eigenvectors define the orientations relative to a Cartesian coordinate system. The eigenvalues define the size and shape of each fracture (Figure S2). The largest and smallest eigenvalues are not strictly equal to, but represent, the length and aperture of the fractures. From the eigenvalues, we calculated the anisotropy (1 minus the minimum eigenvalue divided by the maximum eigenvalue) and elongation (1 minus the intermediate eigenvalue divided by the maximum eigenvalue) of each fracture. We also included the volume of each fracture as a model feature. To determine whether or not a fracture grows or closes from one scan to the next (after a stress step increase), we calculated the change in volume of the fracture. This binary classification of whether a fracture grows or closes is the outcome that we trained the models to predict.

One may expect that boundary effects due to friction between the pistons and core interfaces could influence the location of the population of closing and growing fractures. To assess this influence, we examined the spatial distribution of these populations of fractures relative to the piston positions at the top and bottom of the sample (Figure S3). The distributions of vertical positions of the growing and closing fractures are similar to each other in each experiment. Closing fractures are not preferentially located near the pistons, as could be expected. Boundary effects do not appear to influence whether fractures grow or close.

2.3. Logistic Regression Models

We used one of the most common linear classification methods to predict the binary outcome of fracture growth or closure: logistic regression (e.g., Cox, 1958). Logistic regression is a statistical approach that uses a logistic function to produce a binary (true/false) prediction from input data (i.e., features). We choose to develop logistic regression models because we wished to predict the binary outcome of whether a fracture grew or not. In addition, logistic regression provides output that is relatively easy to interpret because the model assumes a linear trend between model features (e.g., Hosmer et al., 2013).

In this study, we developed individual logistic regression models for each experiment, and 50 individual models on randomly selected subsets of the data for each experiment. The number of identified growing fractures exceeds the number of closing fractures in each experiment. To account for this imbalance in determining the model success, and to aid the robustness of the results, we built 50 individual logistic regression models from randomly selected subsets of the data of each experiment. We used all of the fractures identified as closing fractures, counted the number of these fractures, and then randomly selected the same number of growing fractures. Then we trained each model using 80% of the fractures identified at each stress step and tested the success of the model with the remaining 20% of the data in each of the experiments. The training and testing data sets were entirely separate in that we only included data from a particular fracture at a given stress step in either the training or testing data sets. We performed a cross-validated grid search over the parameters of the models to find the best set of parameters. We employed the Python Scikit-learn library to build, train, and test these models (Pedregosa et al., 2011).

We used recursive feature elimination (Guyon et al., 2002) with threefold cross validation (RFECV) to identify the best explanatory, or predictive, features of the model. RFECV orders the features by coefficient magnitude (smallest to largest) and then removes the features one by one, refitting and scoring the model using a selected scoring metric. As features are removed, the scoring metric typically remains the same or decreases until the model has an acceptable minimum score. The remaining features represent the characteristics that are the best predictors of the outcomes of the model. Here we used the accuracy scoring metric for RFECV. Accuracy is defined as the number of true model predictions out of the number of total (true and false) predictions.

3. Results

3.1. Success of Logistic Regression Models

We developed and trained logistic regression models for the four experiments to predict whether a fracture grows or closes using 14 characteristics of each fracture. We assess the success of the models using the recall and precision scoring metrics. The recall reflects the positive predictive value, while the precision reflects the sensitivity (e.g., Müller & Guido, 2016). Higher scores indicate greater model success, with scores of 1

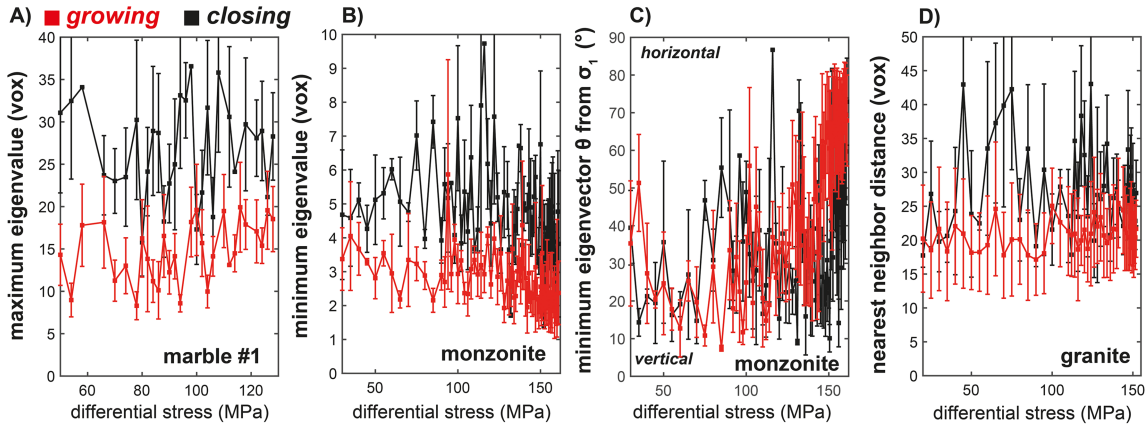

Figure 2. Evolution of controls on fracture growth. Recursive feature elimination highlights the best predictors of growth (Figure S6): the (a) maximum and (b) minimum eigenvalues of the fractures, (c) the orientation of the eigenvector with the minimum eigenvalue relative to σ_1, and (d) the nearest-neighbor distance from each fracture. Red and black lines and markers show the mean ± one standard deviation of population of fractures that are growing and closing between subsequent stress steps. The lengths are in units of the edge length of the voxels of the tomograms (1 vox. = 6.5 μm).

indicating sets of perfect model predictions. We report the mean ± one standard deviation of the scores produced by the 50 models for each experiment (Figure S4).

The recall and precision of the models increase as we remove fractures that are growing or closing by increasing percentages of their volume (i.e., data removal threshold; Figures S4 and S5). This increase in performance may arise from the segmentation procedure used to extract fractures. Segmentation may influence the model success if a fracture translates in space between scan acquisitions (and thus stress steps) but does not grow or close. This translation may produce apparent changes in the number of voxels included in the fracture (volume) due to differences in the intersection of the fracture with the predefined voxel grid of the scan. The increasing success of the models with increasing data removal threshold suggests that differences in fracture segmentation across subsequent tomograms may produce artificial changes in volume that do not reflect fracture propagation, opening or closing. Although this thresholding reduces the amount of data used to train and test the models, it improves the quality of the data and thus the models' success.

In the subsequent exploration of the importance of each characteristic on the predictions of the models, we focus on populations of fractures growing or closing by more than 50% of their volume in one stress step, from one scan to the next. For fractures growing or closing more than 50% of their volume, the recall and precision scores are 0.70–0.80 (Figure S4). Consequently, this threshold produces models with acceptably high success rates and includes a larger population of growing and closing fractures than higher thresholds.

3.2. Importance of Fracture Characteristics on Growth

To extract the fracture network characteristics that are the best predictors of fracture development, we employed recursive feature elimination with cross validation (RFECV). This technique ranks the importance of each feature on the model predictions, indicating the best explanatory, or most predictive, features (Guyon et al., 2002). We used recursive feature elimination to select the features that are the best predictors of fracture growth in the 50 independent logistic regression models of the four experiments, producing 200 rankings of the importance of each feature.

The most important features selected by recursive feature elimination in the 50 models of the four experiments include characteristics of the geometry of each fracture, its orientation with respect to the applied stress, and the clustering of the local and global fracture network (Figure S6). We identify the most important features across all the experiments as those that produce >75% of the maximum cumulative importance. These features include the volume of the fracture; the largest, intermediate, and minimum eigenvalues; the orientation of the eigenvector with the minimum eigenvalue; and the minimum distance between fracture centroids.

We now focus on the differences between these characteristics of the population of fractures that are growing and closing. Figure 2a shows the mean ± one standard deviation of the maximum and minimum

eigenvalues, indicative of the fracture length and aperture, of the growing and closing fractures in the marble and monzonite experiments. The maximum eigenvalues of closing fractures are greater than the maximum eigenvalue of growing fractures in these experiments (Figure 2a). In contrast to the expectations from stress intensity formulations, shorter fractures are more likely to grow than are longer fractures. Similarly, the minimum eigenvalues of closing fractures are larger than the minimum eigenvalues of growing fractures (Figure 2b). Thinner fractures are more likely to grow than are thicker fractures. Consistent with these trends, closing fractures tend to have higher volumes and larger intermediate eigenvalues than do growing fractures.

Figure 2c shows the mean ± one standard deviation of the orientation of the eigenvector with the minimum eigenvalue of the growing and closing fractures in the monzonite experiment. This orientation is the orientation of smallest dimension of the fracture relative to the principal stress directions. Both closing and growing fractures have similar ranges of this orientation until the rock begins to approach failure. However, above a differential stress of 125 MPa, the population of closing fractures tend to have these eigenvectors near to parallel to the maximum compressive stress, $\sigma 1$ (Figure 2c). Growing fractures tend to have these eigenvectors at more oblique orientations relative to closing fractures, from 30° to 80° from σ_1.

Figure 2d shows the mean ± one standard deviation of the nearest-neighbor distance between sets of growing and closing fractures in the granite experiment. The nearest-neighbor distances of growing fractures are smaller than the distances of closing fractures (Figure 2d). Fractures that grow near another fracture have a greater likelihood of propagation than do fractures that grow at greater distances from other fractures in the network.

4. Discussion

This analysis of four in situ triaxial compression dynamic microtomography experiments indicates that the characteristics that provide the most accurate predictions of fracture growth are the following: the volume and eigenvalues of the fracture (indicative of fracture length and aperture), the orientation of the eigenvector with the smallest eigenvalue (fracture orientation), and the nearest-neighbor distance between fracture centroids (fracture network clustering).

4.1. Fracture Network Clustering

The mean and median distances to nearby fractures (within the closest 25th percentile of the distances between fractures) are not strong predictors of fracture development, and neither are the mean and median distances to all of the identified fractures in the system (Figure S6). The only clustering measure that ranks highly in importance is the distance to the closest fracture. More clustered fractures, which are close to at least one other fracture, are more likely to propagate than are more dispersed fractures (Figure 2d).

This trend is consistent with field observations indicating that an earthquake that begins on one fault is more likely to trigger a seismic event on an adjacent fault if the faults are within a few kilometers of each other than if the faults are further apart (Wesnousky, 2006). Although earthquakes are primarily shear rupture events and the experimental fracture growth we detect must contain opening-mode deformation, the trends observed in earthquake triggering and experimental fracture growth are similar because both opening-mode and shear deformation perturb the local stress and strain field.

The elastic perturbation of the local stress and strain fields due to slip and opening allow fractures and faults to interact at some distance away from each other and not only when their segments comprise one continuous fault surface. This interaction causes nearby fault segments to produce cumulative along-strike slip distributions that match the slip distributions of individual faults, with approximately bell-shaped or elliptical distributions (e.g., Bürgmann et al., 1994). Similarly, the power law relationship observed in X-ray tomography experiments between the distance to macroscopic failure and fracture volume may arise from long-range elastic interactions between fractures in the network (Kandula et al., 2019).

Our results suggest that field analyses that aim to understand fracture development should focus on the nearest-neighbor distance between fractures. These analyses may not need to consider the position of the fracture within the larger fault network to provide robust predictions of fault development, but only the distance to the closest fault. This result may simplify the difficult task of selecting the appropriate system size

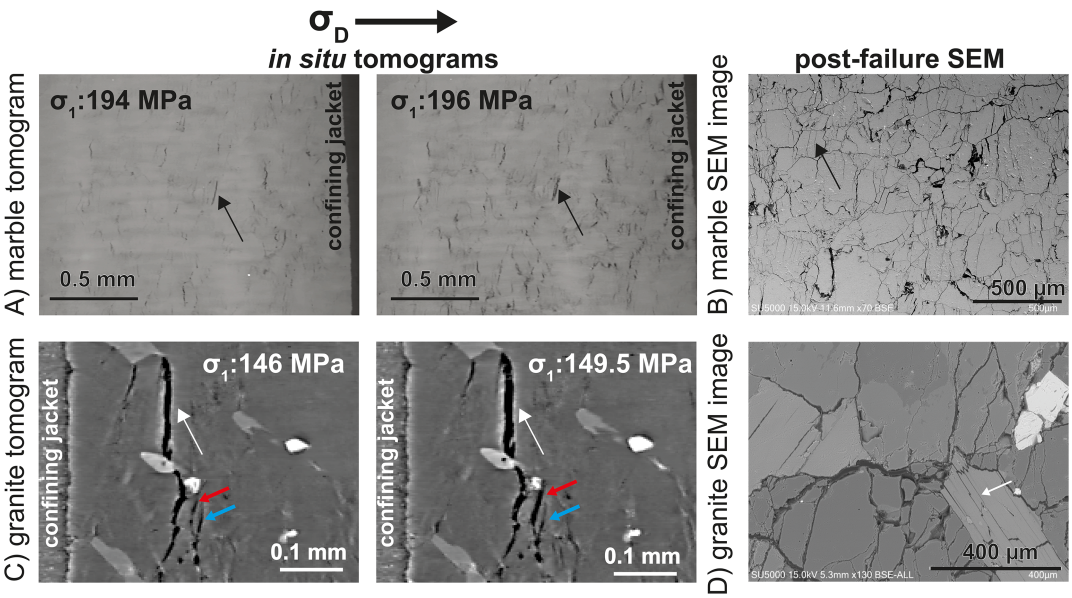

Figure 3. Influence of heterogeneities on fracture propagation. Two-dimensional slices of in situ X-ray tomograms of the (a) marble and (c) granite experiments, and scanning electron microscopy images of post-failure (b) marble and (d) granite cores recovered after experiments. (a, b) Black arrows indicate fractures pinned by grain boundaries. (c, d) White arrows indicate fractures impeded by minerals and grain boundaries. (c) Red arrow shows fracture that grows near to fracture that closes (blue arrow).

and thus population of faults to assess. However, differences between the observability of experimental fracture networks and crustal fault networks may limit the applicability of this finding.

Another key factor in this analysis is the appropriate length scale of faults to consider. Whereas we can detect all of the open fractures in the tomograms, field analyses must select the appropriate length scale of faults to consider when searching for nearest neighbors. Nominally intact crustal rock contains preexisting fractures surrounding plate boundary faults, so potential analyses of the nearest-neighbor distance between faults in the field must decide on the spatial scale of faults to include.

4.2. Fracture Length

Our analysis shows that closing fractures tend to have greater maximum eigenvalues (length) than do growing fractures (Figure 2a). The stress intensity factor at a fracture tip indicates the likelihood of fracture

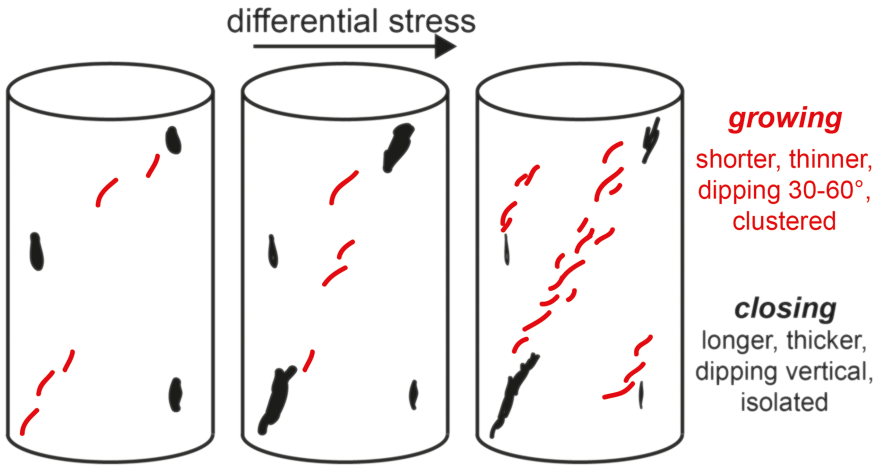

Figure 4. Characteristics of growing and closing fractures. Schematic illustration of characteristics of fractures that are growing (red) and closing (black) with increasing differential stress. Growing fractures tend to be shorter, thinner, more obliquely dipping to σ_1, and clustered than do closing fractures. Fractures may transition from growing to closing as fractures coalesce, forming thicker fractures that are less optimally oriented for slip. New fractures may nucleate and grow near closing fractures as closure amplifies local stress concentrations.

propagation using the length and shape of the fracture (e.g., Isida, 1971; Raju & Newman, 1979). Longer mode I fractures produce greater stress intensity factors, increasing the likelihood of propagation in the absence of changes in the external stress field. Our results conflict with the expectations of linear elastic fracture mechanics because the fractures do not develop in isolation in our experiments. As fractures propagate and coalesce, they modify the local stress field, producing and propagating into regions with varying magnitudes of normal and shear stress. Shorter fractures may have a higher likelihood of fracture propagation than do longer fractures because they tend to be more clustered than do longer fractures, as measured with the nearest-neighbor distance (Figure 2d).

The heterogeneous strength distribution of the rocks may also impact the observed trend of shorter fractures growing and longer fractures closing. Two-dimensional slices of tomograms and scanning electron microscope images show intragranular fractures that terminate at the edges of grain boundaries in the marble experiment (Figures 3a and 3b). These fractures likely exploit cleavage planes within the calcite grains but then arrest at the grain boundaries because these boundaries have higher tensile strength than the cleavage planes. Similarly, slices of the tomograms of the granite experiment show fractures that terminate at the edges of biotite grains (Figures 3c and 3d).

Tapponnier and Brace (1976) also observed the impeding influence of biotite relative to the surrounding quartz and feldspar in granite. In the field, fault propagation may also be modulated by heterogeneous strength distributions, such as foliated rock that produces well-defined directions of lower and higher strength (e.g., McBeck et al., 2017).

4.3. Fracture Aperture

In addition to fracture length, fracture aperture is among the best predictors of fracture development in these experiments (Figure S6). Similar to the trend observed for fracture length, growing fractures tend to have smaller minimum eigenvalues than closing fractures (Figure 2B). These trends are consistent with analytical formulations of the stress intensity factor because thinner fractures are predicted to develop higher stress intensity factors than thicker fractures (Isida, 1971). In addition, sharper crack tips are predicted to develop higher stress intensity factors than rounded crack tips (Huang & Li, 2004). Thinner fractures may tend to have sharper tips than thicker fractures. The trend of thinner fractures growing, and thicker fractures closing may also arise from the ability of thicker fractures to close by larger volumes along their smallest dimension than thinner fractures.

4.4. Fracture Orientation

Growing fractures tend to have more horizontal, perpendicular to σ_1, eigenvectors with the minimum eigenvalue than do closing fractures (Figure 2c). This trend may arise in part from the eigenvector with the maximum eigenvalue of fractures becoming more optimally oriented for sliding according to Mohr-Coulomb theory (Dahlen, 1984). Within the later stages of the monzonite experiment (100- to 150-MPa differential stress), the orientations of the long axis of the growing fractures match orientations that host the maximum Coulomb shear stress, τ/σ_n, 30–60° from σ_1, while the short axes of the closing fractures become perpendicular to σ_1 (Figure 2c).

5. Conclusions

Our analysis shows that growing fractures tend to be smaller in volume, shorter, thinner, more obliquely dipping from the main compressive stress direction, and more clustered, to at least one neighbor, than do closing fractures (Figure 4). Assuming that elastic interactions control the tendency for fractures to grow or close, we may cautiously extrapolate our results to crustal scales. Field analyses of crustal fault networks should focus on the length, orientation, and clustering of faults in order to robustly predict their likelihood of propagation. Such analyses may only need to consider the distance to the closest fault, rather than system-scale measures of clustering, for robust predictions of fault development.

Acknowledgments
We thank Elodie Boller, Paul Tafforeau, and Alexander Rack for providing advice on the design of the tomography setup and Sanchez Technology for building the deformation apparatus. Joachim Mathiesen, Paul Meakin, and Yehuda Ben-Zion provided suggestions on an early version of the manuscript that improved the study. The Norwegian Research Council funded this work (grant 272217). Beamtime was allocated at the European Synchrotron Radiation Facility (Long-Term Proposal ES-295). The Python scripts to build, train, and test the logistic regression models, and the corresponding experimental data, are available on GitHub (https://github.com/jmcbeck/Machine_Learning_Rock_Deformation). We thank Editor Lucy Flesch and two anonymous reviewers for suggestions that improved the manuscript.

References

Anderson, E. M. (1942). *The dynamics of faulting and dyke formation with applications to Britain*. Edinburgh and London: Oliver & Boyd. 15s
Asencio-Cortés, G., Martínez-Álvarez, F., Troncoso, A., & Morales-Esteban, A. (2017). Medium–large earthquake magnitude prediction in Tokyo with artificial neural networks. *Neural Computing and Applications*, *28*(5), 1043–1055. https://doi.org/10.1007/s00521-015-2121-7

Asim, K. M., Martínez-Álvarez, F., Basit, A., & Iqbal, T. (2017). Earthquake magnitude prediction in Hindukush region using machine learning techniques. *Natural Hazards*, *85*(1), 471–486. https://doi.org/10.1007/s11069-016-2579-3

Bergen, K. J., Johnson, P. A., Maarten, V., & Beroza, G. C. (2019). Machine learning for data-driven discovery in solid Earth geoscience. *Science*, *363*(6433). https://doi.org/10.1126/science.aau0323

Bürgmann, R., Pollard, D. D., & Martel, S. J. (1994). Slip distributions on faults: Effects of stress gradients, inelastic deformation, heterogeneous host-rock stiffness, and fault interaction. *Journal of Structural Geology*, *16*(12), 1675–1690. https://doi.org/10.1016/0191-8141(94)90134-1

Cox, D. R. (1958). The regression analysis of binary sequences. *Journal of the Royal Statistical Society: Series B: Methodological*, *20*(2), 215–232.

Dahlen, F. A. (1984). Noncohesive critical Coulomb wedges: An exact solution. *Journal of Geophysical Research*, *89*(B12), 10,125–10,133. https://doi.org/10.1029/JB089iB12p10125

Griffith, A. A. (1921). VI. The phenomena of rupture and flow in solids. Philosophical Transactions of the Royal Society of London. *Series A, Containing Papers of a Mathematical or Physical Character*, *221*(582-593), 163–198.

Guyon, I., Weston, J., Barnhill, S., & Vapnik, V. (2002). Gene selection for cancer classification using support vector machines. *Machine Learning*, *46*(1/3), 389–422. https://doi.org/10.1023/A:1012487302797

Hosmer, D. W. Jr., Lemeshow, S., & Sturdivant, R. X. (2013). *Applied logistic regression* (Vol. 398). Hoboken, NJ: John Wiley & Sons.

Huang, M., & Li, Z. (2004). Dislocation emission criterion from a blunt crack tip. *Journal of the Mechanics and Physics of Solids*, *52*(9), 1991–2003. https://doi.org/10.1016/j.jmps.2004.03.003

Hubbert, M. (1951). Mechanical basis for certain familiar geologic structures. *Geological Society of America Bulletin*, *62*(4), 355–372. https://doi.org/10.1130/0016-7606(1951)62[355:MBFCFG]2.0.CO;2

Irwin, G. (1957). Analysis of stresses and strains near the end of a crack traversing a plate. *Journal of Applied Mechanics*, *24*, 361–364.

Isida, M. (1971). Effect of width and length on stress intensity factors of internally cracked plates under various boundary conditions. *International Journal of Fracture Mechanics*, *7*(3), 301–316.

Kandula, N., Cordonnier, B., Boller, E., Weiss, J., Dysthe, D. K., & Renard, F. (2019). Dynamics of microscale precursors establish brittle-compressive failure as a critical phenomenon in Carrara marble. *Journal of Geophysical Research: Solid Earth*, *124*, 6121–6139. https://doi.org/10.1029/2019JB017381

McBeck, J., Cooke, M., & Madden, E. (2017). Work optimization predicts the evolution of extensional step overs within anisotropic host rock: Implications for the San Pablo Bay, CA. *Tectonics*, *36*, 2630–2646. https://doi.org/10.1002/2017TC004782

Müller, A. C., & Guido, S. (2016). *Introduction to machine learning with Python: A guide for data scientists*. Sebastopol, CA: O'Reilly Media, Inc.

Pedregosa, F., Varoquaux, G., Gramfort, A., Michel, V., Thirion, B., Grisel, O., et al. (2011). Scikit-learn: Machine learning in Python. *Journal of Machine Learning Research*, *12*(Oct), 2825–2830.

Raju, I. S., & Newman, J. C. Jr. (1979). Stress-intensity factors for a wide range of semi-elliptical surface cracks in finite-thickness plates. *Engineering Fracture Mechanics*, *11*(4), 817–829. https://doi.org/10.1016/0013-7944(79)90139-5

Renard, F., Cordonnier, B., Dysthe, D. K., Boller, E., Tafforeau, P., & Rack, A. (2016). A deformation rig for synchrotron microtomography studies of geomaterials under conditions down to 10 km depth in the earth. *Journal of Synchrotron Radiation*, *23*(4), 1030–1034. https://doi.org/10.1107/S1600577516008730

Renard, F., Cordonnier, B., Kobchenko, M., Kandula, N., Weiss, J., & Zhu, W. (2017). Microscale characterization of rupture nucleation unravels precursors to faulting in rocks. *Earth and Planetary Science Letters*, *476*, 69–78. https://doi.org/10.1016/j.epsl.2017.08.002

Renard, F., Weiss, J., Mathiesen, J., Ben-Zion, Y., Kandula, N., & Cordonnier, B. (2018). Critical evolution of damage toward system-size failure in crystalline rock. *Journal of Geophysical Research: Solid Earth*, *123*, 1969–1986. https://doi.org/10.1002/2017JB014964

Reyes, J., Morales-Esteban, A., & Martínez-Álvarez, F. (2013). Neural networks to predict earthquakes in Chile. *Applied Soft Computing*, *13*(2), 1314–1328. https://doi.org/10.1016/j.asoc.2012.10.014

Rouet-Leduc, B., Hulbert, C., Lubbers, N., Barros, K., Humphreys, C. J., & Johnson, P. A. (2017). Machine learning predicts laboratory earthquakes. *Geophysical Research Letters*, *44*, 9276–9282. https://doi.org/10.1002/2017GL074677

Rybicki, E. F., & Kanninen, M. F. (1977). A finite element calculation of stress intensity factors by a modified crack closure integral. *Engineering Fracture Mechanics*, *9*(4), 931–938. https://doi.org/10.1016/0013-7944(77)90013-3

Sih, G. C. (1974). Strain-energy-density factor applied to mixed mode crack problems. *International Journal of Fracture*, *10*(3), 305–321. https://doi.org/10.1007/BF00035493

Tapponnier, P., & Brace, W. F. (1976). Development of stress-induced microcracks in Westerly granite. In *International Journal of Rock Mechanics and Mining Sciences & Geomechanics Abstracts* (Vol. 13, No. 4, pp. 103–112). Pergamon: Pergamon Press.

Wesnousky, S. G. (2006). Predicting the endpoints of earthquake ruptures. *Nature*, *444*(7117), 358–360. https://doi.org/10.1038/nature05275

Geophysical Research Letters

Supporting Information for

Isolating the factors that govern fracture development in rocks throughout dynamic in situ X-ray tomography experiments

J. McBeck[1], N. Kandula[1], J. M. Aiken[2,3], B. Cordonnier[1,4], F. Renard[1,5]

[1] Physics of Geological Processes, The Njord Centre, Department of Geosciences, University of Oslo, Oslo, Norway.
[2] Center for Computing in Science Education, Department of Physics, University of Oslo, Oslo, Norway.
[3] Department of Physics and Astronomy, Michigan State University, East Lansing, Michigan, USA.
[4] The European Synchrotron and Radiation Facility, Grenoble, France.
[5] University Grenoble Alpes, University Savoie Mont Blanc, CNRS, IRD, IFSTTAR, ISTerre, 38000 Grenoble, France.

Contents of this file

Introduction

This supporting information includes two tables and four figures. Table 1 describes the experimental conditions. Table 2 describes the features used in the logistic regression models. Figure S1 describes the work flow of this analysis. Figure S2 shows a schematic representation of a subset of the features of individual fractures used as input in the logistic regression models. Figure S3 shows the vertical distribution of the growing and closing fractures in each experiment. Figure S4 shows the success of the models with various data removal thresholds. Figure S5 shows the distribution of the change in volume for growing and closing fractures. Figure S6 shows the cumulative importance of the 14 features identified in the 50 logistic regression models of the 4 experiments.

Table S1. Experimental conditions of the four analyzed experiments, parameters of tracking algorithm, and resulting total number of fractures identified from tracking.

	Carrara marble #1	**Carrara marble #2**	**Monzonite**	**Westerly Granite**
Dominant minerals	calcite	calcite	plagioclase, K- feldspar	quartz, K-feldspar
Height of rock cylinder (mm)	10	10	10	10
Radius of rock cylinder base (mm)	5	5	4	4
Confining stress (MPa)	20	25	25	10
Axial stress at failure (MPa)	130	196	161.5	152.5
Total number of scans in experiment	43	100	78	65
Differential stresses used in tracking algorithm (MPa)	40-130	150-196	20-161.5	20-150
Number of fractures identified in tracking algorithm	6800	21000	12500	72000

Table S2. Fracture characteristics used as feature inputs in logistic regression models.

Category	**Feature**	**Representative fracture characteristic**
Shape	Volume	Size
	Elongation	Flatness
	Anisotropy	Thinness
Eigenvalue	Maximum	Length along the largest dimension
	Intermediate	Length along the second largest dimension
	Minimum	Length along the smallest dimension, Aperture
Eigenvector	With maximum eigenvalue	Orientation of largest dimension
	With intermediate eigenvalue	Orientation of second largest dimension
	With minimum eigenvalue	Orientation of smallest dimension
Distance between fracture centroids	Median distance to closest 25^{th} percentile of fractures	Clustering of local fracture network
	Mean distance to closest 25^{th} percentile of fractures	Clustering of local fracture network
	Median distance to all fractures	Clustering of complete fracture network
	Mean distance to all fractures	Clustering of complete fracture network
	Minimum distance	Clustering of neighboring fractures

Figure S1. Analysis steps. Flow chart of steps performed in the analysis to find the best predictors of fracture growth.

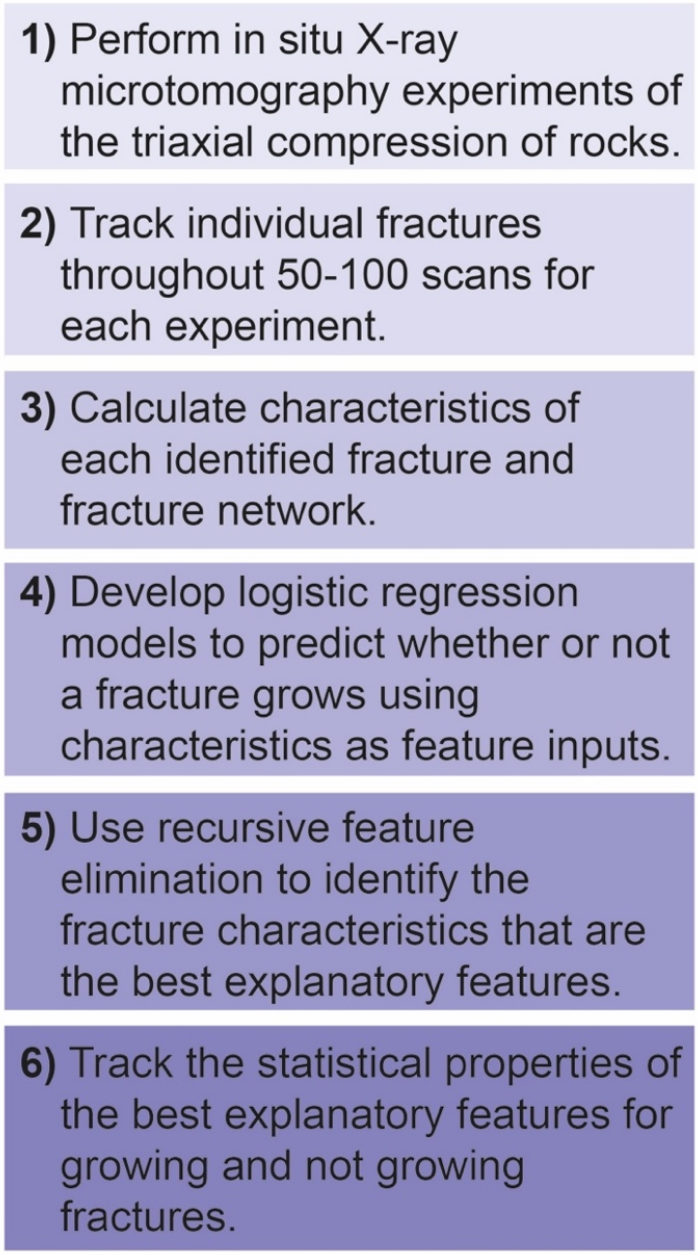

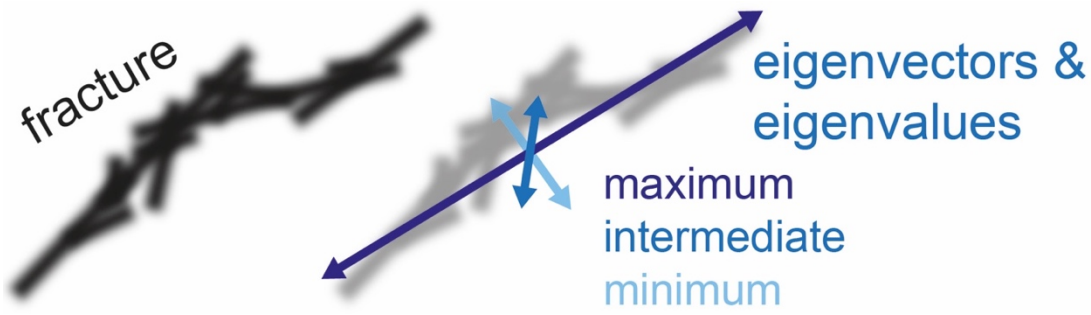

Figure S2. Feature extraction. Schematic illustration of the eigenvectors and eigenvalues derived from the cluster of connected pixels that define each identified fracture. Finding these eigenvectors and eigenvalues produces eight of the feature inputs.

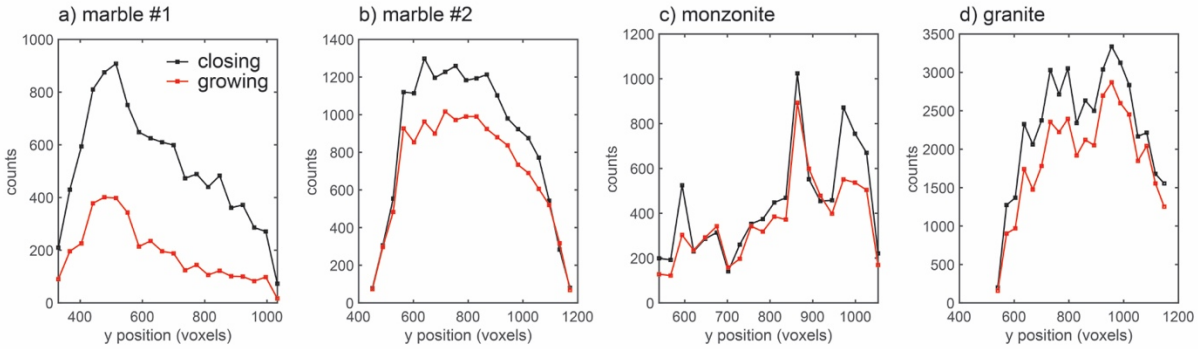

Figure S3. Spatial distribution of closing and growing fractures in experiments on a) marble #1, b) marble #2, c) monzonite, and d) granite. Spatial distribution shown as the *y*-position of the centroid of the fracture in voxels from the bottom of the scan. The vertical spatial distributions of the closing and growing fractures are similar to each other in each experiment. The closing fractures do not tend to localize near the axial pistons.

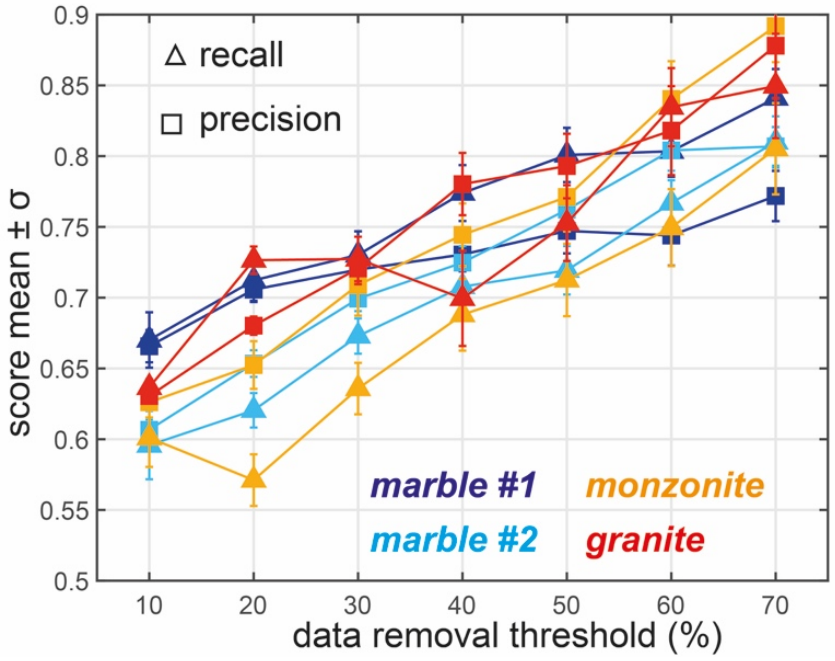

Figure S4. Model success. Success of models measured by the mean ± one standard deviation of the recall (triangles) and precision (squares) for the 50 independent logistic regression models for each experiment and each data removal threshold. Colors correspond to each experiment: marble #1 (dark blue), marble #2 (light blue), monzonite (yellow), granite (red). The success of the models increases as they include fractures that are growing or closing by increasing percentages of their volume (i.e., data removal threshold).

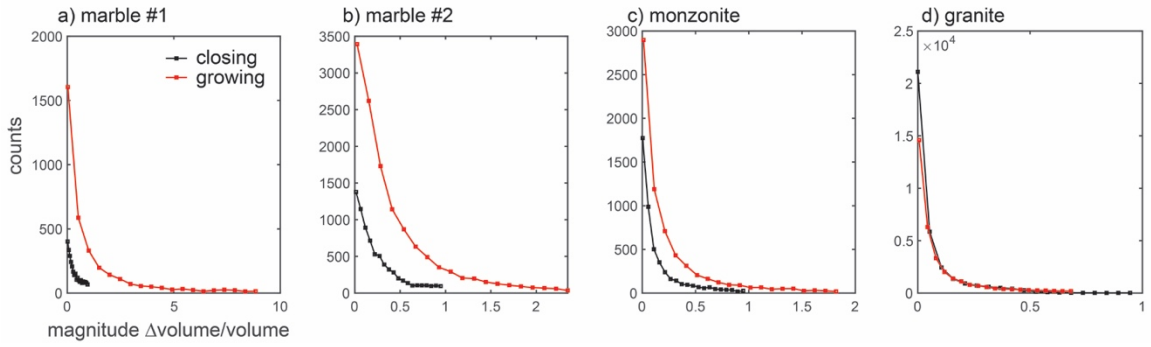

Figure S5. Histograms of the magnitude of the volume change of fractures (from one stress step to the next) relative to their current volume. Thresholding fractures with the data removal threshold (change in volume/volume) reduces the number of data points, but improves the quality of the data, resulting in greater model success (Figure S4).

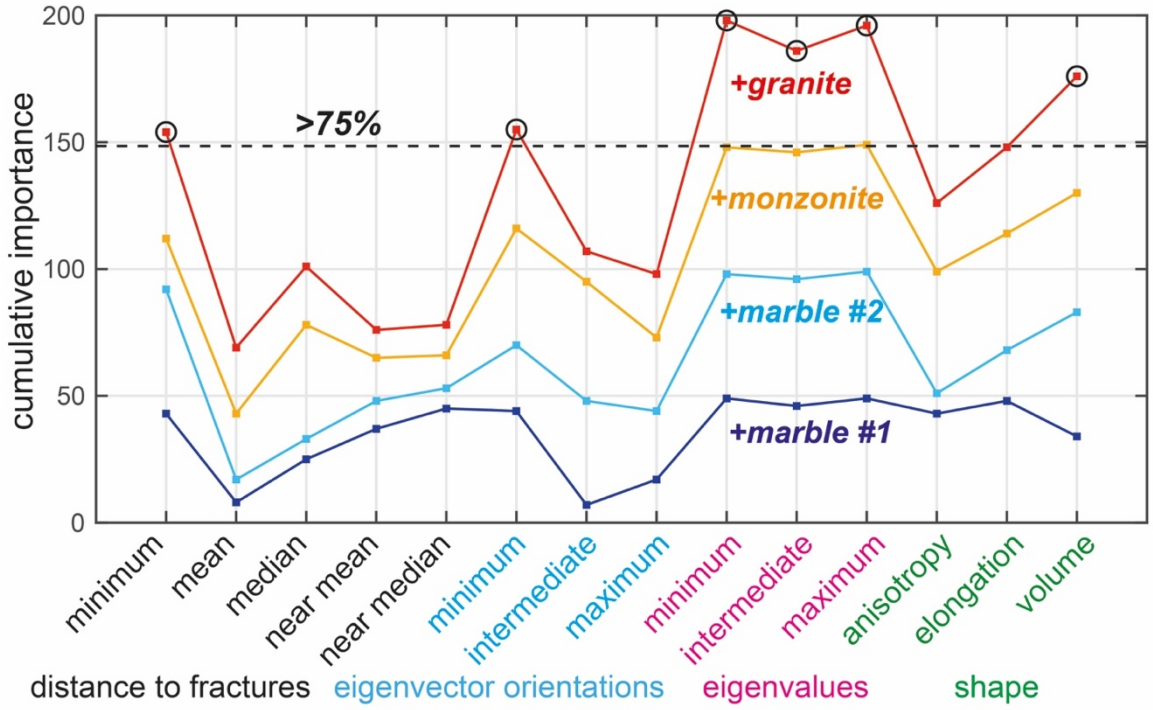

Figure S6. Dominant controls on fracture development revealed by recursive feature elimination. Recursive feature elimination selects the features that are the most important to model predictions. Solid lines show the number of times recursive feature elimination selects a feature as important in the 50 models of the four experiments (i.e., cumulative importance): in the marble #1 experiment (dark blue), marble #1+marble #2 (light blue), marble #1+marble #2+monzonite (orange), and marble #1+marble #2+monzonite+granite (red). If all of the 50 models of each experiment select a particular feature, then the cumulative importance is 200. Dashed lines show the 75% of the maximum cumulative importance. The features with cumulative importance >75% of the maximum (black circles) are the fracture volume and eigenvalues, i.e., fracture length and aperture, orientation of the eigenvector with the minimum eigenvalue, and the minimum distance between fracture centroids. We use this threshold in order to select the features that are most important to the model predictions.

7 Conclusion and Outlook

Using the novel experimental technique of triaxial deformation coupled with dynamic X-ray micro tomography, the evolution of microstructures of rock types with porosities varying from less than 1% to 23% are explored in this thesis. Results allow identifying properties of brittle failure that could not be inferred previously due to limitations of experimental techniques. This thesis present three kinds of results. Firstly, precursory events precede system-size failure in laboratory experiments on rock core samples. At microscale, these events correspond to microfractures originating from microscale heterogeneities in non-porous rocks. Dynamics of these precursors show an evolution towards macroscopic failure following power-laws. Using theoretical models (Amitrano et al., 1999; Girard et al., 2010; Girard et al., 2012) developed to explain fracture in heterogeneous solids, brittle compressive failure in non-porous rocks (centimeter scale) is argued to behave as a critical phenomenon. However, my observations of the breaking of scaling laws very close to failure is linked to localization of a shear fault and can be proposed as a new a precursory signal for macroscopic failure. Therefore, failure can be predicted to some extent. Secondly, strain localization in porous rocks has microstructural origins. Under brittle compressive failure conditions, dominant strain localization mechanisms contain contributions from the three components of strain: dilation, shear and compaction. Porosity evolutions are strongly linked to the incremental strain components computed between successive loading steps. Applied confinement is a guiding parameter for defining dominant mechanisms of strain localization. Presence of pore fluid facilitates strain localization much earlier in the approach to macroscopic failure. Thirdly, microstructural mechanisms guiding localization under brittle compression conditions are dependent on rock types and their porosities. In non-porous rocks, growth of subcritical cracks and system spanning faults explain the localization of shear faults and breaking of scaling laws when samples approach failure. The sandstones I used are porous rocks characterized by normal distributions for grain and pore sizes. In these sandstones, deformation is accumulated through pore space dilation, pore collapse and grain crushing, resulting in grain size reduction. Whereas, the limestones I used are characterized by bimodal pore size distributions and deformation mechanisms are strongly influenced by this complexity in porosity. Damage localizes around the large pores giving rise to a halo of cataclasis resulting in pore collapse. Pore emanating cracks propagate across the sample length and produce shear localization.

Precursory activity and interpretation of progressive damage in our experiments as a critical phenomenon can be related to fracture processes at the fault scale. Several studies have attempted to apply the concept of a critical point and precursory phenomena to geological scales (Main, 1996; Bowman et al., 1998; Grasso et al., 1998). Foreshock activity before large earthquakes shows sometimes scaling laws, such as power-law distributions of earthquake energies (Gutenberg and Richter, 1944) and fractal clustering of hypocentres (Kagan and Knopoff, 1980). Stress released during earthquake drives the fault system away from criticality while progressive tectonic loading drives it towards a future critical state (Jaumé & Sykes, 1999). Therefore, the probability of occurrence of a future large earthquake is increased. Behavior of such fault systems was explained by two successive phases: the Gutenberg-Richter phase is characterized by a power-law distribution of slip event sizes with an exponential cut-off, and a runaway phase is characterized by small events as well as quasi-periodic occurrence of system-size earthquakes (Dahmen et al., 1998). These findings may agree with results produced in this thesis. The Gutenberg-Richter phase would be analogous to the pre-failure, damage development phase in a rock, controlled by elastic long-range stress interactions and characterized by the emergence of power-laws. The runaway phase would be equivalent to the system-size failure resulting from the formation of a percolating cluster leading to frictional sliding. Such an evolution is also in line with the recent proposition that small volumetric deformations away from the main faults could participate to the long-term localization of strain, leading to large earthquakes (Kato and Ben-Zion, 2021). Evolution of deformations produced by multiscale fracturing of the crust can be tracked in space and time (Marsan et al., 2004). Therefore, scaling laws obtained for these strain fields in space and time can be theoretically linked to scaling laws obtained for fracture clustering events at laboratory scale (Girard et al., 2010). However, the use of precursory activity as an earthquake forecasting tool remains elusive so far. Significant difference exist between compressive failure of initially un-faulted rocks (this work), and nucleation of earthquake along a pre-existing crustal fault. Further theoretical and experimental work as well as geophysical data analysis is required to better characterize the fracture at geological scale.

Results discussed in this thesis could lead to follow-up studies. Theoretical models that describe failure as a critical phenomenon could be tested on different rock types to obtain a generalized observation and validity of these models in laboratory experiments. Finite element modeling can also be used to model fluid flow by considering the effects of deformation produced

from experiments, as described by Linga et al., (2017), and can be studied for various rock types. Strain localization in porous rocks is strongly influenced by applied confinement and therefore, porous rocks could be tested for a range of confining pressures to provide a detailed analysis of influence of this parameter on the microscale mechanisms.

In non-porous rocks, damage localizes as microfractures, which nucleate, grow and coalesce to form clusters. These fracture clusters show fractal symmetries. I have performed fractal analysis on Carrara marble samples (unpublished) and computed the fractal dimension for microfractures of individual segmented volumes, for every stress step increase in applied stress. Fractal dimension plotted for applied stress steps (Figure 7.1), is linear (one slope) for low axial stress and bilinear (two slopes) when failure is approached. Fractal dimension of 1.8 corresponds to linear elongated microfractures while 2.6 corresponds to localization as a shear band. Presence of non-linear fractal dimension can be a key identifier for understanding localization of damage. Therefore, a multifractal analysis on segmented tomograms can further be explored to provide more insights into brittle failure in crustal rocks.

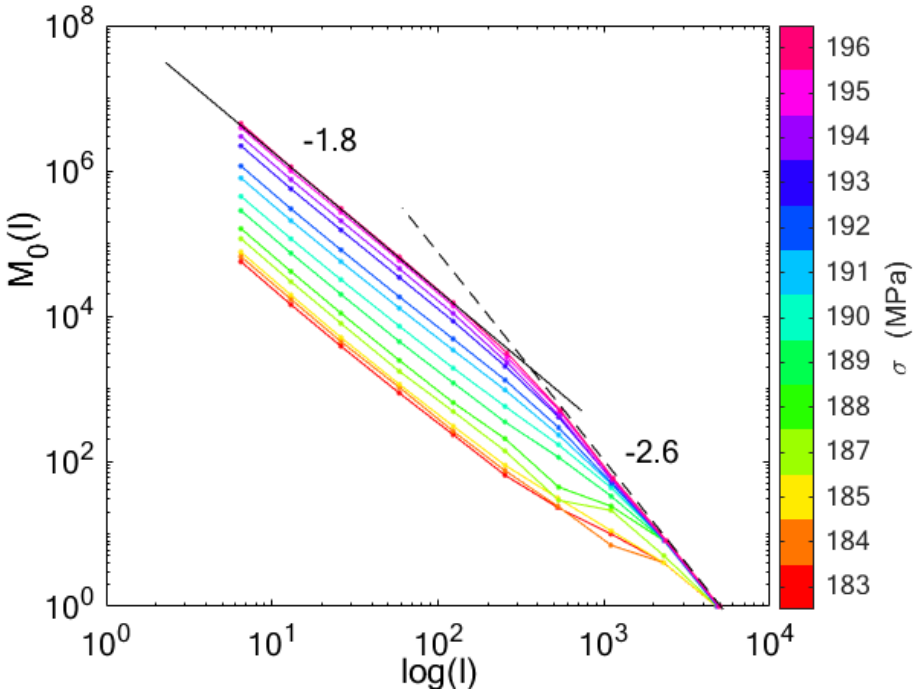

Figure 7.1: Fractal dimension plotted for axial stress steps in Carrara marble. Microfracture network shows two fractal dimensions, 1.8 and 2.6 on approaching failure. Axial stress at failure is 196 MPa.

To conclude, microstructural characterization of brittle deformation in crustal rocks is an active research topic. Experimental and computational techniques developed in this thesis are versatile tools to explore microstructure of rocks under deformation at crustal conditions. Dynamic X-ray microtomography is a transformative innovation in experimental rock physics and new series of experiments in the coming years should allow to progress on the prediction of laboratory earthquakes, the detailed mechanisms of faulting and the development of fracture networks in crustal rocks.

References

Alava, M. J., Nukala, P. K., & Zapperi, S. (2006). Statistical models of fracture. *Advances in Physics*, *55*(3-4), 349-476.

Alava, M. J., Nukala, P. K., & Zapperi, S. (2008). Role of disorder in the size scaling of material strength. *Physical Review Letters*, 100(5), 055502.

Amitrano, D. (2003). Brittle-ductile transition and associated seismicity: Experimental and numerical studies and relationship with the b value. *Journal of Geophysical Research: Solid Earth*, *108*(B1), 2044.

Amitrano, D. (2006). Rupture by damage accumulation in rocks. *International Journal of Fracture*, *139*(3-4), 369.

Amitrano, D. (2012). Variability in the power-law distributions of rupture events. *The European Physical Journal Special Topics*, *205*(1), 199-215.

Amitrano, D., Grasso, J. R., & Hantz, D. (1999). From diffuse to localised damage through elastic interaction. *Geophysical Research Letters*, *26*(14), 2109-2112.

Amitrano, D., Grasso, J. R., & Senfaute, G. (2005). Seismic precursory patterns before a cliff collapse and critical point phenomena. *Geophysical Research Letters*, *32*(8), L08314

Ashby, M. F. A., & Hallam, S. D. (1986). The failure of brittle solids containing small cracks under compressive stress states. *Acta Metallurgica*, *34*(3), 497-510.

Ashby, M. F., & Sammis, C. G. (1990). The damage mechanics of brittle solids in compression. *Pure and Applied Geophysics*, *133*(3), 489-521.

Austrheim, H. (1987). Eclogitization of lower crustal granulites by fluid migration through shear zones. *Earth and Planetary Science Letters*, *81*(2-3), 221-232.

Austrheim, H., & Boundy, T. M. (1994). Pseudotachylytes generated during seismic faulting and eclogitization of the deep crust. *Science*, *265*(5168), 82-83.

Baud, P., Exner, U., Lommatzsch, M., Reuschlé, T., & Wong, T. F. (2017). Mechanical behavior, failure mode, and transport properties in a porous carbonate. *Journal of Geophysical Research: Solid Earth*, *122*(9), 7363-7387.

Baud, P., Schubnel, A., & Wong, T. F. (2000). Dilatancy, compaction, and failure mode in Solnhofen limestone. *Journal of Geophysical Research: Solid Earth*, *105*(B8), 19289-19303.

Bakun, W. H., Aagaard, B., Dost, B., Ellsworth, W. L., Hardebeck, J. L., Harris, R. A.,.... & Michael, A. J. (2005). Implications for prediction and hazard assessment from the 2004 Parkfield earthquake. *Nature*, *437*(7061), 969-974.

Bhatt, J. J., Carroll, M. M., & Schatz, J. F. (1975). Spherical model calculation for volumetric response of porous rocks. *Journal of Applied Mechanics*, *42*(2), 363-368.

Blenkinsop, T., Kruckenberg, S. C., Morgan, S., & Newman, J. (2013). A perspective on the emergence of modern structural geology: Celebrating the feedbacks between historical-based and process-based approaches. *The web of geological sciences: Advances, impacts, and interactions*, *500*, 65.

Bouchon, M., Karabulut, H., Aktar, M., Özalaybey, S., Schmittbuhl, J., & Bouin, M. P. (2011). Extended nucleation of the 1999 Mw 7.6 Izmit earthquake. *Science*, *331*(6019), 877-880.

Bowman, D. D., Ouillon, G., Sammis, C. G., Sornette, A., & Sornette, D. (1998). An observational test of the critical earthquake concept. *Journal of Geophysical Research: Solid Earth*, *103*(B10), 24359-24372.

Brace, W. F., & Martin Iii, R. J. (1968, September). A test of the law of effective stress for crystalline rocks of low porosity. In *International Journal of Rock Mechanics and Mining Sciences & Geomechanics Abstracts* (Vol. 5, No. 5, pp. 415-426). Pergamon.

Brace, W. F., & Riley, D. K. (1972, March). Static uniaxial deformation of 15 rocks to 30 kb. In *International Journal of Rock Mechanics and Mining Sciences & Geomechanics Abstracts* (Vol. 9, No. 2, pp. 271-288). Pergamon.

Brace, W. F., Silver, E., Hadley, K., & Goetze, C. (1972). Cracks and pores: A closer look. *Science*, *178*(4057), 162-164.

Buades, A., Coll, B., & Morel, J. M. (2005, June). A non-local algorithm for image denoising. In *2005 IEEE Computer Society Conference on Computer Vision and Pattern Recognition (CVPR'05)* (Vol. 2, pp. 60-65). IEEE.

Buljac, A., Jailin, C., Mendoza, A., Neggers, J., Taillandier-Thomas, T., Bouterf, A., & Roux, S. (2018). Digital volume correlation: review of progress and challenges. *Experimental Mechanics*, *58*(5), 661-708.

Byerlee, J. D. (1970). The mechanics of stick-slip. *Tectonophysics*, *9*(5), 475-486.

Campbell, L. R., Menegon, L., Fagereng, Å., & Pennacchioni, G. (2020). Earthquake nucleation in the lower crust by local stress amplification. *Nature communications*, *11*(1), 1-9.

Cartwright, J. A., Trudgill, B. D., & Mansfield, C. S. (1995). Fault growth by segment linkage: an explanation for scatter in maximum displacement and trace length data from the Canyonlands Grabens of SE Utah. *Journal of Structural Geology*, *17*(9), 1319-1326.

Castillo-Villa, P. O., Baró, J., Planes, A., Salje, E. K., Sellappan, P., Kriven, W. M., & Vives, E. (2013). Crackling noise during failure of alumina under compression: the effect of porosity. *Journal of Physics: Condensed Matter*, 25(29), 292202.

Charalampidou, E. M., Hall, S. A., Stanchits, S., Lewis, H., & Viggiani, G. (2011). Characterization of shear and compaction bands in a porous sandstone deformed under triaxial compression. *Tectonophysics*, *503*(1-2), 8-17.

Chessa, A., Vespignani, A., & Zapperi, S. (1999). Critical exponents in stochastic sandpile models. *Computer Physics Communications*, *121*, 299-302.

Cierniak, R. (2011). *X-ray computed tomography in biomedical engineering*. Springer Science & Business Media.

Coward, M. P., & Kim, J. H. (1981). Strain within thrust sheets. *Geological Society, London, Special Publications*, *9*(1), 275-292.

Curran, J. H., & Carroll, M. M. (1979). Shear stress enhancement of void compaction. *Journal of Geophysical Research: Solid Earth*, *84*(B3), 1105-1112.

Dahmen, K., Ertaş, D., & Ben-Zion, Y. (1998). Gutenberg-Richter and characteristic earthquake behavior in simple mean-field models of heterogeneous faults. *Physical Review E*, *58*(2), 1494.

Das, S., & Scholz, C. H. (1983). Why large earthquakes do not nucleate at shallow depths. *Nature*, *305*(5935), 621-623.

De Arcangelis, L., Redner, S., & Herrmann, H. J. (1985). A random fuse model for breaking processes. *Journal de Physique Lettres*, *46*(13), 585-590.

Deschanel, S., Vanel, L., Godin, N., Vigier, G., & Ciliberto, S. (2009). Experimental study of crackling noise: conditions on power law scaling correlated with fracture precursors. *Journal of Statistical Mechanics: Theory and Experiment*, *2009*(01), P01018.

Dieterich, J. H. (1979). Modeling of rock friction: 1. Experimental results and constitutive equations. *Journal of Geophysical Research: Solid Earth*, *84*(B5), 2161-2168.

Dubsky, S., Hooper, S. B., Siu, K. K., & Fouras, A. (2012). Synchrotron-based dynamic computed tomography of tissue motion for regional lung function measurement. *Journal of The Royal Society Interface*, *9*(74), 2213-2224.

Ellsworth, W. L., & Beroza, G. C. (1995). Seismic evidence for an earthquake nucleation phase. *Science*, *268*(5212), 851-855.

Escartin, J., Hirth, G., & Evans, B. (1997). Effects of serpentinization on the lithospheric strength and the style of normal faulting at slow-spreading ridges. *Earth and Planetary Science Letters*, *151*(3-4), 181-189.

Flannery, B. P., Deckman, H. W., Roberge, W. G., & D'AMICO, K. L. (1987). Three-dimensional X-ray microtomography. *Science*, *237*(4821), 1439-1444.

Fossen, H. (2010). Extensional tectonics in the North Atlantic Caledonides: a regional view. *Geological Society, London, Special Publications*, *335*(1), 767-793.

Fossen, H. (2016). *Structural geology*. Cambridge University Press.

Fossen, H., & Cavalcante, G. C. G. (2017). Shear zones–A review. *Earth-Science Reviews*, *171*, 434-455.

Fossen, H., Soliva, R., Ballas, G., Trzaskos, B., Cavalcante, C., & Schultz, R. A. (2018). A review of deformation bands in reservoir sandstones: geometries, mechanisms and distribution. *Geological Society, London, Special Publications*, *459*(1), 9-33.

Fredrich, J. T., Menendez, B., & Wong, T. F. (1995). Imaging the pore structure of geomaterials. *Science*, *268*(5208), 276-279.

Frohlich, C., & Davis, S. D. (1993). Teleseismic b values; or, much ado about 1.0. *Journal of Geophysical Research: Solid Earth*, *98*(B1), 631-644.

Fusseis, F., & Handy, M. R. (2008). Micromechanisms of shear zone propagation at the brittle–viscous transition. *Journal of Structural Geology*, *30*(10), 1242-1253.

Fusseis, F., Regenauer-Lieb, K., Liu, J., Hough, R. M., & De Carlo, F. (2009). Creep cavitation can establish a dynamic granular fluid pump in ductile shear zones. *Nature*, *459*(7249), 974-977.

Garcimartin, A., Guarino, A., Bellon, L., & Ciliberto, S. (1997). Statistical properties of fracture precursors. *Physical Review Letters*, *79*(17), 3202.

Girard, L., Amitrano, D., & Weiss, J. (2010). Failure as a critical phenomenon in a progressive damage model. *Journal of Statistical Mechanics: Theory and Experiment*, *2010*(01), P01013.

Girard, L., Weiss, J., & Amitrano, D. (2012). Damage-cluster distributions and size effect on strength in compressive failure. *Physical Review Letters*, *108*(22), 225502.

Goncalves, P., Poilvet, J. C., Oliot, E., Trap, P., & Marquer, D. (2016). How does shear zone nucleate? An example from the Suretta nappe (Swiss Eastern Alps). *Journal of Structural Geology*, *86*, 166-180.

Grasso, J. R., & Sornette, D. (1998). Testing self-organized criticality by induced seismicity. *Journal of Geophysical Research: Solid Earth*, *103*(B12), 29965-29987.

Griggs, D. T. (1936). Deformation of rocks under high confining pressures: I. Experiments at room temperature. *The Journal of Geology*, *44*(5), 541-577.

Griggs, D., & Miller, W. B. (1951). Deformation of Yule marble: part I—compression and extension experiments on dry Yule marble at 10,000 atmospheres confining pressure, room temperature. *Geological Society of America Bulletin*, *62*(8), 853-862.

Guarino, A., Garcimartin, A., & Ciliberto, S. (1998). An experimental test of the critical behaviour of fracture precursors. *The European Physical Journal B-Condensed Matter and Complex Systems*, 6(1), 13-24.

Guermani, A., & Pennacchioni, G. (1998). Brittle precursors of plastic deformation in a granite: an example from the Mont Blanc massif (Helvetic, western Alps). *Journal of Structural Geology*, *20*(2-3), 135-148.

Gueguen, Y., Reuschlé, T., & Darot, M. (1990). Single-crack behaviour and crack statistics. In *Deformation processes in minerals, ceramics and rocks* (pp. 48-71). Springer, Dordrecht.

Gurson, A. L. (1977). Continuum theory of ductile rupture by void nucleation and growth: Part I—Yield criteria and flow rules for porous ductile media. *Journal of Engineering Materials and Technology*, *99*, 2-15.

Gutenberg, B., & Richter, C. F. (1944). Frequency of earthquakes in California. *Bulletin of the Seismological Society of America*, *34*(4), 185-188.

Hall, S. A. (2006). A methodology for 7D warping and deformation monitoring using time-lapse seismic data. *Geophysics*, *71*(4), O21-O31.

Hall, S. A., Bornert, M., Desrues, J., Pannier, Y., Lenoir, N., Viggiani, G., & Bésuelle, P. (2010). Discrete and continuum analysis of localised deformation in sand using X-ray μCT and volumetric digital image correlation. *Géotechnique*, *60*(5), 315-322.

Hansen, A., Roux, S., & Herrmann, H. J. (1989). Rupture of central-force lattices. *Journal de Physique*, *50*(7), 733-744.

Hawkes, I., & Mellor, M. (1970). Uniaxial testing in rock mechanics laboratories. *Engineering Geology*, *4*(3), 179-285.

Heard, H. C. (1960). Transition from brittle fracture to ductile flow in Solenhofen limestone as a function of temperature, confining pressure, and interstitial fluid pressure. *Memoir of the Geological SocIety of America, 79*, 193-226.

Herrmann, H. J., & Roux, S. (Eds.). (2014). *Statistical models for the fracture of disordered media*. Elsevier.

Hild, F., & Roux, S. (2008). CorreliQ4: A software for finite element displacement field measurements by digital image correlation. *Rapport interne LMT Cachan, 269*, 195.

Hirata, T. (1989). Fractal dimension of fault systems in Japan: fractal structure in rock fracture geometry at various scales. In *Fractals in geophysics* (pp. 157-170). Birkhäuser, Basel.

Hirata, T., Satoh, T., & Ito, K. (1987). Fractal structure of spatial distribution of microfracturing in rock. *Geophysical Journal International, 90*(2), 369-374.

Hoek, E., & Brown, E. T. (1997). Practical estimates of rock mass strength. *International journal of rock mechanics and mining sciences*, *34*(8), 1165-1186.

Hoek, E., & Franklin, J. A. (1968). Simple triaxial cell for field or laboratory testing of rock. *Transactions of the Institution of Mining and Metallurgy*, *77*, A22-26.

Holcomb, D. J., & Olsson, W. A. (2003). Compaction localization and fluid flow. *Journal of Geophysical Research: Solid Earth*, *108*(B6), 2290.

Hull, J. (1988). Thickness-displacement relationships for deformation zones. *Journal of Structural Geology*, *10*(4), 431-435.

Ingles, J., Lamouroux, C., Soula, J. C., Guerrero, N., & Debat, P. (1999). Nucleation of ductile shear zones in a granodiorite under greenschist facies conditions, Néouvielle massif, Pyrenees, France. *Journal of Structural Geology*, *21*(5), 555-576.

Jaeger, J. C., Cook, N. G., & Zimmerman, R. (2009). *Fundamentals of rock mechanics*. John Wiley & Sons.

Jaumé, S. C., & Sykes, L. R. (1999). Evolving towards a critical point: A review of accelerating seismic moment/energy release prior to large and great earthquakes. In: *Seismicity patterns, their statistical significance and physical meaning*, Eds. Max Wyss, Kunihiko Shimazaki, Akihiko Ito, pp. 279-305, Springer.

Ji, Y., Baud, P., Vajdova, V., & Wong, T. F. (2012). Characterization of pore geometry of Indiana limestone in relation to mechanical compaction. *Oil & Gas Science and Technology–Revue d'IFP Energies nouvelles*, *67*(5), 753-775.

Ji, Y., Baud, P., Vajdova, V., & Wong, T. F. (2012). Characterization of pore geometry of Indiana limestone in relation to mechanical compaction. *Oil & Gas Science and Technology–Revue d'IFP Energies nouvelles*, *67*(5), 753-775.

Ji, Y., Hall, S. A., Baud, P., & Wong, T. F. (2015). Characterization of pore structure and strain localization in Majella limestone by X-ray computed tomography and digital image correlation. Geophysical Journal International, 200(2), 701-719.

Jha, D., Sørensen, H. O., Dobberschütz, S., Feidenhans'l, R., & Stipp, S. L. S. (2014). Adaptive center determination for effective suppression of ring artifacts in tomography images. *Applied Physics Letters*, *105*(14), 143107.

Kagan, Y. Y., & Knopoff, L. (1980). Spatial distribution of earthquakes: the two-point correlation function. *Geophysical Journal International*, *62*(2), 303-320.

Kandula, N., Cordonnier, B., Boller, E., Weiss, J., Dysthe, D. K., & Renard, F. (2019). Dynamics of microscale precursors during brittle compressive failure in Carrara marble. *Journal of Geophysical Research: Solid Earth*, *124*(6), 6121-6139.

Kato, A., & Ben-Zion, Y. (2021). The generation of large earthquakes. *Nature Reviews Earth & Environment*, 1-14.

Kato, A., Obara, K., Igarashi, T., Tsuruoka, H., Nakagawa, S., & Hirata, N. (2012). Propagation of slow slip leading up to the 2011 Mw 9.0 Tohoku-Oki earthquake. *Science*, *335*(6069), 705-708.

Katz, O., & Reches, Z. E. (2004). Microfracturing, damage, and failure of brittle granites. *Journal of Geophysical Research: Solid Earth*, *109*(B1), B01206.

Ketcham, R. A., & Carlson, W. D. (2001). Acquisition, optimization and interpretation of X-ray computed tomographic imagery: applications to the geosciences. *Computers & Geosciences*, *27*(4), 381-400.

King, G. (1983). The accommodation of large strains in the upper lithosphere of the earth and other solids by self-similar fault systems: the geometrical origin of b-value. *Pure and Applied Geophysics*, *121*(5-6), 761-815.

Kyle, J. R., & Ketcham, R. A. (2015). Application of high resolution X-ray computed tomography to mineral deposit origin, evaluation, and processing. *Ore Geology Reviews*, *65*, 821-839.

Lapusta, N., & Rice, J. R. (2003). Nucleation and early seismic propagation of small and large events in a crustal earthquake model. *Journal of Geophysical Research: Solid Earth*, *108*(B4), 2205.

Lenoir, N., Bornert, M., Desrues, J., Bésuelle, P., & Viggiani, G. (2007). Volumetric digital image correlation applied to X-ray microtomography images from triaxial compression tests on argillaceous rock. *Strain*, *43*(3), 193-205.

Linga, G., Mathiesen, J., & Renard, F. (2017). Self-similar distributions of fluid velocity and stress heterogeneity in a dissolving porous limestone. *Journal of Geophysical Research: Solid Earth*, *122*(3), 1726-1743.

Lion, M., Skoczylas, F., & Ledésert, B. (2004). Determination of the main hydraulic and poro-elastic properties of a limestone from Bourgogne, France. *International Journal of Rock Mechanics and Mining Sciences*,41(6), 915-925.

Lockner, D. A., & Beeler, N. M. (2002). Rock failure and earthquakes. *International Geophysics Series*, *81*(A), 505-538.

Lockner, D. A., & Byerlee, J. D. (1995). Precursory AE patterns leading to rock fracture. *Series on rock and soil mechanics*, *19*, 45-58.

Lockner, D., Byerlee, J. D., Kuksenko, V., Ponomarev, A., & Sidorin, A. (1991). Quasi-static fault growth and shear fracture energy in granite. *Nature*, *350*(6313), 39-42.

Main, I. (1996). Statistical physics, seismogenesis, and seismic hazard. *Reviews of Geophysics*, *34*(4), 433-462.

Main, I. G., Kwon, O., Ngwenya, B. T., & Elphick, S. C. (2000). Fault sealing during deformation-band growth in porous sandstone. *Geology*, *28*(12), 1131-1134.

Main, I. G., Meredith, P. G., & Jones, C. (1989). A reinterpretation of the precursory seismic b-value anomaly from fracture mechanics. *Geophysical Journal International*, *96*(1), 131-138.

Mancktelow, N. S. (2002). Finite-element modelling of shear zone development in viscoelastic materials and its implications for localisation of partial melting. *Journal of Structural Geology*, *24*(6-7), 1045-1053.

Mandal, N., Misra, S., & Samanta, S. K. (2004). Role of weak flaws in nucleation of shear zones: an experimental and theoretical study. *Journal of Structural Geology*, *26*(8), 1391-1400.

Mancktelow, N. S., & Pennacchioni, G. (2005). The control of precursor brittle fracture and fluid–rock interaction on the development of single and paired ductile shear zones. *Journal of Structural Geology*, *27*(4), 645-661.

Marsan, D., Stern, H., Lindsay, R., & Weiss, J. (2004). Scale dependence and localization of the deformation of Arctic sea ice. *Physical Review Letters*, *93*(17), 178501.

Maso, J. C., & Lerau, J. (1980, April). Mechanical behaviour of Darney sandstone (Vosges, France) in biaxial compression. In *International Journal of rock mechanics and mining sciences & geomechanics abstracts* (Vol. 17, No. 2, pp. 109-115). Pergamon.

McBeck, J., Kandula, N., Aiken, J. M., Cordonnier, B., & Renard, F. (2019). Isolating the factors that govern fracture development in rocks throughout dynamic in situ X-ray tomography experiments. *Geophysical Research Letters*, *46*(20), 11127-11135.

McBeck, J., Kobchenko, M., Hall, S. A., Tudisco, E., Cordonnier, B., Meakin, P., & Renard, F. (2018). Investigating the onset of strain localization within anisotropic shale using digital volume correlation of time-resolved X-ray microtomography images. *Journal of Geophysical Research: Solid Earth*, *123*(9), 7509-7528.

Means, W. D. (1995). Shear zones and rock history. *Tectonophysics*, *247*(1-4), 157-160.

Meng, F., Wong, L. N. Y., & Zhou, H. (2019). Power law relations in earthquakes from microscopic to macroscopic scales. *Scientific reports*, *9*(1), 1-11.

Mirone, A., Brun, E., Gouillart, E., Tafforeau, P., & Kieffer, J. (2014). The PyHST2 hybrid distributed code for high speed tomographic reconstruction with iterative reconstruction and a priori knowledge capabilities. *Nuclear Instruments and Methods in Physics Research Section B: Beam Interactions with Materials and Atoms*, *324*, 41-48.

Misra, S., & Mandal, N. (2007). Localization of plastic zones in rocks around rigid inclusions: Insights from experimental and theoretical models. *Journal of Geophysical Research: Solid Earth*, *112*(B9), B09206.

Moore, D. E., & Lockner, D. A. (1995). The role of microcracking in shear-fracture propagation in granite. *Journal of Structural Geology*, *17*(1), 95-114.

Mori, J., & Abercrombie, R. E. (1997). Depth dependence of earthquake frequency-magnitude distributions in California: Implications for rupture initiation. *Journal of Geophysical Research: Solid Earth*, *102*(B7), 15081-15090.

Murrell, S. A. F. (1965). The effect of triaxial stress systems on the strength of rocks at atmospheric temperatures. *Geophysical Journal International*, *10*(3), 231-281.

Nukala, P. K. V., Zapperi, S., & Šimunović, S. (2005a). Statistical properties of fracture in a random spring model. *Physical Review E*, *71*(6), 066106.

Nechad, H., Helmstetter, A., El Guerjouma, R., & Sornette, D. (2005). Creep ruptures in heterogeneous materials. *Physical review letters*, *94*(4), 045501.

Nemat-Nasser, S., & Horii, H. (1982). Compression-induced nonplanar crack extension with application to splitting, exfoliation, and rockburst. *Journal of Geophysical Research: Solid Earth*, *87*(B8), 6805-6821.

Ogata, Y., & Katsura, K. (1993). Analysis of temporal and spatial heterogeneity of magnitude frequency distribution inferred from earthquake catalogues. *Geophysical Journal International*, *113*(3), 727-738.

Ohnaka, M. (1973). The quantitative effect of hydrostatic confining pressure on the compressive strength of crystalline rocks. *Journal of Physics of the Earth*, *21*(2), 125-140.

Ojala, I. O., Main, I. G., & Ngwenya, B. T. (2004). Strain rate and temperature dependence of Omori law scaling constants of AE data: Implications for earthquake foreshock-aftershock sequences. *Geophysical Research Letters*, *31*, *L24617*.

Omori, F. (1894). On the after-shocks of earthquakes. *J. Coll. Sci., Imp. Univ., Japan*, 7 , 111-200.

Ottosen, N. S., & Ristinmaa, M. (2005). *The mechanics of constitutive modeling*. Elsevier.

Paganin, D., Gureyev, T. E., Pavlov, K. M., Lewis, R. A., & Kitchen, M. (2004). Phase retrieval using coherent imaging systems with linear transfer functions. *Optics Communications*, *234*(1-6), 87-105.

Pan, B., Qian, K., Xie, H., & Asundi, A. (2009). Two-dimensional digital image correlation for in-plane displacement and strain measurement: a review. *Measurement science and technology*, *20*(6), 062001.

Paterson, M. S., & Wong, T. F. (2005). *Experimental rock deformation-the brittle field*. Springer Science & Business Media.

Paterson, M. S. (1970, September). A high-pressure, high-temperature apparatus for rock deformation. In *International Journal of Rock Mechanics and Mining Sciences & Geomechanics Abstracts* (Vol. 7, No. 5, pp. 517-526). Pergamon.

Pennacchioni, G., & Mancktelow, N. S. (2007). Nucleation and initial growth of a shear zone network within compositionally and structurally heterogeneous granitoids under amphibolite facies conditions. *Journal of Structural Geology*, *29*(11), 1757-1780.

Pennacchioni, G., & Zucchi, E. (2013). High temperature fracturing and ductile deformation during cooling of a pluton: The Lake Edison granodiorite (Sierra Nevada batholith, California). *Journal of Structural Geology*, *50*, 54-81.

Phillips, T. B., Jackson, C. A., Bell, R. E., Duffy, O. B., & Fossen, H. (2016). Reactivation of intrabasement structures during rifting: A case study from offshore southern Norway. *Journal of Structural Geology*, *91*, 54-73.

Picallo, C. B., & López, J. M. (2008). Energy dissipation statistics in the random fuse model. *Physical Review E*, *77*(4), 046114.

Pollitz, F. F., Stein, R. S., Sevilgen, V., & Bürgmann, R. (2012). The 11 April 2012 east Indian Ocean earthquake triggered large aftershocks worldwide. *Nature*, *490*(7419), 250-253.

Pratt, H. R., Brown, W. S., & Brace, W. F. (1970, January). In situ determination of strength properties in a quartz diorite rock mass. In *The 12th US Symposium on Rock Mechanics (USRMS)*. American Rock Mechanics Association.

Prieto, G. A., Froment, B., Yu, C., Poli, P., & Abercrombie, R. (2017). Earthquake rupture below the brittle-ductile transition in continental lithospheric mantle. *Science Advances*, *3*(3), e1602642.

Qiu, D., & Seeram, E. (2016). Does iterative reconstruction improve image qual-ity and reduce dose in computed tomography. *Radiol Open J*, *1*(2), 42-54.

Ramsay, J. G. (1980). Shear zone geometry: a review. *Journal of structural geology*, *2*(1-2), 83-99.

Ramsay, J. G., & Graham, R. H. (1970). Strain variation in shear belts. *Canadian Journal of Earth Sciences*, *7*(3), 786-813.

Ramsay, J. G., & Wood, D. S. (1973). The geometric effects of volume change during deformation processes. *Tectonophysics*, *16*(3-4), 263-277.

Renard, F., Cordonnier, B., Dysthe, D. K., Boller, E., Tafforeau, P., & Rack, A. (2016). A deformation rig for synchrotron microtomography studies of geomaterials under conditions down to 10 km depth in the Earth. *Journal of Synchrotron Radiation*, *23*(4), 1030-1034.

Renard, F., Cordonnier, B., Kobchenko, M., Kandula, N., Weiss, J., & Zhu, W. (2017). Microscale characterization of rupture nucleation unravels precursors to faulting in rocks. *Earth and Planetary Science Letters*, *476*, 69-78.

Renard, F., Weiss, J., Mathiesen, J., Ben-Zion, Y., Kandula, N., & Cordonnier, B. (2018). Critical evolution of damage toward system-size failure in crystalline rock. *Journal of Geophysical Research: Solid Earth*, *123*(2), 1969-1986.

Renard, F., McBeck, J., Cordonnier, B., Zheng, X., Kandula, N., Sanchez, J. R., Kobchenko, M., Noiriel, C., Zhu, W., Meakin, P., Fusseis, F., & Dysthe, D. K. (2019a) Dynamic in situ three-dimensional imaging and digital volume correlation analysis quantify strain localization and fracture coalescence in sandstone, *Pure and Applied Geophysics*, 176, 1083-1115, https://doi.org/10.1007/s00024-018-2003-x.

Renard, F., McBeck, J., Kandula, N., Cordonnier, B., Meakin, P., & Ben-Zion, Y. (2019b). Volumetric and shear processes in crystalline rock approaching faulting. *Proceedings of the National Academy of Sciences*, *116*(33), 16234-16239.

Renard, F., Kandula, N., McBeck, J., & Cordonnier, B. (2020). Creep burst coincident with faulting in marble observed in 4-D synchrotron X-ray imaging triaxial compression experiments. *Journal of Geophysical Research: Solid Earth*, *125*(9), e2020JB020354.

Robertson, E. C. (1955). Experimental study of the strength of rocks. *Geological Society of America Bulletin*, *66*(10), 1275-1314.

Rutter, E. H., Holdsworth, R. E., & Knipe, R. J. (2001). The nature and tectonic significance of fault-zone weakening: an introduction. *Geological Society, London, Special Publications*, *186*(1), 1-11.

Rutter, E. H., Maddock, R. H., Hall, S. H., & White, S. H. (1986). Comparative microstructures of natural and experimentally produced clay-bearing fault gouges. *Pure and Applied Geophysics*, *124*(1), 3-30.

Sammis, C. G., & Ashby, M. F. (1986). The failure of brittle porous solids under compressive stress states. *Acta metallurgica*, *34*(3), 511-526.

Sanchez, S., Fernandez, V., Pierce, S. E., & Tafforeau, P. (2013). Homogenization of sample absorption for the imaging of large and dense fossils with synchrotron microtomography. *Nature protocols*, *8*(9), 1708.

Scholz, C. H. (1968). The frequency-magnitude relation of microfracturing in rock and its relation to earthquakes. *Bulletin of the seismological society of America*, *58*(1), 399-415.

Scholz, C. H. (1968). Experimental study of the fracturing process in brittle rock. *Journal of Geophysical Research*, *73*(4), 1447-1454.

Scholz, C. H. (2019). *The mechanics of earthquakes and faulting*. Cambridge university press.

Schorlemmer, D., Wiemer, S., & Wyss, M. (2005). Variations in earthquake-size distribution across different stress regimes. *Nature*, *437*(7058), 539-542.

Segall, P., & Simpson, C. (1986). Nucleation of ductile shear zones on dilatant fractures. *Geology*, *14*(1), 56-59.

Sethna, J. P., Dahmen, K. A., & Myers, C. R. (2001). Crackling noise. *Nature*, *410*(6825), 242-250.

Sibson, R. H. (1977). Fault rocks and fault mechanisms. *Journal of the Geological Society*, *133*(3), 191-213.

Soliva, R., & Benedicto, A. (2004). A linkage criterion for segmented normal faults. *Journal of Structural Geology*, *26*(12), 2251-2267.

Soliva, R., Benedicto, A., & Maerten, L. (2006). Spacing and linkage of confined normal faults: importance of mechanical thickness. *Journal of Geophysical Research: Solid Earth*, *111*(B1), B01402.

Sornette, D., & Andersen, J. V. (1998). Scaling with respect to disorder in time-to-failure. *The European Physical Journal B-Condensed Matter and Complex Systems*, *1*(3), 353-357.

Sornette, D., & Sammis, C. G. (1995). Complex critical exponents from renormalization group theory of earthquakes: Implications for earthquake predictions. *Journal de Physique I*, *5*(5), 607-619.

Sornette, A., & Sornette, D. (1989). Self-organized criticality and earthquakes. *EPL (Europhysics Letters)*, *9*(3), 197.

Smith, W. D. (1981). The b-value as an earthquake precursor. *Nature*, *289*(5794), 136-139.

Smith, J. L., De Vries, K. L., Bushnell, D. J., & Brown, W. S. (1969). Fracture data and stress-strain behavior of rocks in triaxial compression. *Experimental Mechanics*, *9*(8), 348-355.

Spiers, C. J., Schutjens, P. M. T. M., Brzesowsky, R. H., Peach, C. J., Liezenberg, J. L., & Zwart, H. J. (1990). Experimental determination of constitutive parameters governing creep of rocksalt by pressure solution. *Geological Society, London, Special Publications*, *54*(1), 215-227.

Stanchits, S., Vinciguerra, S., & Dresen, G. (2006). Ultrasonic velocities, acoustic emission characteristics and crack damage of basalt and granite. *Pure and Applied Geophysics*, *163*(5), 975-994.

Sternberg, S. R. (1983). Biomedical image processing. *IEEE computer*, *16*(1), 22-34.

Stipp, M., StuÈnitz, H., Heilbronner, R., & Schmid, S. M. (2002). The eastern Tonale fault zone: a 'natural laboratory'for crystal plastic deformation of quartz over a temperature range from 250 to 700 C. *Journal of structural geology*, *24*(12), 1861-1884.

Sutton, M. A., Wolters, W. J., Peters, W. H., Ranson, W. F., & McNeill, S. R. (1983). Determination of displacements using an improved digital correlation method. *Image and vision computing*, *1*(3), 133-139.

Tagliaferri, F., Waller, J., Andò, E., Hall, S. A., Viggiani, G., Bésuelle, P., & DeJong, J. T. (2011). Observing strain localisation processes in bio-cemented sand using x-ray imaging. *Granular Matter*, *13*(3), 247-250.

Tape, C., Holtkamp, S., Silwal, V., Hawthorne, J., Kaneko, Y., Ampuero, J. P., & West, M. E. (2018). Earthquake nucleation and fault slip complexity in the lower crust of central Alaska. *Nature Geoscience*, *11*(7), 536-541.

Tapponnier, P., & Brace, W. F. (1976, April). Development of stress-induced microcracks in Westerly granite. In *International Journal of Rock Mechanics and Mining Sciences & Geomechanics Abstracts* (Vol. 13, No. 4, pp. 103-112). Pergamon.

Trugman, D. T., & Ross, Z. E. (2019). Pervasive foreshock activity across southern California. *Geophysical Research Letters*, *46*(15), 8772-8781.

Tudisco, E., Andò, E., Cailletaud, R., & Hall, S. A. (2017). TomoWarp2: A local digital volume correlation code. *SoftwareX*, *6*, 267-270.

Tudisco, E., Hall, S. A., Charalampidou, E. M., Kardjilov, N., Hilger, A., & Sone, H. (2015). Full-field measurements of strain localisation in sandstone by neutron tomography and 3D-volumetric digital image correlation. *Physics Procedia*, *69*, 509-515.

Vajdova, V., Baud, P., & Wong, T. F. (2004). Compaction, dilatancy, and failure in porous carbonate rocks. *Journal of Geophysical Research: Solid Earth*, *109*(B5), B05204.

Vajdova, V., Zhu, W., Chen, T. M. N., & Wong, T. F. (2010). Micromechanics of brittle faulting and cataclastic flow in Tavel limestone. *Journal of Structural Geology*, 32(8), 1158-1169.

Van Der Walt, S., Colbert, S. C., & Varoquaux, G. (2011). The NumPy array: a structure for efficient numerical computation. *Computing in science & engineering*, *13*(2), 22-30.

Vardoulakis, I., & Aifantis, E. C. (1991). A gradient flow theory of plasticity for granular materials. *Acta mechanica*, *87*(3), 197-217.

Vauchez, A., Egydio-Silva, M., Babinski, M., Tommasi, A., Uhlein, A., & Liu, D. (2007). Deformation of a pervasively molten middle crust: insights from the neoproterozoic Ribeira-Araçuaí orogen (SE Brazil). *Terra Nova*, *19*(4), 278-286.

Vauchez, A., Tommasi, A., & Mainprice, D. (2012). Faults (shear zones) in the Earth's mantle. *Tectonophysics*, *558*, 1-27.

Vitale, S., & Mazzoli, S. (2008). Heterogeneous shear zone evolution: the role of shear strain hardening/softening. *Journal of Structural Geology*, *30*(11), 1383-1395.

Vu, C. C., Weiss, J., Ple, O., Amitrano, D., & Vandembroucq, D. (2018). Revisiting statistical size effects on compressive failure of heterogeneous materials, with a special focus on concrete. *Journal of the Mechanics and Physics of Solids*, *121*, 47-70.

Vu, C. C., Amitrano, D., Plé, O., & Weiss, J. (2019). Compressive failure as a critical transition: Experimental evidence and mapping onto the universality class of depinning. *Physical Review Letters*, *122*(1), 015502.

Vutukuri, V. S., Lama, R. D., & Saluja, S. S. (1974). Handbook on mechanical properties of rocks.

Walsh, J. B., & Brace, W. F. (1972, January). Elasticity of rock in uniaxial strain. In *International Journal of Rock Mechanics and Mining Sciences & Geomechanics Abstracts* (Vol. 9, No. 1, pp. 7-15). Pergamon.

Weibull, W. (1952). A survey of statistical effects in the field of material failure. *Applied Mechanics Review*, *5*(11), 449-451.

Wiebols, G. A., & Cook, N. G. W. (1968, November). An energy criterion for the strength of rock in polyaxial compression. In *International Journal of Rock Mechanics and Mining Sciences & Geomechanics Abstracts* (Vol. 5, No. 6, pp. 529-549). Pergamon.

Wong, T. F. (1990). Mechanical compaction and the brittle—ductile transition in porous sandstones. *Geological Society, London, Special Publications*, *54*(1), 111-122.

Wong, T. F., & Baud, P. (2012). The brittle-ductile transition in porous rock: A review. *Journal of Structural Geology*, 44, 25-53.

Wong, T. F., Szeto, H., & Zhang, J. (1992). Effect of loading path and porosity on the failure mode of porous rocks. *Applied Mechanics Review*, 45, 281-293.

Wong, T. F., Wong, R. H., Chau, K. T., & Tang, C. A. (2006). Microcrack statistics, Weibull distribution and micromechanical modeling of compressive failure in rock. *Mechanics of Materials*, *38*(7), 664-681.

Zapperi, S., Nukala, P. K. V., & Šimunović, S. (2005). Crack roughness and avalanche precursors in the random fuse model. *Physical Review E*, *71*(2), 026106.

Zhu, W., Baud, P., & Wong, T. F. (2010). Micromechanics of cataclastic pore collapse in limestone. *Journal of Geophysical Research: Solid Earth*, *115*(B4), B04405.

Other co-authored publications

Renard, F., Kandula, N., McBeck, J., & Cordonnier, B. (2020). Creep burst coincident with faulting in marble observed in 4-D synchrotron X-ray imaging triaxial compression experiments. *Journal of Geophysical Research: Solid Earth*, *125*(9), e2020JB020354.

Mukherji, S., Kandula, N., Sood, A. K., & Ganapathy, R. (2019). Strength of mechanical memories is maximal at the yield point of a soft glass. *Physical Review Letters*, *122*(15), 158001.

Renard, F., McBeck, J., Cordonnier, B., Zheng, X., Kandula, N., Sanchez, J. R., & Dysthe, D. K. (2019). Dynamic in situ three-dimensional imaging and digital volume correlation analysis to quantify strain localization and fracture coalescence in sandstone. *Pure and Applied Geophysics*, *176*(3), 1083-1115.

Renard, F., Weiss, J., Mathiesen, J., Ben-Zion, Y., Kandula, N., & Cordonnier, B. (2018). Critical evolution of damage toward system-size failure in crystalline rock. *Journal of Geophysical Research: Solid Earth*, *123*(2), 1969-1986.

Renard, F., Cordonnier, B., Kobchenko, M., Kandula, N., Weiss, J., & Zhu, W. (2017). Microscale characterization of rupture nucleation unravels precursors to faulting in rocks. *Earth and Planetary Science Letters*, *476*, 69-78.

Conference abstracts

Kandula, N., Renard, F., Weiss, J., Cordonnier, B., & Kobchenko, M. (2017, April). The route to shear failure in a non-porous rock revealed by X-ray microtomography. In *EGU General Assembly Conference Abstracts* (p. 11081).

Kandula, N., Renard, F., Weiss, J., Dysthe D K., Cordonnier, B., & Kobchenko, M. (2017, May). Time resolved X-ray microtomography reveals route to shear failure in a non-porous rock. In *Hercules Specialized Course HSC19 Conference Abstract.*

Kandula, N., Renard, F., Weiss, J., Cordonnier, B., & Kobchenko, M. (2017, June). Time resolved X-ray microtomographic studies of shear failure in a non-porous rock. In *3rd International Conference on Tomography of Materials and Structures Abstracts*.

Kandula, N., Renard, F., Weiss, J., Dysthe D K., Cordonnier, B., & Kobchenko, M. (2018, March). Dynamics of Microscale Precursors Establish Brittle-Compressive Failure in Rocks as a Critical Phenomena. In *MAXIV-ESS-FUN Annual Meeting Abstract.*

Kandula, N., Renard, F., Weiss, J., Dysthe D K., Cordonnier, B., & Kobchenko, M. (2018, August). Dynamics of Microscale Precursors Establish Brittle-Compressive Failure in Carrara marble as a Critical Phenomena. In *Gordon Research Conference Abstract.*

Kandula, N., Renard, F., Weiss, J., Dysthe D K., Cordonnier, B. (2019, February). Dynamics of microscale precursors establish brittle compressive failure as a critical phenomenon in Carrara marble. In *Avalanche Dynamics and Precursors of Catastrophic Events Workshop Abstract*.